Dynamics of Multi-functional Acoustic Holograms in Contactless Ultrasonic Energy Transfer Systems

Marjan Bakhtiari-Nejad

Dissertation submitted to the faculty of the
Virginia Polytechnic Institute and State University
in partial fulfillment of the requirements for the degree of

Doctor of Philosophy
in
Engineering Mechanics

Shima Shahab, Chair
Muhammad R. Hajj
Rafael V. Davalos
Eli Vlaisavljevich
Raffaella De Vita

July 31, 2020
Blacksburg, Virginia

Keywords: acoustic hologram, acoustic patterning, ultrasonic power transfer, acoustic impedance matching layers, high-intensity focused ultrasound, nonlinear acoustics, piezoelectric transducers, stable cavitation, ultrasound microbubble dynamics

Dynamics of Multi-functional Acoustic Holograms in Contactless Ultrasonic Energy Transfer Systems

Marjan Bakhtiari-Nejad

ABSTRACT

Contactless ultrasonic power transfer (UPT), using piezoelectric transducers, is based on transferring energy using acoustic waves, in which the waves are generated by an acoustic source or transmitter and then transferred through an acoustic medium such as water or human tissue to a sensor or receiver. The receiver then converts the mechanical strain induced by the incident acoustic waves to electricity and delivers to an electrical load, in which the electrical power output of the system can be determined. The execution and efficiency of this technology can be significantly enhanced through patterning, focusing, and localization of the transmitted acoustic energy in space to simultaneously power pre-determined distributed sensors or devices. A passive 3D-printed acoustic hologram plate alongside a single transducer can generate arbitrary and pre-designed ultrasound fields in a particular distance from the hologram mounted on the transmitter, i.e., a target plane. This dissertation presents the use of these simple, cost-effective, and high-fidelity acoustic holograms in UPT systems to selectively enhance and pattern the electrical power output from the receivers. Different holograms are numerically designed to create single and multi-focal pressure patterns in a target plane where an array of receivers are placed. The incident sound wave from a transmitter, after passing through the hologram, is manipulated, hence, the output field is the desired pressure field, which excites the receivers located at the pre-determined focal points more significantly. Furthermore, multi-functional holograms are designed to generate multiple images at different target planes and driving frequencies, called, respectively, multi-image-plane and multi-frequency patterning holograms. The multiple desired pressure distributions are encoded on the single hologram plate and each is reconstructed by changing the axial distance and by switching the frequency. Several proof-of-concept experiments are performed to verify the functionality of the computationally designed holograms, which are fabricated using modern 3D-printers, i.e., the desired wavefronts are encoded in the hologram plates' thickness profile, being input to the 3D-printer. The experiments include measurement of

output pressure fields in water using needle hydrophones and acquisition of receivers' voltage output in UPT systems.

Another technique investigated in this dissertation is the implementation of acoustic impedance matching layers deposited on the front leading surface of the transmitter and receiver transducers. Current UPT systems suffer from significant acoustic losses through the transmission line from a piezoelectric transmitter to an acoustic medium and then to a piezoelectric receiver. This is due to the unfavorable acoustic impedance mismatch between the transducers and the medium, which causes a narrow transducer bandwidth and a considerable reflection of the acoustic pressure waves at the boundary layers. Using matching layers enhance the acoustic power transmission into the medium and then reinforce the input as an excitation into the receiver. Experiments are performed to identify the input acoustic pressure from a cylindrical transmitter to a receiver disk operating in the 33-mode of piezoelectricity. Significant enhancements are obtained in terms of the receiver's electrical power output when implementing a two-layer matching structure. A design platform is also developed that can facilitate the construction of high-fidelity acoustically matched transducers, that is, the material layers' selection and determination of their thicknesses. Furthermore, this dissertation presents a numerical analysis for the dynamical motions of a high-intensity focused ultrasound (HIFU)-excited microbubble or stable acoustic cavitation, which includes the effects of acoustic nonlinearity, diffraction, and absorption of the medium, and entails the problem of several biomedical ultrasound applications. Finally, the design and use of acoustic holograms in microfluidic channels are addressed which opens the door of acoustic patterning in particle and cell sorting for medical ultrasound systems.

Dynamics of Multi-functional Acoustic Holograms in Contactless Ultrasonic Energy Transfer Systems

Marjan Bakhtiari-Nejad

GENERAL AUDIENCE ABSTRACT

This dissertation presents several techniques to enhance the wireless transfer of ultrasonic energy in which the sound wave is generated by an acoustic source or transmitter, transferred through an acoustic medium such as water or human tissue to a sensor or receiver. The receiver transducer then converts the vibrational energy into electricity and delivers to an electrical load in which the electrical power output from the system can be determined. The first enhancement technique presented in this dissertation is using a pre-designed and simple structured plate called an acoustic hologram in conjunction with a transmitter transducer to arbitrarily pattern and shape ultrasound fields at a particular distance from the hologram mounted on the transmitter. The desired wavefront such as single or multi-focal pressure fields or an arbitrary image such as a VT image pattern can simply be encoded in the thickness profile of this hologram plate by removing some of the hologram material based on the desired shape. When the sound wave from the transmitter passes this structured plate, it is locally delayed in proportion to the hologram thickness due to the different speed of sound in the hologram material compared to water. In this dissertation, various hologram types are designed numerically to implement in the ultrasonic power transfer (UPT) systems for powering receivers located at the predetermined focal points more significantly and finally, their functionality and performances are verified in several experiments.

Current UPT systems suffer from significant acoustic losses through the transmission from a transmitter to an acoustic medium and then to a receiver due to the different acoustic impedance (defined as the product of density and sound speed) between the medium and transducers material, which reflects most of the incident pressure wave at the boundary layers. The second enhancement technology addressed in this dissertation is using intermediate materials, called acoustic impedance matching layers, bonded to the front side of the transmitter and receiver face to alleviate the acoustic impedance mismatch. Experiments are performed to identify the input acoustic pressure from a transmitter to a receiver. Using a two-layer matching structure, significant enhancements are observed in terms of the receiver's electrical power output. A design platform is also developed

that can facilitate the construction of high-fidelity acoustically matched transducers, that is, the material layers' selection and determination of their thicknesses. Furthermore, this dissertation presents a numerical analysis for the dynamical motions of a microbubble exposed to a high-intensity focused ultrasound (HIFU) field, which entails the problem of several biomedical ultrasound applications such as microbubble-mediated ultrasound therapy or targeted drug delivery. Finally, an enhancement technique involving the design and use of acoustic holograms in microfluidic channels is addressed which opens the door of acoustic patterning in particle and cell sorting for medical ultrasound systems.

To my beloved husband, ***Omidreza Sadeghi****, supportive parents,* ***Firooz Bakhtiari-Nejad*** *and* ***Roxana Ketabestan****, and my caring sisters,* ***Maryam****,* ***Faezeh****, and* ***Mahsan*** *(my twin).*
They have given me their love throughout this challenging journey.

Acknowledgments

I would first like to express my sincere appreciation to my advisor, Dr. Shima Shahab, for all the encouragement, guidance, and support. I would like to extend my deep gratitude to the rest of my committee members: Dr. Mohammad Hajj, for all his valuable contributions in my research, constructive comments, and continuous support. Dr. Rafael Davalos, for providing me an opportunity to build microfluidic devices in his lab and his valuable comments. Dr. Eli Vlaisavljevich for which we had great research-based discussions in his lab and his helpful comments and continuous support. Dr. Raffaella De Vita, for her valuable time and insightful remarks.

I would like to truly thank my labmates, Omidreza Sadeghi, Ahmed Elnahhas, Eric Dupuis, Aarushi Bhargava, Vamsi Meesala, Thomas Winnard, and Ahmed Sallam for their friendship and help in my research. Especial thanks go to Omidreza Sadeghi and Ahmed Elnahhas for their help with my experiments, their fantastic ideas, and helpful comments. I also gratefully thank all of my dear friends for their true friendship along this challenging journey. I would also like to thank the department of biomedical engineering and mechanics for partially sponsoring my Ph.D. studies through graduate teaching assistant positions, particularly, in summer 2020, where their support helped me finishing my experiments. Moreover, I would like to thank the National Science Foundation (NSF; Grant NO. ECCS-1711139) and Institute for Critical Technology and Applied Science (ICTAS) at Virginia Tech, for partially sponsoring my research and graduate education.

Last but not the least, I am forever indebted to my dear family and would like to profoundly thank them: My father, Dr. Firooz Bakhtiari-Nejad, professor of mechanical engineering, who introduced me to the engineering world and immensely inspired me to become an ethical researcher. My mother, Roxana Ketabestan, whose incredible emotional support has always helped me through both my life and academic journey. My older sisters, Maryam and Faezeh, and my twin sister, Mahsan, who have always been there for me and helped me emotionally and conceptually. Above all, I give my most special and deepest thanks to my beloved husband, Omidreza, for his patience, sacrifices and understanding, emotional support, and tremendous help in my research. I could not have done it without you!

Contents

List of figures

List of tables

Chapter 1

Introduction

The main research goal of this dissertation lays on the enhancement of contactless ultrasonic power transfer (UPT) systems using piezoelectric transducers in which the sound wave is generated by an acoustic source or transmitter and then transferred through an acoustic medium such as water or human tissue to a sensor or receiver [1-4]. The execution and efficiency of this technology can be significantly enhanced through patterning, focusing, and localization of the transmitted acoustic energy in space via acoustic holography. This work aims to provide the design platform for the functional monolithic passive acoustic holograms to shape ultrasonic fields of complex and arbitrary spatial distributions using planer single element transducers in UPT systems.

1.1 Background and Motivation

Implementing a simple acoustic hologram alongside a single ultrasonic transducer [2, 5, 6] enables new capabilities in multifocal focusing, acoustic patterning, and the contactless ultrasonic power transfer (UPT) for receivers/sensors. To accomplish the goal of power enhancement in UPT, the main objectives cover a broad range, from fundamental theoretical and experimental investigation to high impact implementations by (1) electro-elastic-acoustic modeling and testing of various static acoustic holograms in UPT systems focusing on the acoustic wave propagation and guiding mechanisms [7]; identifying and clarifying the key parameters in the holograms to generate multiple acoustic images at different depths [5, 8] and to create different dynamic acoustic fields [9-12]; validating and leveraging the theory of the acoustic-elastic models for high-fidelity hologram designs and measuring the desired ultrasonic fields in practice [5-7, 13-15], (2) implementing acoustic impedance matching layers in UPT [16], and (3) Analyzing oscillations of

focused ultrasound (FU)-excited microbubbles [17] and design of acoustic holograms that can be used in microfluidic channels for microbubble, particle, and cell sorting and patterning.

This dissertation is focused on the enhancement of wireless UPT systems by designing high-fidelity metamaterial-based acoustic holograms, i.e., three-dimensional printed holographic lenses; implementing acoustic impedance matching layers in UPT; and analyzing acoustic nonlinearity due to high-intensity focused ultrasound (HIFU) field. Passive acoustic holograms store the phase or/and amplitude profile of the desired wavefront in a two-dimensional design [5, 15], which is used to reconstruct the acoustic pressure field when illuminated with a coherent acoustic source; and matching layers alleviate the acoustic impedance mismatch between transducer materials and medium. Recently acoustic holograms have shown promising results in various applications including therapeutic ultrasound [18-20], diagnostic ultrasound imaging [21], ultrasonic power transfer [7], and particle or cell manipulation [5, 22-24] techniques. Building on various methods including analytical, computational, and experimental tools, this dissertation has answered fundamental questions such as "how to modulate the wavefront of a passing sound wave and shape ultrasound pressure fields?","how to increase the effective degrees of freedom that can be attained in the reconstruction of the wavefront?", "how to improve the efficiency of ultrasonic systems and minimize acoustic losses?", and "what are the effects of finite-amplitude sound and nonlinear acoustics during FU insonation?"

We investigate the use of passive acoustic holograms to create multifocal pressure patterns in a plane where target receivers are located at specific focal points or regions. First, a phase-shifting hologram is mathematically designed. Then, a multi-physics acoustic-electro-elastic model is presented for an axially vibrating cylindrical transmitter in conjunction with the hologram to power multiple piezoelectric receivers. Experiments were performed to measure ultrasound fields and to show the capability of an acoustic hologram to selectively power an array of the receivers and the results show the potential of acoustic holograms in constructing and patterning desired single and multi-focal acoustic fields to selectively transmit energy to the receiver(s) located at the predetermined focal point(s) with dramatic electrical power output enhancements. The design of acoustic impedance matching layers is also presented to alleviate unfavorable acoustic impedance mismatch and hence improve the power transfer in ultrasonic acoustic energy transfer (UAET) systems. Furthermore, we provide some design ideas to fabricate acoustic holograms that can be used in microfluidic devices for possible manipulation of microbubbles, particles, and cells in medical diagnostic and therapeutic ultrasound applications.

Among all the classes of wireless energy transfer, acoustic energy transfer is the safest technology to adopt. In particular, biomedical applications offer great potential for contactless ultrasonic energy transfer, e.g., battery charging for medical implants without surgery is tremendously valuable. One of the main challenges for UPT is to desirably focus and pattern the transmitted energy and hence locally power wireless piezoelectric-based sensors. As an alternative to the expensive and complex phase-shifting circuity and transducer arrays, the use of a passive monolithic hologram alongside a single ultrasonic transducer is a new approach that potentially has endless medical diagnostic and therapeutic ultrasound applications. This technique is inexpensive and allows for the simplicity of the design and fabrication of 3D-printed holographic lenses. These systems influence the design of efficient ultrasonic systems allowing for enhanced and selective transfer of acoustic energy by taking advantage of beam-steering and multi-focal patterning generated by the hologram.

This research through conducting experimentally-validated multiphysics modeling aims at filling a knowledge gap in terms of focusing and spatial patterning of the transmitted acoustic energy in UPT systems. The research findings in acoustic wave propagation and guiding mechanisms enable enhanced and selective powering of medical sensors or ultrasonic implanted transducers, improving diagnostic medical imaging, and generating selective heating/energy deposition for therapeutic applications. Generation, focusing, and patterning the desired sound fields by means of passive acoustic holograms in UPT has the potential to benefit the medical diagnostic and therapeutic ultrasound fields or employing in more general applications such as efficiently powering sensor networks, e.g., in localized low power wireless transfer system for distributed automotive sensing. The findings will also open the door for using acoustic holograms in microfluidic devices in ultrasound therapy as well as acoustic sensing, energy deposition, and medical diagnostic imaging. We also performed a numerical/analytical study to analyze single-bubble dynamics in the nonlinear HIFU pressure field [17], which covers several medical ultrasound applications such as employing FU-excited drug-loaded microbubbles for delivering and releasing of chemotherapeutic drugs and antibodies in the treatments of neurodegenerative diseases such as Parkinson's and Alzheimer's disease as well as glioma treatment [25-30].

Moreover, this work addresses the implementation of acoustic impedance matching layers deposited on the front leading surface of the source and receiver transducers [16, 31-38]. Current UPT systems suffer from significant acoustic losses through the transmission line from a piezoelectric transmitter to an acoustic medium and then to a piezoelectric receiver. This is due to

the unfavorable acoustic impedance mismatch between the transducers and the medium, which causes a narrow transducer bandwidth and a considerable reflection of the acoustic pressure waves at the boundary layers. Using a two-layer matching structure enhances the acoustic power transmission into the medium and then reinforces the input as an excitation into the receiver.

1.2 Intellectual Merit

The conventional approach for generating three-dimensional complex sound fields rely on a large number of active transducers and phase shifting circuits. However, these can only be used in small numbers in ultrasound applications, which limits the complexity or degrees of freedom that can be attained in the wavefront. As an alternative to the costly and complex phase-shifting circuity and transducer arrays, the use of cost-effective passive 3D-printed acoustic phase holograms alongside a single and simple ultrasonic transducer is a transformative technology for shaping ultrasound fields with significantly higher degrees of freedom and high fidelity, that potentially has endless applications. This dissertation, for the first time, introduces the concept of implementing acoustic holograms for the contactless transfer of ultrasonic power. This will lead to a new understanding of acoustic holography systems that will influence the design of efficient UAET systems. Moreover, a design platform developed in this dissertation can facilitate the construction of high-fidelity acoustically matched transducers, that is, the material layers selection and determination of their thicknesses.

1.3 Outline of the dissertation

This dissertation presents the outcomes of three research projects, each aims to enhance the ultrasonic power transfer (UPT) systems covering different objectives. Firstly, chapters 2 and 3 address the holographic reconstruction of desired acoustic images using various kinds of acoustic holograms for focusing and patterning the contactless transfer of ultrasonic power. Secondly, chapter 4 investigates the use of acoustic impedance matching layers in UPT systems to reduce losses associated with acoustic reflections. Lastly, a numerical study is presented in chapter 5 to examine the effects of acoustic nonlinearity, due to high-intensity focused ultrasound (HIFU) field, on a microbubble dynamics, and is covered a brief theoretical study of implementing acoustic holography in microfluidic devices.

- **Chapter 2** introduces the concept of implementing acoustic holography via 3D-printed high-fidelity passive acoustic phase holograms in UPT systems. This chapter defines

acoustic power transmission for heterogeneous media and explains the angular spectrum approach (ASA) for the forward and backward propagation of acoustic waves. The steps of the optimization algorithm, iterative angular spectrum approach (IASA), to design acoustic holograms for a particular field are listed in detail, and the distributed parameter piezoelectric model is presented to compute the ultrasonic power transfer from the hologram alongside a single transmitter to spatially-distributed receivers located in a target plane. Finally, this chapter covers the results for computational and experimental holographic reconstruction of different acoustic images, acquisition of receivers' voltage output in UPT experiments using multi-focal holograms, as well as error metrics outcomes for quality evaluation of the multi-focal holograms.

- **Chapter 3** provides the computational and experimental realization of multiple acoustic images using a single multi-functional hologram of two types, namely multi-image-plane and multi-frequency patterning holograms. The extension needed for the IASA optimization algorithm to compute each type of multi-functional holograms is described, and error metrics are presented to determine the fidelity of various holographic reconstruction of multiple images.
- **Chapter 4** develops a design platform for the simple construction of acoustically matched transducers using a two-layer matching structure to enhance the wireless ultrasonic transfer of power. In this matching configuration, we consider one of the layers as the used glue for bonding the other layer to the front side of the transmitter and receiver, hence, in this way, we take into account the thickness of glue which is a significant performance factor. A transfer matrix method is explained to determine the material layers' thickness to match the transducers at a particular frequency to an acoustic medium of interest. Perfect matching is achieved by equating the equivalent acoustic impedance of the heterogeneous media, including an acoustic medium, matching layers, and a transducer, to the acoustic impedance of the acoustic medium. Furthermore, comprehensive and detailed lists of applicable materials for matching layers with their acoustic properties are tabulated in this chapter.
- **Chapter 5** addresses the dynamics of a microbubble exposed to nonlinear high-intensity focused ultrasound (HIFU) field, which forms fundamentals of acoustic stable cavitation, i.e., oscillations of bubbles in size and shape without a violent collapse. The focused ultrasound (FU)-induced stable cavitation covers a wide range of biomedical applications

such as ultrasonic targeted drug delivery. Finally, this chapter illustrates a process to design acoustic holograms that can be used in microfluidic devices for possible manipulation, acoustic patterning, and sorting cells, particles, and microbubbles in diagnostic and therapeutic medical applications.

- Lastly, **Chapter 6** summarizes the concluding remarks of the aforementioned chapters and proposes several future research directions for the techniques presented in this dissertation.

Bibliography

[1] Roes, M.G., Duarte, J.L., Hendrix, M.A., and Lomonova, E.A., *Acoustic energy transfer: A review.* IEEE Transactions on Industrial Electronics, 2013. **60**(1): p. 242-248.

[2] Shahab, S., Gray, M., and Erturk, A., *Ultrasonic power transfer from a spherical acoustic wave source to a free-free piezoelectric receiver: Modeling and experiment.* Journal of Applied Physics, 2015. **117**(10): p. 104903.

[3] Shahab, S. and Erturk, A., *Contactless ultrasonic energy transfer for wireless systems: acoustic-piezoelectric structure interaction modeling and performance enhancement.* Smart Materials and Structures, 2014. **23**(12): p. 125032.

[4] Basaeri, H., Christensen, D.B., and Roundy, S., *A review of acoustic power transfer for biomedical implants.* Smart Materials and Structures, 2016. **25**(12).

[5] Melde, K., Mark, A.G., Qiu, T., and Fischer, P., *Holograms for acoustics.* Nature, 2016. **537**(7621): p. 518.

[6] Zhang, J., Yang, Y., Zhu, B., Li, X., Jin, J., Chen, Z., Chen, Y., and Zhou, Q., *Multifocal point beam forming by a single ultrasonic transducer with 3D printed holograms.* Applied Physics Letters, 2018. **113**(24): p. 243502.

[7] Bakhtiari-Nejad, M., Elnahhas, A., Hajj, M.R., and Shahab, S., *Acoustic holograms in contactless ultrasonic power transfer systems: Modeling and experiment.* Journal of Applied Physics, 2018. **124**(24): p. 244901.

[8] Zhu, Y., Hu, J., Fan, X., Yang, J., Liang, B., Zhu, X., and Cheng, J., *Fine manipulation of sound via lossy metamaterials with independent and arbitrary reflection amplitude and phase.* Nature communications, 2018. **9**(1): p. 1632.

[9] Brown, M.D., Cox, B.T., and Treeby, B.E., *Design of multi-frequency acoustic kinoforms.* Applied Physics Letters, 2017. **111**(24): p. 244101.

[10] Cox, L., Melde, K., Croxford, A., Fischer, P., and Drinkwater, B.W., *Acoustic Hologram Enhanced Phased Arrays for Ultrasonic Particle Manipulation.* Physical Review Applied, 2019. **12**(6): p. 064055.

[11] Brown, M.D., Cox, B.T., and Treeby, B.E., *Stackable acoustic holograms.* Applied Physics Letters, 2020. **116**(26): p. 261901.

[12] Norasikin, M.A., Martinez Plasencia, D., Polychronopoulos, S., Memoli, G., Tokuda, Y., and Subramanian, S. *SoundBender: dynamic acoustic control behind obstacles*. in *Proceedings of the 31st Annual ACM Symposium on User Interface Software and Technology*. 2018.

[13] Brown, M., Nikitichev, D., Treeby, B., and Cox, B., *Generating arbitrary ultrasound fields with tailored optoacoustic surface profiles.* Applied Physics Letters, 2017. **110**(9): p. 094102.

[14] Xie, Y., Shen, C., Wang, W., Li, J., Suo, D., Popa, B.-I., Jing, Y., and Cummer, S.A., *Acoustic holographic rendering with two-dimensional metamaterial-based passive phased array.* Scientific reports, 2016. **6**: p. 35437.

[15] Brown, M.D., *Phase and amplitude modulation with acoustic holograms.* Applied Physics Letters, 2019. **115**(5): p. 053701.

[16] Bakhtiari-Nejad, M., Hajj, M.R., and Shahab, S., *Dynamics of acoustic impedance matching layers in contactless ultrasonic power transfer systems.* Smart Materials and Structures, 2020. **29**(3): p. 035037.

[17] Bakhtiari-Nejad, M. and Shahab, S. *Effects of Nonlinear Propagation of Focused Ultrasound on the Stable Cavitation of a Single Bubble*. in *Acoustics*. 2018. Multidisciplinary Digital Publishing Institute.

[18] Jiménez-Gambín, S., Jiménez, N., Benlloch, J.M., and Camarena, F., *Holograms to focus arbitrary ultrasonic fields through the skull.* Physical Review Applied, 2019. **12**(1): p. 014016.

[19] Maimbourg, G., Houdouin, A., Deffieux, T., Tanter, M., and Aubry, J.-F., *3D-printed adaptive acoustic lens as a disruptive technology for transcranial ultrasound therapy using single-element transducers.* Physics in Medicine & Biology, 2018. **63**(2): p. 025026.

[20] Ferri, M., Bravo, J.M., Redondo, J., and Sánchez-Pérez, J.V., *Enhanced numerical method for the design of 3-d-printed holographic acoustic lenses for aberration correction of single-element transcranial focused ultrasound.* Ultrasound in medicine & biology, 2019. **45**(3): p. 867-884.

[21] Kruizinga, P., van der Meulen, P., Fedjajevs, A., Mastik, F., Springeling, G., de Jong, N., Bosch, J.G., and Leus, G., *Compressive 3D ultrasound imaging using a single sensor.* Science advances, 2017. **3**(12): p. e1701423.

[22] Melde, K., Choi, E., Wu, Z., Palagi, S., Qiu, T., and Fischer, P., *Acoustic fabrication via the assembly and fusion of particles.* Advanced Materials, 2018. **30**(3): p. 1704507.

[23] Ma, Z., Holle, A.W., Melde, K., Qiu, T., Poeppel, K., Kadiri, V.M., and Fischer, P., *Acoustic Holographic Cell Patterning in a Biocompatible Hydrogel.* Advanced Materials, 2020. **32**(4): p. 1904181.

[24] Gu, Y., Chen, C., Rufo, J., Shen, C., Wang, Z., Huang, P.-H., Fu, H., Zhang, P., Cummer, S.A., and Tian, Z., *Acoustofluidic Holography for Micro-to Nanoscale Particle Manipulation.* ACS Nano, 2020.

[25] Tung, Y.-S., Vlachos, F., Feshitan, J.A., Borden, M.A., and Konofagou, E.E., *The mechanism of interaction between focused ultrasound and microbubbles in blood-brain barrier opening in mice.* The Journal of the Acoustical Society of America, 2011. **130**(5): p. 3059-3067.

[26] Wang, S., Samiotaki, G., Olumolade, O., Feshitan, J.A., and Konofagou, E.E., *Microbubble type and distribution dependence of focused ultrasound-induced blood–brain barrier opening.* Ultrasound in medicine & biology, 2014. **40**(1): p. 130-137.

[27] Fan, C.-H., Ting, C.-Y., Chang, Y.-C., Wei, K.-C., Liu, H.-L., and Yeh, C.-K., *Drug-loaded bubbles with matched focused ultrasound excitation for concurrent blood–brain barrier opening and brain-tumor drug delivery.* Acta biomaterialia, 2015. **15**: p. 89-101.

[28] Baseri, B., Choi, J.J., Tung, Y.-S., and Konofagou, E.E., *Multi-modality safety assessment of blood-brain barrier opening using focused ultrasound and definity microbubbles: a short-term study.* Ultrasound in medicine & biology, 2010. **36**(9): p. 1445-1459.

[29] Jordão, J.F., Ayala-Grosso, C.A., Markham, K., Huang, Y., Chopra, R., McLaurin, J., Hynynen, K., and Aubert, I., *Antibodies targeted to the brain with image-guided focused ultrasound reduces amyloid-β plaque load in the TgCRND8 mouse model of Alzheimer's disease.* PloS one, 2010. **5**(5): p. e10549.

[30] Liu, H.-L., Hua, M.-Y., Chen, P.-Y., Chu, P.-C., Pan, C.-H., Yang, H.-W., Huang, C.-Y., Wang, J.-J., Yen, T.-C., and Wei, K.-C., *Blood-brain barrier disruption with focused ultrasound enhances delivery of chemotherapeutic drugs for glioblastoma treatment.* Radiology, 2010. **255**(2): p. 415-425.

[31] Ozeri, S. and Shmilovitz, D., *Ultrasonic transcutaneous energy transfer for powering implanted devices.* Ultrasonics, 2010. **50**(6): p. 556-566.

[32] Meng, M. and Kiani, M., *Design and optimization of ultrasonic wireless power transmission links for millimeter-sized biomedical implants.* IEEE transactions on biomedical circuits and systems, 2017. **11**(1): p. 98-107.

[33] Ozeri, S. and Shmilovitz, D., *Simultaneous backward data transmission and power harvesting in an ultrasonic transcutaneous energy transfer link employing acoustically dependent electric impedance modulation.* Ultrasonics, 2014. **54**(7): p. 1929-1937.

[34] Ozeri, S., Shmilovitz, D., Singer, S., and Wang, C.-C., *Ultrasonic transcutaneous energy transfer using a continuous wave 650 kHz Gaussian shaded transmitter.* Ultrasonics, 2010. **50**(7): p. 666-674.

[35] Hu, Y.-C., Liao, P.-L., Shih, W.-P., Wang, X.-Y., and Chang, P.-Z. *Study on the acoustic impedance matching of human tissue for power transmitting/charging system of implanted*

biochip. in *2009 IEEE 3rd International Conference on Nano/Molecular Medicine and Engineering*. 2009. IEEE.

[36] Denisov, A. and Yeatman, E. *Ultrasonic vs. inductive power delivery for miniature biomedical implants*. in *2010 International Conference on Body Sensor Networks*. 2010. IEEE.

[37] Song, S.H., Kim, A., and Ziaie, B., *Omnidirectional ultrasonic powering for millimeter-scale implantable devices.* IEEE Transactions on Biomedical Engineering, 2015. **62**(11): p. 2717-2723.

[38] Christensen, D.B. and Roundy, S., *Non-dimensional analysis of depth, orientation, and alignment in acoustic power transfer systems.* Smart Materials and Structures, 2018. **27**(12): p. 125013.

Chapter 2

Acoustic holograms in contactless ultrasonic power transfer systems

This chapter contains excerpts reproduced from an article published in the *Journal of Applied Physics* [1], with the permission of AIP Publishing, and a conference paper published in *SPIE Smart Structures/Nondestructive Evaluation* proceeding [2]. In this chapter, we investigate the effects of implementing designed high-fidelity acoustic holograms on the enhancement of contactless ultrasonic power transfer (UPT).

Abstract

Contactless ultrasonic acoustic energy transfer (UAET) is a new technology that eliminates risks or impracticalities associated with wired electrical connections or batteries that need to be replaced on a regular basis. This technology, which is based on the reception of acoustic waves at ultrasonic frequencies by piezoelectric receivers, can be used to wirelessly charge low-power electronics. The execution and efficiency of this technology can be significantly enhanced through patterning and focusing of the transmitted acoustic energy in space to simultaneously power distributed sensors or devices. This chapter investigates the use of an acoustic hologram to create a multifocal pressure pattern in a plane where target receivers are located at specific focal points or regions. First, a phase-shifting hologram is designed using an iterative angular spectrum approach (IASA). Then, a multi-physics acoustic-electro-elastic model is presented for an axially vibrating cylindrical transmitter used to power multiple piezoelectric receivers, in conjunction with the hologram. Experiments are also performed to show the capability of an acoustic hologram to selectively power an array of the receivers. Both analytical and experimental results show dramatic enhancement of power transfer to receivers exposed to a multi-focal pressure pattern created by

the hologram. As two case studies, bi-focal and five-element receiver setup are investigated where one specific receiver in the two-element array and two specific receivers in the five-element array are targeted. The UAET simulations predict significant power transfer enhancements to the targeted receivers, which are verified by the proof-of-concept experiments. The effects of system parameters such as input frequency, hologram aperture size, and hologram position with respect to the ultrasonic source are also reported.

2.1 Introduction

The generation and control of three-dimensional sound fields is a long-standing problem, with applications that include ultrasound medical treatment (e.g. targeted drug delivery) and imaging [3-5], energy transfer [6], and particle manipulation [7, 8]. Initially, acoustic manipulation was conducted using phased array transducers [9-12], but the cost associated with active transducers and their phase-shifting circuitry was a deterrent for their implementation. Over the past decade, acoustic metamaterials have been investigated and characterized, with demonstrated effects such as beam-steering [13-16], acoustic focusing [17-20], multifocal focusing [13, 21, 22], negative refraction [14, 23], broadband impedance matching [24], analog computing [25], acoustic cloaking [26], as well as passive acoustic holography [13, 21, 22], which has attracted significant interest because it can be used to generate arbitrarily complex acoustic fields. Passive acoustic holograms store the phase and amplitude profile of the desired wavefront in a two-dimensional design, which is used to reconstruct the acoustic pressure field when illuminated with a coherent acoustic source. These holograms can be implemented using one of two approaches, unit-based acoustic metamaterials such as labyrinthine cells [13, 21, 22], and continuous three-dimensional printed phase-shifting lenses [27-31]. Both the acoustic metamaterial and three-dimensional printing implementation offer full phase control (0 to 360 degrees), while only the acoustic metamaterials are capable of demodulating amplitude and phase controls [13, 22]. However, the simplicity of design and fabrication of the 3D-printed holographic lenses allows for their implementation in applications such as particle manipulation [27] and optically generated ultrasound [29-31].

During the same period, ultrasonic acoustic energy transfer (UAET) has emerged as a new approach for contactless energy transfer (CET). UAET relies on transferring energy using sound waves and is primarily implemented using piezoelectric transmitters and receivers. Several proof-of-concept experiments have been conducted through different media reporting various efficiencies. A review highlighting major advancements is presented by Roes *et al* [6]. One of the challenges for enhancing wireless power transmission and selectively charging sensors or devices

is patterning and focusing the transmitted acoustic energy in space. The localization of energy is important as it can be used for biomedical applications such as lithotripsy [32] (kidney stone removal), or more general applications such as efficiently powering sensor networks. Furthermore, there are scenarios where localizing the energy transfer is not only a desire but a must due to the delicacy of the system in which energy transfer is implemented. Such examples include sensor nodes [33] or neural dust sensing motes placed throughout the human brain [34]. One scenario is the use of high-intensity focused ultrasound (HIFU) technology [35] or acoustic mirroring concept [36-38] to focus the transmitted energy in space, and, thereby, strongly excite the receiver. However, focusing should obviously be carefully employed in UAET since HIFU may yield substantial energy localization and heating [35], with levels that may not be allowable because safety regulations require acoustic intensity that is lower than 94 mW/cm^2 and limit the operating frequency to 100 kHz [39].

In this chapter, we investigate the capability of a 3D-printed acoustic hologram for contactless acoustic power transfer and conduct both theoretical and experimental studies to prove the potential of this technology. To this end, we propose to combine UAET systems with the diffraction-limited acoustic holograms employing the customized fabrication procedure that was first presented by Melde *et al* [27]. We utilize an iterative angular spectrum approach (IASA) [40] to create a desired acoustic pressure pattern for the hologram fabrication. The output pressure pattern is then used in conjunction with a distributed parameter piezoelectric model [36, 41] to compute the power transfer to spatially-distributed 33-mode receivers. The effects of varying the excitation frequency, size of the hologram aperture, and position of the hologram on the target image resolution are investigated. Experiments are conducted to show the potential of acoustic holograms in constructing single- and two-focus acoustic fields to selectively power the piezoelectric receiver(s). In section 2.2, we develop the theoretical background and model for the proposed UAET-hologram system. Results from simulations performed using the derived model are presented in section 2.3. Details and results from the holographic reconstruction of the desired single-focus and multi-focal pressure fields are, respectively, discussed in sections 2.4 and 2.5 alongside the experimental validation of the computational outcomes. A summary and conclusions are presented in section 2.6.

2.2 Analysis

Figure 2.1a displays a schematic of an acoustic hologram combined with a UAET system, which includes an array of piezoelectric receivers placed in a target plane that is excited by an incident

acoustic wave from a transmitter and manipulated by the hologram. Figure 2.1b shows a schematic of the continuum model used to analyze the voltage output from the receivers.

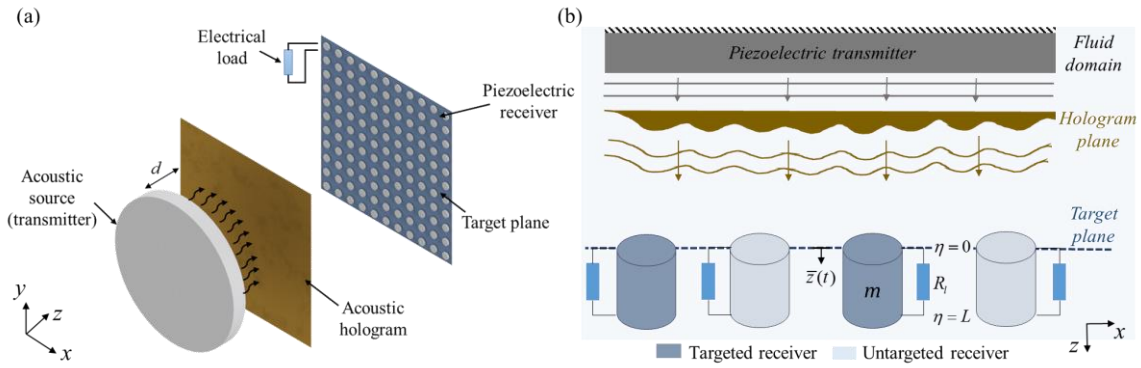

Figure 2.1. Schematic representations of (a) an ultrasound energy transfer system with an acoustic hologram and (b) the longitudinal excitation of piezoelectric receivers (located in a target plane) by the transmitter and single acoustic hologram. Each receiver's axis of symmetry is perpendicular to the target plane.

The transfer matrix for the nth material layer with characteristic acoustic impedance Z_n and thickness t_n, with one of the layers being the acoustic hologram, considering a normal incident wave through multilayer systems was derived by Callens *et al.* [42] and Hill and Dardiry [43], and is written as:

$$T_n = \begin{bmatrix} \cos(k_n t_n) & jZ_n \sin(k_n t_n) \\ \dfrac{j\sin(k_n t_n)}{Z_n} & \cos(k_n t_n) \end{bmatrix}, \tag{2.1}$$

where k_n is the wave number in the nth material. The transfer matrix represents the relation between pressure and normal particle velocity at the left and right boundary of the layer satisfying two boundary conditions, namely the *continuity of the pressure* and *continuity of the normal component of the velocity*. The equivalent transfer matrix for the s system is derived by defining $T^{eq} = T_1 T_2 ... T_{n-2} = \begin{bmatrix} T_{11}^{eq} & T_{12}^{eq} \\ T_{21}^{eq} & T_{22}^{eq} \end{bmatrix}$. Hence, the resultant equivalent acoustic impedance is written as

$$Z^{eq} = \frac{T_{11}^{eq} Z_n + T_{12}^{eq}}{T_{21}^{eq} Z_n + T_{22}^{eq}}. \tag{2.2}$$

Having calculated the equivalent acoustic impedance, the power (intensity) reflection coefficient R_I can be derived by replacing the multilayered boundary system with an equivalent single boundary system to write [44]

$$R_I = \left| \frac{Z^{eq} - Z_1}{Z^{eq} + Z_1} \right|^2 . \tag{2.3}$$

The power (intensity) transmission coefficient T_I is then derived as $T_I = 1 - R_I$.

Placing a hologram in the multilayer acoustic structure between the source (transmitter) and the target plane (four-layer system), we can calculate the power transmission coefficient as

$$\begin{aligned} T_I(x,y)\big|_{\text{four-layer}} = {} & 8Z_0{}^3 Z_h{}^2 Z_s / [4Z_0{}^3 Z_h{}^2 Z_s + 2(Z_0{}^6 + Z_h{}^4 Z_s{}^2)\sin^2(k_0 d)\sin^2(k_h t(x,y)) \\ & + (Z_0{}^3 Z_h{}^3 + Z_0{}^3 Z_h Z_s{}^2 - Z_0{}^5 Z_h - Z_0 Z_h{}^3 Z_s{}^2)\sin(2k_0 d)\sin(2k_h t(x,y)) \\ & + 2(Z_0{}^4 Z_h{}^2 + Z_0{}^2 Z_h{}^2 Z_s{}^2)\cos^2(k_h t(x,y)) + 2(Z_0{}^2 Z_h{}^4 + Z_0{}^4 Z_s{}^2) \\ & \cos^2(k_0 d)\sin^2(k_h t(x,y))], \end{aligned} \tag{2.4}$$

where $t(x,y)$ is the thickness of a pixel in the hologram plane at a position (x,y) and d is the distance between transmitter and hologram as shown in figure 2.1a, and k_0 and k_h are the wave numbers in the medium and in the hologram body, respectively. Moreover, in equation (2.4), Z_h, Z_0 and Z_s are the acoustic impedance of the hologram, medium, and transmitter, respectively. For any material m, the characteristic acoustic impedance is given by $Z_m = \rho_m c_m$, where ρ_m and c_m are, respectively, the material density and speed of sound. Equation (2.4) is derived using the aforementioned equivalent transfer matrix method in which Z_1, $Z_2 = Z_4$ and Z_3 correspond to Z_s, Z_0 and Z_h, respectively.

Accordingly, if the acoustic hologram is mounted on the transmitter (three-layer system), the power transmission coefficient is derived as

$$T_I(x,y)\big|_{\text{three-layer}} = 4Z_h{}^2 Z_0 Z_s / [(Z_h{}^2 + Z_0 Z_s)^2 \sin^2(k_h t(x,y)) + Z_h{}^2 (Z_0 + Z_s)^2 \cos^2(k_h t(x,y))]. \tag{2.5}$$

Similarly, equation (2.5) is derived using the equivalent transfer matrix method in which Z_1, Z_2 and Z_3 correspond to Z_s, Z_h and Z_0, respectively. In this chapter, we investigate employing the acoustic hologram, which is mounted on the transmitter, and we aim to determine the desired pressure field in the target plane where the receivers are located.

2.2.1 Acoustic wave propagation from transmitter and hologram

To find the transducer output pressure field, the acoustic pressure close to the transmitter, where the hologram is located, is calculated using the Fast Nearfield Method (FNM) [45, 46]. FNM is a

simulation method that takes advantage of the one-dimensional integral approach to determine the pressure near acoustic sources. The integral is the simplified form of the Rayleigh–Sommerfeld diffraction formula [47] and accounts for a uniform surface velocity of the circular source [48]. To predict the acoustic field distribution at a target plane, we use the Angular Spectrum Approach (ASA) in which the complex acoustic pressure wave is represented as the summation of plane waves [49] and write

$$p_0(x, y, z = 0) = |p_0|(x, y, z = 0)e^{j\Delta\phi(x,y,z)} = \sum_{k_x}\sum_{k_y} P_0(k_x, k_y, z = 0)e^{j(k_x x + k_y y + k_z z)}, \tag{2.6}$$

where $|p_0|$ and $\Delta\phi$ are, respectively, the amplitude and relative phase of the complex input acoustic pressure and j is the unit imaginary number. The time dependency of $p_0(x, y, 0)$ is excluded for the sake of brevity. Equation (2.6) satisfies the Helmholtz equation $\nabla^2 p(\omega) + k^2 p(\omega) = 0$ in the frequency (ω) domain, providing that $k^2 = k_x{}^2 + k_y{}^2 + k_z{}^2$, where $k = \omega / c$ is the wave number and c is the speed of sound in the fluid domain. The angular spectrum of the pressure wave at constant $z = 0$, $P_0(k_x, k_y, z = 0)$, is obtained from the two-dimensional Fourier transform as

$$P_0(k_x, k_y, 0) = \int_{-\infty}^{\infty}\int_{-\infty}^{\infty} p_0(x, y, 0)e^{-j(k_x x + k_y y)}dxdy. \tag{2.7}$$

The ASA computes the pressure at any arbitrary plane (target plane) using pressure field information at a parallel plane, e.g. $z = 0$ (hologram plane). Hence, when the angular spectrum of input pressure $P_0(k_x, k_y, 0)$ is identified, the angular spectrum at every parallel plane *z* is obtained as

$$P(k_x, k_y, z) = P_0(k_x, k_y, 0)H(k_x, k_y, z), \tag{2.8}$$

where $H(k_x, k_y, z)$ is the propagation function [50] written as

$$H(k_x, k_y, z) = e^{jk_z z}, \tag{2.9}$$

Accordingly, the pressure distribution at any desired (target) plane *z* is calculated using the inverse two-dimensional Fourier transform as

$$p(x, y, z) = \frac{1}{4\pi^2}\int_{-\infty}^{\infty}\int_{-\infty}^{\infty} P(k_x, k_y, z)e^{j(k_x x + k_y y)}dk_x dk_y. \tag{2.10}$$

Similarly, the ASA can be used to compute the backpropagation of the pressure field from the target plane to the hologram plane in which the corresponding angular spectrum at $z=0$ is calculated as

$$P_0(k_x,k_y,0)=P(k_x,k_y,z)H(k_x,k_y,-z), \tag{2.11}$$

where $H(k_x,k_y,-z)$ is the backpropagation function written as $H(k_x,k_y,-z)=e^{-jk_z z}$.

It should be noted that a more accurate method of obtaining the transducer output pressure field is experimentally measuring the field fairly close to the transmitter (using a hydrophone, e.g., in the water domain) and then numerically backpropagating to the transducer face via the ASA.

The ASA theory explained in this section is employed for the Near-field Acoustic Holography (NAH) method. NAH is a technique that has been used for sound source identification [51-55] and it is particularly effective for an inverse problem, i.e., backpropagation of the sound pressure from a target plane to a plane close to the acoustic source. NAH constructs the pressure field in a plane, as well as the fluid velocity and acoustic intensity vectors based upon the pressure information of a parallel plane [49]. In this chapter, by using the NAH, we show the capability to design an acoustic hologram to focus the acoustic energy in the desired pattern. The procedure will be explained in the next two sections.

2.2.2 Iterative angular spectrum approach optimization algorithm

To obtain the desired acoustic pressure pattern in the target plane, the Iterative Angular Spectrum Approach (IASA) is used. Implementing the IASA starts by specifying the desired constraints, i.e., boundary conditions in the hologram plane and target plane [27]. Initially, the amplitude of the pressure field in the hologram plane is set to the amplitude of the transducer output pressure field computing via the FNM or by experimentally measuring the pressure field fairly close to the transmitter and then numerically back-propagated to the transducer face, and the phase distribution is set to zero. In the target plane, upon calculating the forward-propagated pressure field via the ASA, we impose the desired target image amplitude on the field without changing the phase. Again, the pressure field in the hologram plane is computed via the backpropagation of the wave from the target plane to the hologram plane. Then, the acoustic pressure amplitude of the hologram plane is set to that of the initial pressure amplitude (close to the transmitter or the transducer output pressure field) while considering the transmission losses, $\left|p_h(x,y,0)\right|=\sqrt{T_I(x,y)}\ \left|p_0(x,y,0)\right|$, and preserving the back-propagated phase. The IASA is repeated until the acoustic pressure field in

the target plane converges to the desired target image, which in turn leads to the construction of the final thickness map of the hologram plate.

Additionally, we note that multiple forward and backward propagations of the acoustic field lead to the reflection of higher spatial frequencies [27]. Therefore, we extend our computational domain in the *x*-*y* plane to 1.3-3 times the diameter of the transmitter and impose zero pressure outside the hologram area.

The thickness change of each pixel of the hologram (from the base thickness of the hologram plate t_0) neglecting shear waves is estimated as

$$\Delta t(x, y) = \frac{\Delta \phi_h(x, y)}{k_0 - k_h}, \tag{2.12}$$

where $\Delta \phi_h(x, y)$ is the relative phase map calculated in the hologram plane and $\Delta t(x, y) = t_0 - t(x, y)$.

In summary, the IASA optimization algorithm [27, 40] used to design the acoustic hologram consists of the following steps:

1. The transmitter output pressure field $p_0(x, y, 0)$ is computed via the FNM at the hologram plane close to the transmitter face or by experimentally measuring the pressure field fairly close to the transmitter and then numerically back-propagated to the transducer face. In the hologram plane, the amplitude of the field is set to the amplitude of the transmitter output pressure field and the phase map is set to zero.
2. The complex acoustic pressure in the desired target plane $p_t(x, y, z)$ is computed via the ASA using the propagation function.
3. The propagated pressure field is then compared to that of the target image.
4. If the comparison is satisfactory, the IASA is complete; otherwise, the acoustic pressure amplitude in the target plane is set to that of the desired target amplitude and the forward-propagated phase remains unchanged.
5. The imposed field is back-propagated to the hologram plane via the ASA using the backpropagation function.
6. The thickness map of the hologram and power transmission coefficient are calculated.

7. The back-propagated acoustic pressure amplitude in the hologram plane $|p_h(x, y, 0)|$ is again set to the amplitude of the transmitter output pressure field, and the transmission losses are applied using equation (2.5). The back-propagated phase remains unchanged.
8. The process is repeated from step 2 until a satisfactory distribution is obtained.

2.2.3 Acoustic propagation and piezoelectric receivers coupling in UAET: closed-form voltage response at steady state

The receiver disks in the target plane are free-free PZT (lead zirconate titanate) cylinders operating in the 33-mode of piezoelectricity with fundamental resonance frequencies above the human audible frequency range (see figure 2.1b). For the fluid-loaded and electrically-loaded free-free piezoelectric receiver disk excited by the acoustic wave, the coupled partial differential equations for longitudinal vibrations of the receivers and the AC electrical circuit equation are given by [36, 41, 56]

$$\begin{aligned} &-EA\frac{\partial^2 w(\eta,t)}{\partial \eta^2} - c_\gamma \frac{\partial^3 w(\eta,t)}{\partial \eta^2 \partial t} + \left\{c_\mu + R_r[\delta(\eta) + \delta(\eta - L)]\right\}\frac{\partial w(\eta,t)}{\partial t} \\ &+m\frac{\partial^2 w(\eta,t)}{\partial t^2} - \kappa v(t)[\delta(\eta - L) - \delta(\eta)] = f_{top}(t)[\delta(\eta)] - f_{bottom}(t-\tau)[\delta(\eta - L)], \end{aligned} \tag{2.13}$$

$$C_p \frac{dv(t)}{dt} + \frac{v(t)}{R_l} + \int_0^L \kappa \frac{\partial^2 w(\eta,t)}{\partial t \partial \eta} d\eta = 0, \tag{2.14}$$

where $w(\eta, t)$ is the displacement response of the disk at the axial position η and time t, $v(t)$ is the voltage output across the electrical load, E is Young's modulus at the constant electric field, A is the cross-sectional area, m is the mass per unit length, c_γ is the stiffness-proportional damping coefficient, c_μ is the mass-proportional damping coefficient, κ is the electromechanical coupling term in physical coordinates, and $\delta(\eta)$ is the Dirac delta function. The parameters C_p and R_l, respectively, represent the internal capacitance of the piezoelectric receivers and the external load resistance. The excitation forces due to the incident acoustic pressure, $f_{top}(t) = p_t(t)A$ at $\eta = 0$ and $f_{bottom}(t-\tau) = \Gamma p_t(t-\tau)A$ at $\eta = L$, given in terms of the acoustic pressure in the target plane $p_t(t)$ (see section 2.2.2), are evaluated at the top surface $(\eta = 0)$ and the bottom surface $(\eta = L)$ of the receivers, where Γ is the ratio of the acoustic pressure on the bottom surface to that on the top surface and τ is the time delay of f_{bottom} relative to f_{top}. Moreover, the dissipative term R_r in equation (2.13) is the resistive component of the fluid radiation impedance (see figure 10.19 in

[57]). The excitation of the receiver is such that the linear piezoelectricity is assumed and the elastic coupling and dissipative nonlinearities are not prominent.

The linear displacement at the free end of the piezoelectric receiver disk ($\bar{z}(t)$ in figure 2.1b, where $\bar{z}(t) = w(0,t)$) due to harmonic excitation at or around the fundamental longitudinal (axial) vibration mode is obtained by modal analysis of the distributed-parameter electromechanical system for the fundamental mode of vibration. The longitudinal tip displacement of the piezoelectric receiver disk at time *t* is then written as

$$\bar{z}(t) = w(\eta, t)\big|_{\eta=0} = \varphi(0)\chi(t), \tag{2.15}$$

where $\varphi(0)$ and $\chi(t)$ are the mass-normalized eigenfunction evaluated at $\eta = 0,$ figure 2.1b, and the generalized modal coordinate for the longitudinal vibration mode of a free-free uniform disk, respectively. The mass normalized elastic-mode eigenfunction, calculated from the corresponding undamped and electromechanically uncoupled (short-circuit) free vibration, is obtained as [36]

$$\begin{aligned}\varphi(\eta) = &\left[\cos(\alpha\eta/L) - \alpha\frac{m_r}{mL}\sin(\alpha\eta/L)\right]\times \\ &\left[\int_0^L m\left(\cos(\alpha\eta/L) - \alpha\frac{m_r}{mL}\sin(\alpha\eta/L)\right)^2 d\eta + m_r\left(\cos(\alpha) - \alpha\frac{m_r}{mL}\sin(\alpha)\right)^2 + m_r\right]^{-1/2},\end{aligned} \tag{2.16}$$

where the eigenvalue, α, of the fundamental mode is the first non-zero root of the transcendental equation $[\alpha^2(m_r/mL)^2 - 1]\sin\alpha - 2\alpha(m_r/mL)\cos\alpha = 0$, where $m_r = X_r/\omega$ is the radiation mass, i.e., added mass, due to reactive component of fluid radiation impedance X_r (see figure 10.19 in [57]) and ω is the excitation frequency.

The electromechanically coupled equations of forced vibration and current balance for the fundamental mode in the lumped-parameter form (reduced from distributed-parameter solution) are expressed as

$$\begin{aligned}&\ddot{\bar{z}}(t) + \left[2\zeta\omega_n + R_r\varphi^2(0) + R_r\varphi^2(L)\right]\dot{\bar{z}}(t) + \omega_n^2\bar{z}(t) - \kappa[\varphi(0)\varphi(L) - \varphi^2(0)]v(t) \\ &= \left[f_{top}(t)\varphi(0) - f_{bottom}(t-\tau)\varphi(L)\right]\varphi(0),\end{aligned} \tag{2.17}$$

$$\left[C_p\dot{v}(t) + v(t)/R_l\right]\varphi(0) + \kappa[\varphi(L) - \varphi(0)]\dot{\bar{z}}(t) = 0, \tag{2.18}$$

where the over-dot represents differentiation with respect to time and ζ is the damping ratio.[58] Here, acoustic absorption, nonlinearity, and scattering effects are assumed to be negligible for the frequency range of interest and receiver dimensions.

The steady-state electromechanical response to harmonic excitation is also harmonic and is of the form $\bar{z}(t) = |\bar{z}| e^{j\omega t}$ and $v(t) = |v| e^{j\omega t}$ based on the linear system assumption. Here, $|\bar{z}|$ and $|v|$ denote amplitudes of the axial displacement and voltage output, respectively. As a result, the fundamental-mode output voltage amplitude frequency response function (FRF) is obtained as [36]

$$|v| = \left| \frac{j\omega\kappa |p_t| A\left[\varphi(0) - \Gamma\varphi(L)e^{-j\psi}\right]\left[\varphi(0) - \varphi(L)\right]}{\left\{\omega_n^2 - \omega^2 + j\omega\left[2\zeta\omega_n + R_r\left(\varphi^2(0) + \varphi^2(L)\right)\right]\right\}\left(1/R_l(\omega) + j\omega C_p\right) + j\omega\kappa^2\left(\varphi(L) - \varphi(0)\right)^2} \right|, \quad (2.19)$$

where $\psi = \omega\tau$ is the phase angle between the excitation forces at the top and bottom surfaces of the cylindrical receivers. Consequently, the power output FRF of the piezoelectric receiver disks (Π) is calculated using equation $\Pi = v^2 / R_l$.

As a new method, combining the developed piezoelectric-based UAET formulations with the acoustic holography technique, imposing constraints on the amplitude of pressure distribution in the target plane, enables us to construct a desired multi-focal acoustic field where power transmission to receivers are focally achieved and enhanced dramatically. The analysis presented in this section starts with defining a desired pressure pattern in the target plane where multiple receivers are placed. Then, by applying acoustic holography, the thickness map of a hologram is determined. This map is used to form the hologram. The combination of the acoustic source and designed hologram enables the selective powering of the piezoelectric cylindrical receivers. We expect that the developed theory for using holograms in the contactless transfer of acoustic power will provide new insights into applications of UAET.

2.3 Theoretical results for holographic reconstruction of a VT image

2.3.1 Acoustic pressure distributions and the thickness map of the hologram

In this section, the numerical simulation of constructing the pressure fields and hence obtaining the information needed for fabrication of an acoustic hologram is illustrated. Having computed the initial pressure field close to the face of the circular transmitter using the FNM at 1 MHz, the ASA is used to compute the pressure field in the target plane at $z = 50$ mm in the water domain. The operating frequency of 1 MHz is selected to achieve the reasonable solution quality (the effects of

different frequencies are explored in section 2.3.3) and the target depth of 50 mm is a common depth in the UAET applications. The acoustic hologram is numerically designed to be driven by a piezo transducer disk with a diameter of 100 mm.

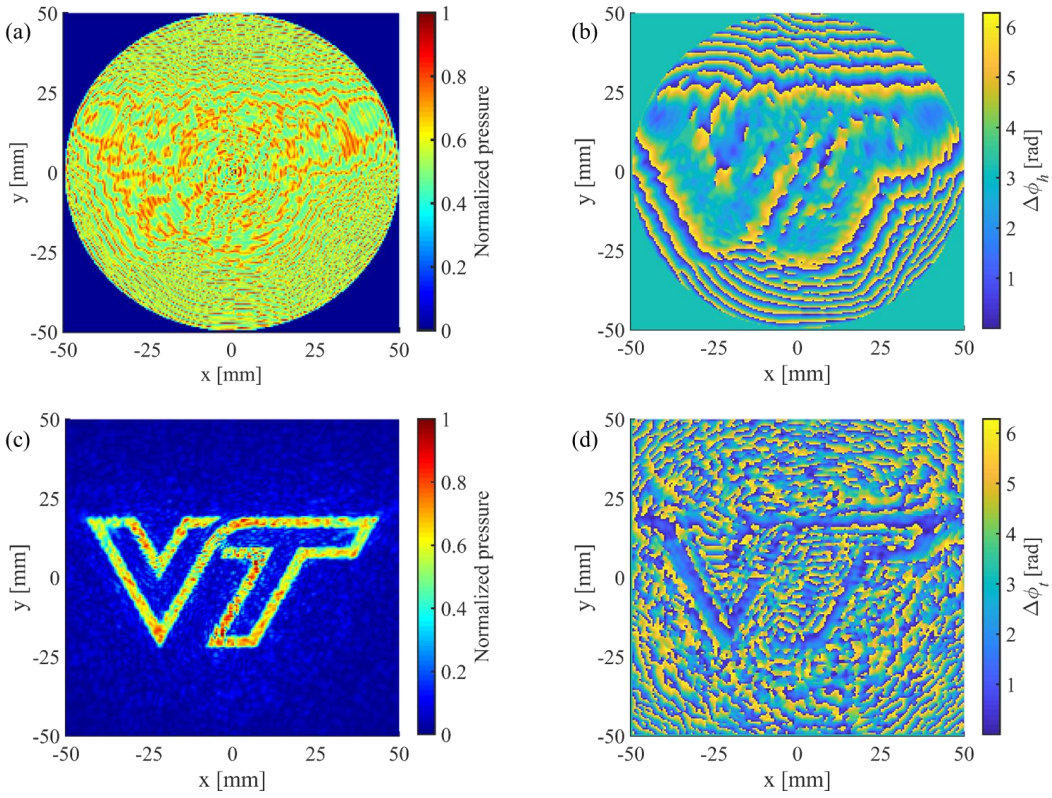

Figure 2.2. Acoustic pressure distributions for the holographic reconstruction of a VT image: Pressure field in the hologram plane close to the transmitter face, after transmission through the acoustic hologram: the (a) amplitude and (b) relative phase. Resultant propagated pressure field in the target plane at $z = 50$ mm: the (c) amplitude and (d) relative phase. The driving frequency is 1 MHz.

Figure 2.2 shows the pressure distributions after 50 iterations obtained by implementing the IASA algorithm in section 2.2.2. In figures 2.2a and b, the amplitude and phase of the back-propagated final pressure distribution in the hologram plane, p_h after transmission through the hologram (step 7 in the IASA algorithm) are shown. The resultant amplitude and phase of the pressure field p_t at the target plane are, respectively, shown in figures 2.2c and d. The pressure field p_t in the target plane results from step 4 in the IASA algorithm, which converges to the target image when the IASA is complete. Here, we have chosen the university logo, VT shape, as the target image in order to show the potential of the computational simulation to reconstruct the complex pressure pattern. The resultant acoustic pressure distribution matches well with the VT shape desired pattern that we imposed upon the target plane, which shows the capability of the designed hologram in

multi-focal lensing and acoustic pressure transmission to generate higher amplitudes over specified patterned areas, compared to the case in which there is no hologram. The comparison indicates a 32% increase in the average acoustic pressure. In this simulation, the number of pixels associated with the diffraction-limited acoustic hologram is 201×201 with a resolution of $\lambda/3$, where λ is the wavelength, and the computational domain size is 601×601.

The final thickness map of the hologram is then computed using the final relative phase map, figure 2.2b, and equation (2.12). Figure 2.3a illustrates this map, with the base thickness of 5 mm, which is later used as an input to the 3D printer for the fabrication of the hologram shown in figure 2.3b. The hologram was printed with a 3D printer (Form 2, Formlabs) using Clear Resin material with a resolution of 50 µm. The simulations were performed using the properties for water and axially vibrating cylindrical PZT transmitter with densities of 1000 kg/m^3 and 7800 kg/m^3 and the speed of sound of 1500 m/s and 4000 m/s, respectively. Moreover, the hologram properties were set to 1100 kg/m^3 for the density and 2424 m/s for the speed of sound in the material.

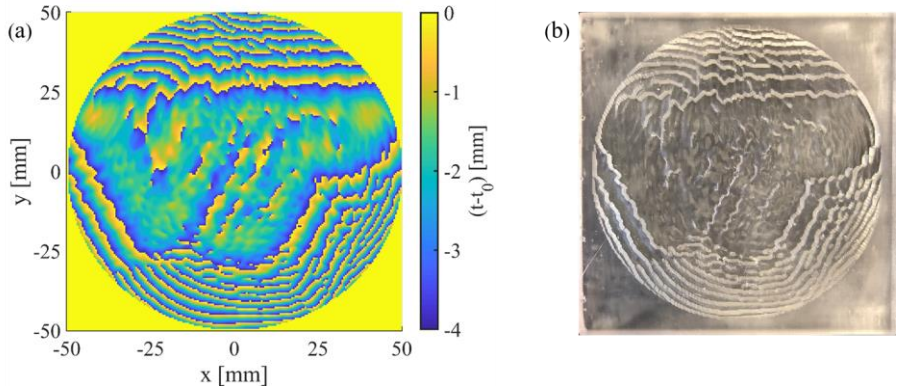

Figure 2.3. (a) Final thickness map of the hologram plate for the holographic reconstruction of the VT image, operating at 1 MHz, obtained from the IASA and (b) the 3D-printed hologram plate.

2.3.2 Receivers' power output in the target plane

In this section, the receivers' power output in the target plane is calculated using the obtained pressure distribution in the plane, where 1024 PZT receivers were equally distributed. Each receiver investigated in this case study is a cylindrical 33-mode PZT disk (PIC 255 from Physik Instrumente (PI) GmbH & Co. KG [59]) with a diameter of 3 mm and a thickness of 2 mm, and a short-circuit fundamental resonance frequency of 1 MHz in free-free boundary conditions. The material properties are given by the manufacturer in [60]. The whole setup (in figure 2.1) is submerged under the water. Using the analytical model, further simulations were conducted to obtain the electrical power output for the PZT receivers in the target plane at $z = 50$ mm for

two cases, i.e. with and without the hologram. The power output for the receivers is calculated at 1.08 MHz, the underwater open-circuit resonance frequency, and the load resistance is fixed to $R_l = 12\,\mathrm{k}\Omega$ (see figure A.1 in appendix A.1). The pressure amplitude in the target plane at each receiver's location is used to calculate the external force acting on the surfaces of the receiver and is used in equation (2.19) to compute the output voltage amplitude from each receiver. This voltage is used in conjunction with the electrical load to calculate the power output. Since the pressure distribution over the surface of each receiver is not uniform, the pressure field in the target plane is divided into a coarser grid that has the nominal dimension of the diameter of the receivers. The pressure over each grid point is then averaged and is multiplied by the receiver area to estimate the external force over each receiver's surfaces.

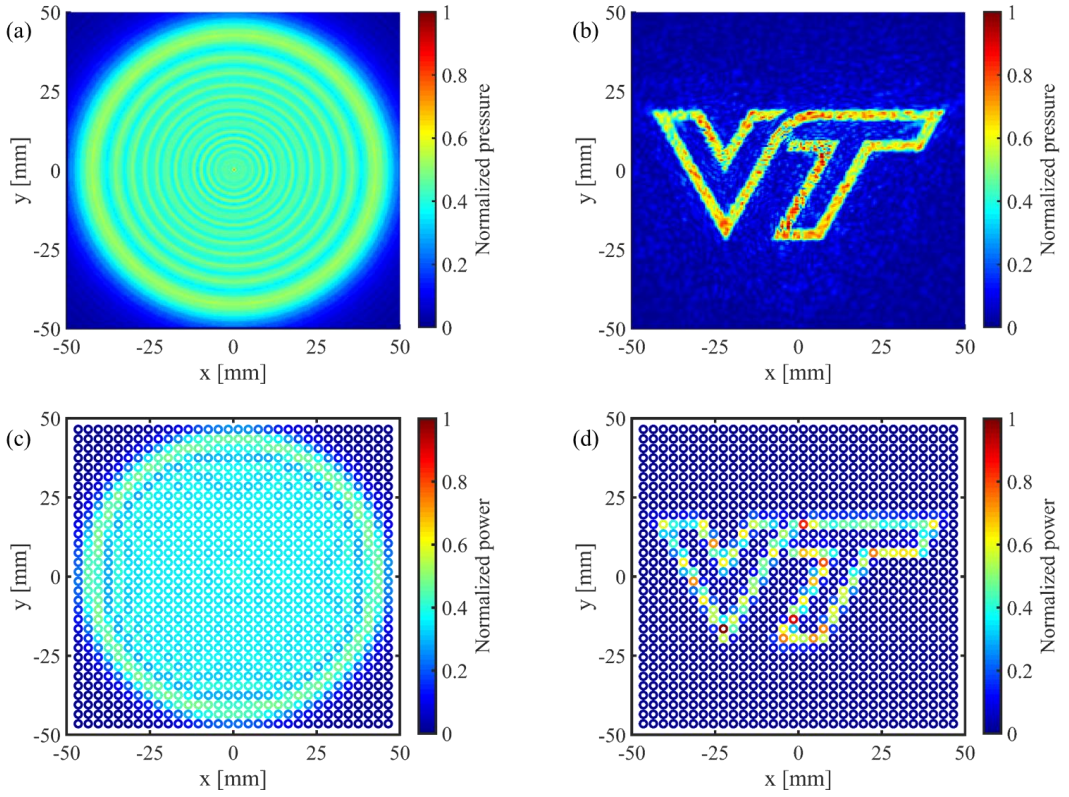

Figure 2.4. Acoustic pressure distributions for the holographic reconstruction of the VT image in the target plane at $z = 50$ mm: (a) when there is no acoustic hologram and (b) in the presence of the hologram. Corresponding power output for the piezoelectric receivers in the target plane at $z = 50$ mm: (c) when there is no hologram and (d) in the presence of the hologram. The pressure and power output are, respectively, normalized by the maximum value in (b) and (d).

Figures 2.4a and b show the normalized pressure distribution in the target plane when there is no acoustic hologram and in the presence of the hologram, respectively. Correspondingly, the

normalized power output without the presence of the hologram is shown in figure 2.4c, while figure 2.4d shows the normalized power output using the acoustic hologram. The figures depict an array of receivers that covers the domain in the target plane corresponding to the hologram aperture. It is determined that the acoustic hologram enables a new capability in shaping the acoustic pressure field and transferring power to the receivers only at focal points (in the VT pressure pattern), selectively. For this case study, in addition to pattering, employing the hologram in the UAET setup leads to a 9% increase in the average power output.

Furthermore, figure 2.4d shows that the receiver with the highest power or normalized power output equals to 1 when the acoustic hologram was used, is located at x = -22.5 and y = -16.5 mm in the target plane. Comparing with the corresponding receiver in the same location, where the normalized power output equals 0.33 without employing a hologram (figure 2.4c), the receiver's power output was increased by 200%. The power can be further increased with impedance mismatch alleviation and the inclusion of impedance-matching layers between the transmitter, hologram, and receivers [42].

2.3.3 Effects of various parameters on pressure pattern in the target plane and thickness map of the hologram

In this section, we aim to analyze the effects of various parameters on the reconstruction of the target pressure pattern and fabrication of the hologram plate via its thickness map. The propagated pressure fields in the target plane at $z = 50$ mm for six different operating frequencies, namely 100 kHz, 250 kHz, 500 kHz, 1.5 MHz, 2.5 MHz, and 3.3 MHz, are shown in figure 2.5. The aforementioned frequencies were selected to visualize the effects of operating frequencies on the fidelity of the system. Moreover, there is a limit for the ASA to which the frequency can be increased depending on the distance from the hologram plane to the target plane and also on the desired pattern. For our case study, the frequency cannot be increased more than 3.3 MHz (with $\lambda/2$ sampling criteria to avoid aliasing); however, at a smaller distance, e.g., $z = 20$ mm, the hologram can be constructed at much higher frequencies such as 7 MHz or above. Comparing the results obtained in figure 2.2c at 1 MHz and figures 2.5a-c, it is concluded that the hologram potential in generating the desired pressure pattern and hence performance quality and accuracy decrease as the frequency is decreased. On the other hand, figures 2.5d-f illustrate that increasing the frequency from 1 MHz to 1.5-3.3 MHz significantly improves the quality and uniformity of the patterned distribution of pressure in the target plane. Hence, increasing the operating frequency enhances the efficiency of power transfer. Considering the corresponding thickness maps of the

hologram that are shown in figure 2.6, we note that the resultant thickness map from the IASA before 3D printing is considerably affected by the excitation frequency.

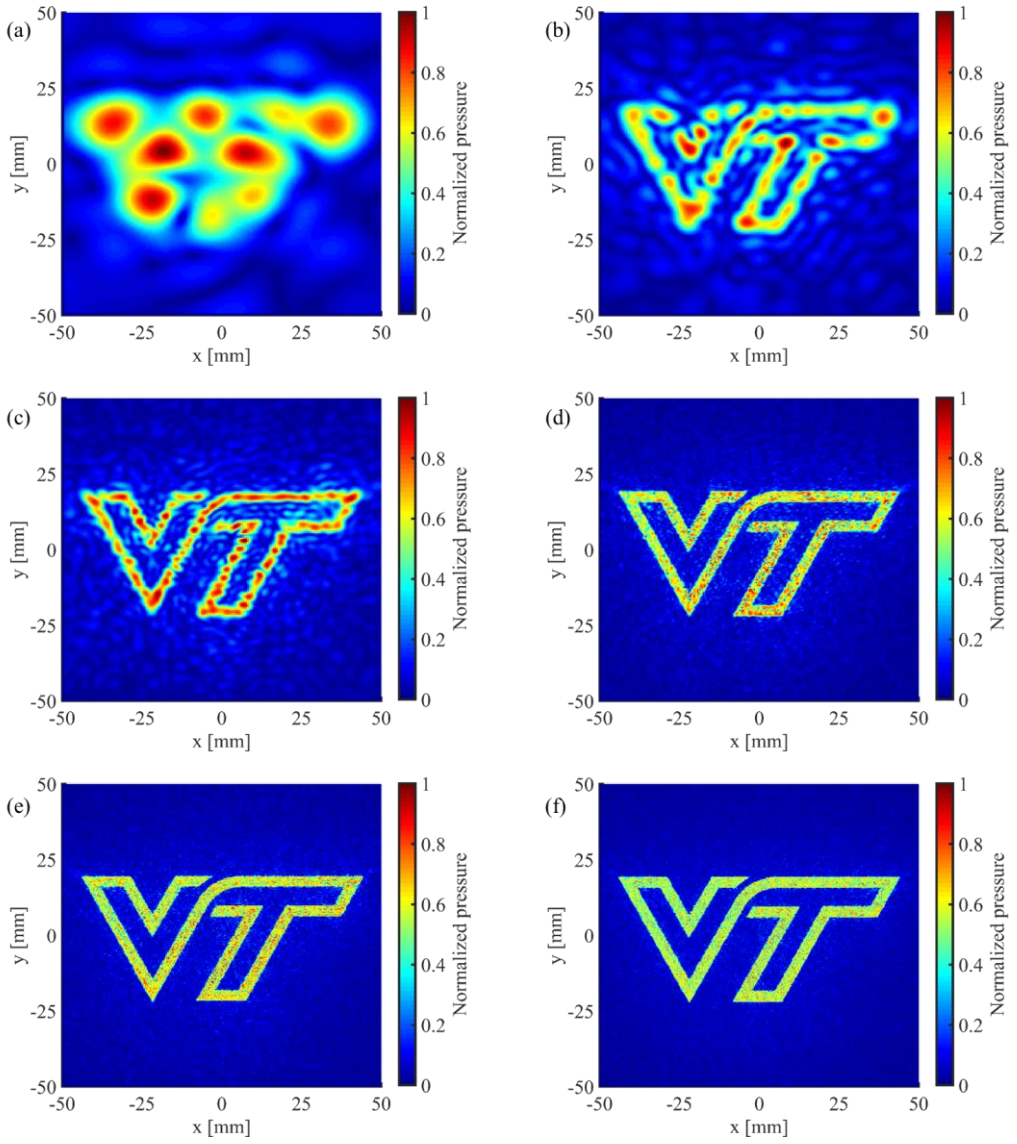

Figure 2.5. Propagated pressure fields for the holographic reconstruction of the VT image in the target plane at $z = 50$ mm for excitation frequencies of (a) 100 kHz, (b) 250 kHz, (c) 500 kHz, (d) 1.5 MHz, (e) 2.5 MHz, and (f) 3.3 MHz.

Apparently, over the frequency range below 1 MHz (figures 2.6a-c), a low-quality designed thickness map is obtained which in turn leads to the fabrication of an imperfect hologram plate; thus, it generates a pressure pattern with less consistency in comparison to the desired target VT pattern. In contrast, figures 2.6d-f show considerable improvements in the quality of the construction of desired holographic design when operating at 1.5-3.3 MHz with a more detailed structure of the pattern in comparison with the pattern of figure 2.3a at 1 MHz. Furthermore, at

higher frequencies, the hologram plate can begin with smaller base thickness since it requires less amount of maximum material removal, which results in a more consistent thickness map for the pixels of the hologram with lower acoustic attenuation. This is one of the important features in making a consistent desired pattern since, in a holographic technique, each pixel of the hologram acts as a single transducer in transmitting the acoustic field.

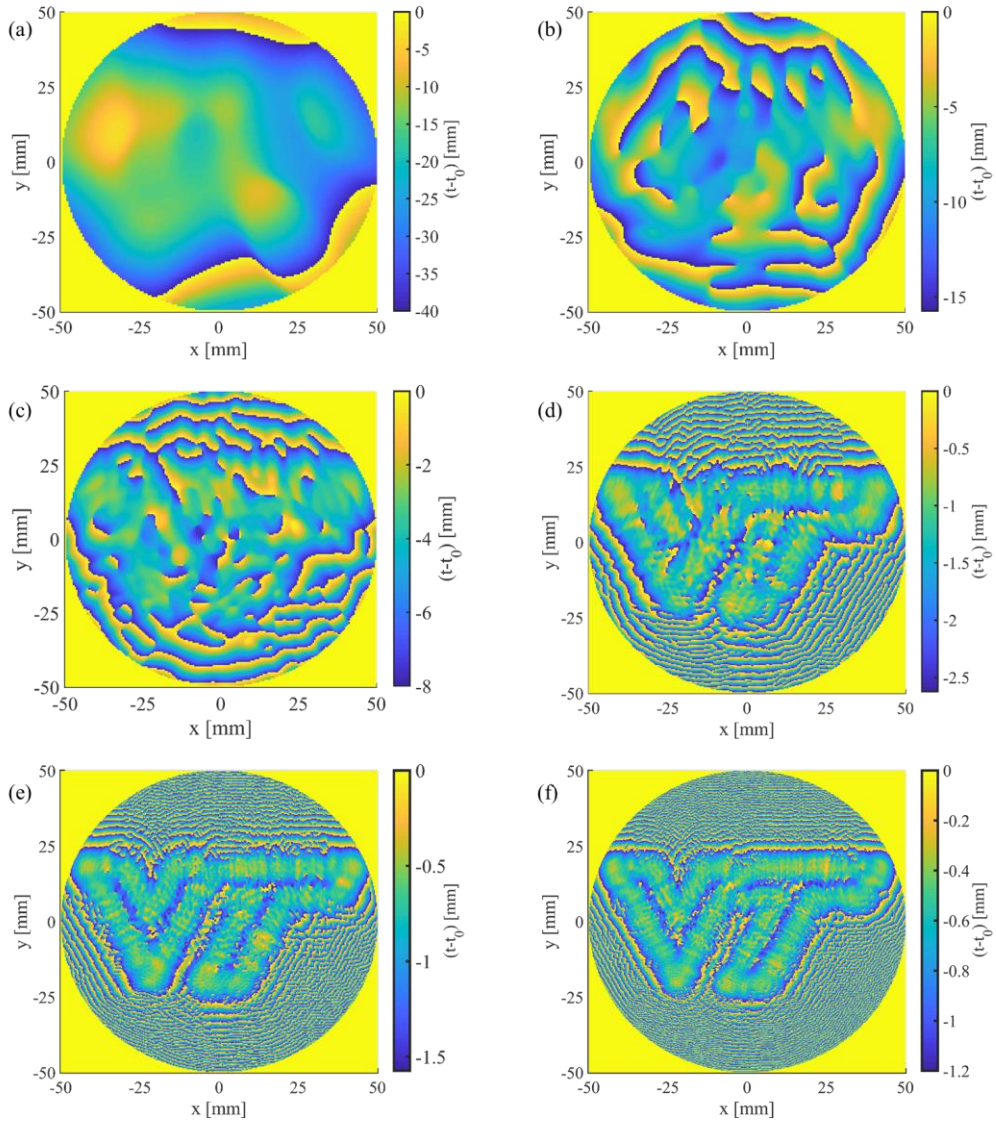

Figure 2.6. Final thickness map of the hologram plate for the holographic reconstruction of the VT image, obtained from the IASA, for excitation frequencies of (a) 100 kHz ($t_0 = 42$ mm), (b) 250 kHz ($t_0 = 17$ mm), (c) 500 kHz ($t_0 = 10$ mm), (d) 1.5 MHz ($t_0 = 5$ mm), (e) 2.5 MHz ($t_0 = 2$ mm), and (f) 3.3 MHz ($t_0 = 1.5$ mm).

The resolutions for each frequency in the simulations are chosen to ensure that a reasonable solution quality, which requires a feasible computational time, is achieved. The number of pixels

associated with the diffraction-limited acoustic hologram for the excitation frequency of 100 kHz is 161×161 with a resolution of $\lambda/24$ and the computational domain size is 481×481. For the frequencies of 1.5 MHz, 2.5 MHz, and 3.3 MHz, the hologram plane is respectively comprised of 301×301, 334×334, and 441×441 number of pixels and the computational domain size is 901×901, 1001×1001, and 1321×1321, respectively. The spatial sampling of $\lambda/3$ is used for the frequency of 1.5 MHz and the frequencies of 2.5 MHz and 3.3 MHz are operated with the $\lambda/2$ sampling criteria. Other simulations are performed with the same number of hologram pixels and computational size as the one used for 1 MHz (section 2.3.1). However, the resolution for driving frequencies of 250 kHz and 500 kHz are $\lambda/12$ and $\lambda/6$, respectively. Likewise, we investigated the effects of various hologram aperture size and diameter of the PZT transducer disk. The results show that using a larger disk/aperture size will improve the quality of the hologram design and therefore enhance the reconstruction quality of the pressure pattern as well as the designed thickness map. For that, as an alternative, we suggest using the equivalent source method (ESM) method for NAH that can administer sources with arbitrary geometry, i.e. multi-aperture acoustic holography method [51, 61, 62]. The results of changing the aperture size are presented in appendix A.2, figure A.2, which are analogous to those regarding the effects of changing the frequency. The size of reconstructed features in the target plane is diffraction-limited, hence, increasing the operating frequency and aperture size, as far as possible, will enhance the image fidelity. An example of acoustic power transmission coefficient variation for three layers versus operating frequency and layer thickness for different frequencies are shown, respectively, in figures A.3a and b in appendix A.3. Also, the calculated power transmission coefficient in the hologram plane at 1 MHz for the computational case study is shown in figure A.3c.

Figure 2.7 shows the results of VT image reconstruction for the case when the hologram is not fixed to the transmitter disk and instead, is placed between the transmitter and the target plane (see figure 2.1 in section 2.2). In figure 2.7, $d = 75$ mm and $z = 50$ mm; please note that $z = 0$ is the hologram plane, hence, the maximum distance (between the transducer and the target plane) is 125 mm. The amplitude of the reconstructed pressure fields (after 50 iterations of the IASA algorithm) at the hologram and target plane are shown in figures 2.7a and c, respectively, while figures 2.7b and d show the corresponding phase of the pressure fields. Figures 2.7e and f show, respectively, the acoustic power transmission (see equation (2.4)) and the hologram thickness map calculated from the phase map in figure 2.7b.

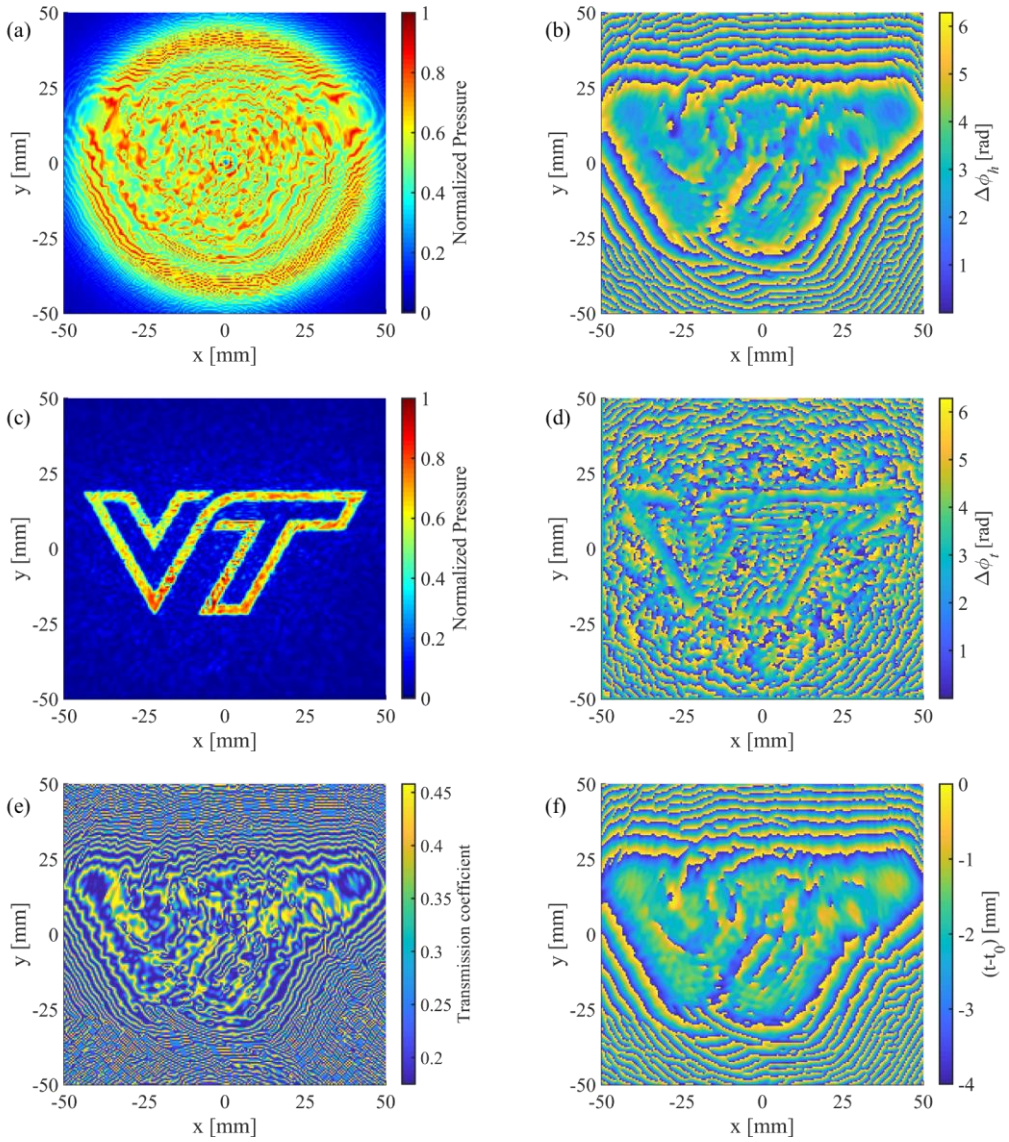

Figure 2.7. Acoustic pressure distributions for the holographic reconstruction of the VT image when $d = 75$ mm and $z = 50$ mm. Pressure field in the hologram plane: the (a) amplitude and (b) relative phase. Resultant propagated pressure field in the target plane: the (c) amplitude and (d) relative phase. (e) Corresponding acoustic power transmission coefficient and (f) thickness map of the acoustic phase hologram. The driving frequency is 1 MHz and the base thickness is 5 mm.

Comparing figures 2.7a-d to that of figures 2.2a-d, one can see that although there are some differences in the details of the reconstruction pattern, both cases lead to satisfactorily results generating the desired pattern at the target plane. Thus, the hologram does not necessarily need to be attached to the transducer [63], which could provide more flexibility and capabilities for the energy transfer applications, where larger distances between the transmitter and receivers might be required. However, the sound beam diffraction and acoustic attenuation when placing hologram

in between will be stronger leading to more loss of acoustic energy. Moreover, at some axial distances, the acoustic power transmission drops due to the sinusoidal nature of the power transmission coefficient (see figure A.3b in appendix A.3). Figure A.4c in appendix A.4 illustrates the case ($d = z = 50\ mm$) when the power maximum transmission coefficient for the VT pattern reconstruction decreases, though the pressure field at the target plane adequately converges to the desired field (figure A.4b). Another example is seen in figure A.5 of appendix A.4, where $d = 50\ mm$ and $z = 100\ mm$. In this example, the homogeneity of the amplitude distribution at the target plane enhances (figure A.5b). However, comparing the thickness map of the hologram in figures A.5d with that of A.4d, we can conclude that unwanted phase jumps lead to larger thickness variations between some adjacent pixels causing thickness anomalies [64], which makes the fabrication of 3D-printed acoustic phase holograms difficult, and decreases the holograms' focusing performance in practice.

2.4 Experimental results for a two-element receiver array setup

2.4.1 Hologram fabrication and UAET experimental setup

The experiments were performed to show the functionality of the acoustic hologram in UAET. The hologram is designed, using the IASA algorithm, to generate a single acoustic focus on the left side of a target plane at a distance $z = 40$ mm from the hologram plane with the excitation frequency of 1MHz. The focal area is defined to encompass a piezoelectric receiver disk and after 60 iterations, the solution converges to the desired pressure pattern as shown in figure 2.8a. The final thickness map, with a base thickness of 5 mm, is presented in figure 2.8b, which was rendered into a 3D-printed acoustic hologram using Clear Resin material with the properties described in section 2.3.1.

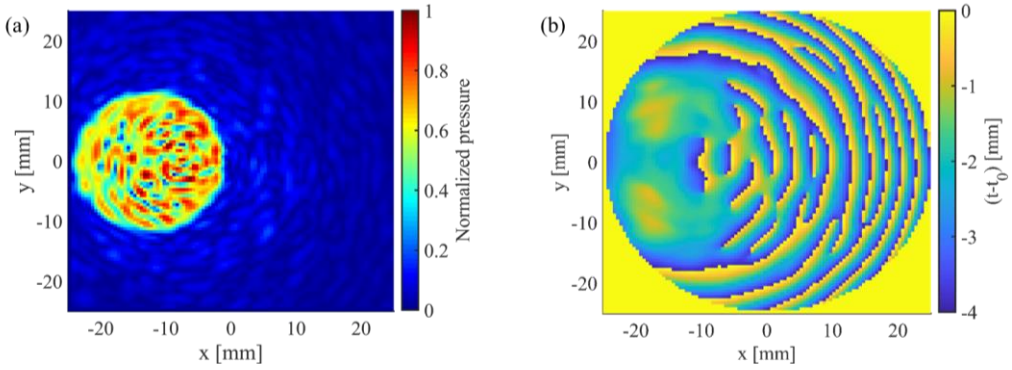

Figure 2.8. Normalized acoustic pressure distribution for the holographic reconstruction of a left-side-single-focus image obtained from the IASA computational simulation in the target plane at $z = 40$ mm and (b) the corresponding final thickness map of the hologram plate. The driving frequency is 1 MHz.

The UAET experimental setup with the acoustic hologram is shown in figure 2.9. The acoustic source (transmitter) is a PZT disk with a diameter of 50 mm and a thickness of 2.1 mm operating at the thickness mode of 1 MHz. We used two PZT receiver disks with a diameter of 19 mm, a thickness of 2 mm, and the resonance frequency (thickness mode) of 1 MHz and placed them in the target plane. All the disks are cylindrical 33-mode modified PZT-4 (Steiner & Martins, INC. [65]) and the material properties are given by the manufacturer in [66]. The hologram was mounted on the transmitter with a thin layer of high-shear-strength epoxy (3M DP460 Scotch-Weld Epoxy Adhesive). The backside of the disks was fixed to a fabricated acrylic holder using the same epoxy with the method described in [67].

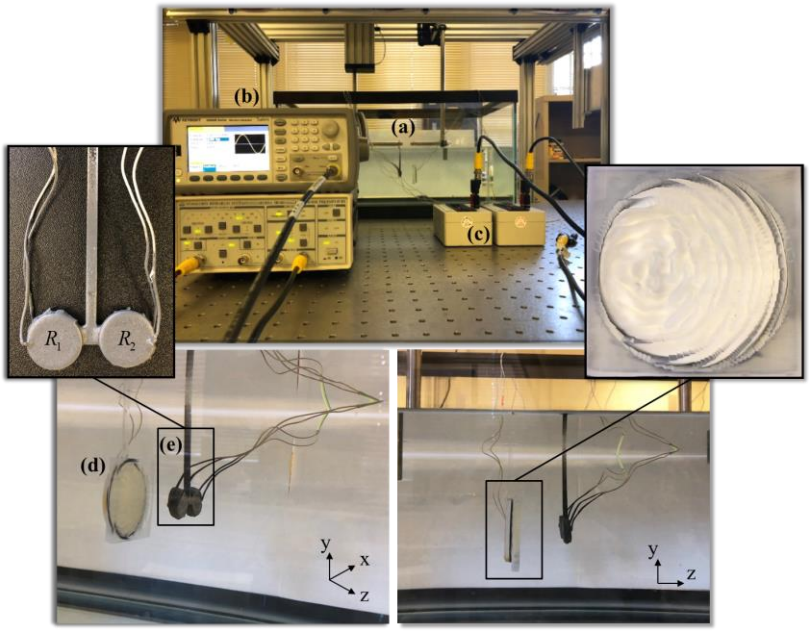

Figure 2.9. Experimental setup showing implementation of the acoustic hologram with the transmitter-receivers in UAET (a: deionized water tank, b: waveform generator and preamplifier, c: load resistors, d: transmitter and hologram, and e: receivers).

The transmitter was actuated using a waveform generator (Keysight 33500B series) that was connected to an amplifier (Krohn-Hite Corp, model 7500). The receivers (R_1 and R_2 in figure 2.9) were connected to load resistors (RS-201W Wide-Range Precision Resistance Substituter) and a preamplifier (Stanford Research Systems Model SR560, Low-Noise Preamplifier) was used to amplify the receiver's signal. The data from the receivers were then acquired using NI SignalExpress® software through a National Instrument data acquisition device (PCI-6115). Furthermore, the data were bandpass filtered between 900 kHz and 1.1 MHz to reduce noise. The transmitter, hologram, and receivers were fully submerged in 615×318×325 mm tank of deionized

water. Based on the desired pressure pattern from the acoustic holography, figure 2.8a, the voltage output from the receiver R_1 was expected to be higher than that of the receiver R_2. This outcome is illustrated in the next section.

2.4.2 Patterning in UAET using hologram: pressure distribution and receivers' voltage response

The objective of the experiment is to excite the fixed-free receiver disks in the target plane by the transmitter and single acoustic hologram that were discussed above. The detailed theoretical modeling for longitudinal excitation of a fixed-free cylindrical piezoelectric receiver is described in [68] and chapter 4, section 4.2.2. We measured the sound pressure in the target plane at $z = 40$ mm using a calibrated 1 mm needle hydrophone (Precision Acoustics Ltd with the sensitivity of 1154 mV/MPa at 1 MHz) mounted on a manufactured custom 3D positioning system. The hydrophone preamplifier was connected to a DC coupler with power supply (Precision Acoustics Ltd) referenced to the PCI-6115 card in which the hydrophone signal was acquired using a built-in MATLAB function (for data acquisition) and a developed script that 2D scans the acoustic field in the target plane. The data from the hydrophone was also bandpass filtered between 900 kHz and 1.1 MHz. Figures 2.10a and b show the normalized peak pressure as measured by the hydrophone (see figure A.6 in appendix A.5) in the target plane when there is no acoustic hologram and in the presence of the hologram, respectively. Noticeably, using the acoustic hologram enhances the pressure amplitude in the targeted area and produces the focal point. Comparing the experimental results in the presence of the acoustic hologram, figure 2.10b, with the theoretical results, figure 2.8a, we observe a good agreement where the target pressure pattern, (i.e., single desired focal point on the left side of the acoustic field) is clearly realized. Also, we have verified the functionality of the acoustic hologram in generating the patterned distribution of pressure at frequencies within ±20% of the operating frequency.

The dashed circles in figure 2.10b represent the locations of the PZT receivers in the target plane for the UAET experiment (see figure 2.9) and the normalized average pressure in the plot is calculated for the six selected segments of the field as shown in figure 2.10c. The results presented in this section were verified in two ways. Firstly, we verified the functionality of the designed acoustic hologram using the IASA, in generating the patterned distribution of pressure by comparing figure 2.8a with figure 2.10b. Secondly, we compared the time histories of the measured voltage output across the electrical load connected to the receivers with UAET modeling results for the PZT receivers excited by the given average pressure in figure 2.10c. The average pressure

in the segment including receiver 1 (R_1) is almost double $(1/0.51=1.96)$ that of the receiver 2 (R_2), which means $p_t|_{\text{for R1}} = 1.96\, p_t|_{\text{for R2}}$. Time histories of the measured voltage output across the electrical load connected to the receivers R_1 and R_2 are presented in figure 2.10d. The ratio of the amplitudes of the voltage output is $v|_{\text{for R1}} = 2.02\, v|_{\text{for R2}}$. A very good agreement is noted between these values and those predicted by the model in that the voltage response is linearly proportional to the input pressure as derived in equation (2.19), i.e., $v \propto p_t$. Hence, by using the designed acoustic hologram, a significantly higher voltage output from R_1 is achieved, which shows the potential of the acoustic hologram in transferring localized and higher power to a receiver at the predetermined focal point.

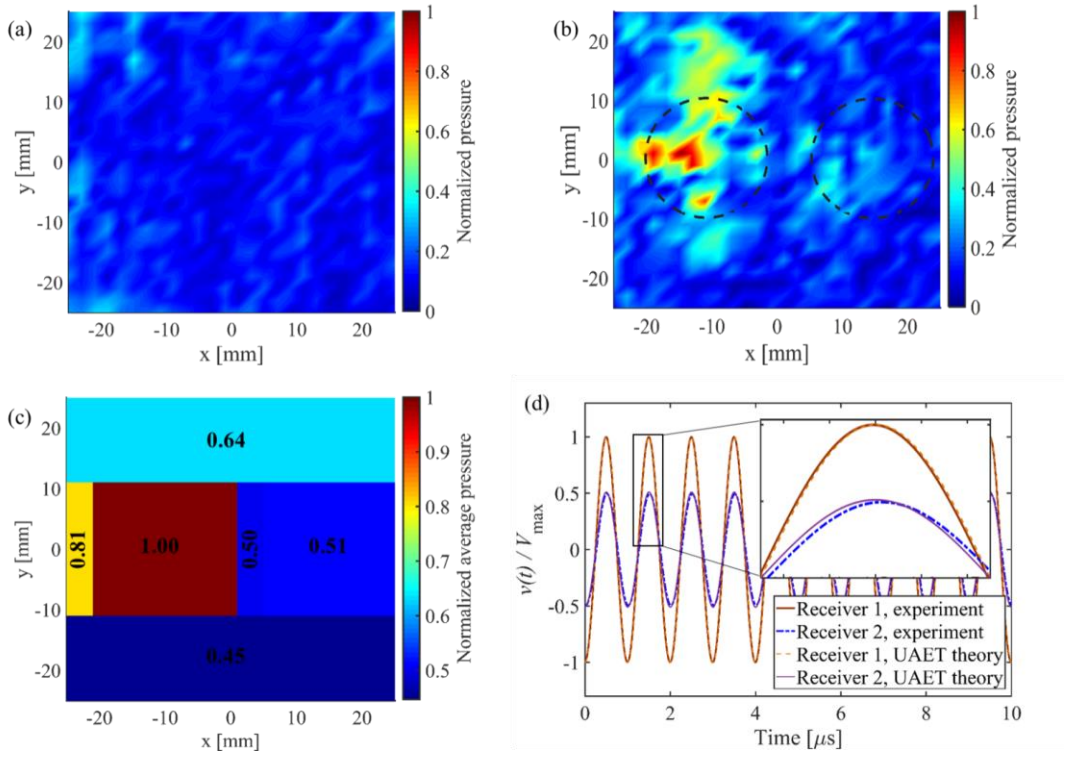

Figure 2.10. Experimentally measured acoustic pressure distribution for the holographic reconstruction of the left-side-single-focus image in the target plane at $z = 40$ mm: (a) when there is no hologram and (b) in the presence of the hologram. (c) The average pressure calculations with the hologram, in defined segments, and (d) the corresponding normalized experimentally measured voltage output from the two receivers located in the target plane compared with the UAET modeling results. The pressures and average pressures are normalized by the maximum value in (b) and (c), respectively. The driving frequency is 1 MHz.

2.5 Multi-focal image patterning holograms

In this section, we aim to design holograms that can generate more complex pressure fields, i.e., multi-focal patterning to implement it in practice for the enhancement of ultrasonic power transfer (UPT). The experiments were performed to obtain a piezo transmitter disk output pressure field. The transmitter disk is a cylindrical 33-mode modified PZT disk (PIC255 from PI Ceramic GmbH [69]) and the material properties are given by the manufacturer. The disk has a diameter of 50 mm and a fundamental resonance frequency (thickness mode) of 2.3 MHz in the water domain (measured by the HP4192A impedance analyzer).

2.5.1 Computational holographic reconstruction of the multi-focal image patterning

We measured the sound pressure in a plane at the distance 9.3 mm from the transmitter disk (see figure 2.11a) using a calibrated 0.2 mm needle hydrophone (Precision Acoustics Ltd with the sensitivity 44 mV/MPa at 2 MHz) mounted on a manufactured custom 3D positioning system as depicted in figure A.7 in appendix A.5. The disk was bonded to a thin brass plate using a thin layer of high shear-strength epoxy (3M DP460 Scotch-Weld Epoxy Adhesive) and then the plate was mounted in a watertight box made of an acrylic sheet with the help of a neoprene rubber sheet as shown in figure A.7 and similarly to the procedure explained in [27]. We used the box to electrically insulate the PZT transducer in water and to construct the air-backed transducer which reflects almost all power from the backside of the transducer toward the transmission line and enhances the power transfer. The box including the PZT disk was fully submerged in 615 mm × 318 mm × 325 mm tank of deionized water. Before submerging the hydrophone, the water inside the tank was properly degassed using a fabricated degassing device for 2 hours. The hydrophone preamplifier was connected to a DC coupler with power supply (Precision Acoustics Ltd) referenced to a 1-GS/s digital oscilloscope (Tektronix TBS 2000 series, model TBS2104) with a sampling rate of 500 MHz, a waveform record length of 2000 points, and 128 averages in which the hydrophone signal was acquired. A developed MATLAB script is used that scans the acoustic field in the 2D measurement plane. The disk was actuated using a waveform generator (Keysight 33500B series) that was connected to an amplifier (E&I RF power amplifier, model A075). The low driving voltage of 30.4 V peak-to-peak was applied for hydrophone scans to ensure that the PZT disk maintains the same performance over the 9-hour hydrophone scan. The deionized water tank was partially lined with acoustic absorber sheets (Aptflex F28, Precision Acoustics Ltd) to avoid reflections from the tank walls. The measurement at each position on a plane at 9.3 mm distance from the transmitter was averaged over four times.

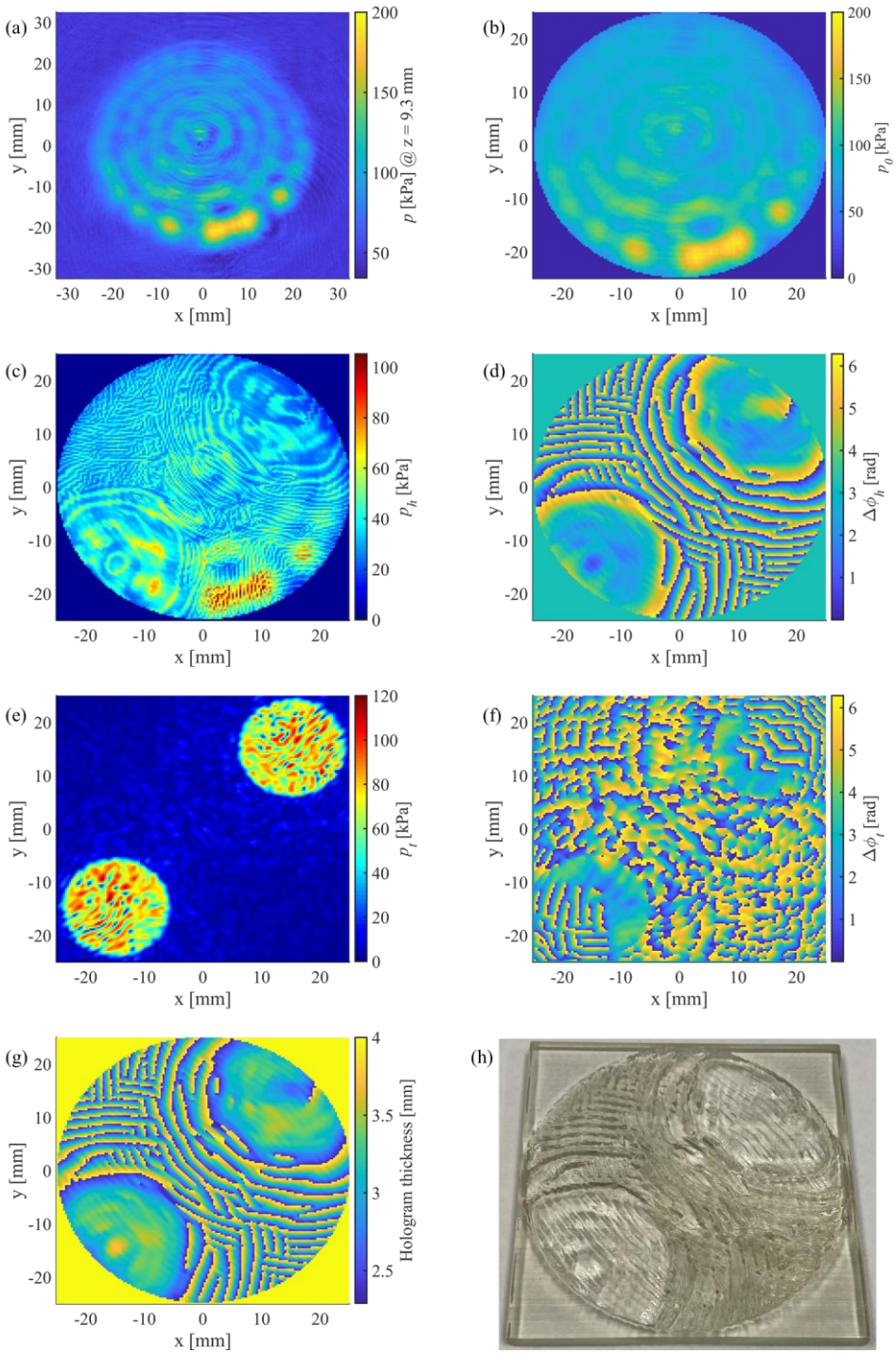

Figure 2.11. Acoustic pressure distributions for the source reconstruction: (a) experimentally measured pressure field in the plane with a distance of 9.3 mm from the ultrasonic source and (b) the numerically back-propagated transmitter output pressure field. Acoustic pressure distributions after 40 iterations of the IASA algorithm for holographic reconstruction of a two-focus image, including the acoustic field in the hologram plane: the (c) amplitude and (d) relative phase and the pressure field in the target plane at $z = 60$ mm: the (e) amplitude and (f) relative phase. Two-focus hologram fabrication: (g) calculated hologram thickness from the hologram phase map in (d); and (h) the manufactured 3D-printed acoustic phase hologram. The driving frequency is 2.3 MHz.

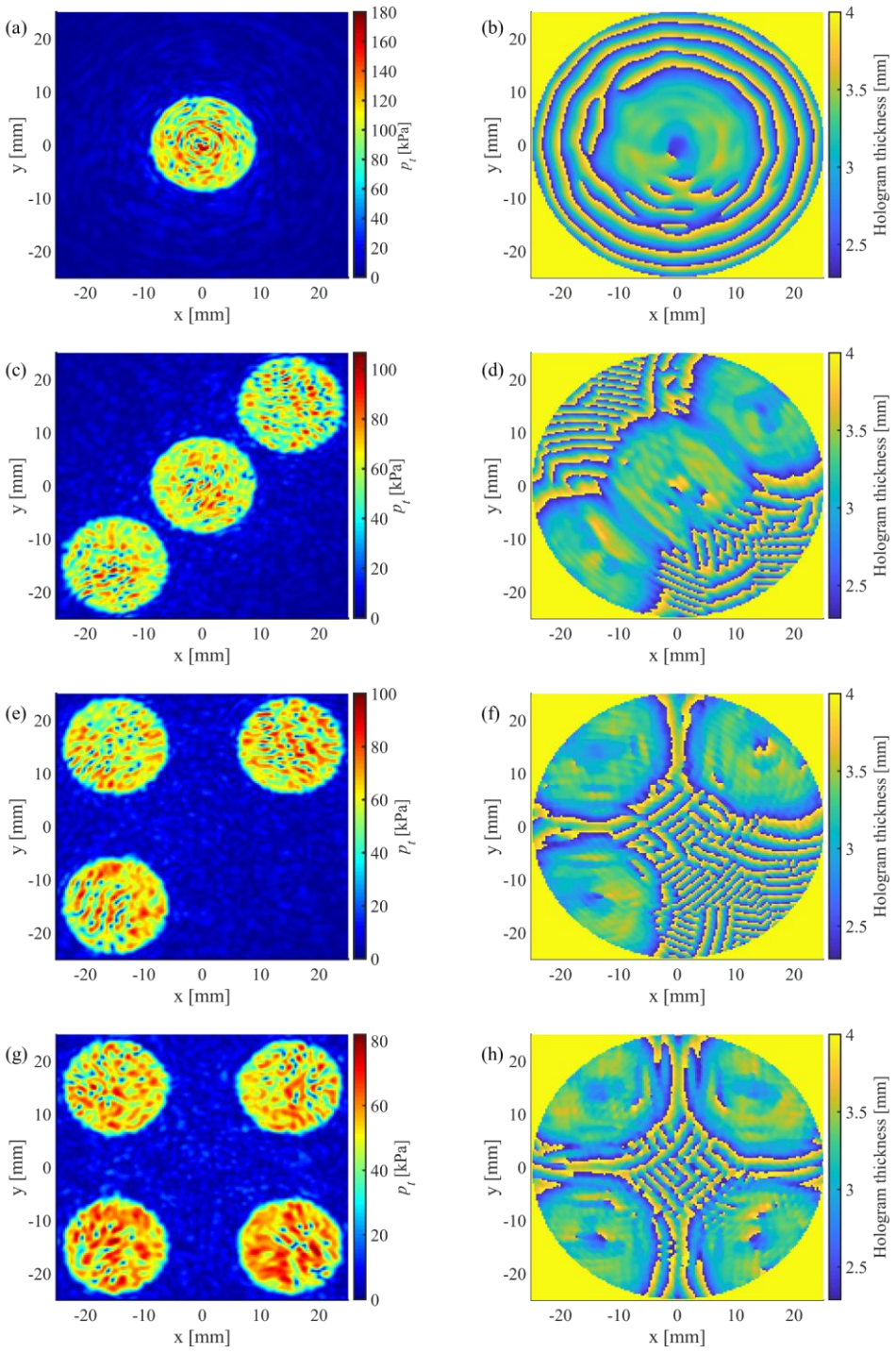

Figure 2.12. Holographic reconstruction of a single-focus image: (a) the acoustic pressure amplitude in the target plane at $z = 60$ mm and (b) the calculated hologram thickness. Holographic reconstruction of a three-focus I image: (c) the acoustic pressure amplitude in the target plane at $z = 60$ mm and (d) the calculated hologram thickness. Holographic reconstruction of a three-focus II image: (e) the acoustic pressure amplitude in the target plane at $z = 60$ mm and (f) the calculated hologram thickness. Holographic reconstruction of a four-focus image: (g) the acoustic pressure amplitude in the target plane at $z = 60$ mm and (h) the calculated hologram thickness. The holograms are numerically constructed after 30-40 iterations of the IASA optimization algorithm and the driving frequency is 2.3 MHz.

The aperture of the measurement plane was about 30% wider than the diameter of the disk (65.28 mm × 65.28 mm) and we set the spatial resolution to 0.32 mm, which is about the one-half wavelength in the water medium at the driving frequency of 2.3 MHz, to avoid aliasing [70]. The experimentally measured pressure field is then numerically back-propagated to the transmitter face to reconstruct the acoustic source field [52, 70] using the Near-field Acoustic Holography (NAH) method [49, 53, 54] via the ASA. figure 2.11b shows the transmitter output pressure field, which is the back-propagated field at the boundary between the transmitter and water from the measured field in figure 2.11a. The acquisition window was chosen to start at least $t_{\text{ring}} + z/c_0$, where t_{ring} is the ring-up time that the transducer takes to reach full output, and finish less than $3z/c_0$ after the start of the electrical excitation since multiple reflections between the transducer and hydrophone can start after the time equals $3z/c_0$ [71]. Hence, for $z = 9.3$ mm, we set the acquisition time in the digital oscilloscope from 10 µs to 14 µs.

In this section, we have designed different acoustic holograms to reconstruct complex multi-focal patterns, including single-, two-, three- (I and II patterns), and four-focus patterning holograms as seen in figures 2.11e and 2.12a, c, e, and g. The multi-focal patterns were initially created using the Autodesk Inventor and then be used as bitmap image file (BMP) formats in a MATLAB code for the IASA algorithm. Figures 2.11c-f show the pressure distributions (amplitude and phase maps) at the hologram and target planes, after 40 iterations of the IASA algorithm for holographic construction of the two-focus hologram at $z = 60$ mm, which is later verified with experiments as shown in figures 2.14c-f. The thicknesses of the multi-focal holograms, shown in figures 2.11g and 2.12b, d, f, and h, are calculated based on the holograms' phase maps using equation (2.12), e.g., the phase map in figure 2.11d is used to determine the thickness map of the two-focus hologram illustrated in figure 2.11g, This thickness map is then converted into the Standard Tessellation Language (STL) file format using MATLAB and finally as an input to a modern 3D printer (J750™, Stratasys Ltd) in VeroClear material with a density of 1185 kg/m^3 and the speed of sound of 2424 m/s [27]. Figure 2.11h shows the 3D-printed two-focus transmission hologram manufactured by the Stratasys company after providing the STL file to the company.

Figure A.8a in appendix A.6 presents the acoustic pressure attenuation factor $\Lambda(x, y) = e^{-\beta_h t(x,y)}$ (see section 4.2.3 in chapter 4) for each pixel of thickness $t(x, y)$, where β_h is a frequency-dependent sound attenuation coefficient in the hologram (VeroClear) material ($\beta_h = 63.3$ Np/m measured at 2 MHz [27]). We use this attenuation factor to update the amplitude of the multi-focal

holograms' pressure fields as $\left|p_h(x,y,0)\right| = \Lambda(x,y)\sqrt{T_I(x,y)}\ \left|p_0(x,y,0)\right|$ in each IASA iteration. Moreover, the acoustic attenuation of water is also considered in the computational simulations as $\beta_{\text{water}} = 0.023$ Np/m [72] (measured at 1 MHz)[a]. The acoustic power transmission coefficient map using the two-focus hologram calculated from the equation (2.5) is also shown in figure A.8b, which is the ratio of the output acoustic power to the input acoustic power for each pixel.

Material selection for acoustic holograms plays an important role in their thickness profile (see figures 2.11g and 2.12b, d, f, and h), which depends on the holograms' acoustic properties, i.e., their density and speed of sound. The characteristic acoustic impedance of hologram shall not be close or too much different from an acoustic medium (such as water). This is to avoid large thickness variations or extra-fine thickness range (micrometer scale) in the manufacturing process using 3D printers with limited control and resolution [73]. Two error metrics are used to analyze the quality of our designed holograms, namely the signal-to-noise ratio (SNR) and parameter image correlation [22]. The SNR is calculated for each hologram as the ratio of the average pressure in the target region where we imposed a non-zero amplitude to that of the average pressure in the region where we imposed zero amplitude (see figures 2.15a and b). The correlation evaluates the similarity between the computational or experimental image (e.g., figure 2.11e or 2.14e for the two-focus hologram) with that of the target image we imposed during the IASA (e.g., figure 2.15a for the two-focus hologram). To calculate the correlation, denoted by r_c, we write

$$r_c = \frac{\sum_i \sum_j \left(\left|p_{t,ij}\right| - \left|\bar{p}_t\right|\right)\left(\left|T_{ij}\right| - \left|\bar{T}\right|\right)}{\sqrt{\left(\sum_i \sum_j \left(\left|p_{t,ij}\right| - \left|\bar{p}_t\right|\right)^2\right)\left(\sum_i \sum_j \left(\left|T_{ij}\right| - \left|\bar{T}\right|\right)^2\right)}}, \tag{2.20}$$

where p_t is the computational or experimental acoustic pressure in the target plane, T is the imposed target image amplitude (figure 2.15a), $\bar{p}_t$ is the average pressure value of the pixels in the matrix p_t, and $\bar{T}$ is the average value of the target image amplitude, in the matrix T.

Higher values of correlation indicate a good similarity between the two images and $r_c = 1$ only happens when the two images are identical. The SNR and correlation are calculated for each computational image for the multi-focal holograms, as seen in figure 2.13. The results in figure

[a] The acoustic attenuation are calculated assuming a proportional increase of losses to the first power of frequency for VeroClear and to the second power of frequency for water.

2.13a suggest that as the target pattern becomes more complex, the signal-to-noise ratio decreases and comparing two different images of three-focus patterning (I and II), one can see that a symmetrical pattern leads to a higher SNR. Furthermore, the image correlation for all multi-focal patterning shows promising results as the values are between 0.94-0.95 (see figure 2.13b), which demonstrates good similarities between the computational holographic images and their respective imposed target images.

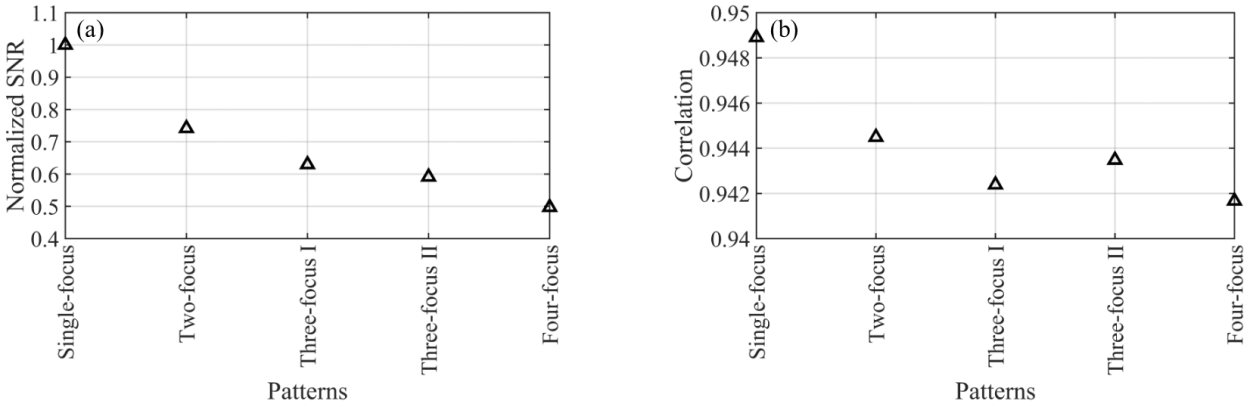

Figure 2.13. Error metrics to evaluate the quality of computational holographic reconstruction of multi-focal image patterning: (a) signal-to-noise ratio (SNR), normalized by the maximum SNR value, and (b) correlation between the computational holographic images and their respective imposed target images.

2.5.2 Patterning in UPT using the two-focus hologram: experimental holographic reconstruction of the two-focus image and receivers'electrical power output

Experiments were conducted firstly to measure the holographic pressure fields generated using the passive two-focus hologram alongside the single ultrasonic transducer (see figure A.7) with the properties defined earlier. After the computational image is reconstructed (figure 2.11e) and the thickness profile of the field is obtained (figure 2.11g), the 3D-printed acoustic phase hologram was fabricated (figure 2.11h) and used in conjunction with the transmitter disk. The hologram is temporarily fixed to the brass plate, in which the disk was bonded to, using high vacuum grease (Dow Corning; Mcmaster-Carr), which provides reasonable acoustic coupling (see figure 2.16b). Moreover, with this temporary fixing, we can implement various holograms as they can easily be attached and detached from the brass plate. Please note that we have used other holograms in chapter 3 with the same fabricated ultrasonic source device comprising the box, transmitter disk, and brass plate. We have experimentally verified the computational pressure fields (amplitude and phase, figures 2.11c-f) in the two-focus hologram plane and target plane at $z = 60$ mm. The measurements were performed using the 0.2 mm needle hydrophone with the same setup and same

measurement, acquisition, and driving parameters as explained in section 2.5.1. The only parameters that change are the sampling rate and acquisition time for measuring the pressure field at $z = 60$ mm when we set the acquisition time in the oscilloscope from 60 μs to 68 μs with a sampling rate of 250 MHz.

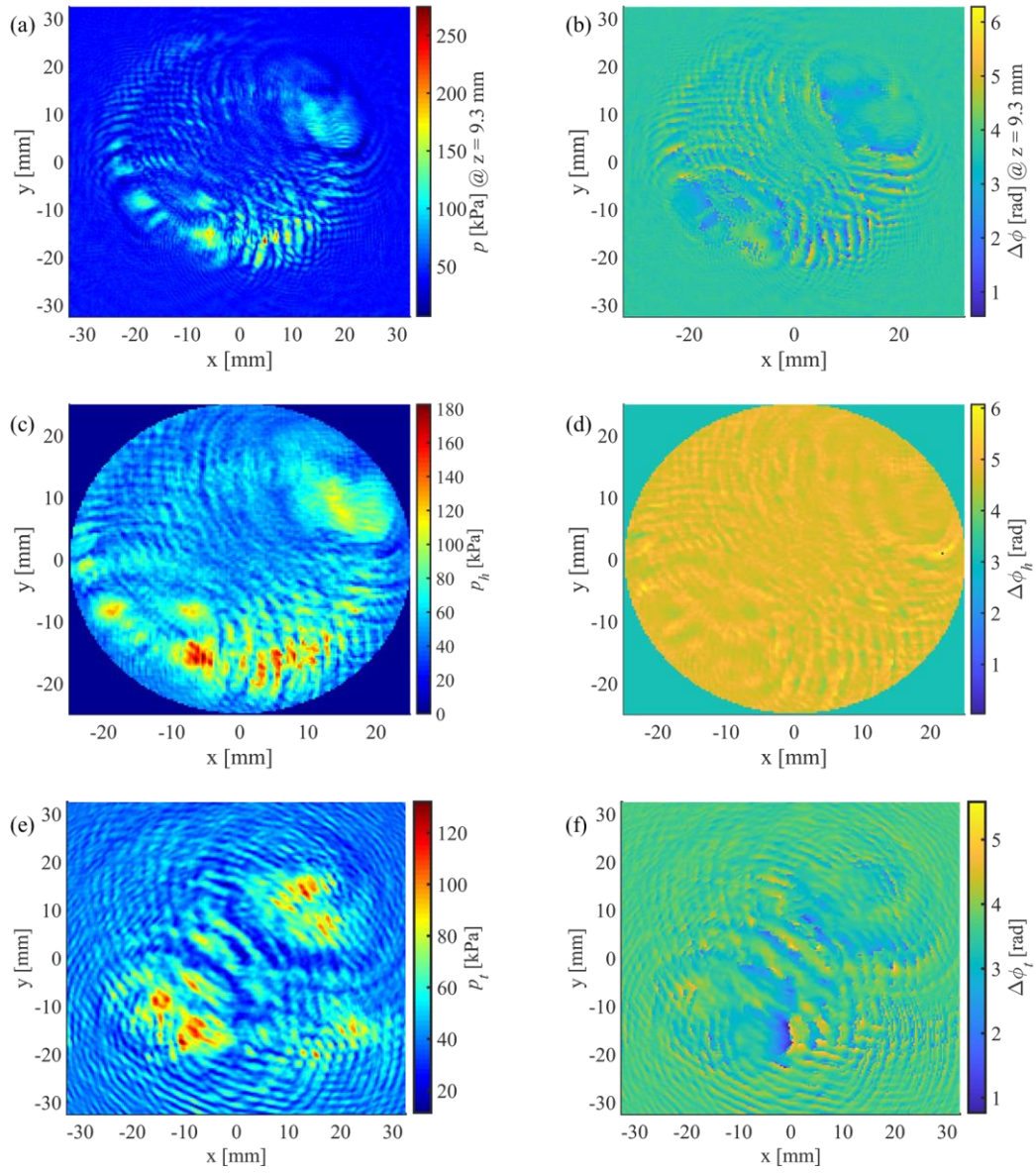

Figure 2.14. Experimentally measured acoustic pressure field in the plane with a distance of 9.3 mm from the two-focus hologram: the (a) amplitude and (b) relative phase. The numerically back-propagated pressure field at the two-focus hologram: the (c) amplitude and (d) relative phase, and the experimentally measured pressure field in the target plane at $z = 60$ mm: the (e) amplitude and (f) relative phase. The driving frequency and voltage are 2.3 MHz and 30.4 V peak-to-peak, respectively, and the measurement at each position in (a), (b), (e), and (f) was averaged over three times.

We first measure the pressure field at $z = 9.3$ mm, as depicted in figures 2.14a and b, then we numerically back-propagated the measured field to the hologram plane to obtain the pressure field shown in figures 2.14c and d in the hologram plane. Finally, we axially moved the hydrophone to the target plane at $z = 60$ mm and measured the corresponding pressure field, depicted in figures 2.14e and f. It should be noted that the relative phase at each point is determined by calculating the phase lag between the output hydrophone signal and the input signal generated by the waveform generator driving the transducer. Comparing the experimental holographic fields with that of theoretical/computational images, we observe a good agreement where the desired target pressure pattern of two focal points is realized.

Introducing a new error metric called reconstruction efficiency [74, 75], we have also examined the quality of our fabricated transmission hologram in terms of acoustic power. The reconstruction efficiency is calculated by

$$\eta_r = \frac{P_{t,t_r}}{P_t} = \frac{\sum_{i \in t_r} I_{t,i} \Delta x \Delta y}{\sum_{i \in t_p} I_{t,i} \Delta x \Delta y} = \frac{\sum_{i \in t_r} p^2{}_{t,i}}{\sum_{i \in t_p} p^2{}_{t,i}}, \tag{2.21}$$

where P_t is the total acoustic power in the target plane, denoted by t_p, P_{t,t_r} is the acoustic power corresponds to the region where we imposed the non-zero target image amplitude (see figures 2.15a and b), which is called target region, denoted by t_r, and $I_{t,i} = p^2{}_{t,i} / 2\rho_0 c_0$ is the acoustic intensity driven from the measured pressure for each pixel. Hence, equation (2.21) computes the ratio of acoustic power in the target region to that of the total acoustic power in the target plane. The reconstruction efficiencies for the computational image in figure 2.15b and the experimental image in figure 2.15d are, respectively, 95.66% and 25.08%; and the image correlations are 0.9445 for the computational image (see figure 2.13b) and 0.5272 for the experimental image. Very good image correlation and high reconstruction efficiency are achieved for the computational image whereas due to various experimental error, these error matrices are lower for the experimental image. Major errors in our experiments include (i) changes in the environment or functionality of the transducer caused by temperature drift or water evaporation due to long times of each 2D scan, which is around 9 hours; (ii) The finite thickness of the brass plate, which does not exactly equal one-half wavelength at 2.3 MHz, to obtain optimal ultrasonic power transfer, can reduce the source performance to some extent; (iii) Reflection and diffraction of sound waves due to the presence of the hydrophone, tank walls, and surfaces, which may interfere with the measurement plane; (iv)

instrumental errors such as those related to the oscilloscope, hydrophone's calibration or spatial errors of our manufactured positioning system; (v) errors associated with the manufacturing process of the source device due to the soldering point on the surface of the disk, located at areas between x = 0 to 20 mm and y = -20 to -12 mm, or due to the disk bonding to the brass plate, which both may cause some unwanted hotspots and nonuniformities in the transducer output pressure field, as they are apparent in figure 2.15d, as well as figures 2.11a and b; and (vi) random errors such as those associated with alignment of components in the experiment which may slightly change the location of the desired pattern (see figures 2.15c and d). However, the experimental results are generally satisfactory as the patterning goal is achieved, which was to reproduce a two-focus target image to generate higher amplitudes of pressure and in return obtain higher electrical power output from specified receivers at the target plane.

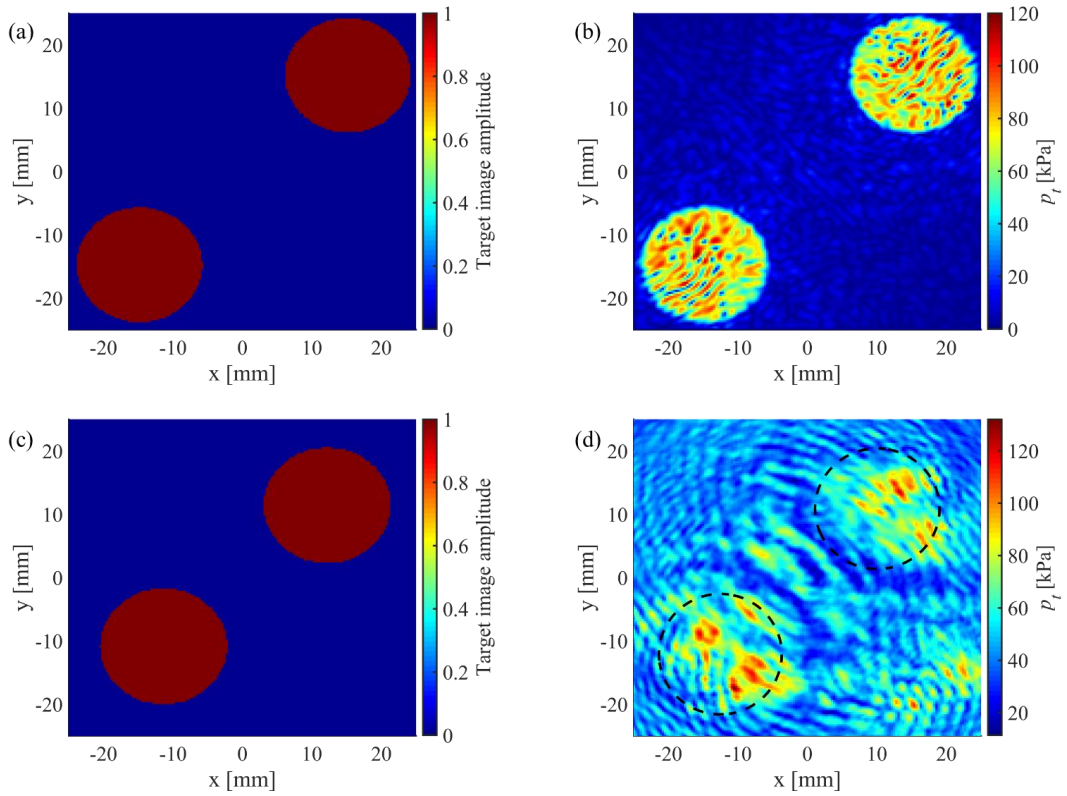

Figure 2.15. Comparison between the computational and experimental holographic reconstruction of the two-focus image: (a) imposed target binary amplitude image, (b) the reconstructed computational pressure field at the target plane at $z = 60$ mm, (c) the apparent changes in the location of the target amplitude image in the experiments, and (d) the reconstructed experimentally measured pressure field in the target plane at $z = 60$ mm.

After measuring the pressure field in the target plane at $z = 60$ mm, we placed a five-element receiver array in the target plane facing our ultrasonic apparatus containing the ultrasound source device (transmitter disk, box, and brass plate) and the two-focus 3D-printed transmission acoustic phase hologram. The receiver disks are cylindrical 33-mode modified PZT disks (PIC255 from PI Ceramic GmbH) and the material properties are given by the manufacturer. The identical disks have a diameter of 16 mm and a fundamental resonance frequency (thickness mode) of 2.3 MHz in the water domain (measured by the HP4192A impedance analyzer) similar to the transmitter disk. The backside of the receiver disks was fixed to a custom-built acrylic holder (designed with the Autodesk Inventor and manufactured by a laser cutter as seen in figure 2.16b) using a thin layer of high shear-strength epoxy (3M DP460 Scotch-Weld Epoxy Adhesive) with the method described in [67]. It is worth emphasizing that special cares need to be taken to ensure bubble-free surface contacts between any two parts that are bonded together in experiments.

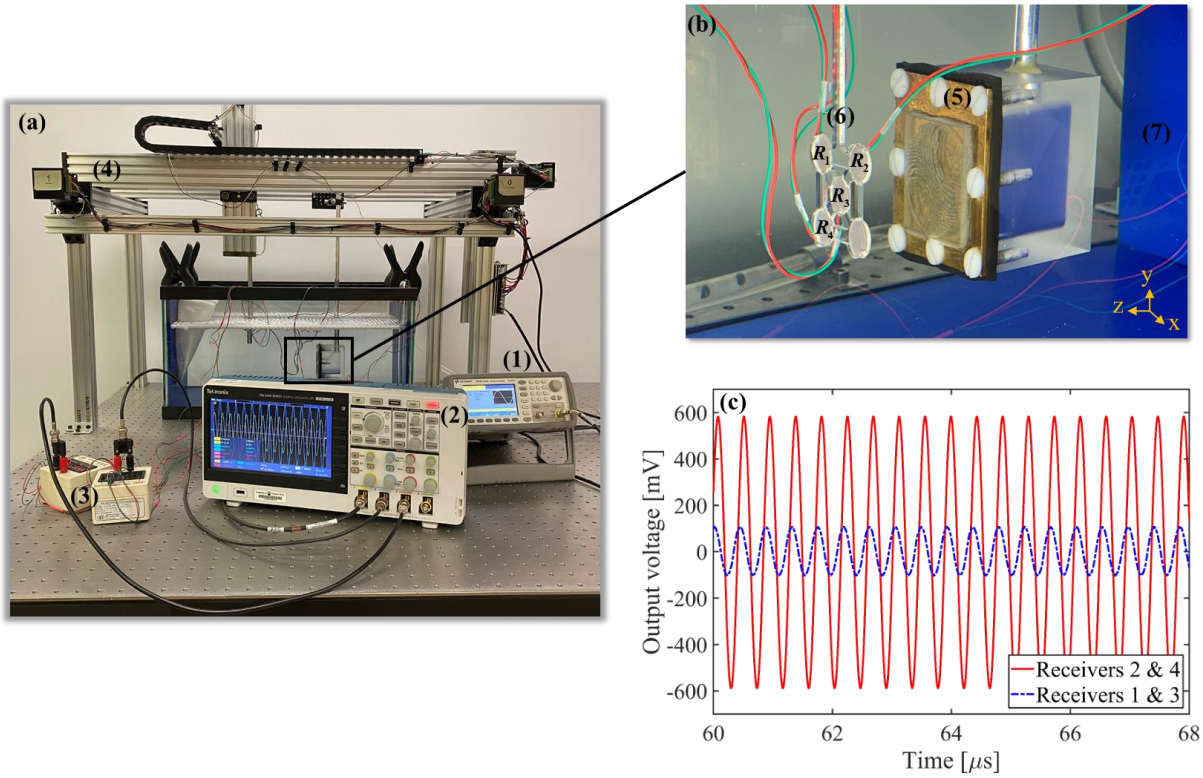

Figure 2.16. Two-focus patterning in UPT: (a)-(b) experimental setup showing implementation of the two-focus 3D-printed transmission acoustic phase hologram alongside the fabricated ultrasonic source device, comprising the box, single transmitter disk, and brass plate, to excite the five-element receiver array. (1: waveform generator, 2: digital oscilloscope, 3: load resistors, 4: positioning system, 5: ultrasonic source device, 6: receivers, and 7: acoustic absorber sheet); (c) experimentally measured voltage output from the parallel combination of receivers 2 & 4, located at two focal points, and receivers 1 & 3 in the target plane at $z = 60$ mm.

Sound waves are generated by the ultrasonic apparatus using the waveform generator driving the transmitter, with an input voltage of 30.4 V peak-to-peak, and then transferred through the water domain to the array of receivers. Receivers R_2 & R_4 and R_1 & R_3, in figure 2.16b, were connected in parallel to load resistors (RS-200-2W High-Power Resistance Box) with the optimal electrical load resistances set to $R_l = 60\ \Omega$. The optimal load resistance was experimentally identified by sweeping the load resistance from 1-300 Ω to find the optimal load that gives the maximum electrical average power output $\Pi_{\text{avg}} = v_{rms}{}^2 / R_l$ from each receiver disk, where $v_{rms} = |v| / \sqrt{2}$ is the root mean square (RMS) voltage output. The experiment for finding the optimal load was performed with the same setup in figure 2.16 and the aforementioned driving conditions. It should be noted that receivers R_2 & R_4 were located at the two predetermined focal points in the target plane. The voltage output signals from the receivers, in figure 2.16c, were acquired using the digital oscilloscope with a sampling rate of 250 MHz, a waveform record length of 2000 points, 128 averages, and the time acquisition of 60 μs to 68 μs. A large RMS voltage ratio of 5.5 comparing output signals from two parallel receivers R_2 & R_4 with R_1 & R_3 is observed in figure 2.16c, which results in a significant electrical average power output ratio of 30.3 obtained in one set of data acquisition. To further verify this outcome, the electrical average power enhancement was calculated averaged over different times conducting several sets of the UPT experiment by moving the receiver array ±0.1 to ±0.5 mm in the axial *z*-direction and the ratio of 23.4 was obtained. These promising results show the potential of the high-fidelity acoustic holograms in focusing and arbitrarily patterning the contactless transfer of ultrasonic power, which is of great importance in acoustic energy transfer systems.

2.6 Conclusions

Contactless ultrasonic power transfer is a promising approach for many potential applications such as wireless charging of medical implants used in therapy and sensor networks. One of the main challenges for ultrasonic acoustic energy transfer (UAET) is to desirably focus and pattern the transmitted energy and hence locally power wireless piezoelectric-based sensors. We investigated the use of acoustic holograms in UAET through which high amplitudes of acoustic pressure can be patterned to accomplish energy localization at predetermined focal points. An iterative angular spectrum approach was implemented to numerically design a metamaterial-based acoustic hologram for the holographic reconstruction of the multi-focal pressure pattern. Further simulations were performed to analyze ultrasonic power transfer (UPT) to multiple cylindrical

receivers in a target plane. The results show that using the hologram in conjunction with UPT systems allows for enhanced and selective transfer of acoustic energy by taking advantage of beam steering and multi-focal patterning generated by the hologram. The effects of various parameters, such as operating frequency, hologram aperture size, and hologram's position, on accuracy and quality of reconstruction of the desired pattern, were investigated. It is shown that the performance quality and fidelity of the system are strongly affected by these parameters. The performed experiments show the potential of acoustic holograms in the holographic reconstruction of single- and two-focus acoustic patterns to selectively transmit acoustic energy to the receiver(s) located at the predetermined focal point(s) with dramatic electrical power output enhancements.

Acknowledgments

This work was supported by the National Science Foundation (NSF) Grant NO. ECCS-1711139, which is gratefully acknowledged. We would like to thank Omidreza Sadeghi for helping with experiments.

Appendix A

A.1 Analytical electrical impedance

Deriving an expression for the impedance of the fluid-loaded receivers is useful for the identification of its parameters such as underwater short- and open-circuit natural frequencies ω_n under electrical excitation. In equation (2.17), changing the input to $v(t) = Ve^{j\omega t}$ and setting $f_{top}(t) = f_{bottom}(t-\tau) = 0$, while in equation (2.18), replacing the current output $v(t)/R_l$ by the actuation current input $-i(t) = -Ie^{j\omega t}$, yields

$$Z(\omega) = \frac{1}{j\omega\left[C_p + \dfrac{\kappa^2[\phi(L)-\phi(0)]^2}{\omega_n^2 - \omega^2 + j\omega\left[2\zeta\omega_n + R_r\phi^2(0) + R_r\phi^2(L)\right]}\right]} \tag{A.1}$$

for the fluid-loaded receivers' electromechanical impedance ($Z = V/I$), which includes the fundamental longitudinal vibration mode only.

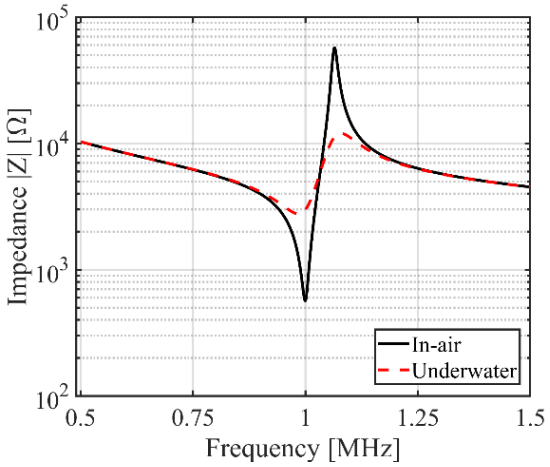

Figure A.1. In-air and underwater electromechanical impedance FRFs of the piezoelectric receiver disk in free-free boundary conditions.

The analytical impedance FRFs for in-air and underwater actuation are shown in figure A.1 as obtained from equation (A.1). The impedance curves capture the fundamental resonance and anti-resonance frequencies of the receiver disk, which are also called the short- and open-circuit resonance frequencies, and they have the values of 1 and 1.08 MHz, respectively. The effects of the added mass and damping due to water loading are clearly observed in figure A.1, and the model

successfully represents the underwater dynamics of the receiver near resonance. It should be noted that the resistive and reactive components of the radiation impedance determine the fluid-induced damping and fluid-loaded resonance frequency, and they depend on the size of the receiver.

A.2 Aperture size effects on the target image fidelity

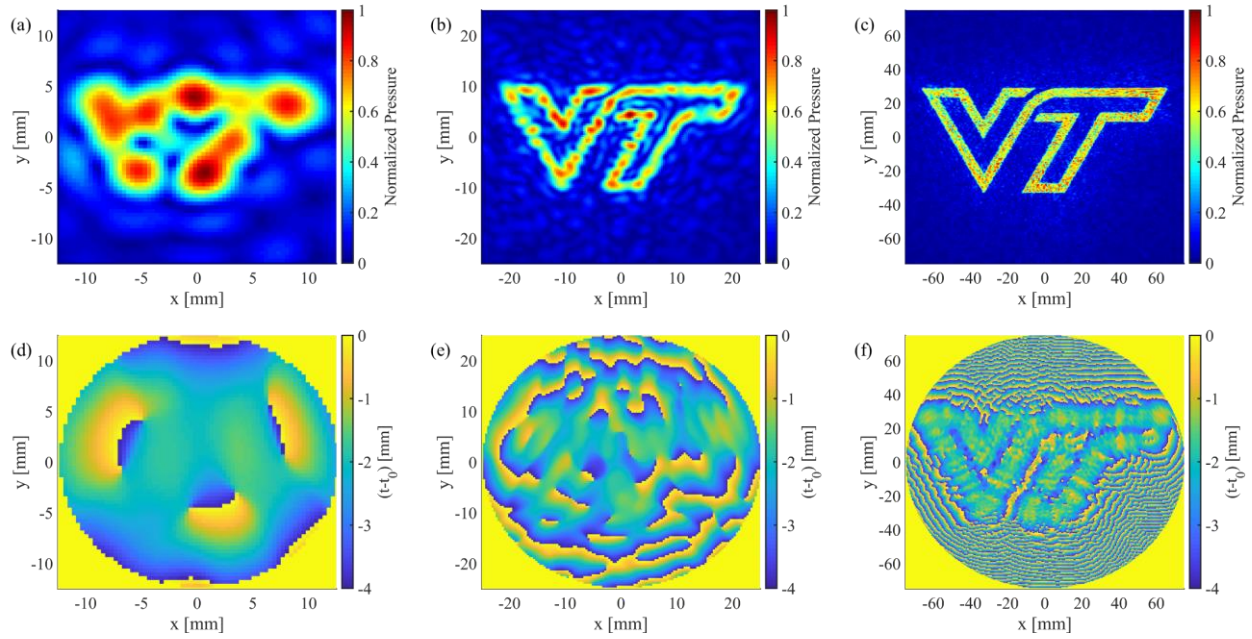

Figure A.2. Propagated acoustic pressure amplitude in the target plane at $z = 50$ mm (VT acoustic image) and with the excitation frequency of 1 MHz for aperture sizes (transmitter disk diameter) of (a) 25 mm, (b) 50 mm, and (c) 150 mm. Corresponding final thickness map of the hologram plate obtained from the IASA for aperture sizes of (d) 25 mm, (e) 50 mm, and (f) 150 mm. The base thickness is 5 mm.

A.3 Power transmission coefficient for the VT pattern

Figure A.3 shows examples of power transmission coefficient calculations with three layers where an acoustic hologram is mounted on a transmitter. Figure A.3a and b demonstrate the general case of a three-layer system (assuming that the hologram has a uniform thickness) analyzing two effects of the operating frequency of the transmitter and a layer (hologram) thickness, respectively. The result in figure A.3a is obtained for the layer thickness of 5 mm and it indicates that the peak transmission occurs at certain frequencies such as 1.1 MHz. Figure A.3b reveals that layer thickness also plays a significant role in the power transmission coefficient. It confirms the fact that both frequency and thickness should be carefully analyzed and selected in order to achieve the highest possible acoustic transmission. Moreover, as the frequency increases, the curve shows more fluctuations within the layer thickness range presented in the plot. Figure A.3c illustrates the

power transmission coefficient in the hologram plane at 1 MHz for the computational results obtained in section 2.3.1. Clearly, the VT pattern is depicted in the plot and the maximum transmission matches with that of figures 2.4(b) and (d).

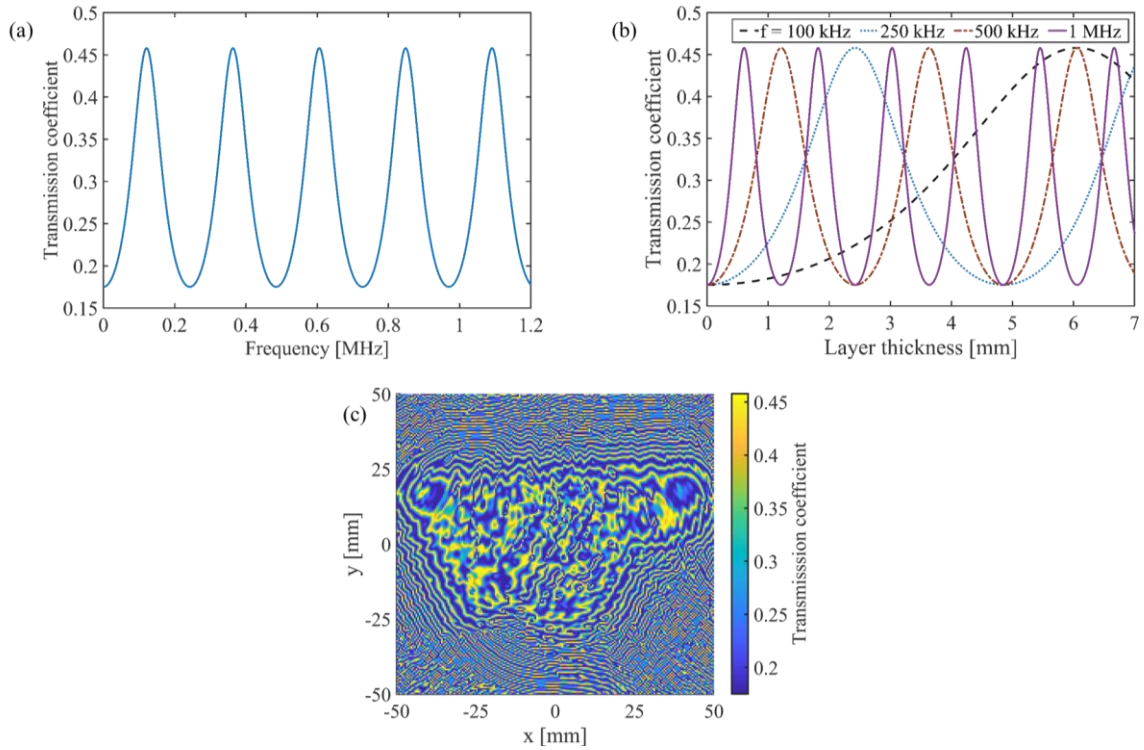

Figure A.3. Power transmission coefficient variation for three layers (a) versus operating frequency with the layer thickness of 5 mm, and (b) versus the layer thickness for different frequencies. (c) The calculated power transmission coefficient for the pixels of the hologram, at 1 MHz for the computational case study shown in figure 2.2.

A.4 More examples showing the effects of detaching the acoustic phase hologram from the transmitter disk and placing it between the transmitter and the target plane

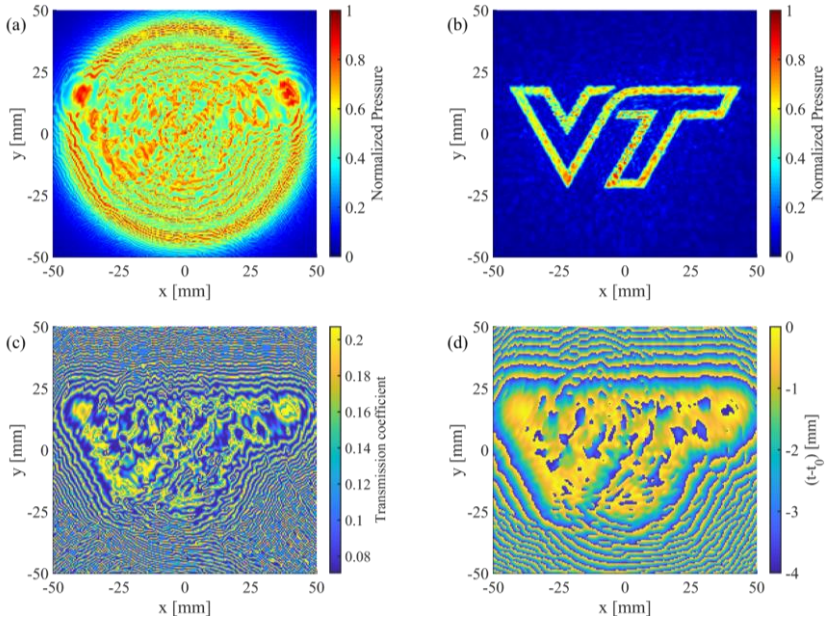

Figure A.4. Acoustic pressure distributions for the holographic reconstruction of the VT image when $d = 50$ mm and $z = 50$ mm. Pressure field in the hologram plane: the (a) amplitude and (b) relative phase. (c) Corresponding acoustic power transmission coefficient and (d) thickness map of the acoustic phase hologram. The driving frequency is 1 MHz and the base thickness is 5 mm.

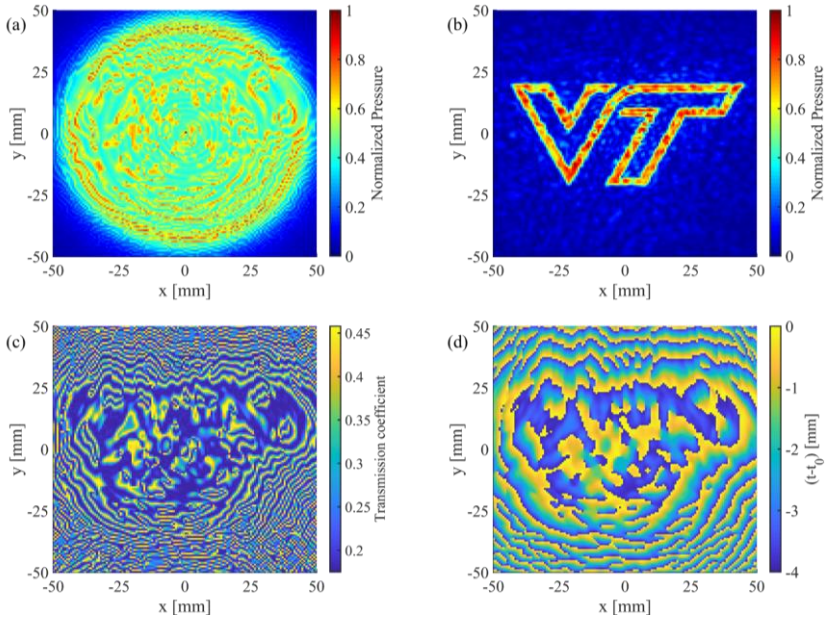

Figure A.5. Acoustic pressure distributions for the holographic reconstruction of the VT image when $d = 50$ mm and $z = 100$ mm. Pressure field in the hologram plane: the (a) amplitude and (b) relative phase. (c) Corresponding acoustic power transmission coefficient and (d) thickness map of the acoustic phase hologram. The driving frequency is 1 MHz and the base thickness is 5 mm.

A.5 Hydrophone experimental setups

Figure A.6a and b show pictures of the experimental setup showing the hydrophone measurements in the target plane when there is no acoustic hologram and in the presence of the left-side-single-focus hologram, respectively.

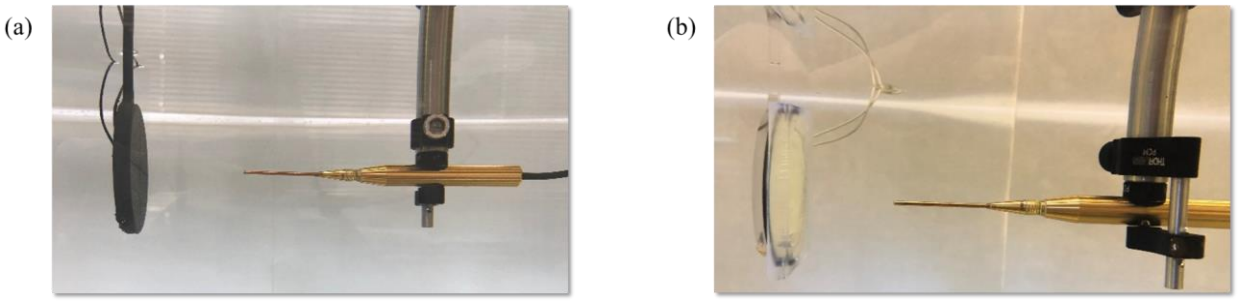

Figure A.6. Experimental setup showing the 1 mm needle hydrophone measurements in the target plane (a) when there is no acoustic hologram and (b) in the presence of the left-side-single-focus hologram.

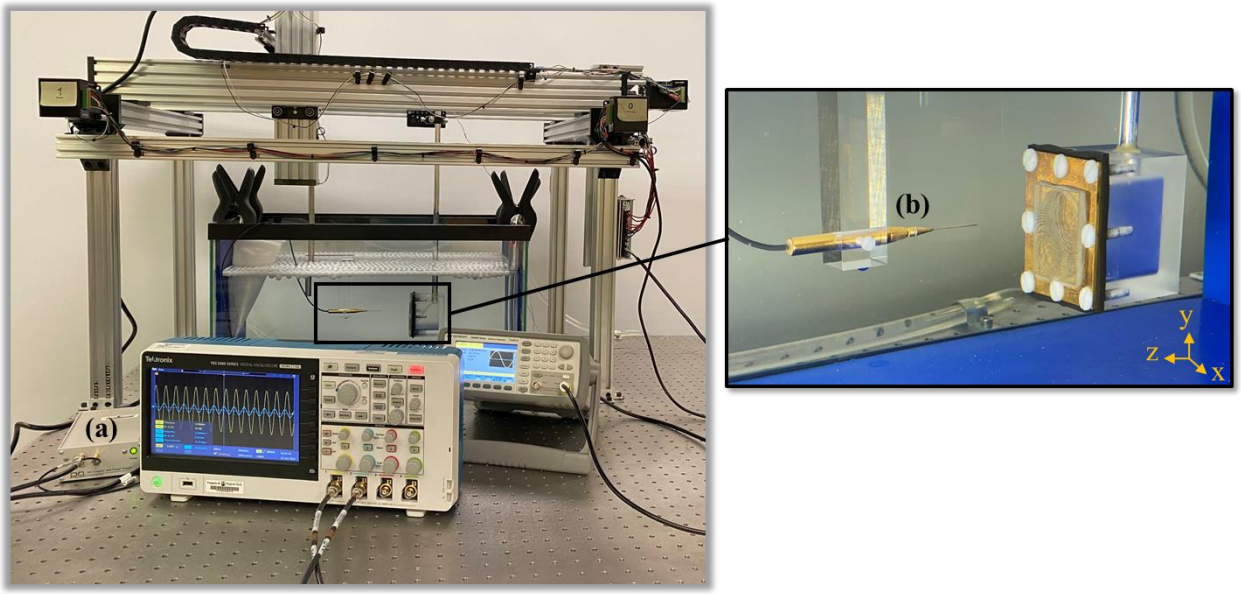

Figure A.7. Experimental setup for measurement of acoustic pressure generated by the passive two-focus hologram with the single PZT transmitter disk enclosed in the watertight box: (a) DC coupler with power supply and (b) 0.2 mm needle hydrophone.

A.6 Power transmission coefficient and acoustic attenuation for the two-focus pattern

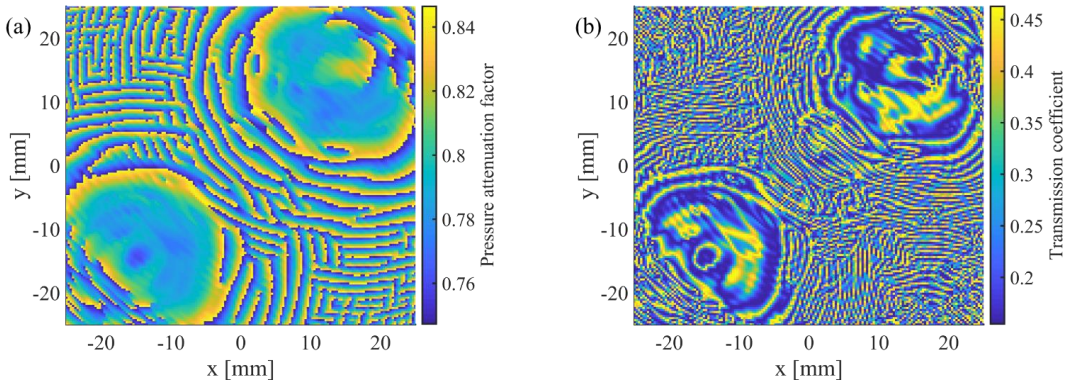

Figure A.8. Acoustic attenuation and transmission losses for the pixels of the two-focus hologram at 2.3 MHz: (a) acoustic pressure attenuation factor and (b) power transmission coefficient map.

Bibliography

[1] Bakhtiari-Nejad, M., Elnahhas, A., Hajj, M.R., and Shahab, S., *Acoustic holograms in contactless ultrasonic power transfer systems: Modeling and experiment.* Journal of Applied Physics, 2018. **124**(24): p. 244901.

[2] Bakhtiari-Nejad, M., Elnahhas, A., Hajj, M.R., and Shahab, S. *Passive metamaterial-based acoustic holograms in ultrasound energy transfer systems*. in *Active and Passive Smart Structures and Integrated Systems XII*. 2018. International Society for Optics and Photonics.

[3] Castle, J., Butts, M., Healey, A., Kent, K., Marino, M., and Feinstein, S.B., *Ultrasound-mediated targeted drug delivery: recent success and remaining challenges.* American Journal of Physiology-Heart and Circulatory Physiology, 2012. **304**(3): p. H350-H357.

[4] Pitt, W.G., Husseini, G.A., and Staples, B.J., *Ultrasonic drug delivery–a general review.* Expert opinion on drug delivery, 2004. **1**(1): p. 37-56.

[5] Shung, K.K., *Diagnostic ultrasound: Imaging and blood flow measurements*. 2015: CRC press.

[6] Roes, M.G., Duarte, J.L., Hendrix, M.A., and Lomonova, E.A., *Acoustic energy transfer: A review.* IEEE Transactions on Industrial Electronics, 2013. **60**(1): p. 242-248.

[7] Andrade, M.A., Pérez, N., and Adamowski, J.C., *Particle manipulation by a non-resonant acoustic levitator.* Applied Physics Letters, 2015. **106**(1): p. 014101.

[8] Glynne-Jones, P., Boltryk, R.J., and Hill, M., *Acoustofluidics 9: Modelling and applications of planar resonant devices for acoustic particle manipulation.* Lab on a Chip, 2012. **12**(8): p. 1417-1426.

[9] Marzo, A., Seah, S.A., Drinkwater, B.W., Sahoo, D.R., Long, B., and Subramanian, S., *Holographic acoustic elements for manipulation of levitated objects.* Nature communications, 2015. **6**: p. 8661.

[10] Hertzberg, Y. and Navon, G., *Bypassing absorbing objects in focused ultrasound using computer generated holographic technique.* Medical physics, 2011. **38**(12): p. 6407-6415.

[11] Szabo, T.L., *Diagnostic ultrasound imaging: inside out*. 2004: Academic Press.

[12] Dunn, F., Hartmann, W., Campbell, D., and Fletcher, N.H., *Springer handbook of acoustics*. 2015: Springer.

[13] Tian, Y., Wei, Q., Cheng, Y., and Liu, X., *Acoustic holography based on composite metasurface with decoupled modulation of phase and amplitude.* Applied Physics Letters, 2017. **110**(19): p. 191901.

[14] Xie, Y., Wang, W., Chen, H., Konneker, A., Popa, B.-I., and Cummer, S.A., *Wavefront modulation and subwavelength diffractive acoustics with an acoustic metasurface.* Nature communications, 2014. **5**: p. 5553.

[15] Gerard, N.J., Li, Y., and Jing, Y., *Investigation of acoustic metasurfaces with constituent material properties considered.* Journal of Applied Physics, 2018. **123**(12): p. 124905.

[16] Li, Y., Jiang, X., Liang, B., Cheng, J.-c., and Zhang, L., *Metascreen-based acoustic passive phased array.* Physical Review Applied, 2015. **4**(2): p. 024003.

[17] Qi, S., Li, Y., and Assouar, B., *Acoustic focusing and energy confinement based on multilateral metasurfaces.* Physical Review Applied, 2017. **7**(5): p. 054006.

[18] Tang, W. and Ren, C., *Beam aperture modifier design with acoustic metasurfaces.* Journal of Physics D: Applied Physics, 2017. **50**(42): p. 425104.

[19] Yuan, B., Cheng, Y., and Liu, X., *Conversion of sound radiation pattern via gradient acoustic metasurface with space-coiling structure.* Applied Physics Express, 2015. **8**(2): p. 027301.

[20] Li, Y., Liang, B., Gu, Z.-m., Zou, X.-y., and Cheng, J.-c., *Reflected wavefront manipulation based on ultrathin planar acoustic metasurfaces.* Scientific reports, 2013. **3**: p. 2546.

[21] Xie, Y., Shen, C., Wang, W., Li, J., Suo, D., Popa, B.-I., Jing, Y., and Cummer, S.A., *Acoustic holographic rendering with two-dimensional metamaterial-based passive phased array.* Scientific reports, 2016. **6**: p. 35437.

[22] Zhu, Y., Hu, J., Fan, X., Yang, J., Liang, B., Zhu, X., and Cheng, J., *Fine manipulation of sound via lossy metamaterials with independent and arbitrary reflection amplitude and phase.* Nature communications, 2018. **9**(1): p. 1632.

[23] Liu, B., Ren, B., Zhao, J., Xu, X., Feng, Y., Zhao, W., and Jiang, Y., *Experimental realization of all-angle negative refraction in acoustic gradient metasurface.* Applied Physics Letters, 2017. **111**(22): p. 221602.

[24] Xie, Y., Konneker, A., Popa, B.-I., and Cummer, S.A., *Tapered labyrinthine acoustic metamaterials for broadband impedance matching.* Applied Physics Letters, 2013. **103**(20): p. 201906.

[25] Zuo, S.-Y., Tian, Y., Wei, Q., Cheng, Y., and Liu, X.-J., *Acoustic analog computing based on a reflective metasurface with decoupled modulation of phase and amplitude.* Journal of Applied Physics, 2018. **123**(9): p. 091704.

[26] Zhang, S., Xia, C., and Fang, N., *Broadband acoustic cloak for ultrasound waves.* Physical Review Letters, 2011. **106**(2): p. 024301.

[27] Melde, K., Mark, A.G., Qiu, T., and Fischer, P., *Holograms for acoustics.* Nature, 2016. **537**(7621): p. 518.

[28] Brown, M.D., Cox, B.T., and Treeby, B.E., *Design of multi-frequency acoustic kinoforms.* Applied Physics Letters, 2017. **111**(24): p. 244101.

[29] Brown, M., Nikitichev, D., Treeby, B., and Cox, B., *Generating arbitrary ultrasound fields with tailored optoacoustic surface profiles.* Applied Physics Letters, 2017. **110**(9): p. 094102.

[30] Brown, M.D., Jaros, J., Cox, B.T., and Treeby, B.E., *Control of broadband optically generated ultrasound pulses using binary amplitude holograms.* The Journal of the Acoustical Society of America, 2016. **139**(4): p. 1637-1647.

[31] Brown, M.D., Martin, E., Cox, B.T., and Treeby, B.E. *Single pulse illumination of multi-layer photoacoustic holograms for patterned ultrasound field generation*. in *Ultrasonics Symposium (IUS), 2016 IEEE International*. 2016. IEEE.

[32] Yoshizawa, S., Ikeda, T., Ito, A., Ota, R., Takagi, S., and Matsumoto, Y., *High intensity focused ultrasound lithotripsy with cavitating microbubbles.* Medical & biological engineering & computing, 2009. **47**(8): p. 851-860.

[33] Akyildiz, I.F., Su, W., Sankarasubramaniam, Y., and Cayirci, E., *Wireless sensor networks: a survey.* Computer networks, 2002. **38**(4): p. 393-422.

[34] Seo, D., Carmena, J.M., Rabaey, J.M., Maharbiz, M.M., and Alon, E., *Model validation of untethered, ultrasonic neural dust motes for cortical recording.* Journal of neuroscience methods, 2015. **244**: p. 114-122.

[35] ter Haar, G. and Coussios, C., *High intensity focused ultrasound: physical principles and devices.* International Journal of Hyperthermia, 2007. **23**(2): p. 89-104.

[36] Shahab, S., Gray, M., and Erturk, A., *Ultrasonic power transfer from a spherical acoustic wave source to a free-free piezoelectric receiver: Modeling and experiment.* Journal of Applied Physics, 2015. **117**(10): p. 104903.

[37] Carrara, M., Cacan, M., Leamy, M., Ruzzene, M., and Erturk, A., *Dramatic enhancement of structure-borne wave energy harvesting using an elliptical acoustic mirror*. Applied Physics Letters, 2012. **100**(20): p. 204105.

[38] Carrara, M., Kulpe, J., Leadenham, S., Leamy, M., and Erturk, A., *Fourier transform-based design of a patterned piezoelectric energy harvester integrated with an elastoacoustic mirror.* Applied Physics Letters, 2015. **106**(1): p. 013907.

[39] Shmilovitz, D., Ozeri, S., Wang, C.-C., and Spivak, B., *Noninvasive control of the power transferred to an implanted device by an ultrasonic transcutaneous energy transfer link.* IEEE Transactions on Biomedical Engineering, 2014. **61**(4): p. 995-1004.

[40] Mellin, S.D. and Nordin, G.P., *Limits of scalar diffraction theory and an iterative angular spectrum algorithm for finite aperture diffractive optical element design.* Optics Express, 2001. **8**(13): p. 705-722.

[41] Shahab, S. and Erturk, A., *Contactless ultrasonic energy transfer for wireless systems: acoustic-piezoelectric structure interaction modeling and performance enhancement.* Smart Materials and Structures, 2014. **23**(12): p. 125032.

[42] Callens, D., Bruneel, C., and Assaad, J., *Matching ultrasonic transducer using two matching layers where one of them is glue.* Ndt & E International, 2004. **37**(8): p. 591-596.

[43] Hill, R. and El-Dardiry, S.M., *A theory for optimization in the use of acoustic emission transducers.* The Journal of the Acoustical Society of America, 1980. **67**(2): p. 673-682.

[44] Lawrence, E.K., Austin, R.F., Alan, B.C., and James, V.S., *Fundamentals of acoustics.* New yorks: John wileys, c2000, 2000: p. 169-151.

[45] McGough, R.J., *Rapid calculations of time-harmonic nearfield pressures produced by rectangular pistons.* The Journal of the Acoustical Society of America, 2004. **115**(5): p. 1934-1941.

[46] Zeng, X. and McGough, R.J., *Evaluation of the angular spectrum approach for simulations of near-field pressures.* The Journal of the Acoustical Society of America, 2008. **123**(1): p. 68-76.

[47] Goodman, J.W., *Introduction to Fourier optics*. 2005: Roberts and Company Publishers.

[48] Kelly, J.F. and McGough, R.J., *A time-space decomposition method for calculating the nearfield pressure generated by a pulsed circular piston.* IEEE transactions on ultrasonics, ferroelectrics, and frequency control, 2006. **53**(6): p. 1150-1159.

[49] Williams, E.G., *Fourier acoustics: sound radiation and nearfield acoustical holography*. 1999: Academic press.

[50] Liu, D.-L. and Waag, R.C., *Propagation and backpropagation for ultrasonic wavefront design.* IEEE transactions on ultrasonics, ferroelectrics, and frequency control, 1997. **44**(1): p. 1-13.

[51] Grande, E.F. and Jacobsen, F., *Near-field acoustic holography with sound pressure and particle velocity measurements.* DTU Electrical Engineering, 2012.

[52] Jacobsen, F., Moreno-Pescador, G., Fernandez-Grande, E., and Hald, J., *Near field acoustic holography with microphones on a rigid sphere (L).* The Journal of the Acoustical Society of America, 2011. **129**(6): p. 3461-3464.

[53] Veronesi, W. and Maynard, J.D., *Nearfield acoustic holography (NAH) II. Holographic reconstruction algorithms and computer implementation.* The Journal of the Acoustical Society of America, 1987. **81**(5): p. 1307-1322.

[54] Maynard, J.D., Williams, E.G., and Lee, Y., *Nearfield acoustic holography: I. Theory of generalized holography and the development of NAH.* The Journal of the Acoustical Society of America, 1985. **78**(4): p. 1395-1413.

[55] Williams, E.G. and Maynard, J., *Holographic imaging without the wavelength resolution limit.* Physical review letters, 1980. **45**(7): p. 554.

[56] Shahab, S., Gray, M., and Erturk, A. *An experimentally validated contactless acoustic energy transfer model with resistive-reactive electrical loading*. in *Active and Passive Smart Structures and Integrated Systems 2015*. 2015. International Society for Optics and Photonics.

[57] Butler, J.L. and Sherman, C.H., *Transducers and arrays for underwater sound*. 2016: Springer.

[58] Erturk, A. and Inman, D.J., *Piezoelectric energy harvesting*. 2011: John Wiley & Sons.

[59] https://www.piceramic.com/en/company/.

[60] https://www.piceramic.com/en/products/piezoceramic-materials/.

[61] Koopmann, G.H., Song, L., and Fahnline, J.B., *A method for computing acoustic fields based on the principle of wave superposition.* The Journal of the Acoustical Society of America, 1989. **86**(6): p. 2433-2438.

[62] Sarkissian, A., *Method of superposition applied to patch near-field acoustic holography.* The Journal of the Acoustical Society of America, 2005. **118**(2): p. 671-678.

[63] Brown, M.D., *Phase and amplitude modulation with acoustic holograms.* Applied Physics Letters, 2019. **115**(5): p. 053701.

[64] Maimbourg, G., Houdouin, A., Deffieux, T., Tanter, M., and Aubry, J.-F., *3D-printed adaptive acoustic lens as a disruptive technology for transcranial ultrasound therapy using single-element transducers.* Physics in Medicine & Biology, 2018. **63**(2): p. 025026.

[65] https://www.steminc.com/PZT/.

[66] http://www.steminc.com/piezo/PZ_property.asp.

[67] Anton, S., Erturk, A., and Inman, D., *Multifunctional self-charging structures using piezoceramics and thin-film batteries.* Smart materials and Structures, 2010. **19**(11): p. 115021.

[68] Bakhtiari-Nejad, M., Hajj, M.R., and Shahab, S., *Dynamics of acoustic impedance matching layers in contactless ultrasonic power transfer systems.* Smart Materials and Structures, 2020. **29**(3): p. 035037.

[69] https://www.piceramic.com/en/.

[70] Sapozhnikov, O.A., Tsysar, S.A., Khokhlova, V.A., and Kreider, W., *Acoustic holography as a metrological tool for characterizing medical ultrasound sources and fields.* The Journal of the Acoustical Society of America, 2015. **138**(3): p. 1515-1532.

[71] Commission, I.E., *IEC/TS 62556 Ultrasonics-Field characterization-Specification and measurement of field parameters for high intensity therapeutic ultrasound (HITU) transducers and systems*. Edition.

[72] Wells, P.N., *Ultrasonic imaging of the human body.* Reports on progress in physics, 1999. **62**(5): p. 671.

[73] Zhang, J., Yang, Y., Zhu, B., Li, X., Jin, J., Chen, Z., Chen, Y., and Zhou, Q., *Multifocal point beam forming by a single ultrasonic transducer with 3D printed holograms.* Applied Physics Letters, 2018. **113**(24): p. 243502.

[74] Melde, K., Choi, E., Wu, Z., Palagi, S., Qiu, T., and Fischer, P., *Acoustic fabrication via the assembly and fusion of particles.* Advanced Materials, 2018. **30**(3): p. 1704507.

[75] Melde, K., *The Acoustic Hologram and Particle Manipulation with Structured Acoustic Fields*. 2020: KIT Scientific Publishing.

Chapter 3

Multi-functional transmission acoustic holograms for contactless transfer of ultrasonic power

This chapter presents the computational and experimental realization of holographic ultrasonic fields using multi-functional holograms for further enhancements of ultrasonic power transfer (UPT) systems. The first group of holograms can generate multiple image patterns at different target planes or distances from the ultrasonic source apparatus. The second group is dynamic holograms that can encode multiple images, each responsive to different driving frequencies.

Abstract

Using a cost-effective and single static acoustic hologram in conjunction with ultrasonic power transfer (UPT) systems allows for enhanced and selective acoustic transmission from a single ultrasonic transmitter to an array of receivers at a particular location. More enhancements can be achieved in UPT patterning by introducing new holographic capabilities using multi-functional holograms. These holograms are designed to generate multiple image patterns of acoustic fields at different target planes or distances from the ultrasonic source apparatus, called multi-image-plane patterning holograms; and to generate multiple acoustic patterns by switching the driving frequency, called multi-frequency patterning holograms, which enable dynamic real-time adaptive controls over the ultrasonic system. This chapter investigates the use of these multi-functional acoustic holograms for possible implementation in UPT systems to provide more flexibility in acoustic power enhancement. Essential modifications are applied to the iterative angular spectrum approach (IASA) optimization algorithm for reconstruction of multiple images at different target planes, i.e., volumetric acoustic fields, and via different driving frequencies, i.e., dynamic acoustic fields. The modified IASA is then used to design various phase-shifting multi-image-plane and

multi-frequency transmission holograms for UPT purposes. Proof-of-concept experiments are also performed to show the functionality of these multi-functional holograms to spatially and dynamically reconstruct multiple desired acoustic patterns, which show satisfactory results.

3.1 Introduction

As an alternative to the expensive and complex phase-shifting circuity and active phased transducer arrays, the use of a passive monolithic hologram in conjunction with a single transducer is a transformative technology to shape sound fields. Holographic reconstruction using acoustic transmission holograms involves storing the phase or/and amplitude profile of the desired wavefront in a two-dimensional designed structure, which alongside a single ultrasonic source, can reproduce arbitrary acoustic fields in a transmission configuration [1-4]. These holograms can be fabricated using conventional 3D printers, which make the design procedure simple and are cost-effective. Another significant advantage of the combination of a hologram and transducer over a phased array is that the hologram provides higher fidelity and information content, which is only limited by the printer's build size and resolution, results in enhancing the system's degrees of freedom. The 3D-printed acoustic phase hologram used to modulate the phase of the incident wave is chosen to have a different speed of sound compared to that of an acoustic medium (such as water or living tissue). This causes the transmitted wave, generated from the acoustic source, to be locally delayed proportionally to the thickness profile of the hologram [1, 2, 4-6]. Recently acoustic holograms have shown promising results in various applications including techniques of therapeutic ultrasound [7-9], diagnostic ultrasound imaging [10], ultrasonic power transfer [4], and particle or cell manipulation [1, 11, 12]. The holograms can be categorized in the acoustic metamaterial group due to their capability for modulation and manipulation of sound waves [13]; a recent review highlighted the major advancements of acoustic holography using metasurfaces is presented by Zhang *et al* [14]. The work in the previous chapter addressed the use of a single static acoustic transmission hologram to desirably and selectively pattern and focus the contactless transfer of ultrasonic power. In this chapter, we aim to evaluate single-element multi-functional holograms that can reconstruct multiple sound images.

Contrary to active phased array transducers that can be adaptively and dynamically controlled in real-time, conventional acoustic holograms are static. This means that each designed hologram can only reconfigure a distinct field at a specific target plane sensitive to a particular driving frequency. To circumvent the limitation for a field reconstruction at a distinct image plane, one can design and fabricate *multi-image-plane patterning* transmission holograms, i.e., holograms that can

generate multiple images at different target planes [1, 15]. Moreover, *multi-frequency patterning* transmission holograms can be designed and manufactured to dynamically reconfigure acoustic fields by generating multiple patterns as the driving frequency is changed [5]. Alternatively, one can take advantage of dynamical programmability of active phased array holography by implementing static acoustic holograms or metamaterials combined with dynamic phased array transducers, but with fewer elements [16-19], to reconstruct more complex field patterns compared to using an array alone, which requires much more elements. Moreover, to overcome the static nature of conventional holograms, a recent work presented a new approach and showed that using a single transducer with two holograms stacked together, a complex and reconfigurable acoustic pressure field can be generated [20].

The work in this chapter focuses on designing multi-image-plane and multi-frequency holograms for possible implementation in ultrasonic power transfer (UPT) systems [21-24]. In section 3.2, we extend the iterative angular spectrum approach (IASA) optimization algorithm to include the utilization of multiple image planes and multiple driving frequencies. Results from computational and experimental holographic reconstruction for multi-functional holograms are presented in sections 3.3. A summary and conclusions are presented in section 3.4.

3.2 Extension of the IASA optimization algorithm for multi-functional holograms

The iterative angular spectrum approach (IASA) steps which explained in chapter 2, section 2.2.2, are also applied here for multi-functional holograms with simple extensions to cover multiple image planes and multiple driving frequencies. The modifications are as follows:

1. *Multi-image-plane patterning:* firstly, in each iteration, the pressure field from the hologram plane is propagated via the angular spectrum approach (ASA) using the propagation function to each image plane, and the multiple desired target amplitudes are imposed upon each corresponding propagated field. Secondly, the imposed fields are back-propagated via the ASA using the backpropagation function to the hologram plane separately, and then the back-propagated complex fields are added together by summation.
2. *Multi-frequency patterning:* Initially, the transmitter output pressure fields at each driving frequencies are averaged together to obtain a single complex field. The field is then propagated to the target plane using each frequency and the desired target amplitudes are imposed upon each field separately. The imposed fields are back-propagated to the hologram plane, each using their respective frequency and the subsequent complex fields

are summed up. For calculating the thickness map, we compute equation (2.12), in chapter 2, using the lowest designed frequency to ensure the maximum required hologram material removal is taken into account. However, the power transmission coefficient and acoustic attenuation should be calculated independently for each frequency. After adding the back-propagated fields together, the amplitude of the field is updated as $|p_h(x,y,0)| = \Lambda(x,y)\sqrt{T_I(x,y)}\ |p_0(x,y,0)|$ considering pressure attenuation factor Λ and power transmission coefficient T_I for each frequency, and then the resultant fields are averaged together leading to a single complex pressure field in the hologram plane to propagate to the target plane for the next iteration.

It is worth noting that the acoustic pressure attenuation factor $\Lambda(x,y) = e^{-\beta_h t(x,y)}$ for each pixel of thickness $t(x,y)$, where β_h is a frequency-dependent sound attenuation coefficient in the hologram (VeroClear) material, should be updated for every frequency assuming a proportional increase of attenuation loss to the first power of frequency; the attenuation coefficient value was measured and is reported in [1] as 63.3 Np/m measured at 2 MHz. Moreover, the acoustic attenuation of water is also considered in the computational simulations as $\beta_{\text{water}} = 0.023$ Np/m [25] (measured at 1 MHz), assuming a proportional increase of losses to the second power of frequency.

3.3 Experimental and computational results for holographic reconstruction of multiple images

Multi-functional holograms are designed to pattern and focus the contactless transmission of acoustic waves generated by the same ultrasonic apparatus used in chapter 2 (also see figure 3.5a), to a 3×3 (nine-element) receiver array in multiple ways. This is achievable when multiple complex pressure fields are generated using the multi-functional holograms based on different axial distances (from the hologram plane) and different driving frequencies. It means that we can selectively power a different set of receivers by placing multiple receiver arrays at different distances from the ultrasonic apparatus, using multi-image-plane holograms; and a different set of receivers can be powered by switching the frequency when a single array is placed, in a particular distance from the hologram plane, using multi-frequency holograms. Each receiver investigated in these case studies is a cylindrical 33-mode modified PZT disk (PIC255 from PI Ceramic GmbH)

with a diameter of 16 mm and a fundamental resonance frequency (thickness mode) of 2.3 MHz in the water domain (measured by the HP4192A impedance analyzer).

3.3.1 Multi-image-plane patterning holograms

In this section, we aim to design holograms that can generate different complex patterns at different distances from the hologram plane. To begin the IASA algorithm, we need to use the transmitter disk output pressure field for propagating and back-propagating of fields between the hologram plane and target planes. These numerical simulations of acoustic wave propagations have to be performed until the pressure fields at the target planes converge to the desired patterns. To this end, the experimentally obtained transmitter output pressure field is used (see figure 2.11b in chapter 2) as we use the same transmitter disk for generating multiple images. We have created different images using the Autodesk Inventor to accomplish acoustic patterning in UPT for selectively powering the elements of the 3×3 receiver array at two different distances of $z = 30$ mm and $z = 60$ mm from the hologram plane. These patterns can be seen in figures 3.1c and e (plus I & cross shapes); as well as figures 3.3a and b (plus II & corner shapes); figures 3.3d and e (plus III & square shapes); figures 3.3g and h (letters I & Z shapes); each set is for designing a different multi-image-plane hologram. Figures 3.1a-f show, respectively, the pressure distributions (amplitude and phase maps) for the holographic reconstruction of the plus- and cross-shaped patterns, each having five focal points, in the hologram plane and target planes at $z = 30$ mm and $z = 60$ mm, after 60 iterations of the IASA.

The thickness profile of the plus-cross hologram plate is shown in figure 3.1g, calculated using equation (2.12) from the final phase map in the hologram plane in figure 3.1b. This thickness map is, after converting into the Standard Tessellation Language (STL) file format, used as an input for 3D printing the designed plus-cross hologram plate, as depicted in figure 3.1h, using VeroClear material. We then performed experiments to measure the pressure fields at distances of 30 and 60 mm from the hologram, which was temporarily fixed to the brass plate, in which the transmitter disk was bonded to (see section 2.5 for the fabrication procedure, hydrophone measurements, and material properties). Figure 3.2 shows the results of acoustic fields' amplitude and phase measurements using the plus-cross hologram, averaged over 2-3 times, at $z = 30$ mm (figures 3.2a and b) and $z = 60$ mm (figures 3.2c and d). The relative phase at each point is determined by comparing the output hydrophone signal and the input signal generated by the waveform generator driving the transmitter. We set the acquisition time in the oscilloscope from 30 μs to 38 μs and 60 μs to 68 μs for $z = 30$ mm and $z = 60$ mm, respectively, with sampling rates of 250 MHz.

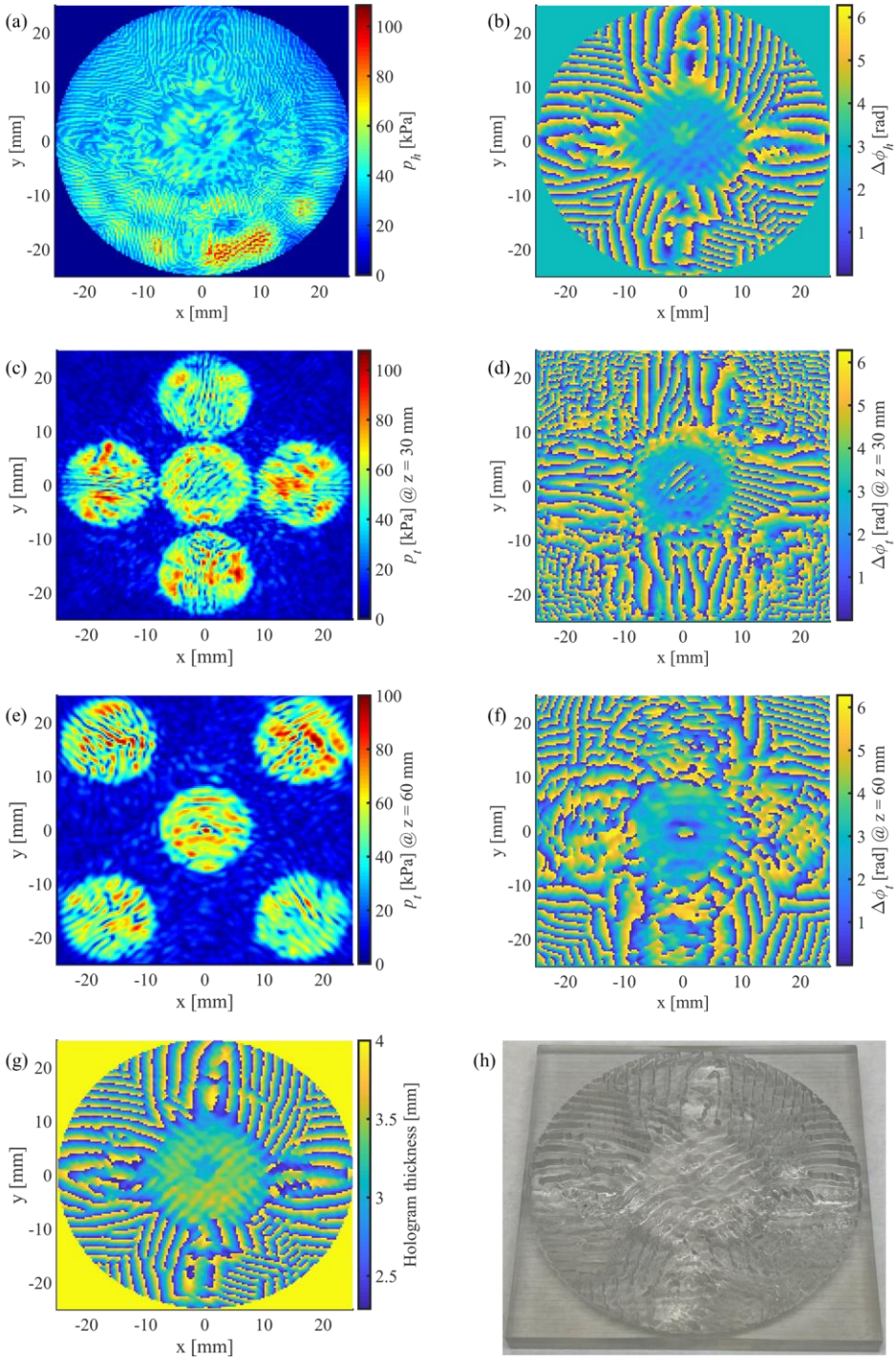

Figure 3.1. Acoustic pressure distributions after 60 iterations of the IASA algorithm for the holographic reconstruction of plus I (5 focal points) & cross (5 focal points) images, including the acoustic field in the hologram plane: the (a) amplitude and (b) relative phase; and the pressure fields in the target planes at $z = 30$ mm: the (c) amplitude and (d) relative phase, and $z = 60$ mm: the (e) amplitude and (f) relative phase. Plus-cross multi-image-plane hologram fabrication: (g) calculated hologram thickness from the hologram phase map in (b); and (h) the manufactured 3D-printed acoustic phase hologram. The driving frequency is 2.3 MHz.

Comparing the experimental holographic fields with that of the computational images, we observe a good agreement where the desired target pressure patterns of plus and cross shape are reasonably realized. The reconstruction efficiencies (see equation (2.21)) for the computational images in figures 3.1c and e are 94.44% and 92.11%, respectively, and for the experimental images in figures 3.2a and c are 30.54% and 30.36%, respectively. There are some amplitude nonuniformities in the experimental holographic reconstruction of multiple images at the two target planes due to the errors associated with the fabrication and instruments, especially those related to the precise alignment and the exact axial distance between the hydrophone and the hologram surface. We have noticed that as we move the hydrophone in the axial *z*-direction by only 0.1 mm, the patterns, particularly the locations of pressure maxima and minima change considerably due to the near-field acoustic pressure fluctuations. To ameliorate this effect, we measured the pressure fields at least 3 times and the final map is obtained by averaging over different times of measurement. The in-depth analysis of the possible experimental errors during experimental hydrophone measurements of the holographic reconstructed pressure fields is provided in section 2.5.2.

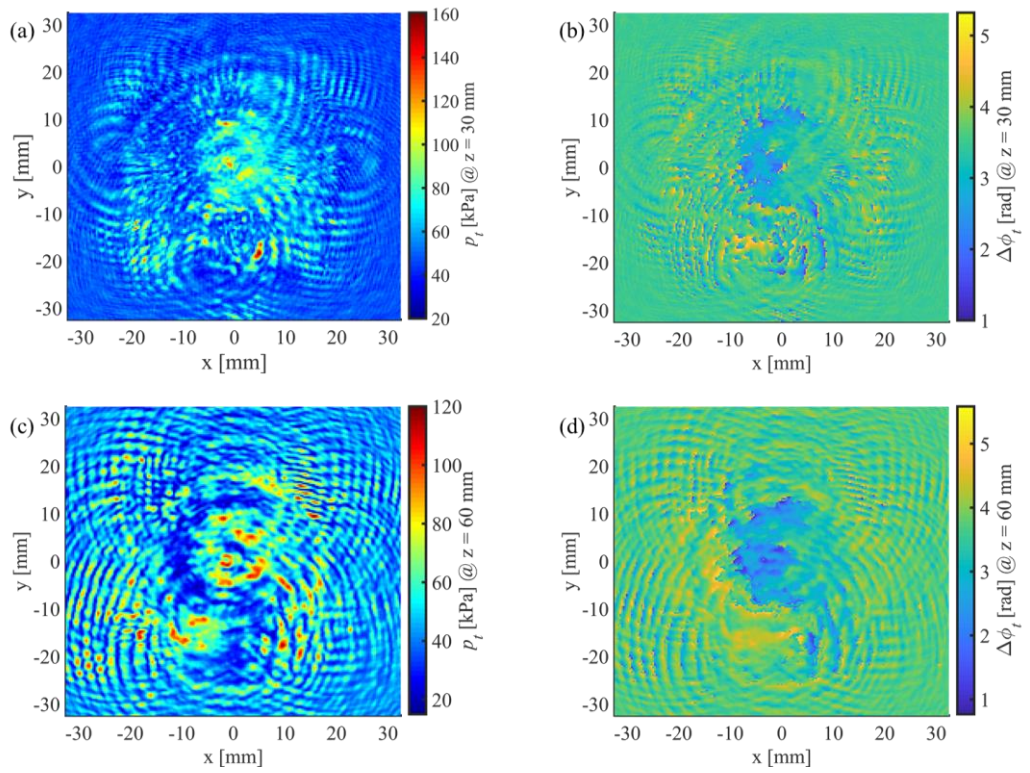

Figure 3.2. Experimentally measured pressure fields using the plus-cross multi-image-plane hologram in the target planes at $z = 30$ mm: the (a) amplitude and (b) relative phase, and $z = 60$ mm: the (c) amplitude and (d) relative phase. The driving frequency and voltage are 2.3 MHz and 30.4 V peak-to-peak, respectively.

Encoding multiple images and hence additional information into a single hologram also causes some reduction in quality and homogeneity of the images. It should be noted that 3D-printed acoustic phase holograms are designed only by modulating the phase of the fields and the finite and flat aperture of the holograms, as well as their fixed distances to target planes, limit the reproduction of the fields. Moreover, the holograms are initially designed by imposing target binary amplitude images, which result in infinitely steep edges, which can not be perfectly generated by physical waves possessing finite frequency bandwidth features [26].

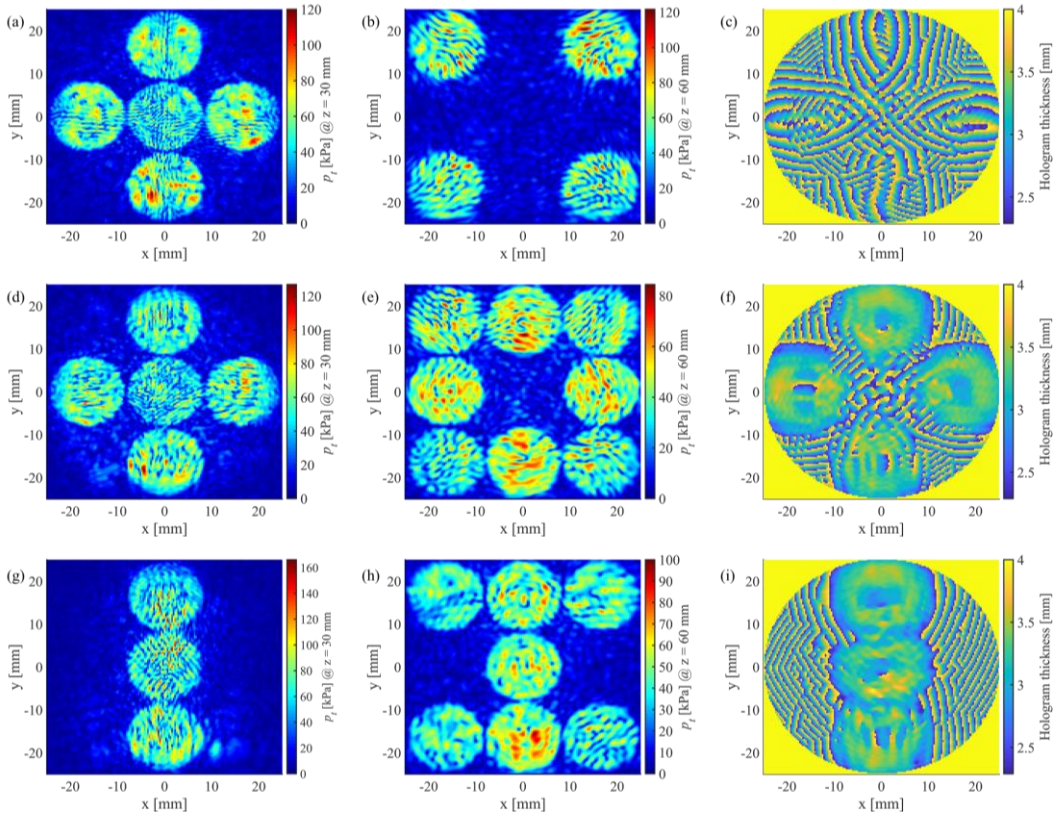

Figure 3.3. Holographic reconstruction of *plus II* (5 focal points) *& corner* (4 focal points) images: the acoustic pressure amplitudes in the target planes at (a) $z = 30$ mm and (b) $z = 60$ mm, and (c) the calculated hologram thickness. Holographic reconstruction of *plus III* (5 focal points) *& square* (8 focal points) images: the acoustic pressure amplitudes in the target planes at (d) $z = 30$ mm and (e) $z = 60$ mm, and (f) the calculated hologram thickness. Holographic reconstruction of letters *I* (3 focal points) *& Z* (7 focal points) images: the acoustic pressure amplitudes in the target planes at (g) $z = 30$ mm and (h) $z = 60$ mm, and (i) the calculated hologram thickness. The driving frequency is 2.3 MHz.

Investigating the final thickness profile of the designed multi-image-plane holograms in figures 3.1g and 3.3c, f, and i, calculated from the final phase maps in the hologram planes, after 60-80 IASA iterations, few thickness irregularities are noticed originating from unwanted phase jumps. These phase anomalies also adversely affect the fidelity of holographic reconstruction of images

at the target planes, which can be observed in the amplitude and phase of the experimental fields of figure 3.2. Despite all aforementioned imperfections, the computations and experiments in this section show satisfactory results by generating higher amplitudes of pressure at nearly predetermined locations to fulfill the goal of possible patterning and focusing the contactless transfer of power in ultrasonic systems at multiple distances from the acoustic source. Figure 3.4 shows the signal-to-noise ratio (SNR) and parameter image correlation for the quality analysis of multiple pattern images of figures 3.1c and e and figures 3.3a and b, 3.3d and e, and 3.3g and h. The SNR for each image pattern is calculated as the ratio of the average pressure amplitude in the target region where we imposed a non-zero amplitude (foreground pressure) to that of the average pressure amplitude in the region where we imposed zero amplitude (background pressure). On the other hand, we introduce another error metric for the multi-image-plane patterning called *distance crosstalk*, the unwanted generation of patterns or artifacts in the field at a particular distance that resembles the patterns imposed for the field at other distance. For calculating the distance crosstalk, the unwanted coupling SNR between two images has to be calculated as the ratio of the average foreground pressure to that of the background pressure of the particular field but considering the image pixels associated with the other field.

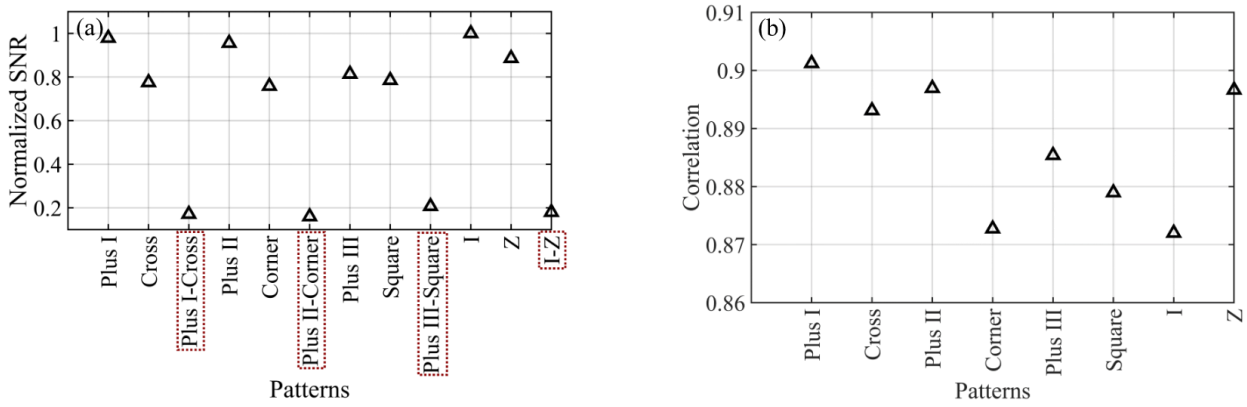

Figure 3.4. Error metrics to evaluate the quality of computational holographic reconstruction of multi-image-plane patterning: (a) signal-to-noise ratio (SNR), normalized by the maximum SNR value, which corresponds to the letter-I-shaped patterning, and (b) correlation between the computational holographic images and their respective imposed target images.

The crosstalks in figure 3.4a are labeled as the unwanted coupling between *Plus I-Cross*, *Plus II-Corner*, *Plus III-Square* shapes, and letters *I-Z* and depicted as dark red dotted rectangles. For each crosstalk metric, we find two values, e.g., for the distance crosstalk between plus and cross images, one value is the SNR calculated for the field of plus shape, but considering the image pixels of the

cross-shaped pattern and the second value is the SNR calculated vice-versa. To find a single value analyzing the distance crosstalk between two images, we compute the average of the two values. Clearly, the lower the distance crosstalk is, the higher fidelity is constructed for the multi-image-plane patterning, whereas a higher value of the SNR for each image (labeled as *Plus I*, *Cross*, *Plus II*, *Corner*, *Plus III*, *Square*, *I*, *Z* in figure 3.4a) indicates that the corresponding hologram encodes higher images' quality. As depicted in figure 3.4a, almost all the designed multi-image-plane holograms show high values of the SNR for each image pattern and relatively low values of distance crosstalk between images, which confirms the high fidelity of these computed holograms. Figure 3.4b shows the image correlations for evaluating the similarities between the computational images with that of the imposed target images (see equation (2.20)) using the multi-image-plane holograms. Comparing with the correlation results of holograms encoding single images (figure 2.13), the image correlations for multiple images at different distances slightly decrease. This is due to the unwanted generation of the crosstalks and artifacts during the holograms' computations and multiple forward and backward propagations, and the fact that unavoidably the waves pass the other target planes as well. We also note that the symmetry and complexity of the patterns, as well as the distances between target planes and the aperture size of the holograms compared to the size of the patterns, significantly influence the performance quality of the multi-image-plane holograms.

3.3.2 Multi-frequency patterning holograms

In this section, we aim to design holograms that can generate different complex patterns by changing the driving frequency. In this way, we somehow overcome the limitation of static and fixed holograms and introducing real-time adaptive controls over the ultrasonic apparatus via employing dynamic holograms that can encode multiple image patterns, each sensitive to different driving frequencies. Using the same ultrasonic apparatus as before, which includes the transmitter disk of 50 mm diameter with the resonance frequency of 2.3 MHz, we performed underwater actuation experiments (see figure 3.5a) to measure the disk's surface velocity frequency response function (FRF). The surface velocity was measured using a laser Doppler vibrometer (LDV, including PolytecOFV-505 sensor head and Polytec OFV-5000 controller) and acquired using the 1-GS/s digital oscilloscope (Tektronix TBS 2000 series, model TBS2104) with the excitation average voltage of 32.8 V peak-to-peak from the waveform generator (Keysight 33500B series) that was connected to the amplifier (E&I RF power amplifier, model A075). As noticed from the surface velocity FRF of the transmitter disk in figure 3.5b, the PZT transducer vibrates

considerably at frequencies of 1.3 and 1.8 MHz, apart from the fundamental frequency of 2.3 MHz. Hence, these three frequencies are chosen as the design frequencies for constructing dynamic multi-frequency holograms.

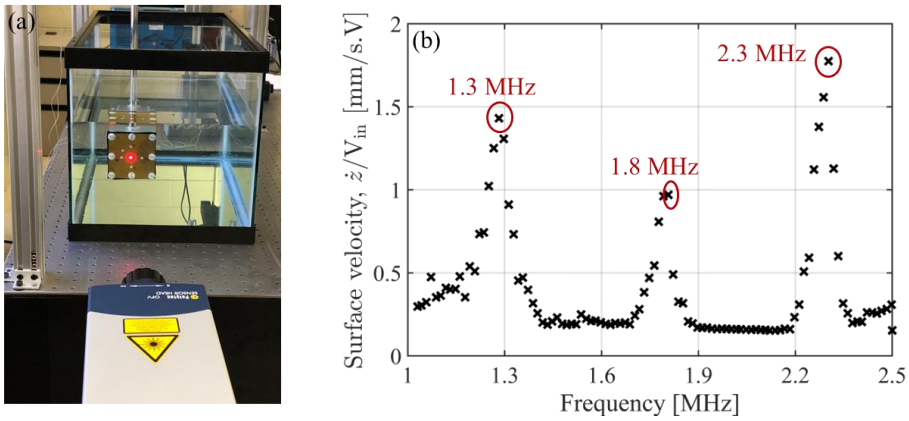

Figure 3.5. (a) Underwater actuation experimental setup and (b) corresponding measured surface velocity of the 50-mm-diameter PZT transducer using laser Doppler vibrometer, versus excitation frequency, which shows the considerable transducer's underwater vibration responses at frequencies of 1.3 and 1.8 MHz, as well as at the fundamental frequency of 2.3 MHz.

The transmitter disk output pressure fields at the design frequencies of 1.3 and 1.8 MHz were also measured, which provides the boundary condition for the ultrasonic source (see figures 2.11a and b for the transducer output at 2.3 MHz). Figures 3.6a and c show the experimentally measured sound pressures at the distance of 9.3 mm from the ultrasonic source, operating at 1.3 and 1.8 MHz, respectively, using the calibrated 0.2 mm needle hydrophone. All the experimental setup, as well as the measurement and acquisition parameters, are the same as that of the hydrophone experiments at the distance of 9.3 mm for the driving frequency of 2.3 MHz (see section 2.5.1). Similarly, the excitation voltages and spatial resolutions were, respectively, set to 30.4 V peak-to-peak and 0.32 mm and the measurements were averaged over four times. Figures 3.6b and d show the numerically back-propagated transmitter output pressure fields driving at 1.3 and 1.8 MHz, respectively, which identify the source boundary conditions at the respective design frequencies.

Using the transducer output pressure fields at the three design frequencies, we compute multi-frequency holograms using the modified IASA optimization algorithm as explained in section 3.2. We have created different images using the Autodesk Inventor to enable real-time reconfiguration control for acoustic patterning in UPT for selectively powering the elements of the 3×3 receiver array, sensitive to the different frequencies of 1.3, 1.8, and 2.3 MHz. These patterns can be seen in figures 3.7 and 3.8c and e (letter I1 & plus shapes); as well as figures 3.10a, b, d, and e (letters U1

& H1 shapes); figures 3.10g, h, j, and k (letters U2 & H2 shapes); figures 3.11a, b, d, and e (letters I2 & Z shapes); figures 3.11g, h, j, and k (letters L & U3 shapes); each set is for designing a different multi-frequency hologram.

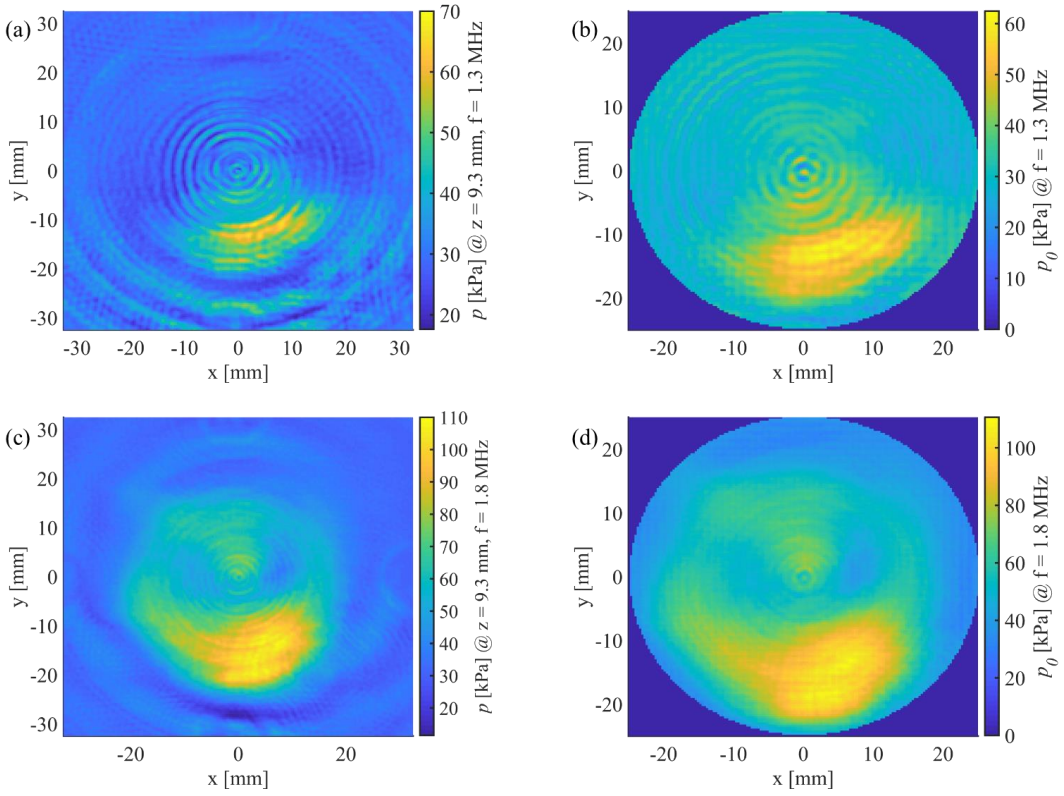

Figure 3.6. Acoustic source boundary conditions: experimentally measured pressure fields in the plane with a distance of 9.3 mm from the ultrasonic source at the driving frequency of (a) 1.3 MHz and (c) 1.8 MHz; the numerically back-propagated transmitter output pressure field at the driving frequency of (b) 1.3 MHz and (d) 1.8 MHz.

Figures 3.7 and 3.8a-f show the pressure distributions (amplitude and phase maps) for the holographic reconstruction of the letter-I- and plus-shaped patterns, with corresponding three and five focal points, reconstructed from multi-frequency holograms sensitive to driving frequencies of 1.3 and 2.3 MHz (figures 3.7a-f) and also frequency set of 1.8 and 2.3 MHz (figures 3.8a-f). Figures 3.7 and 3.8a and b present the pressure fields in the hologram plane and figures 3.7 and 3.8c-f illustrate the fields in a target plane at $z = 51$ mm for driving frequency sets of 1.3 and 2.3 MHz, as well as 1.8 and 2.3 MHz, respectively. The thickness profiles of the letter-I-plus multi-frequency hologram plates are shown in figures 3.7 and 3.8g for the two sets of driving frequencies, i.e., 1.3 and 2.3 MHz, and 1.8 and 2.3 MHz, from the final phase map in the holograms' plane in figures 3.7 and 3.8b, respectively.

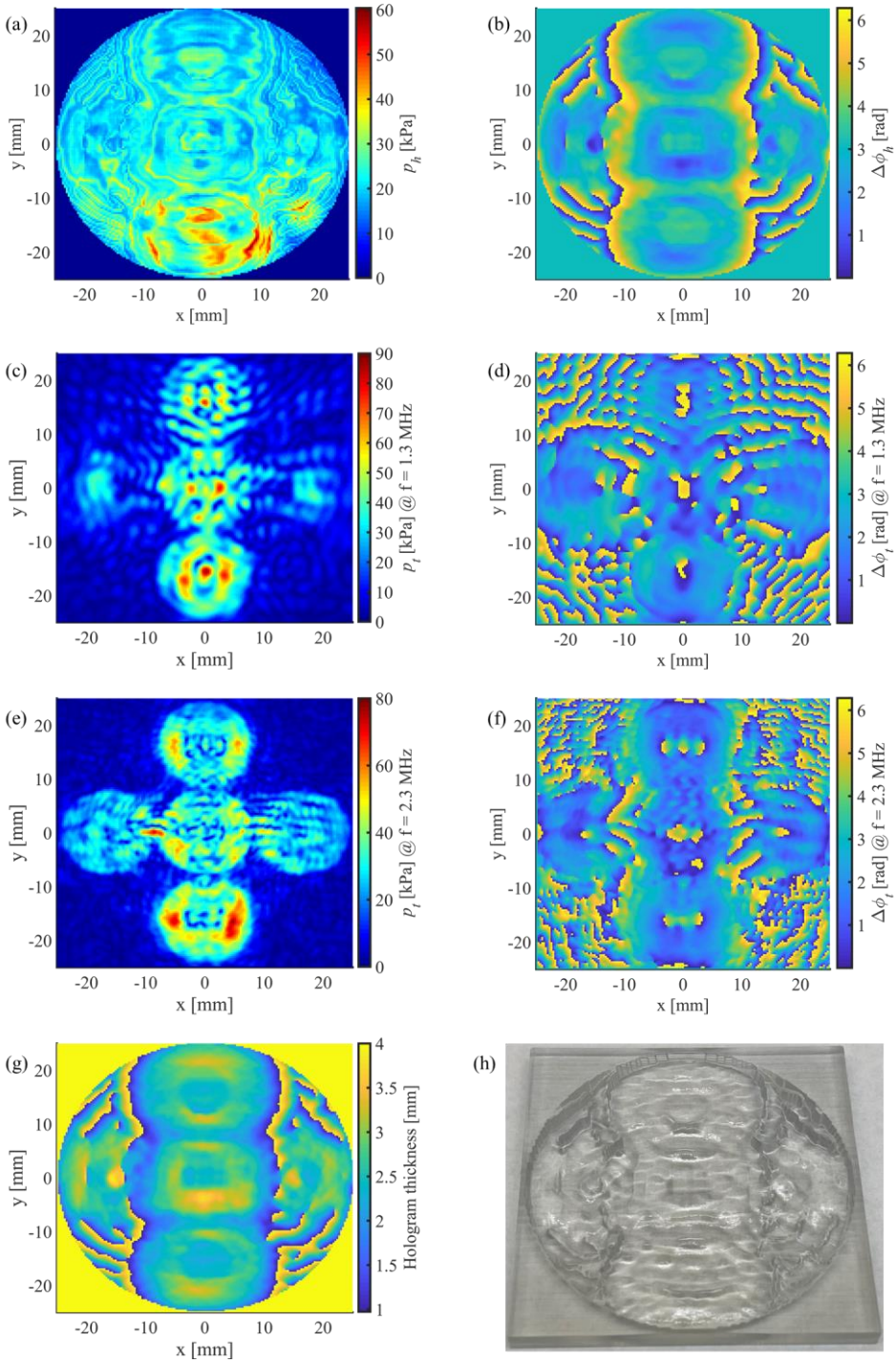

Figure 3.7. Acoustic pressure distributions after 20 iterations of the IASA algorithm for holographic reconstruction of letter I1 (3 focal points) & plus (5 focal points) images, including the average acoustic fields for *driving frequency of 1.3 and 2.3 MHz* in the hologram plane: the (a) amplitude and (b) relative phase; and the pressure fields in the target plane at $z = 51$ mm for driving frequency of 1.3 MHz: the (c) amplitude and (d) relative phase, and for driving frequency of 2.3 MHz: the (e) amplitude and (f) relative phase. Fabrication of letter-I-plus multi-frequency hologram with driving frequency set of 1.3 and 2.3 MHz: (g) calculated hologram thickness from the hologram phase map in (b); and (h) the manufactured 3D-printed acoustic phase hologram.

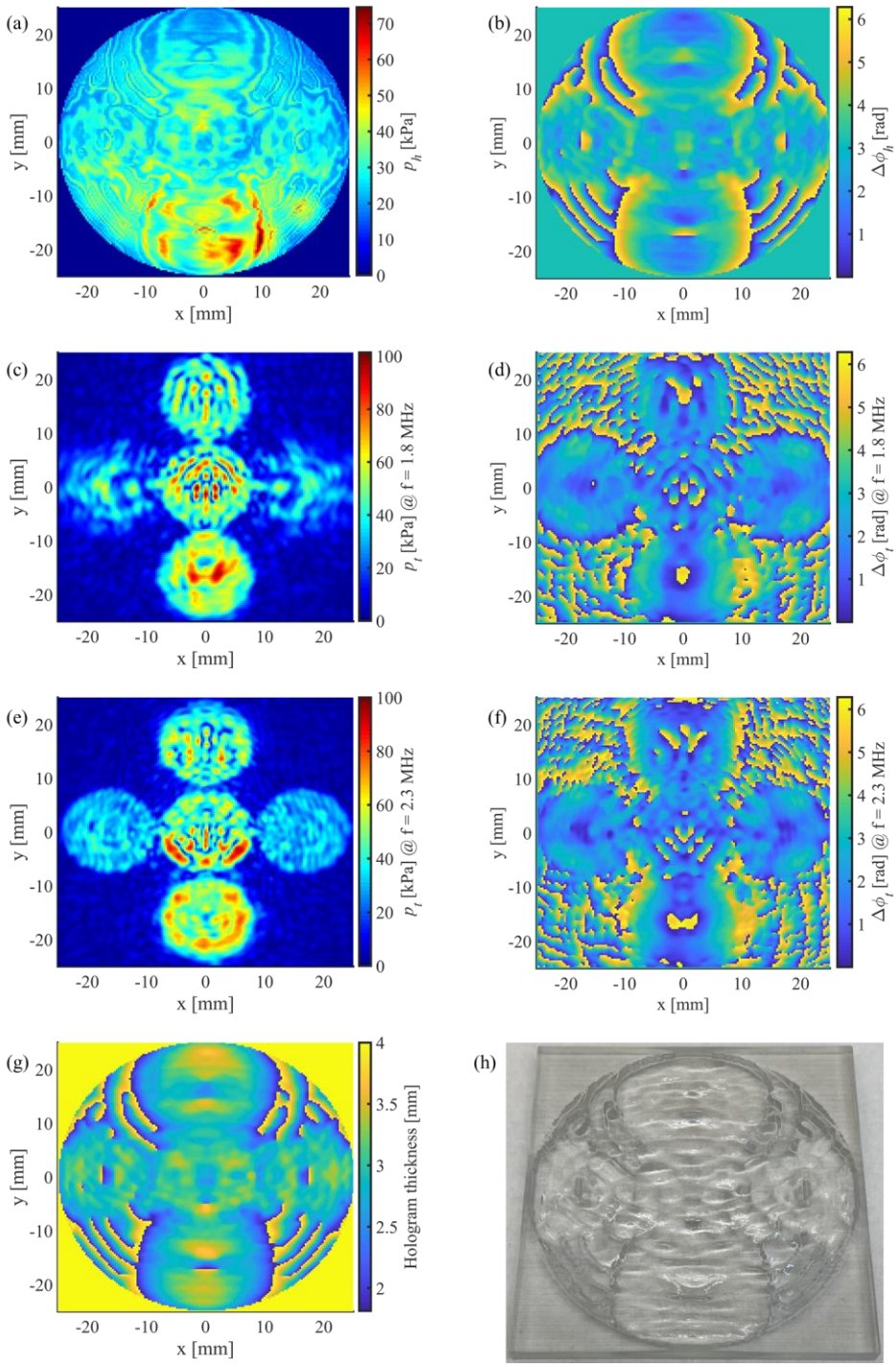

Figure 3.8. Acoustic pressure distributions after 30 iterations of the IASA algorithm for holographic reconstruction of letter I1 (3 focal points) & plus (5 focal points) images, including the average acoustic fields for *driving frequency of 1.8 and 2.3 MHz* in the hologram plane: the (a) amplitude and (b) relative phase; and the pressure fields in the target plane at $z = 51$ mm for driving frequency of 1.8 MHz: (c) the amplitude and (d) relative phase, and for driving frequency of 2.3 MHz: the (e) amplitude and (f) relative phase. Fabrication of letter-I-plus multi-frequency hologram with driving frequency set of 1.8 and 2.3 MHz: (g) calculated hologram thickness from the hologram phase map in (b); and (h) the manufactured 3D-printed acoustic phase hologram.

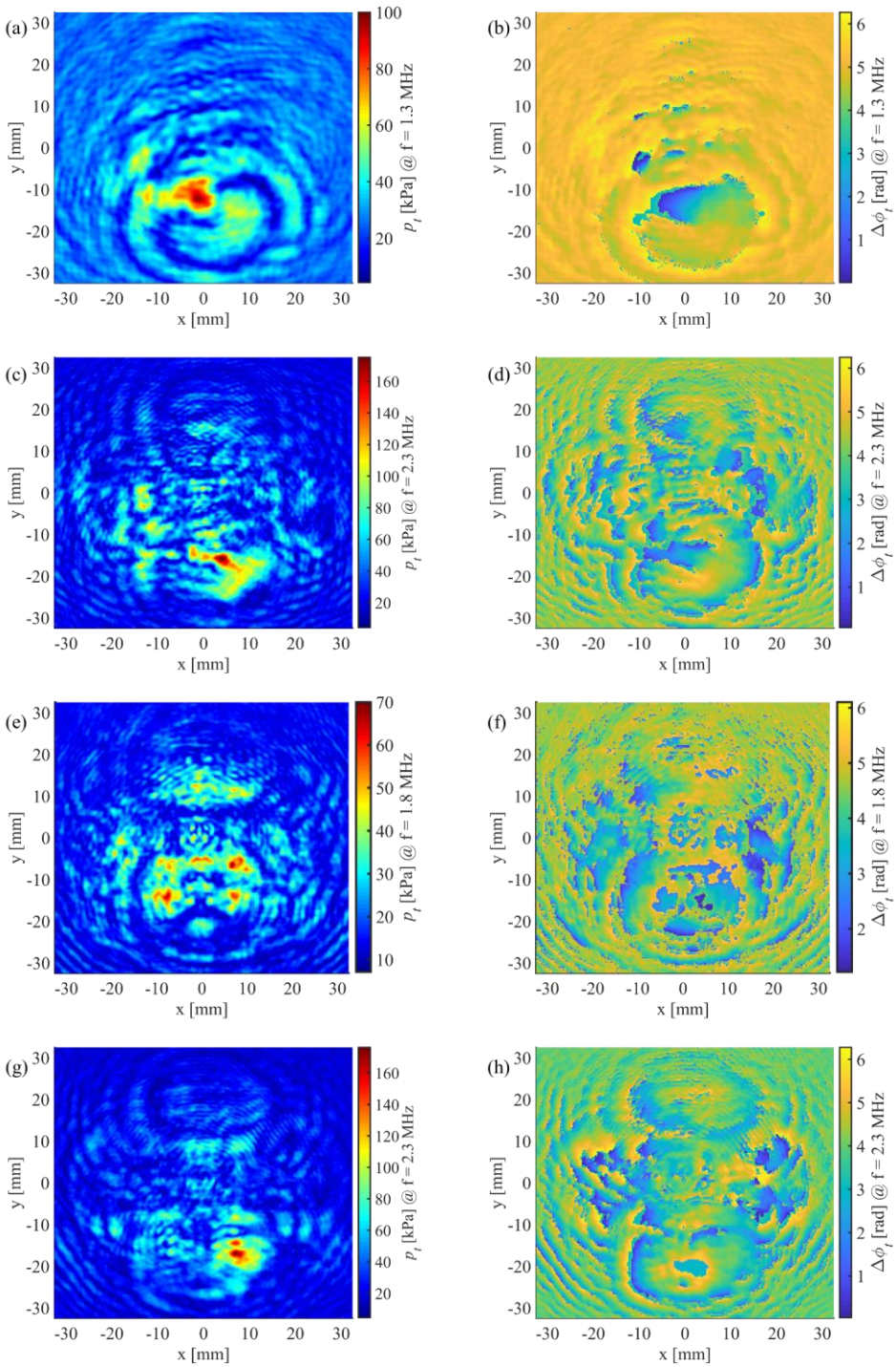

Figure 3.9. Experimentally measured pressure fields in the target plane at $z = 51$ mm using the letter-I-plus multi-frequency hologram, designed for *frequency set of 1.3 and 2.3 MHz*: amplitude maps for driving frequency of (a) 1.3 MHz and (c) 2.3 MHz; phase maps for driving frequency of (b) 1.3 MHz and (d) 2.3 MHz. Experimentally measured pressure fields in the target plane at $z = 51$ mm using the letter-I-plus multi-frequency hologram designed for *frequency set of 1.8 and 2.3 MHz*: amplitude maps for driving frequency of (e) 1.8 MHz and (g) 2.3 MHz; phase maps for driving frequency of (f) 1.8 MHz and (h) 2.3 MHz. The driving voltage for all experiments is set to 30.4 V peak-to-peak.

These thickness maps are then used for 3D printing the designed hologram plates, as depicted in figures 3.7 and 3.8h, using VeroClear material. Compared to the multi-image-plane holograms presented in section 3.3.1, more noticeable and undesirable artifacts are generated in the field at the particular design frequency that resembles the image patterns encoded onto other design frequency, which for multi-frequency holograms called *frequency crosstalk*. Furthermore, we have noticed that the crosstalk increases as the frequency spacing decreases comparing the two sets of 1.3 and 2.3 MHz (figure 3.7c) with that of 1.8 and 2.3 MHz (figure 3.8c). Hydrophone experiments, similar to section 3.3.1, were also performed using the multi-frequency hologram plates shown in figures 3.7 and 3.8h. Figure 3.9 shows the measurement results of acoustic fields' amplitude and phase, averaged over two times, using the letter-I-plus hologram at the design frequency set of 1.3 and 2.3 MHz (figures 3.9a-d) and the other letter-I-plus hologram, this time at the different design frequency set of 1.8 and 2.3 MHz (figures 3.9e-h). The acquisition time in the oscilloscope was set from 60 μs to 68 μs with a sampling rate of 250 MHz.

The reconstruction efficiencies for the computational images in figures 3.7c and e using the multi-frequency hologram for *frequency set of 1.3 and 2.3 MHz* are 76.77% and 92.07%, respectively, and for the experimental images in figures 3.9a and c are 21.85% and 41.15%, respectively. Similarly, the reconstruction efficiencies using the multi-frequency hologram for *frequency set of 1.8 and 2.3 MHz* are 76.84% and 94.77% for the computational images in figures 3.8c and e, and 24.20% and 33.69% for the experimental images in figures 3.9e and g, respectively. The reconstruction efficiency ranges are comparable to that of the computational and experimental images for the designed multi-image-plane hologram presented in figures 3.1 and 3.2, except for the efficiency reductions of around 19-28% associated with lower frequencies of 1.3 and 1.8 MHz. However, the desired patterns are not as realizable as those of the multi-image-plane patterning for experimental images, i.e., less amplitude uniformity is achieved for multi-frequency holograms, which can be seen as pointwise amplitude concentrations (very high-amplitude regions) or faint appearance of patterns (very low-amplitude regions).

Moreover, in each frequency set of the experiments, the target patterns for the driving frequency of 2.3 MHz were better reconstructed and demonstrate higher reconstruction efficiencies compared to those of 1.3 and 1.8 MHz due to shorter wavelength and better reconstruction resolution of higher frequencies. The experimentally reconstructed image for the driving frequency of 1.3 MHz resembles the least similarity to its associated target pattern, probably due to imperfections seen in the phase map/thickness profile of the hologram and the less functionality of the transducer at 1.3

MHz, as was also apparent in the electrical impedance of the underwater transducer disk (measured by the impedance analyzer).

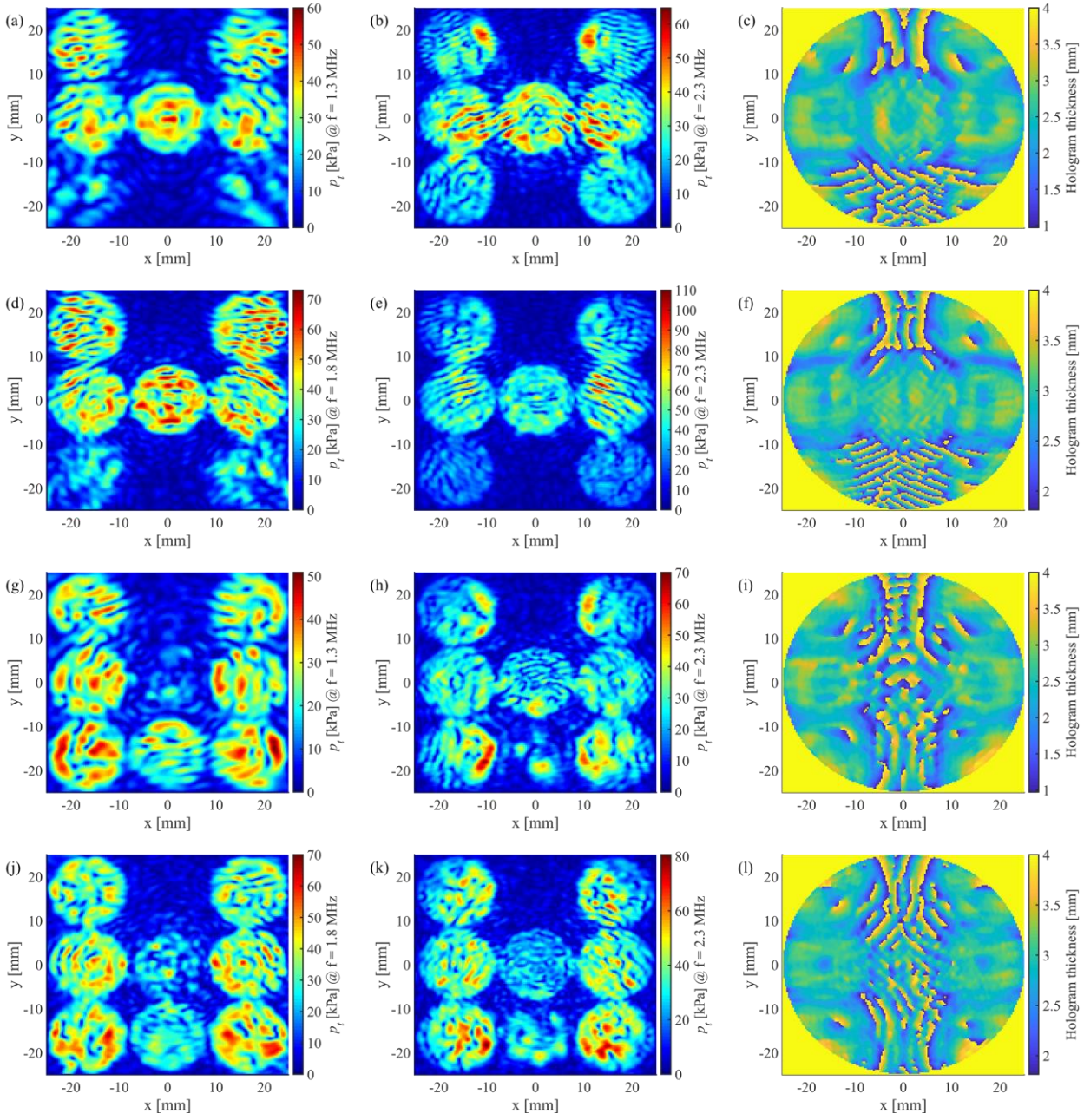

Figure 3.10. Holographic reconstruction of letters *U1* (5 focal points) *& H1* (7 focal points) images for multi-frequency holograms: the acoustic pressure amplitudes for frequency set of (a) 1.3 MHz and (b) 2.3 MHz, and (c) the calculated hologram thickness; the acoustic pressure amplitudes for frequency set of (d) 1.8 MHz and (e) 2.3 MHz, and (f) the calculated hologram thickness. Holographic reconstruction of letters *U2* (7 focal points) *& H2* (7 focal points) images for multi-frequency holograms: the acoustic pressure amplitudes for frequency set of (g) 1.3 MHz and (h) 2.3 MHz, and (i) the calculated hologram thickness; the acoustic pressure amplitudes for frequency set of (j) 1.8 MHz and (k) 2.3 MHz, and (l) the calculated hologram thickness. The target plane for all the images is set to $z = 51$ mm.

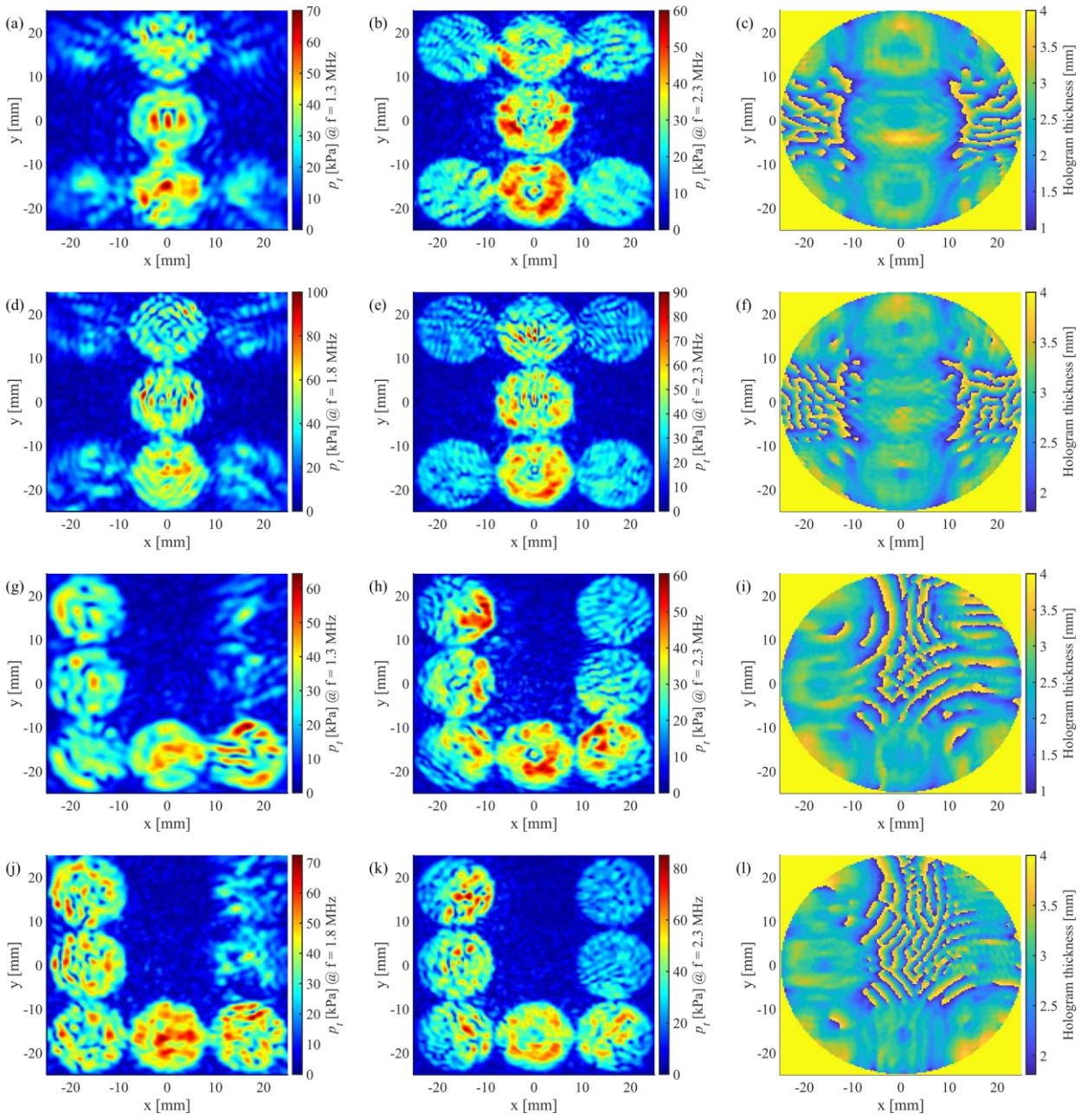

Figure 3.11. Holographic reconstruction of letters *I2* (3 focal points) & *Z* (7 focal points) images for multi-frequency holograms: the acoustic pressure amplitudes for frequency set of (a) 1.3 MHz and (b) 2.3 MHz, and (c) the calculated hologram thickness; the acoustic pressure amplitudes for frequency set of (d) 1.8 MHz and (e) 2.3 MHz; and (f) the calculated hologram thickness. Holographic reconstruction of letters *L* (5 focal points) & *U3* (7 focal points) images for multi-frequency holograms: the acoustic pressure amplitudes for frequency set of (g) 1.3 MHz and (h) 2.3 MHz, and (i) the calculated hologram thickness; the acoustic pressure amplitudes for frequency set of (j) 1.8 MHz and (k) 2.3 MHz; and (l) the calculated hologram thickness. The target plane for all the images is set to $z = 51$ mm.

The general lower performance quality for the reconstruction of multiple computational and experimental images via the multi-frequency holograms, besides the aforementioned experimental

errors, could be due to several factors. One possible reason is that the phase offset used for computation of multi-frequency holograms' thickness profile is not precisely generated based on each specific design frequency. Instead, we have assumed that all phase maps of complex fields have a contribution to the surface profile of the holograms by complex summation of the fields at different design frequencies. This limits the hologram aperture to generate any arbitrary pattern and also increases the crosstalk between patterns. It is believed that simpler and more centric patterns with smaller aperture sizes (e.g., receivers/focal points having smaller diameters) could be better generated with multi-frequency holograms. To confirm this hypothesis, we have computationally designed multi-frequency holograms, shown in figures B.1 and B.2 in appendix B with their associated error metrics in figure B.3, using three design frequencies of 1.3, 1.8, and 2.3 MHz, one to generate patterns enclosing 8-mm-diameter receivers for UPT purposes and the other to generate patterns of numbers *1*, *2*, and *3*. It is also worthwhile to mention that the patterns presented in this section encompassing 16-mm-diameter receivers could generate with much lower quality using the three design frequencies together. Another possibility is that although maximizing the frequency spacing within the transducer bandwidth decreases the crosstalk, as can also be discerned from figure 3.12a (crosstalks are depicted as dark red dotted rectangles), the wavelength difference between design frequencies increases the errors in the phase offset generated by a multi-frequency hologram.

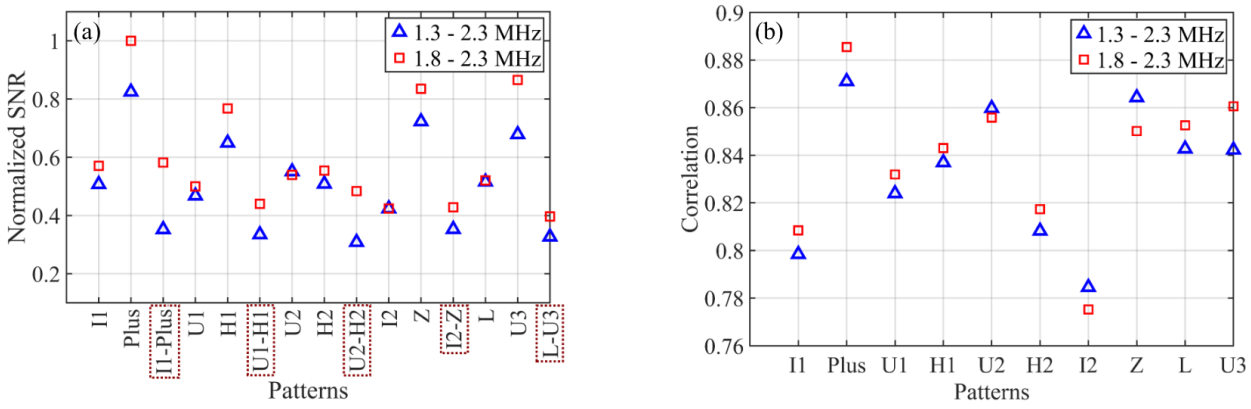

Figure 3.12. Error metrics to evaluate the quality of computational holographic reconstruction of multiple images using multi-frequency holograms with two design frequencies: (a) signal-to-noise ratio (SNR), normalized by the maximum SNR value, and (b) correlation between the computational holographic images and their respective imposed target images.

The phase errors cause large thickness variations between adjacent pixels, which can be observed in the final thickness profile of the designed multi-frequency holograms shown in figures 3.7 and

3.8g and figures 3.10 and 3.11c, f, i, and l, calculated from the final phase maps in the hologram planes, after 20-40 IASA iterations. Regardless of all these errors and imperfections related to the holographic reconstruction of multiple images using the multi-frequency holograms, the computations and experiments, presented in this section, show relatively satisfactory results as the goal of selectively enhancing ultrasonic power transfer is fulfilled. The quality of these holographic images can be further enhanced by introducing some modifications in the IASA optimization algorithm, such as increasing the phase modulation depth (e.g., from 2π to 4π), implementing higher design frequencies and then increasing frequency spacings, enlarging the holograms aperture size, and modulating both amplitude and phase of complex fields, to name a few [27, 28]. However, these modifications should be tailored to meet the essential design requirements of acoustic holograms and transducers, i.e., holograms' thin-element approximations and frequency spacing constraints due to the transducers' bandwidth. Moreover, it should be noted that higher frequencies lead to more attenuation of sound waves in the medium and their implementations are limited by the resolution of the 3D printer devices. On the other hand, the diffraction limit of lower frequencies constrains the capability of reconstruction of arbitrarily holographic images and the realization of fine details of the pattern since the target feature size is diffraction-limited.

Figure 3.12a confirms the fact that using the higher frequency set of 1.8 and 2.3 MHz compared to that of 1.3 and 2.3 MHz enhances the SNR for each desired pattern and conversely increases the unwanted frequency crosstalk between the patterns. Figure 3.12b shows the image correlations for similarity investigations between the computational holographic images and the imposed target images using the multi-frequency holograms. The image correlations for multiple images at different design frequencies decrease to some extent, compared with the correlation results of multi-image-plane holograms in figure 3.4b, due to more generation of artifacts and crosstalks, as well as the additional approximations that were applied to the IASA optimization algorithm for the design of multi-frequency holograms.

3.4 Conclusions

Multi-functional transmission holograms provide new promising potentials in the holographic reconstruction of acoustic field patterns. The multi-image-plane holograms enable a full generation of desired 3D volumetric acoustic fields by reproducing multiple images at different target planes and the multi-frequency holograms enable real-time dynamical reconfiguration of an ultrasonic apparatus reproducing multiple images of acoustic fields via switching the driving frequency. We investigated the use of these multi-functional holograms for possible implementation in ultrasonic

power transfer (UPT) systems to locally power piezoelectric-based sensors in three-dimensional fields, at different distances from the source, and with real-time adaptive control over driving frequency conditions. Modifications were applied to the iterative angular spectrum approach (IASA) optimization algorithm to generate multiple acoustic patternings at different target planes and via different driving frequencies. Computational simulations and experiments were performed to show the functionality of multi-functional holograms to generate multiple acoustic patterns in theory and practice, which show promising results and provide new insights into the enhancement of UPT systems.

Acknowledgments

This work was supported by the National Science Foundation (NSF) Grant NO. ECCS-1711139, which is gratefully acknowledged. We would like to thank Omidreza Sadeghi for helping with experiments.

Appendix B

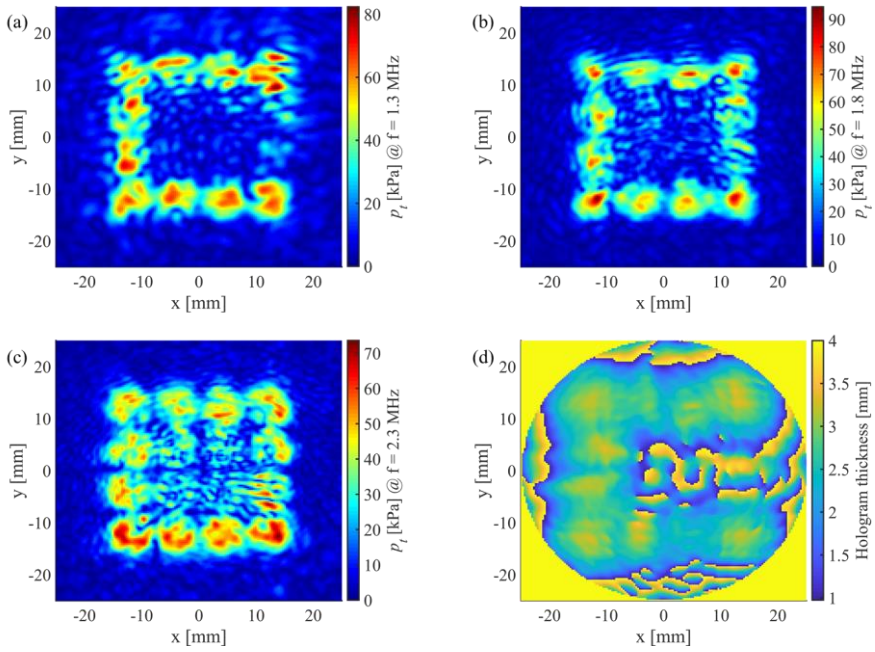

Figure B.1. Holographic reconstruction of letter C (10 focal points), square I (12 focal points), and square II (16 focal points) images for multi-frequency holograms: the acoustic pressure amplitudes in the target plane at $z = 51$ mm for frequency set of (a) 1.3 MHz, (b) 1.8 MHz, and (c) 2.3 MHz, and (d) the calculated hologram thickness.

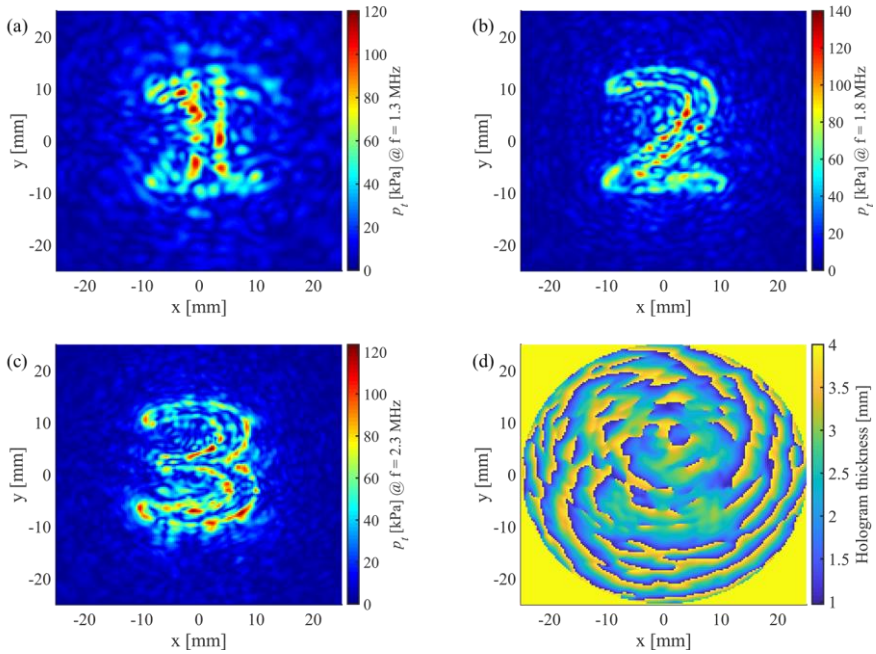

Figure B.2. Holographic reconstruction of numbers 1, 2, and 3 images for multi-frequency holograms: the acoustic pressure amplitudes in the target plane at $z = 51$ mm for frequency set of (a) 1.3 MHz, (b) 1.8 MHz, and (c) 2.3 MHz, and (d) the calculated hologram thickness.

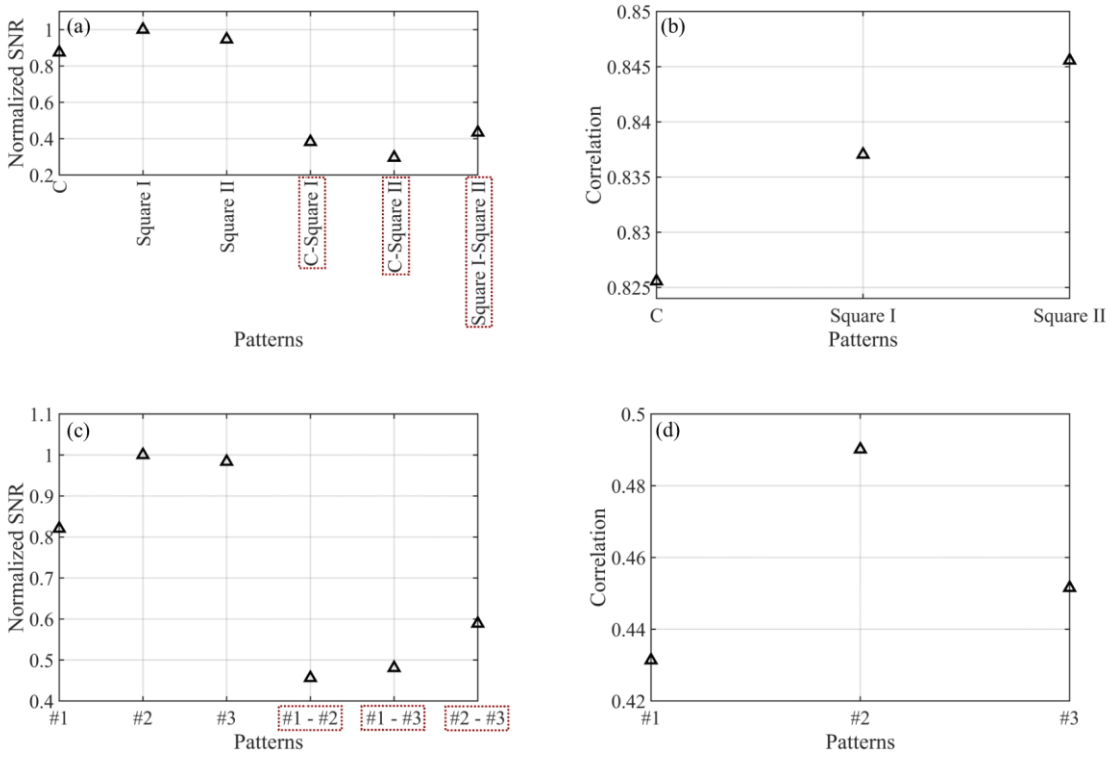

Figure B.3. Error metrics to evaluate the quality of computational holographic reconstruction of *letter C, square I, and square II* images using multi-frequency holograms with three design frequencies of 1.3, 1.8, and 2.3 MHz: (a) signal-to-noise ratio (SNR), normalized by the maximum SNR value, and (b) correlation between the computational holographic images and their respective imposed target images. Error metrics to evaluate the quality of computational holographic reconstruction of *numbers 1, 2, and 3* images using multi-frequency holograms with three design frequencies of 1.3, 1.8, and 2.3 MHz: (c) signal-to-noise ratio (SNR), normalized by the maximum SNR value, and (d) correlation between the computational holographic images and their respective imposed target images.

Bibliography

[1] Melde, K., Mark, A.G., Qiu, T., and Fischer, P., *Holograms for acoustics.* Nature, 2016. **537**(7621): p. 518.

[2] Zhang, J., Yang, Y., Zhu, B., Li, X., Jin, J., Chen, Z., Chen, Y., and Zhou, Q., *Multifocal point beam forming by a single ultrasonic transducer with 3D printed holograms.* Applied Physics Letters, 2018. **113**(24): p. 243502.

[3] Melde, K., Fischer, P., and Weber, P.-k., *Apparatus and method for creating a holographic ultrasound field in an object*. 2018, Google Patents.

[4] Bakhtiari-Nejad, M., Elnahhas, A., Hajj, M.R., and Shahab, S., *Acoustic holograms in contactless ultrasonic power transfer systems: Modeling and experiment.* Journal of Applied Physics, 2018. **124**(24): p. 244901.

[5] Brown, M.D., Cox, B.T., and Treeby, B.E., *Design of multi-frequency acoustic kinoforms.* Applied Physics Letters, 2017. **111**(24): p. 244101.

[6] Brown, M., Nikitichev, D., Treeby, B., and Cox, B., *Generating arbitrary ultrasound fields with tailored optoacoustic surface profiles.* Applied Physics Letters, 2017. **110**(9): p. 094102.

[7] Jiménez-Gambín, S., Jiménez, N., Benlloch, J.M., and Camarena, F., *Holograms to focus arbitrary ultrasonic fields through the skull.* Physical Review Applied, 2019. **12**(1): p. 014016.

[8] Maimbourg, G., Houdouin, A., Deffieux, T., Tanter, M., and Aubry, J.-F., *3D-printed adaptive acoustic lens as a disruptive technology for transcranial ultrasound therapy using single-element transducers.* Physics in Medicine & Biology, 2018. **63**(2): p. 025026.

[9] Ferri, M., Bravo, J.M., Redondo, J., and Sánchez-Pérez, J.V., *Enhanced numerical method for the design of 3-d-printed holographic acoustic lenses for aberration correction of single-element transcranial focused ultrasound.* Ultrasound in medicine & biology, 2019. **45**(3): p. 867-884.

[10] Kruizinga, P., van der Meulen, P., Fedjajevs, A., Mastik, F., Springeling, G., de Jong, N., Bosch, J.G., and Leus, G., *Compressive 3D ultrasound imaging using a single sensor.* Science advances, 2017. **3**(12): p. e1701423.

[11] Melde, K., Choi, E., Wu, Z., Palagi, S., Qiu, T., and Fischer, P., *Acoustic fabrication via the assembly and fusion of particles.* Advanced Materials, 2018. **30**(3): p. 1704507.

[12] Ma, Z., Holle, A.W., Melde, K., Qiu, T., Poeppel, K., Kadiri, V.M., and Fischer, P., *Acoustic Holographic Cell Patterning in a Biocompatible Hydrogel.* Advanced Materials, 2020. **32**(4): p. 1904181.

[13] Xie, Y., Shen, C., Wang, W., Li, J., Suo, D., Popa, B.-I., Jing, Y., and Cummer, S.A., *Acoustic holographic rendering with two-dimensional metamaterial-based passive phased array.* Scientific reports, 2016. **6**: p. 35437.

[14] Zhang, J., Tian, Y., Cheng, Y., and Liu, X., *Acoustic holography using composite metasurfaces.* Applied Physics Letters, 2020. **116**(3): p. 030501.

[15] Zhu, Y., Hu, J., Fan, X., Yang, J., Liang, B., Zhu, X., and Cheng, J., *Fine manipulation of sound via lossy metamaterials with independent and arbitrary reflection amplitude and phase.* Nature communications, 2018. **9**(1): p. 1632.

[16] Cox, L., Melde, K., Croxford, A., Fischer, P., and Drinkwater, B.W., *Acoustic Hologram Enhanced Phased Arrays for Ultrasonic Particle Manipulation.* Physical Review Applied, 2019. **12**(6): p. 064055.

[17] Xie, Y., Wang, W., Chen, H., Konneker, A., Popa, B.-I., and Cummer, S.A., *Wavefront modulation and subwavelength diffractive acoustics with an acoustic metasurface.* Nature communications, 2014. **5**: p. 5553.

[18] Memoli, G., Caleap, M., Asakawa, M., Sahoo, D.R., Drinkwater, B.W., and Subramanian, S., *Metamaterial bricks and quantization of meta-surfaces.* Nature communications, 2017. **8**(1): p. 1-8.

[19] Norasikin, M.A., Martinez Plasencia, D., Polychronopoulos, S., Memoli, G., Tokuda, Y., and Subramanian, S. *SoundBender: dynamic acoustic control behind obstacles*. in *Proceedings of the 31st Annual ACM Symposium on User Interface Software and Technology*. 2018.

[20] Brown, M.D., Cox, B.T., and Treeby, B.E., *Stackable acoustic holograms.* Applied Physics Letters, 2020. **116**(26): p. 261901.

[21] Roes, M.G., Duarte, J.L., Hendrix, M.A., and Lomonova, E.A., *Acoustic energy transfer: A review.* IEEE Transactions on Industrial Electronics, 2013. **60**(1): p. 242-248.

[22] Shahab, S., Gray, M., and Erturk, A., *Ultrasonic power transfer from a spherical acoustic wave source to a free-free piezoelectric receiver: Modeling and experiment.* Journal of Applied Physics, 2015. **117**(10): p. 104903.

[23] Shahab, S. and Erturk, A., *Contactless ultrasonic energy transfer for wireless systems: acoustic-piezoelectric structure interaction modeling and performance enhancement.* Smart Materials and Structures, 2014. **23**(12): p. 125032.

[24] Basaeri, H., Christensen, D.B., and Roundy, S., *A review of acoustic power transfer for biomedical implants.* Smart Materials and Structures, 2016. **25**(12).

[25] Wells, P.N., *Ultrasonic imaging of the human body.* Reports on progress in physics, 1999. **62**(5): p. 671.

[26] Melde, K., *The Acoustic Hologram and Particle Manipulation with Structured Acoustic Fields*. 2020: KIT Scientific Publishing.

[27] Brown, M.D., *Optical and single element transducers for the generation of arbitrary acoustic fields*. 2018, UCL (University College London).

[28] Brown, M.D., *Phase and amplitude modulation with acoustic holograms.* Applied Physics Letters, 2019. **115**(5): p. 053701.

Chapter 4

Dynamics of acoustic impedance matching layers in contactless ultrasonic power transfer systems

This chapter is based on an article published in *Smart Materials and Structures* journal [1], In this chapter, we investigate the effects of implementing acoustic impedance matching layers on the enhancement of ultrasonic power transmission.

Abstract

The acoustic impedance mismatch between transducer materials and medium in ultrasonic power transfer systems narrows the transduction bandwidth and causes losses through the back reflection of progressive pressure waves at the boundary between the transducers and medium. Capturing both resonances and losses due to impedance mismatch of interwoven elements is essential for advancing the development of these systems. We present a unified approach, based on the multiplication of a sequence of transfer matrices, to determine an equivalent acoustic impedance. The analytical model couples the properties of the transmitter and receiver with multiple matching layers and a single classical quarter-wave layer in controlled setups with the objective of minimizing reflections through acoustic impedance mismatch alleviation. Losses due to ultrasonic attenuation in the material layers and medium are also considered. The acoustic field at the receiver location constitutes the input to the coupled electro-elastic equations of the fluid-loaded and electrically-loaded piezoelectric receiver. Experiments are performed to identify the input acoustic pressure from a cylindrical transmitter to a receiver disk operating in the 33-mode of piezoelectricity. The results show significant enhancements in terms of the receiver's electrical power output when implementing a two-layer matching structure. We present the results showing

non-dimensional wave number variations vs. characteristic impedance, which can be used to calculate the materials' thicknesses for acoustically matching ultrasonic power transfer systems to an acoustic medium of interest at any desired resonant frequency while considering any type of glue or epoxy as the bonding layer. The derived physical models facilitate the development of high-fidelity matched systems with enhanced contactless power transmission.

4.1 Introduction

Ultrasonic power transfer (UPT) is based on transferring energy using acoustic waves generated and received by piezoelectric (PZT) transducers. The sound wave is generated by a transmitter and then transferred through an acoustic medium such as water [2, 3], air [4, 5], human tissue [6, 7] or solid wall [8, 9] to a receiver, which in turn converts the mechanical strain induced by the incident acoustic waves to electricity that can be delivered to an electrical load [2]. A review highlighting major advancements in UPT is presented by Roes *et al*. [10]. Various UPT concepts using piezoelectric transduction include: (i) an array of receivers excited by a pulsating sphere, i.e., spherical acoustic transmitter [2, 3], (ii) cylindrical source-cylindrical receiver combination in a separate domain (e.g., as in transcutaneous UPT [6, 11]), (iii) enhanced power transfer by focusing of the source using a high-intensity focused ultrasound (HIFU) transducer [12] or passive acoustic holograms (lenses) when illuminated with an acoustic source such as a PZT (lead zirconate titanate) disk as the active element to generate the desired pressure pattern [13, 14], (iv) identification of electro-elastic nonlinearities in UPT systems [15], and (v) enhanced power transfer by acoustic impedance matching of the transmitter and receiver disks to the medium, which is the scope of this work. The proposed scenarios for performance enhancement and frequency bandwidth improvement of UPT systems mainly include focusing of the transmitted acoustic energy in space and alleviating impedance mismatch issues [3]. To improve the efficiency of UPT systems, minimizing the acoustic losses due to the reflection of acoustic waves must be considered. The characteristic impedance, which depends on the density and speed of sound in materials, is one of the most significant acoustical parameters in acoustic power transmission. Because the characteristic impedance of piezoelectric transducers is much larger than that of acoustic media, i.e. air, liquid, human tissue, or solid wall, the transducers need to be acoustically matched. The acoustic impedance mismatch between the PZT elements and the acoustic medium results in (i) a narrow frequency bandwidth [16-18] and (ii) significant losses through back reflection of the incident pressure waves at the boundary between the PZT and the medium [19]. For example, the pressure reflection coefficient for a soft tissue is 0.9 which means that only 10%

of the incident wave is captured by the piezoelectric receiver. To alleviate the acoustic impedance mismatch, intermediate materials, called acoustic impedance matching layers are used [20]. Such layers are bonded to the front side of the transducer face.

Several theoretical and experimental investigations considered the effects of implementing a single or multiple quarter-wavelength layers in the design of piezoelectric transducers [16-19, 21-34]. Materials ranging from metals, ceramics, or composites, such as silver, titanium, and glass to polymers or plastics, such as parylene and acrylic have been used as matching layers. In a few studies [35-38], a mass-spring matching approach was proposed to determine layer thicknesses in which multi-layer polymer-metal structures such as a double structure of PVDF-copper and polyimide were bonded to a piezoelectric material. The results pointed to a comparable performance to that of the traditional quarter-wave layer matching. Opieliński *et al.* [39] computationally analyzed the influence of changing material thicknesses (different from one-quarter wavelength) for the construction of a three-layer matching system in an ultrasonic airborne transducer. Comparing the results with that of three quarter-wave matching layers, they noted an enhancement in a transfer function relating the acoustic velocity to the input current. Most of the matching techniques require a layer or multi-layer of glue (or epoxy) for bonding purposes; hence, the thickness of glue must be taken into consideration [40]. However, the majority of past investigations considered zero-thickness glue in their design which undermines the performance of the matching systems. As such, the quarter-wave layer techniques, e.g., using a single matching layer whose characteristic impedance is the geometric mean of that of the medium and the transducer material, which also limits the choice of material, could not be practically implemented. Callens *et al.* [41] proposed using a two-layer matching technique in water by considering the glue as one of the matching layers. Once the specific glue is selected, the choice of material for the other layer is very broad. In this approach, the thickness of selected materials needed to match a piezoelectric transducer at a desired resonant frequency can be accurately determined using a transfer matrix [42-44], which does not necessarily correspond to that of the quarter-wavelength material layers.

Recent investigations on UPT systems signified the effects of employing matching layers to further enhance the contactless transfer of power through the acoustic medium between the piezoelectric transmitter and receiver [3, 45]. Accordingly, few analytical and experimental proof-of-concept studies have been conducted employing quarter-wave layer matching structures [46-49] and the aforementioned two-layer matching technique [6, 7, 11, 50] to improve the power transmission for

ultrasonic implanted transducers in biomedical applications. However, the limited existing literature lacks a comprehensive analysis that can guide efforts to determine proper matching configurations for the fabrication process, i.e., the selection of the most efficient material layers and more importantly the estimation of material thicknesses needed to match a transducer at any desired frequency operating in an acoustic medium of interest. In this effort, we investigate a broad range of materials, considering two classifications, namely metals, some ceramics and composites, and polymers (plastics) using the two-layer matching structure first presented by Callens *et al.* [41] in which we take into account the glue thickness. A four-layer matching system including two layers of glue and two layers of different materials is also evaluated to compare the performances of the two- and four-layer matching structures. Additionally, we consider the frequency-dependent ultrasonic material losses [31, 51, 52] for the receiver's electrical power output calculations to establish a trade-off between the attenuation effects and implementing matching layers depending on the acoustic medium.

In the UPT modeling, we assumed a piston-like motion for the piezoelectric receiver disk, where only the thickness mode of the disk resonates. This assumption approximately holds for disks with an aspect ratio (diameter-to-thickness ratio) greater than 20 or less than 0.1 [53, 54]. In this chapter, the expressions *finite aspect ratio* and *finite size* refer to the aspect ratio between 0.1 to 20. We confirm that the disk, given as the case study in this chapter, has an aspect ratio of 2.4, which is not on the reported acceptable range. Hence, using the reduced-order one-dimensional analysis of the finite-size receiver may lead to some deviations in the amplitudes of the electrical power output, when comparing with experiments [55]. However, the studied frequency range (300-700 kHz) was chosen in the domain where the thickness mode of the disk is dominant; it is based on the information given by the manufacturer (APC International, Ltd), which was then validated by the measurement performed using an impedance analyzer (see figure C.1 in appendix C.1). Additionally, the non-planar motion of the disk might also affect the scattered acoustic field through the radiation impedance and reflected acoustic field, which in turn changes the blocked (incident plus reflected) pressure. The study of non-planar motion effects, which are arising due to the finite aspect ratio of disks, can be implemented by a finite element-based approach, which is not the scope of this work. The focus of this work is qualitatively investigating the effects of acoustic impedance matching layers on the power transmission. Therefore, the given results, such as input acoustic pressures and electrical power outputs, are normalized.

Experiments are conducted to characterize the vibration response of the piezoelectric transmitter as well as the input excitation pressure to the receiver. In section 4.2, we present the theoretical model of acoustic impedance matching conditions and develop the model for the UPT-matching layer system, which couples the properties of the transmitter and receiver with the single and multiple matching layers. Results from experimental measurements and analytical models are discussed in section 4.3. A summary and conclusions are presented in section 4.4.

4.2 Analytical modeling: UPT-matching layer system

A schematic of an acoustically matched piezoelectric transducer to an acoustic medium with corresponding characteristic impedances Z_T and Z_0 is presented in figure 4.1a. To quantify the power output enhancement by using matching layers, we consider three cases in a UPT system. The system includes a pair of PZT ultrasonic transducer disks in the transmitter (Tx) and receiver (Rx) configurations operating in water. In case 1, shown in figure 4.1b, no matching layer (ML) is added to the transducers. In case 2, shown in figure 4.1c, matching layers are used for only the Rx transducer. In case 3, shown in figure 4.1d, both Tx and Rx transducers include matching layers.

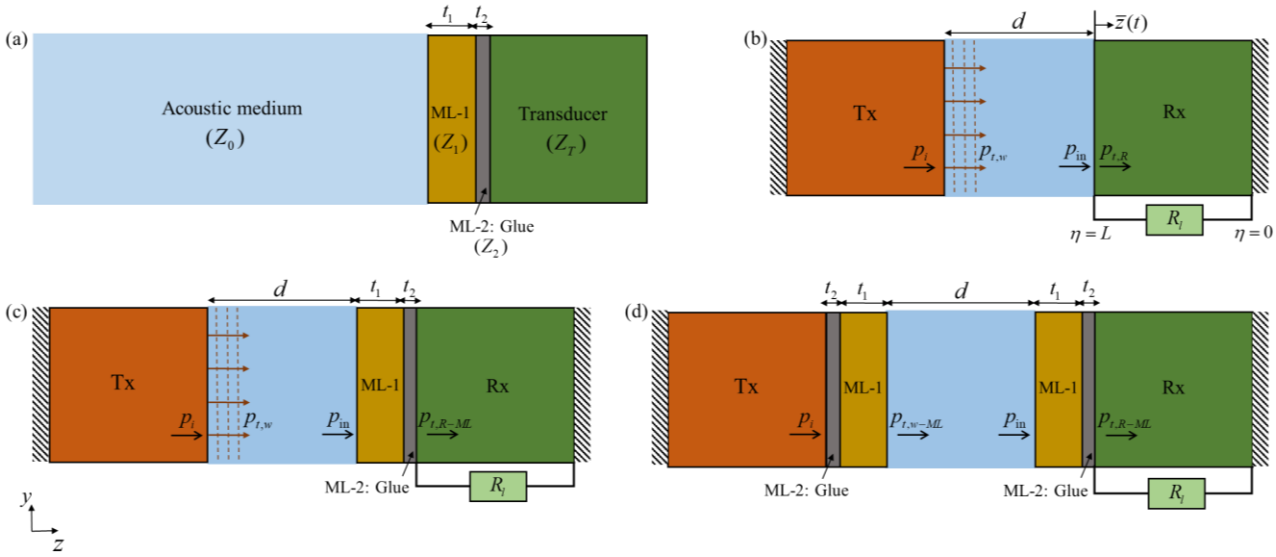

Figure 4.1. Schematic representation of various matching layer concepts. (a) An acoustically matched piezoelectric transducer using two matching layers: ML-1 and glue as ML-2. UPT-matching layer system consisting of Tx and Rx transducers with water as an acoustic medium in three case studies: (b) without matching layers, (c) matching Rx transducer only, and (d) matching both Tx and Rx transducers.

4.2.1 Acoustic matching technique

The transfer matrix for the nth material layer with characteristic acoustic impedance Z_n and thickness t_n, as shown in figure 4.1a, considering a normally incident longitudinal plane wave through a multilayer system is written as [41, 42]

$$T_n = \begin{bmatrix} \cos(k_n t_n) & jZ_n \sin(k_n t_n) \\ \dfrac{j\sin(k_n t_n)}{Z_n} & \cos(k_n t_n) \end{bmatrix}, \tag{4.1}$$

where k_n is the wave number in the nth material. Because the thickness of the PZT transducer element is significantly larger than that of the matching layers, we assume a semi-infinite transmission line for the transducer material. The equivalent transfer matrix for the n-layer system is derived by defining

$$T^{eq} = T_1 T_2 ... T_n = \begin{bmatrix} T_{11}^{eq} & T_{12}^{eq} \\ T_{21}^{eq} & T_{22}^{eq} \end{bmatrix}. \tag{4.2}$$

Hence, the resultant equivalent acoustic impedance is written as

$$Z^{eq} = \frac{T_{11}^{eq} Z_T + T_{12}^{eq}}{T_{21}^{eq} Z_T + T_{22}^{eq}}. \tag{4.3}$$

Having determined the equivalent impedance, the power (intensity) reflection coefficient R_{I-ML} is derived by replacing the multilayer system to the right of the first layer, which according to figure 4.1a represents the acoustic medium, with an equivalent single boundary (two-layer) system to write (see equation (6.3.18) in [56])

$$R_{I-ML} = \left| \frac{Z^{eq} - Z_0}{Z^{eq} + Z_0} \right|^2. \tag{4.4}$$

The power (intensity) transmission coefficient T_{I-ML} is then defined as $T_{I-ML} = 1 - R_{I-ML}$.

Considering the two-layer matching system shown in figure 4.1a, the power transmission coefficient is derived as

$$
\begin{aligned}
T_{I-ML} = {} & 8Z_0Z_1^2Z_2^2Z_T / \{4Z_0Z_1^2Z_2^2Z_T + 2(Z_0^2Z_1^2Z_2^2 + Z_1^2Z_2^2Z_T^2)\cos^2(k_1t_1)\cos^2(k_2t_2) \\
& +2(Z_1^4Z_2^2 + Z_0^2Z_2^2Z_T^2)\sin^2(k_1t_1)\cos^2(k_2t_2) + (Z_1^3Z_2^3 + Z_0^2Z_1Z_2Z_T^2 - Z_0^2Z_1Z_2^3 - Z_1^3Z_2Z_T^2) \\
& \sin(2k_1t_1)\sin(2k_2t_2) + 2(Z_0^2Z_2^4 + Z_1^4Z_T^2)\sin^2(k_1t_1)\sin^2(k_2t_2) + 2(Z_1^2Z_2^4 + Z_0^2Z_1^2Z_T^2) \\
& \cos^2(k_1t_1)\sin^2(k_2t_2)\}.
\end{aligned} \tag{4.5}
$$

Perfect matching is achieved when the equivalent impedance is equal to the impedance of the acoustic medium in which there is a complete transmission. Therefore, the power reflection coefficient becomes zero ($T_{I-ML} = 1,\ R_{I-ML} = 0$). Setting equation (4.3) equal to Z_0 and separating the real and imaginary parts, one obtains two expressions as follows:

$$
\frac{T_{11}^{eq} Z_T}{T_{22}^{eq}} = Z_0, \tag{4.6}
$$

and

$$
\frac{T_{12}^{eq}}{T_{21}^{eq} Z_T} = Z_0, \tag{4.7}
$$

in which equations (4.6) and (4.7) can be written as

$$
A = \frac{Z_1 \tan(k_1t_1)\tan(k_2t_2) - Z_2}{Z_2 \tan(k_1t_1)\tan(k_2t_2) - Z_1}, \tag{4.8}
$$

and

$$
B = \frac{Z_1 \tan(k_1t_1) + Z_2 \tan(k_2t_2)}{Z_1 \tan(k_2t_2) + Z_2 \tan(k_1t_1)}, \tag{4.9}
$$

where $A = \frac{Z_0Z_2}{Z_1Z_T}$ and $B = \frac{Z_0Z_T}{Z_1Z_2}$.

Likewise, the series of corresponding equations in a four-layer matching system containing two layers of glue with identical thickness t_2 ($t_2 = t_4$) and characteristic impedance Z_2, and two layers of different materials with thicknesses t_1 and t_3, and impedances Z_1 and Z_3, are obtained as

$$
\begin{aligned}
A = {} & \{2Z_1Z_2Z_3 \tan(k_1t_1)\tan(k_2t_2) + Z_2^2Z_3 \tan^2(k_2t_2) + Z_1Z_2^2 \tan(k_1t_1)\tan(k_3t_3) \\
& +Z_2^3 \tan(k_2t_2)\tan(k_3t_3) + Z_2Z_3^2 \tan(k_2t_2)\tan(k_3t_3) - Z_1Z_3^2 \tan(k_1t_1)\tan^2(k_2t_2) \\
& \tan(k_3t_3) - Z_2^2Z_3\} / \{2Z_2{}^2Z_3 \tan(k_1t_1)\tan(k_2t_2) + Z_1Z_2Z_3 \tan^2(k_2t_2) + Z_2Z_3^2 \\
& \tan(k_1t_1)\tan(k_3t_3) + Z_1Z_2^2 \tan(k_2t_2)\tan(k_3t_3) + Z_1Z_3^2 \tan(k_2t_2)\tan(k_3t_3) \\
& -Z_2^3 \tan(k_1t_1)\tan^2(k_2t_2)\tan(k_3t_3) - Z_1Z_2Z_3\},
\end{aligned} \tag{4.10}
$$

and

$$
\begin{aligned}
B = \{ & Z_1 Z_2 Z_3 \tan(k_1 t_1) + 2 Z_2^2 Z_3 \tan(k_2 t_2) - Z_1 Z_2 Z_3 \tan(k_1 t_1) \tan^2(k_2 t_2) \\
& + Z_2 Z_3^2 \tan(k_3 t_3) - Z_1 Z_2^2 \tan(k_1 t_1) \tan(k_2 t_2) \tan(k_3 t_3) - Z_1 Z_3^2 \tan(k_1 t_1) \\
& \tan(k_2 t_2) \tan(k_3 t_3) - Z_2^3 \tan^2(k_2 t_2) \tan(k_3 t_3) \} / \{ Z_2{}^2 Z_3 \tan(k_1 t_1) \\
& + 2 Z_1 Z_2 Z_3 \tan(k_2 t_2) - Z_2{}^2 Z_3 \tan(k_1 t_1) \tan^2(k_2 t_2) + Z_1 Z_2^2 \tan(k_3 t_3) \\
& - Z_2^3 \tan(k_1 t_1) \tan(k_2 t_2) \tan(k_3 t_3) - Z_2 Z_3^2 \tan(k_1 t_1) \tan(k_2 t_2) \tan(k_3 t_3) \\
& - Z_1 Z_3^2 \tan^2(k_2 t_2) \tan(k_3 t_3) \}.
\end{aligned}
\tag{4.11}
$$

Using equations (4.8)-(4.11), we determine the thicknesses of glue and other material layers to acoustically match the transducers to the medium at a specific operating resonant frequency. The acoustic properties of the materials such as characteristic impedance and sound speed are known [27, 57, 58]. We compare the power transmission results with the ideal or theoretical quarter-wavelength layer system which uses a single layer whose characteristic impedance is the geometric mean of that of the medium and the transducer material ($Z_{\text{single-layer}} = \sqrt{Z_0 Z_T}$). Inevitably, the matching technique needs the glue layer(s) for bonding purposes and the choice of material whose impedance exactly equals $\sqrt{Z_0 Z_T}$ is limited. Hence, ideal matching could not be implemented in practice.

4.2.2 Closed-form voltage response of a piezoelectric receiver at steady state

The receiver disk treated as a fixed (clamped)-free [59] PZT cylinder operating in the 33-mode of piezoelectricity with fundamental resonant frequency in the range of 420-580 kHz (see figure C.1 in appendix C.1). For the fluid-loaded and electrically-loaded fixed-free piezoelectric receiver disk excited by an acoustic wave (see figure 4.1b), the coupled partial differential equations for longitudinal vibration of the receiver and the AC electrical circuit equation are written as [2, 3]

$$
\begin{aligned}
& -EA \frac{\partial^2 w(\eta,t)}{\partial \eta^2} - c_\gamma \frac{\partial^3 w(\eta,t)}{\partial \eta^2 \partial t} + c_\mu \frac{\partial w(\eta,t)}{\partial t} + R_r[\delta(\eta - L)] \frac{\partial w(\eta,t)}{\partial t} + m \frac{\partial^2 w(\eta,t)}{\partial t^2} \\
& -\kappa v(t)[\delta(\eta - L)] = f(t)[\delta(\eta - L)],
\end{aligned}
\tag{4.12}
$$

$$
C_p \frac{dv(t)}{dt} + \frac{v(t)}{R_l} + \int_0^L \kappa \frac{\partial^2 w(\eta,t)}{\partial t \partial \eta} d\eta = 0, \tag{4.13}
$$

where $w(\eta,t)$ is the displacement response of the disk at the axial position η and time *t*, $v(t)$ is the voltage output across the electrical load, *E* is Young's modulus at the constant electric field, $A=\pi a^2$ is the cross-sectional area, where *a* is the radius of the disk; m is the mass per unit length, c_γ is the stiffness-proportional damping coefficient, c_μ is the mass-proportional damping coefficient, κ is the electromechanical coupling term in physical coordinates, and $\delta(\eta-L)$ is the Dirac delta function. The parameters C_p and R_l, respectively, represent the internal capacitance of the piezoelectric receiver and the external load resistance. The excitation force due to the incident acoustic pressure $f(t)=p_{t,R}(t)A$ or $f(t)=p_{t,R-ML}(t)A$ is evaluated at the free-end surface $(\eta=L)$ of the receiver. The forces are expressed in terms of transmitted acoustic waves captured by the PZT receiver (see figures 4.1b-d). Moreover, the dissipative term R_r in equation (4.12) is the resistive component of the fluid radiation impedance, which is given by equation (56) in [60] in terms of the normalized radiation resistance for an unbaffled circular transducer disk. The excitation of the receiver is such that the linear piezoelectricity is assumed and the elastic coupling and dissipative nonlinearities are not prominent.

The linear displacement at the free end of the piezoelectric receiver disk ($\bar{z}(t)$ in figure 4.1b, where $\bar{z}(t)=w(L,t))$ due to harmonic excitation at or around the fundamental longitudinal axial vibration mode is obtained by modal analysis of the distributed-parameter electromechanical system for the fundamental mode of vibration. The longitudinal tip displacement of the piezoelectric receiver disk at time *t* is then written as

$$\bar{z}(t)=w(\eta,t)\big|_{\eta=L}=\varphi(L)\chi(t), \tag{4.14}$$

where $\varphi(L)$ and $\chi(t)$ are, respectively, the mass-normalized eigenfunction (mode shape) evaluated at $\eta=L$ and the generalized modal coordinate (temporal amplitude) for the longitudinal vibration mode of the fixed-free uniform disk. The mass normalized elastic-mode eigenfunction calculated from the corresponding undamped and electromechanically uncoupled (short-circuit) free vibration, is obtained as

$$\varphi(\eta)=\frac{\sin(\alpha\,\eta/L)}{\sqrt{\dfrac{mL}{2}\left(1-\dfrac{\sin(2\alpha)}{2\alpha}\right)+m_r\sin^2(\alpha)}}, \tag{4.15}$$

where the eigenvalue, α, of the fundamental mode is the first non-zero root of the transcendental characteristic equation $(m_r / mL)\alpha \sin\alpha - \cos\alpha = 0,$ where $m_r = X_r / \omega$ is the radiation mass, i.e., added mass, due to reactive component of the fluid radiation impedance which is given in equation (57) of [60] in terms of the normalized radiation reactance for the unbaffled disk and ω is the excitation frequency. The radiation resistance (R_r) represents the actual power radiated by the vibrating surface to the fluid medium, whereas the radiation reactance (X_r) accounts for the stored energy of vibration near the surface which decreases the resonant frequency. Figure C.2 in appendix C.2 shows the normalized acoustic radiation resistance and reactance for unbaffled and baffled circular pistons (see equation (10.52) in [61]) as would be required in different applications.

The electromechanically coupled equations of forced vibrations and current balance for the fundamental vibration mode in the lumped-parameter form when reduced from the distributed-parameter solution are expressed as

$$\begin{aligned} &\ddot{\bar{z}}(t)\left[1 - m_r\varphi^2(L)\right] + \dot{\bar{z}}(t)\left\{2\zeta\omega_r - c_\gamma\left[\varphi(\eta)\frac{d\varphi(\eta)}{d\eta}\right]_{\eta=L} + R_r\varphi^2(L)\right\} \\ &+\bar{z}(t)\left\{\omega_r^2 - \left[\varphi(\eta)EA\frac{d\varphi(\eta)}{d\eta}\right]_{\eta=L}\right\} - \kappa v(t)\varphi^2(L) = f(t)\varphi^2(L), \end{aligned} \tag{4.16}$$

$$[C_p\dot{v}(t) + v(t)/R_l + \kappa\dot{\bar{z}}(t)]\varphi(L) = 0, \tag{4.17}$$

where the over-dot represents differentiation with respect to time and ζ is the damping ratio defined by the mechanical quality factor Q $(\zeta = 1/2Q)$ [62]. We shall note here that scattering effects and nonlinearity are assumed to be negligible for the receiver dimensions and considering low excitation amplitudes.

The steady-state electromechanical harmonic response is of the form $\bar{z}(t) = |\bar{z}|e^{j\omega t}$ and $v(t) = |v|e^{j\omega t}$ based on the linear system assumption, where j is the unit imaginary number. Here, $|\bar{z}|$ and $|v|$ denote amplitudes of the axial displacement and voltage output, respectively. Applying a damped boundary condition at $\eta = L$ in the modal coordinate, $[EA(d\varphi(\eta)/d\eta)\chi(t) + c_\gamma(d\varphi(\eta)/d\eta)\dot{\chi}(t) - \omega^2 m_r\varphi(\eta)\chi(t)]_{\eta=L} = 0,$ and considering the harmonic vibration responses, the fundamental-mode output voltage amplitude frequency response function (FRF) is derived as

$$|v| = \left| \frac{-j\omega\kappa \times \left\{ \begin{matrix} |p_{t,R}| \text{ or} \\ |p_{t,R-ML}| \end{matrix} \right\} \times A\varphi^2(L)}{\left(j\omega C_p + 1/R_l \right)\left\{ \omega_n^2 - \omega^2 + j\omega\left[2\zeta\omega_n + R_r\varphi^2(L) \right] \right\} + j\omega\kappa^2\varphi^2(L)} \right|, \tag{4.18}$$

where ω_n is the fundamental resonant frequency. Consequently, the electrical power output FRF of the piezoelectric receiver disk (Π) is calculated using the equation $\Pi = v^2 / R_l$.

4.2.3 Implementing the acoustic matching technique in UPT and including ultrasonic material losses

To compare the receiver's power output, we investigate the three case studies shown in figures 4.1b-d. The amplitude of the transmitted pressure wave $p_{t,w}$ generated by the unmatched transmitter shown in figures 4.1b and c is calculated using the power transmission coefficient [56] as follows:

$$T_I = \left(\frac{Z_T}{Z_0} \right)\left(\frac{p_{t,w}}{p_i} \right)^2 = \frac{4Z_0Z_T}{(Z_0 + Z_T)^2}. \tag{4.19}$$

On the other hand, the amplitude of the transmitted pressure wave $p_{t,w-ML}$ generated by the acoustically matched transmitter shown in figure 4.1d is calculated using the derived power transmission coefficient T_{I-ML} when implementing matching layers; $T_{I-ML} = (Z_T / Z_0)(p_{t,w-ML} / p_i)^2$. To find the incident acoustic pressure field, p_i, we measured the pressure distribution fairly close to the transmitter, as presented in section 4.3.3. The experimentally measured pressure field is then numerically back-propagated to the transmitter face to reconstruct the acoustic source [63, 64] using the Near-field Acoustic Holography (NAH) method [65-67] via the Angular Spectrum Approach (ASA), which is explained in detail by the authors in [13] and chapter 2. Similarly, on the receiver side, the transmitted pressure waves $p_{t,R}$ (figure 4.1b) or $p_{t,R-ML}$ (figures 4.1c and d) are computed, respectively, using the expressions $T_I = (Z_0 / Z_T)(p_{t,R} / p_{\text{in}})^2$ and $T_{I-ML} = (Z_0 / Z_T)(p_{t,R-ML} / p_{\text{in}})^2$. Likewise, the input pressure p_{in} is calculated numerically via the ASA by forward-propagating the transmitted pressure field $p_{t,w}$ or

$p_{t,w-ML}$. Finally, the power output for the PZT receiver is calculated using equations (4.18) and $\Pi = v^2 / R_l$.

Additionally, the amplitude of the ultrasonic wave is attenuated as it passes through the medium and material layers. To account for losses of acoustic energy, a lossy Helmholtz equation $\nabla^2 p + \boldsymbol{k}^2 p = 0$ with the complex wave number $\boldsymbol{k} = k - j\beta = \omega / \boldsymbol{c}$ is developed [56], where β is a frequency-dependent attenuation coefficient, $\boldsymbol{c}$ is the complex stiffened wave speed (complex speed of sound), and the harmonic plane wave pressure p is expressed as

$$p = |p| e^{-\beta z} e^{j(\omega t - kz)}. \tag{4.20}$$

The electrical power output for the UPT system is then reduced by a power attenuation factor μ defined as [48, 68]

$$\mu = e^{-2\sum_i \beta_i z_i}, \tag{4.21}$$

where z_i represents the thickness of matching layers, as well as the distance between the transmitter and receiver. It should be noted that the amplitudes of the voltage and electrical power output are, respectively, proportional to the first and second power of the amplitude of the transmitted pressure waves captured by the receiver. As a result, the acoustic power enhancement by implementing matching layers in the UPT system considering the acoustic attenuation is determined.

It also should be emphasized that in the UPT analysis, we consider a lossy transducer using the damping ratio of the PZT transducer through the mechanical quality factor, $\zeta = 1/2Q$, in equation (4.16). However, we neglect a dielectric loss factor which can be easily included considering the complex capacitance for the piezoelectric material [69, 70] ($\boldsymbol{C_p} = C_p(1 - j\delta_{tn})$, where δ_{tn} represents the dielectric loss factor, which usually referred to the loss tangent). Note that the loss tangent of the PZT disk used in this study is around 2%, which only changes the capacitance by 0.02%. Moreover, we take into account the attenuation coefficient β for the medium and matching layers for the decaying plane (pressure) wave in equation (4.20) and later in computing the electrical power output. Note that we neglect the attenuation in specific acoustic impedance calculations. Finally, the effect of fluid damping is included through the dissipative term R_r in equation (4.12).

4.3 Experiments and theoretical results

4.3.1 Frequency response of the transmitter in water: measured surface velocity

The experiments were conducted on a cylindrical 33-mode PZT disk (APC850-Navy II from APC International, Ltd. [71]) having a diameter of 9.5 mm and a thickness of 3.9 mm. The density of the disk is 7600 kg/m^3 [72] and the speed of sound in the PZT material is 4780 m/s, which results in $Z_T = 36.3$ MRayl. The disk's surface velocity was measured using a laser Doppler vibrometer (LDV, including Polytec OFV-505 sensor head and Polytec OFV-5000 controller) and acquired using a 1-GS/s digital oscilloscope (Tektronix TBS 2000 series, model TBS2104) with 512 averages. During underwater actuation experiments, the disk was excited by an average input voltage of 44 V peak-to-peak using a waveform generator (Keysight 33500B series) that was connected to an amplifier (E&I RF power amplifier, model A075). The disk was bonded to a thin brass plate using a thin layer of high-shear-strength epoxy (3M DP460 Scotch-Weld Epoxy Adhesive) and then the plate was mounted in a watertight box made of an acrylic sheet with the help of a neoprene rubber sheet as shown in figure 4.2a and similarly to the procedure explained in [73].

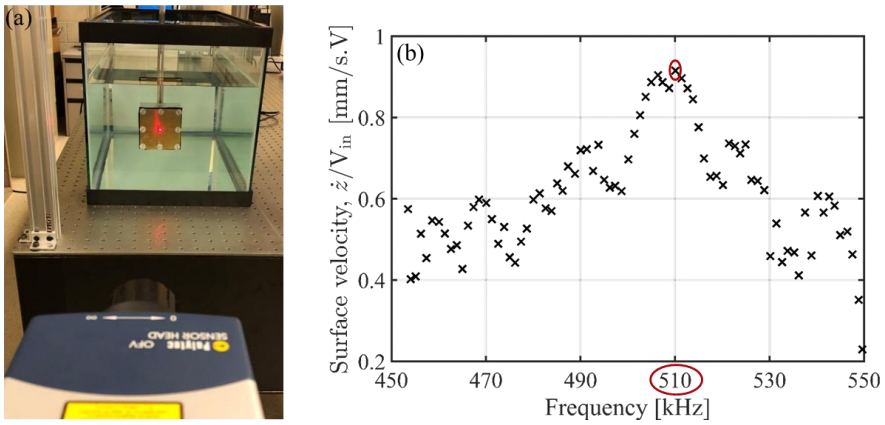

Figure 4.2. (a) Underwater actuation experimental setup and (b) corresponding measured surface velocity of the PZT transducer using laser Doppler vibrometer, versus excitation frequency, which shows a transducer's underwater resonant frequency of 510 kHz.

We used the box in order to electrically insulate the PZT transducer in water and to construct the air-backed transducer which reflects almost all power from the backside of the transducer toward the transmission line and enhances the power transfer. The box including the PZT disk was fully submerged in a 615 mm×318 mm×325 mm tank of deionized water. The surface velocity FRF of the disk is presented in figure 4.2b indicating an underwater fundamental resonant frequency of

510 kHz, which is considered as the desired frequency for acoustically matching the transmitter and receiver transducers using matching layers. Noticeably, the observed both radial and thickness vibration modes occur due to the finite aspect ratio of the disk, which makes the assumption of the piston-like motion, where the disk vibrates only in the thickness direction, not quite accurate but acceptable in the frequency range of interest.

4.3.2 Materials selection in the two-layer acoustic matching technique: Thicknesses determination

For the two-layer structure implemented for matching the PZT disks $(Z_T / Z_0 = 24.2)$, we investigated two main groups of materials: (1) several types of metals as well as some ceramics and composites for the first matching layer (ML-1) and an Araldite glue [57] with a specific acoustic impedance of 3.04 MRayl and longitudinal sound speed of 2620 m/s (glue A) as the second layer (ML-2); and (2) polymers or plastics as ML-1 and an Araldite glue [57] with a specific acoustic impedance of 12.81 MRayl and longitudinal sound speed of 1520 m/s (glue B) as ML-2.

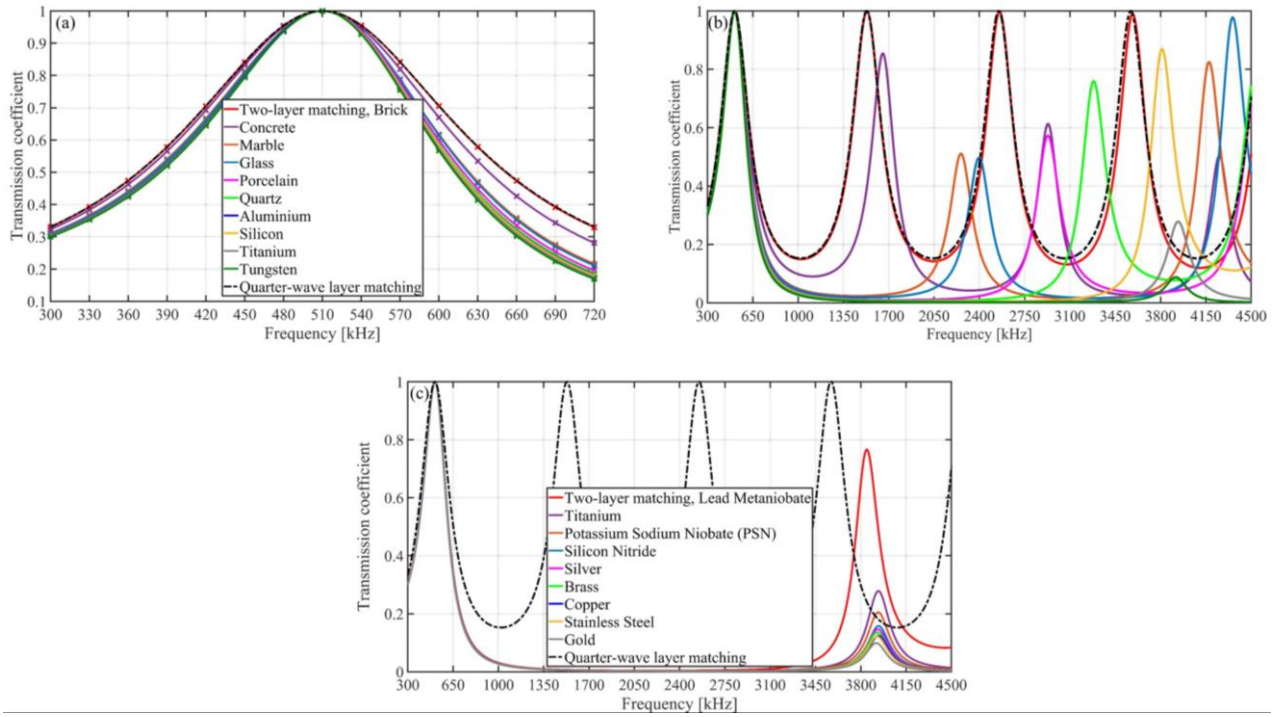

Figure 4.3. The power transmission coefficient of the matched PZT transducer implementing the two-layer matching structure with different materials (metals, ceramics, and composites) as ML-l and glue A as ML-2, compared with the ideal matching system: frequency range from (a) 300-720 kHz, and (b) 300 kHz-4.5 MHz, and (c) investigations of more material choices. The legend in (b) is set the same as that of (a). The cross markers in (a) represent the driving frequencies for which we have experimentally measured the pressure fields generated by the transmitter transducer, later shown in figure 4.9.

Figure 4.3a shows the acoustic power transmission coefficient in the first matching type using materials such as aluminum, titanium, glass, and porcelain for ML-1 and glue A for ML-2 compared with the transmission from the theoretical or ideal single (quarter-wave layer) matching. Apparently, the full width at half maximum (FWHM) of the two-layer system is comparable to that of ideal matching, e.g., using brick as ML-1, the system exhibits almost the same transmission performance as the quarter-wave layer matching. Moreover, the selection of different materials to acquire a relatively good transmission for the frequency range shown in figure 4.3a leads to comparable performances. However, as the frequency range is increased, more peaks appear in which selection of different materials for ML-1 leads to dissimilar performances as shown in figure 4.3b. To illustrate, choosing brick, represented by the red curve in figure 4.3b, as ML-1, one obtains several peaks of transmitted acoustic energy for the transducer, whereas choosing glass, represented by the blue curve in figure 4.3b, as ML-1, results in two peaks of higher transmission other than the fundamental frequency where good transmission is obtained only at a frequency around 4.4 MHz. It should be emphasized that we consider the performance of matching by analyzing only the acoustic power transmission coefficient; however, later for analyzing the electrical power output performance, the acoustic attenuation must also be taken into consideration as detailed in section 4.3.3. Figure 4.3c demonstrates the power transmission coefficient of the matched transducer analyzing other material choices for ML-1 such as commonly used metals like silver, copper, and stainless steel as well as some other ceramics such as lead metaniobate. It is determined that these materials show the same performance in acoustic matching as that of titanium up to about 3 MHz. However, the materials' effectiveness starts to diverge near 3.5 MHz.

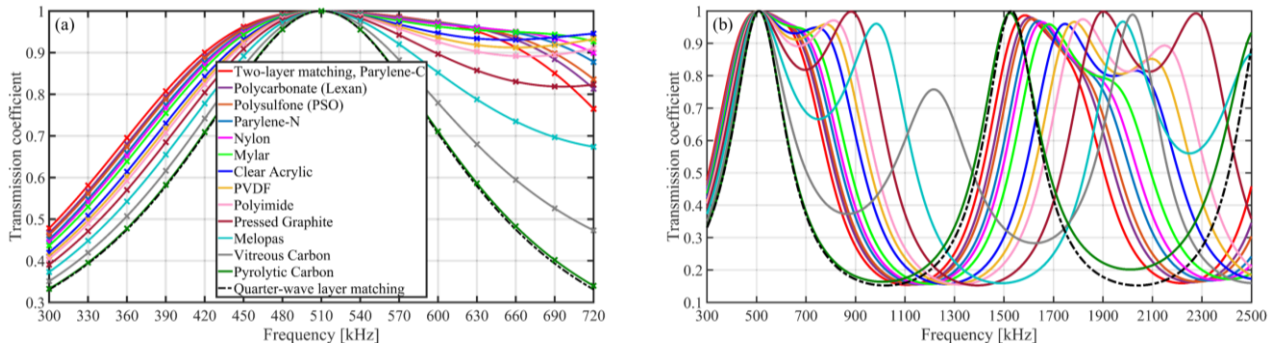

Figure 4.4. The power transmission coefficient of the matched PZT transducer implementing the two-layer matching structure with different polymers (or plastics) as ML-l and glue B as ML-2, compared with the ideal matching system: frequency range from (a) 300-720 kHz, and (b) 300 kHz-4.5 MHz. The legend in (b) is set the same as that of (a). The cross markers in (a) represent the driving frequencies for which we have experimentally measured the pressure fields generated by the transmitter transducer, later shown in figure 4.9.

The second matching type is performed by employing polymers as ML-1 and glue B as ML-2. The power transmission coefficient for the matched transducer is presented in figure 4.4a. Clearly, the two-layer matching technique in this type leads to a wider frequency bandwidth compared to the ideal matching and to the first matching type depicted in figure 4.3. Evaluating the acoustic transmission over the wider frequency range, the observed trends of transmission as shown in figure 4.4b are different than those of figure 4.3b in which the quality and intensity of most of the peaks, generated from the choice of polymers, are more noticeable. Furthermore, it should be noted that at the fundamental frequency of 510 kHz, all material choices lead to the maximum power transmission coefficient of unity as shown in figures 4.3 and 4.4, which shows the reliability of the transfer matrix method in determining the accurate thicknesses for the two layers to match the PZT transducer at the desired resonant frequency operating in water. It is also worthwhile to remark that some of the selected materials in this study are recognized to be biocompatible such as glass [11], titanium [49, 74], pyrolytic carbon [6, 74], and parylene [45].

The results of the acoustic matching techniques presented above were verified in two ways. Firstly, we verified the claim that implementing these techniques enhances the acoustic power transmission at any desired resonant frequency and also improves the transduction bandwidth leading to a wider frequency bandwidth. Figure 4.5a shows three scenarios for constructing a PZT transducer, namely (i) implementing the two-layer matching technique with layers of glass and glue A for the transducer, (ii) implementing a single classical quarter-wave layer matching technique, and (iii) using the transducer without matching layers. The power transmission coefficient for the latter scenario is calculated assuming four material layers of water, acrylic for fixing the backside of the transducer disk to an acrylic holder with a thickness of 3 mm (see figure 8 in [13]), PZT with a thickness of 3.9 mm, and again water (front side of the disk). Figure 4.5a clearly indicates the enhancements of the power transmission at the desired frequency of 510 kHz for the acoustically matched transducers compared to that of the unmatched transducer. The transducer without matching layers has the highest power transmission coefficient value of 0.87 at 598 kHz instead of the unity value at the desired frequency. Moreover, a noticeable bandwidth improvement is observed in the matched transducers. The relative bandwidth at -3dB (half-power bandwidth) at the center frequency of 598 kHz for the transducer without matching layers is 7.9%, compared to that of 47.6% and 55.7% at the center frequency of 510 kHz for the transducers having the two-layer and quarter-wave matching, respectively.

Secondly, we compared the two-layer and quarter-wave matching techniques, which we have assumed the semi-infinite thickness for the PZT transducer, to the KLM model [11, 75] in which the effects of the backing layer, electrical load, and thickness of the PZT material are also taken into account for the power reflection coefficient calculation. Moreover, we consider losses in the KLM model in which the losses are associated with the dielectric loss factor [69, 70, 76] through the loss tangent of 2%, as well as the ultrasonic attenuation which results in the complex stiffened wave speed in the PZT material [69, 70, 76, 77]. Figure 4.5b shows three scenarios for constructing a PZT transducer, namely (i) implementing the two-layer matching technique with layers of glass and glue A, as well as layers of PVDF and glue B for the transducer, (ii) using the same materials for ML-1 and ML-2 with the aforementioned KLM-lossy matching technique, and (iii) using a single classical quarter-wave layer matching. The power transmission coefficient for the matched transducer implementing the KLM-lossy model is calculated as explained in section 4.2.1 with a modification in computing the PZT acoustic impedance, Z_{pzt}, by applying equations (3)-(14) in [11], as well as equations (1) and (4) in [69]. We also set the acoustic impedance of the backing layer, $Z_{backing}$ (see equation (11) in [11]) as that of acrylic material for fixing the backside of the transducer disk. Furthermore, in the KLM model, the electrical load resistance is set to 1.55 kΩ, which is the optimal electrical load at 510 kHz (see figure 4.9d) and no inductor is used.

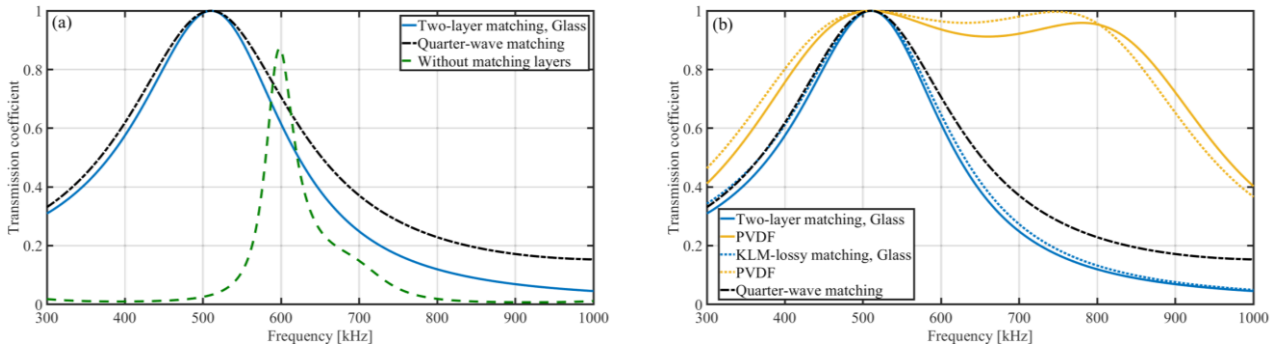

Figure 4.5. Comparing the power transmission coefficient of the acoustically matched PZT transducers using the two-layer and quarter-wave matching techniques (a) to that of the unmatched transducer, and (b) to that of the matched transducers using the KLM-lossy matching technique (dotted lines) adopted from [10, 68]. Glue A and B are used for bonding the layer of glass and PVDF, respectively.

The relative bandwidth at -3dB at the center frequency of 510 kHz for the transducer having the layers of PVDF and glue B using the two-layer matching technique is 124.2%; while for the transducer having the same material layers implementing the KLM-lossy model is 124.1%. For the transducer having the layers of glass and glue A, the relative bandwidth at -3dB at the center

frequency of 510 kHz using the KLM-lossy matching technique is 51.3% compared to that of 47.6% in the two-layer matching model as mentioned before. Hence, although the two-layer matching technique implemented in our study neglects the effects of the backing layer, electrical load, and thickness of the transducer on the acoustic reflection, it is in a very good agreement with that of the KLM-lossy matching technique that considers all the above effects.

Considering all material choices, we present in figure 4.6 a design platform that can be used to guide the development and design of proper two-layer matching configurations using selected glues A or B. Hence, once the specific glue is taken as ML-2, the material for ML-1 can be selected based on its characteristic acoustic impedance. The corresponding thicknesses for both layers, which are the key parameters in matching performance, can then be easily determined. Moreover, benefiting from the non-dimensional wave number kt in figure 4.6, we propose that similar design platforms could be obtained for acoustically matching transducers at any desired resonant frequency operating in an acoustic medium of interest, using any type of glue or epoxy. As a result, we can facilitate the construction of high-fidelity matched transducers to enhance acoustic power transmission. A comprehensive and detailed list of materials analyzed in this study for the two-layer matching system with their acoustic properties obtained from the literature [27, 57, 58] is tabulated in appendix C.3 as tables C.1 and C.2 to aid the readers in the design of acoustically matched transducers. The thicknesses of both ML-1 and ML-2 (glue A or B) calculated for matching the transducer at 510 kHz are also provided in the tables.

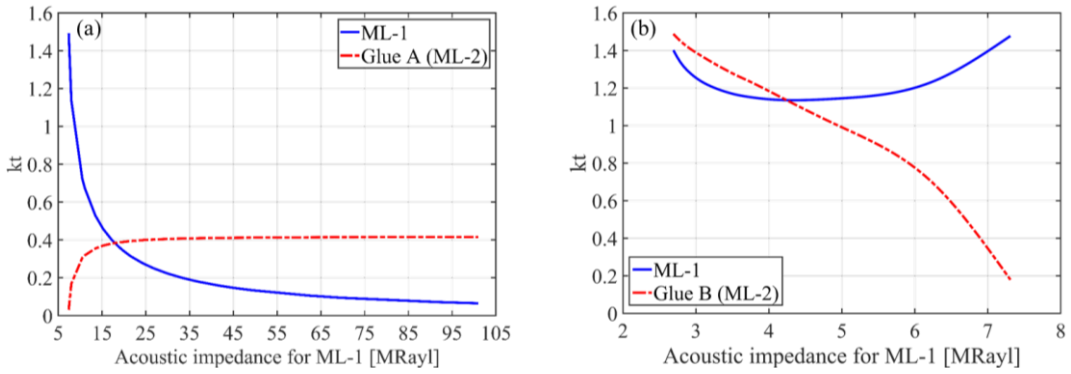

Figure 4.6. Design platform to find the proper two-layer matching configuration to select a material for ML-1 and determine thicknesses for both layers using (a) glue A and (b) glue B.

4.3.3 Electrical power output enhancement in UPT implementing acoustically matched transducers

As noted in section 4.2, we investigate three UPT system cases comprising the piezoelectric transmitter (Tx) and receiver (Rx) disks as shown in figures 4.1b-d and are, respectively, referred to as (1) *without matching layers* case, (2) *only Rx* case, and (3) *Tx and Rx* case. The distance d between the transmitter and receiver is set to 60 mm and it is assumed that the Tx and Rx transducers are perfectly aligned and that the receiver has a fixed-free boundary condition. The electrical power output for the receiver excited by the incident acoustic wave from the transmitter is estimated using equations (4.18) and $\Pi = v^2 / R_l$, considering the aforementioned three case studies to assess system enhancement using matching layers.

The experiments were performed to find the average input excitation force on the receiver disk due to the incident acoustic pressure from the transmitter. To calculate the input force, the transmitter output pressure distribution is reconstructed from the experimentally measured pressure field close to the source via the ASA (see section 4.2.3), which is then used to determine the average pressure on the plane where the receiver is located, at 60 mm from the source, using the propagation function described in [13, 78]. We measured the sound pressure in a plane at the distance 30 mm using a calibrated 0.2 mm needle hydrophone (Precision Acoustics Ltd with the sensitivity 50.6 mV/MPa at 500 kHz) mounted on a manufactured 3D positioning system as depicted in figure 4.7. The hydrophone preamplifier was connected to a DC coupler with power supply (Precision Acoustics Ltd) referenced to the digital oscilloscope in which the hydrophone signal was acquired and a developed MATLAB script is used that scans the acoustic field in the 2D measurement plane. The disk was excited by the low average input voltage of 21 V peak-to-peak to ensure that the PZT disk maintains the same performance over the one-hour hydrophone scan. The deionized water tank was partially lined with acoustic absorber sheets (Aptflex F28, Precision Acoustics Ltd) to avoid reflections from the tank walls. The pressure measurements were conducted over a range of driving frequencies between 300 and 720 kHz with 30 kHz increments. The measurement at each position on a plane at 30 mm distance from the transmitter was averaged over three times. The aperture of the measurement plane was about 50% wider than the diameter of the disk. We set the spatial resolution of 0.2 mm, which is smaller than a one-half wavelength in the medium, to avoid aliasing [64].

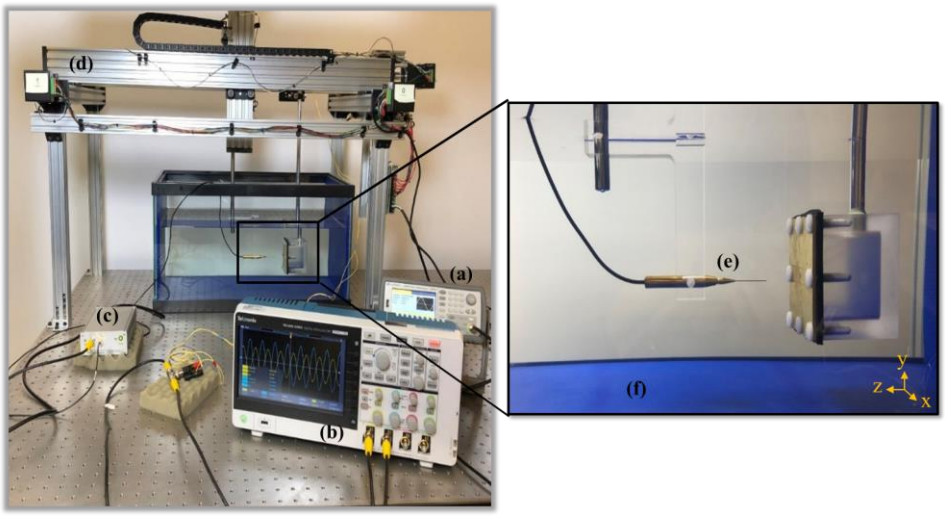

Figure 4.7. Experimental setup for measurement of pressure fields generated by the PZT transmitter disk enclosed in the watertight box: (a) waveform generator, (b) digital oscilloscope, (c) DC coupler with power supply, (d) positioning system, (e) needle hydrophone, and (f) acoustic absorber sheet.

The procedure for calculating the average input acoustic pressure on the receiver is illustrated in figure 4.8, where pressure distributions at 510 kHz using one of the analyzed matching materials are presented. Figure 4.8a shows the back-propagated pressure on the boundary between the transmitter and water, and figures 4.8b and c present the input pressures on the receiver face considering two scenarios of using no impedance matching materials and implementing layers of glass ($\beta_{\text{glass}} = 1.15$ Np/m measured at 2 MHz [79]) and glue A ($\beta_{\text{glue}} = 173$ Np/m measured at 4 MHz [80]) for the transmitter, respectively.

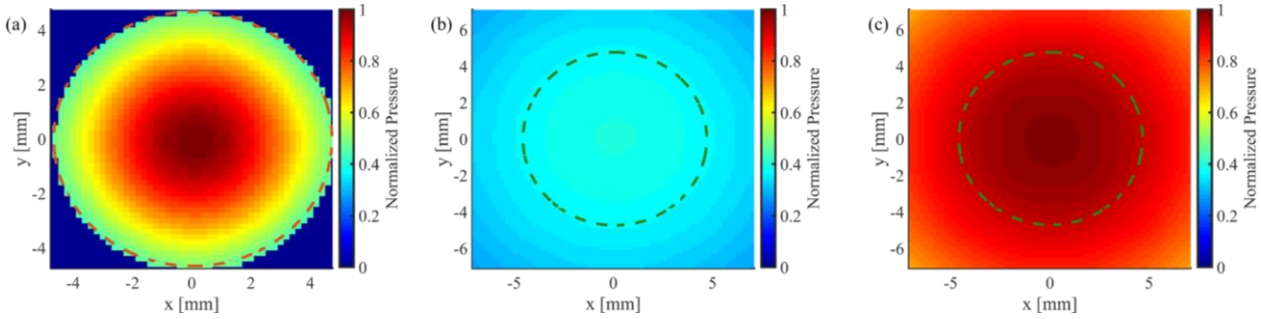

Figure 4.8. Acoustic pressure distributions at 510 kHz including (a) the back-propagated field at the boundary between the transmitter and water from experimentally measured pressure field, normalized by the maximum value in (a); the forward-propagated field in the plane where the receiver is located at $d = 60$ mm in which the disk is excited by the incident acoustic wave from the acoustically (b) unmatched, and (c) matched transmitter using layers of glass and glue A. The pressures in (b) and (c) are normalized by the maximum value in (c).

The dashed circles in figure 4.8 represent the locations of the transmitter (orange circle) and receiver (green circles) disks. It is noted that the average input pressure on the receiver surface using the matched acoustic source is significantly increased, which shows 2.5 times higher value in comparison to that of using the unmatched transmitter (note that $T_I = 0.15$ from equation (4.19) and $p_{t,R} \propto \sqrt{T_I}$). This can also be concluded from a comparison of the values in figures 4.9a and b.

Figure 4.9b and c present the average input pressure values due to acoustic excitation from the transmitter, by implementing the investigated matching materials, including, respectively, the first and second material types as illustrated in figures 4.3a and 4.4a. In order to make a fair comparison between the unmatched and matched cases, the pressure values in figure 4.9a, which are obtained for a UPT system with the unmatched acoustic source, are normalized by the maximum pressure existing for the first matching type shown in figure 4.9b. The results clearly show the effectiveness of using the impedance matching technique. The maximum excitation pressure at 510 kHz is generated using glass, as the first matching type in figure 4.9b, and vitreous carbon, as the second matching type in figure 4.9c. The generated pressure for using glass is slightly higher, compared to that of vitreous carbon. The pressure attenuation factor $e^{-\beta z}$ for each matching structure is taken into account in figure 4.9b and c based on the attenuation coefficient of material layers and the calculated thicknesses for ML-1 and glue. The attenuation in water ($\beta_{\text{water}} = 0.023$ Np/m measured at 1 MHz [81]) is accounted for on the basis of the distance between the transmitter and receiver transducers. The observed values of the attenuation coefficient for the selected materials in this study are provided in appendix C.3 as extracted from the literature. It should be noted that the values are roughly calculated for the frequency range of 300-720 kHz assuming a proportional increase of losses to the first power of frequency for the matching materials and to the second power of frequency for water. As depicted in figure 4.9b and c, brick and PVDF possess the highest acoustical loss leading to the lowest generation of the input acoustic pressure on the receiver using these materials for acoustically matching the transmitter. Evidently, the attenuation plays a significant role in selecting the matching scheme in UPT as noted from the trend of the input pressure in figures 4.9b and c, which is considerably different from that of the power transmission coefficient shown in figures 4.3a and 4.4a. This is due to the fact that in calculating the power transmission coefficient, no attenuation is taken into account leading to the value of unity for all the selected materials at 510 kHz.

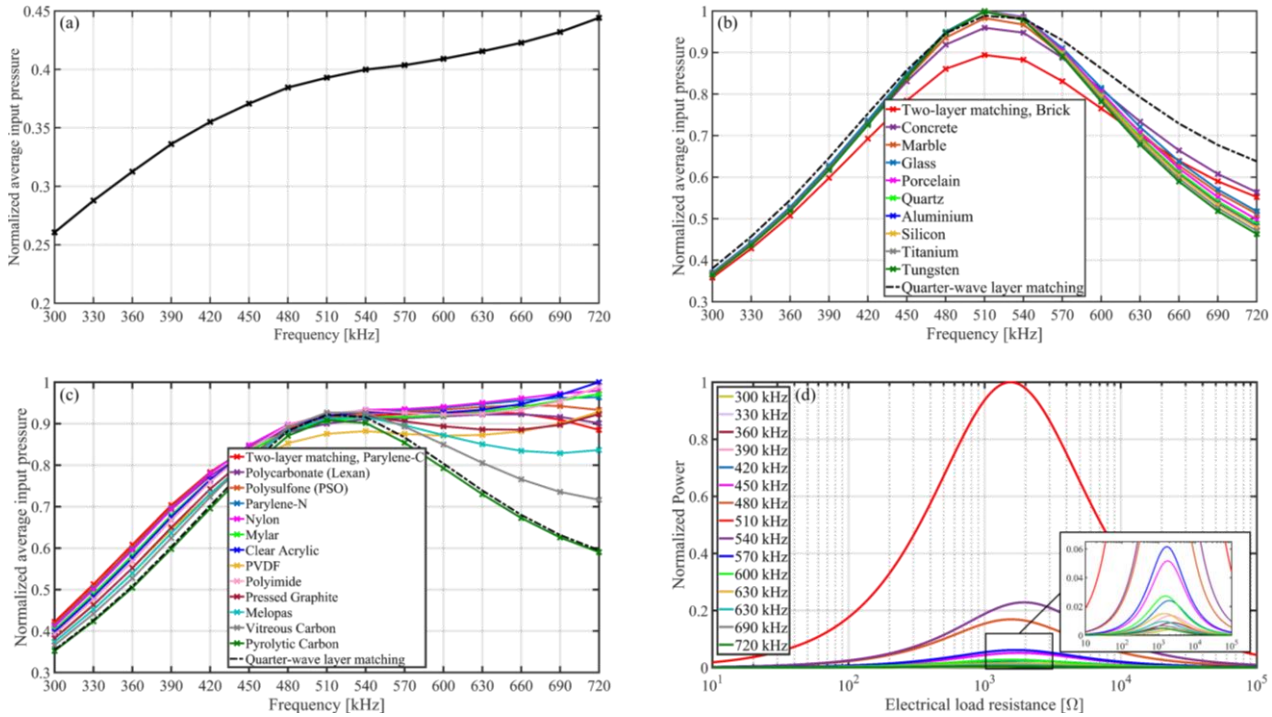

Figure 4.9. Calculated average input pressures on the surface of the receiver excited by (a) the unmatched transmitter. The average input pressures on the receiver excited by the matched transmitter (b) using the first matching type (with glue A), and (c) using the second matching type (with glue B). (d) Electrical power output (normalized with respect to the excitation force squared) versus electrical load resistance for each analyzed driving frequency, showing the optimal load in the range of 1.26-2.85 kΩ. The pressures in (a) are normalized by the maximum value in (b) and the pressures in (b) and (c) are normalized by the maximum value in each type. The results for the single quarter-wave matching system using glue C are also shown in (b) and (c). The power output values in (d) are normalized by the maximum value in (d).

Moreover, in figure 4.9c, one can see that the pressure increases monotonically, even at frequencies greater than 510 kHz. This occurs only due to the higher values of measured pressure at the frequency range of 540-720 kHz while their corresponding power transmission coefficient values in figure 4.4a are slightly less than unity. The input pressure using the quarter-wave matching structure shown in figure 4.9b and c is also calculated with a single layer of another type of Araldite epoxy (glue C) with the specific acoustic impedance of 7.45 MRayl [57], which is close to the geometric mean of water and the transducer PZT material impedances, considering the loss of 173 Np/m (measured at 4 MHz). Of interest is the realization that the maximum pressure is not necessarily achieved using ideal matching conditions. The electrical load resistance in equation (4.18) is set to that of the optimal load that gives the maximum electrical power output at each analyzed driving frequency. The power output normalized with the excitation force ($f(t) = p_{t,R}(t)A$ or $f(t) = p_{t,R-ML}(t)A$) squared is shown in figure 4.9d in which the optimal load

at each frequency can be determined. Other parameters, namely electromechanical coupling, capacitance, and mechanical quality factor of the receiver are, respectively, set to $\kappa = 0.21$ C/m, $C_p = 180$ pF, and $Q = 70$, which were identified by measuring the electrical impedance of the receiver disk in air and fitting it to the UPT analytical model in the frequency range of 420-580 kHz. Figure C.1 in appendix C.1 shows the measured electrical impedance of the unloaded disk in the air using the HP4192A impedance analyzer in the frequency range of 100-700 kHz in which one can see both the radial and thickness vibrational modes of the finite-size receiver disk; in the range of 300-700 kHz, the thickness vibration mode of the disk is dominating.

Figure 4.10 shows the power output of the UPT system analyzed in the three scenarios as depicted in figures 4.1b-d. Noticeably, the maximum power output of the system, at the resonant frequency of 510 kHz, improves when the transducers were acoustically matched with the medium. The results in figures 4.10a and b show a power gain enhancement of 8 dB comparing the maximum power values achieved using glass and vitreous carbon for *only Rx* case with that of *without matching layers* case, as well as comparing the maximum power value for *Tx and Rx* case with that of *only Rx* case. However, the improvements are reduced using other materials with higher attenuation to a maximum level of 36% using brick as shown in figure 4.10a and a maximum level of 20% using PVDF as shown in figure 4.10b. The attenuation variations with frequency for the selected material layers and water in a broad ultrasound frequency range of 20 kHz-10 MHz are presented in figure C.3 in appendix C.4. At higher frequencies, the ultrasonic material losses limit the level of power improvement, particularly in lossy media, i.e., the media with high attenuation coefficient, such as human tissue, which has excessively higher attenuation value than water [82].

In our investigation, PVDF has the highest levels of acoustic loss of 154.3 Np/m [83] (measured at 1 MHz) resulting in a power attenuation factor of $\mu = 0.76$ at 510 kHz and $\mu = 0.57$ at 10 MHz (see figure C.3) for the *Tx and Rx* case results presented in figure 4.10b, which appears that yet the matching technique overcomes the losses in the water at high frequencies. However, considering human tissue, using matching layers most likely downgrades the power enhancement at high frequencies. We shall also note that as the frequency increases, the proportionally thinner matching layers are required to match the transducers, hence, only the power attenuation factor in the acoustic medium increases. Comparing the power output enhancement using two types of matching layers in figures 4.10a and b, an increase of 3% is obtained using glass in comparison to vitreous carbon. However, some enhancements are seen at off-resonance frequencies, noticeably

at higher frequencies, where polymers or plastics appear to be better material choices. Furthermore, the higher power improvement is attained comparing the two-layer structures with glass, porcelain, quartz (X-cut), silicon, aluminum, titanium, tungsten, vitreous carbon, and polyimide, to that of the ideal matching with the single layer of epoxy. In general, it is concluded that implementing acoustic impedance matching layers in UPT systems is of utmost importance for acquiring efficient electrical power output from the receivers/sensors; however, the material losses must be also taken into consideration to ensure that the trade-off between the matching technique and attenuation effects is reasonable.

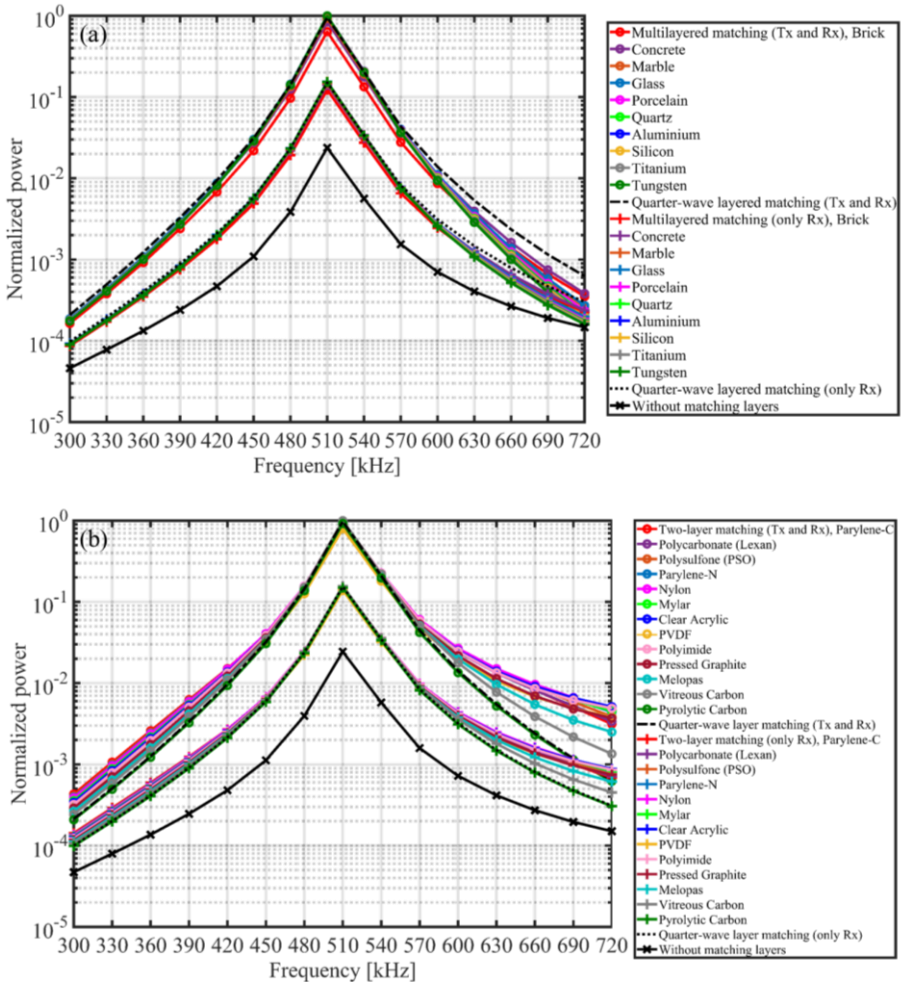

Figure 4.10. (a) Electrical power output for the piezoelectric receiver at $d = 60$ mm excited by the acoustic source, analyzed in three scenarios in the UPT system, namely *without matching layers* case depicted with a cross marker, *only Rx* case depicted with plus sign markers, and *Tx and Rx* case depicted with circle markers using (a) first matching type (with glue A), and (b) second matching type (with glue B). The power output values are normalized by the maximum value in each type. The results for the single quarter-wave matching system are also shown in (a) and (b), which dashed-dot and dotted lines, respectively, represent *Tx and Rx* case and *only Rx* case using glue C.

4.3.4 Implementing a four-layer acoustically matching technique in UPT

We also investigated four-layer matching systems containing two layers of glue A and two layers of different materials such as using a combination of glass and acrylic as shown in figure 4.11a, and also a combination of polymer and metal layers as shown in figure 4.11c, where a layer of polyethylene is selected in conjunction with a metal layer, namely titanium, silver, brass, copper, and steel. In figures 4.11a and c, the thickness of glue layers is, respectively, set to 0.2 and 0.25 mm. Comparing the results of the acoustic power transmission coefficient with those of the two-layer system containing the same glue with a layer of glass and metals, it is concluded that adding matching materials leads to a relatively wider frequency bandwidth in which the FWHM of the four-layer configuration is very close to the ideal matching or slightly enhanced. However, the maximum transmission is achieved for both two and four-layer structures, and only some improvements at off-resonance frequencies are observed.

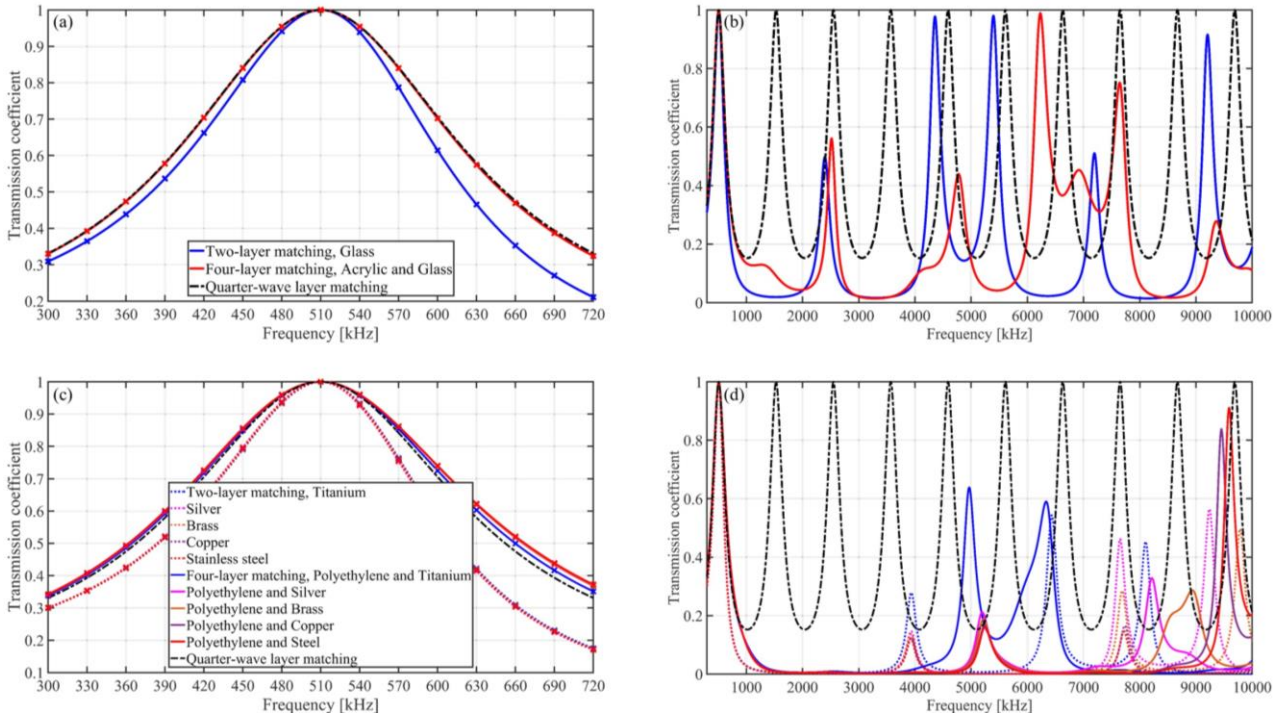

Figure 4.11. The power transmission coefficient of the matched transducer in the four-layer matching structure using two layers of glue A $(t_2 = t_4 = 0.2 \text{ mm})$ with two layers of glass and acrylic, compared with the corresponding two-layer and ideal matching system: (a) frequency range from 300-720 kHz, and (b) wider frequency range from 300 kHz-10 MHz. The power transmission coefficient of the matched transducer in the four-layer system using two layers of glue A $(t_2 = t_4 = 0.25 \text{ mm})$ with the combination of polymer and metal layers, compared with the corresponding two-layer and ideal matching system: (c) frequency range from 300-720 kHz, and (d) wider frequency range from 300 kHz-10 MHz. The legend in (b) and (d) is, respectively, the same as that of (a) and (c).

Analyzing the acoustic transmission of the matched transducer over the wider frequency range shown in figures 4.11b and d, it is concluded that the peak values of transmission occur at different frequencies in the two-layer system and that smoother curves of transmission are generated in comparison to those of the four-layer systems. A list of analyzed materials for the four-layer matching system with their determined thicknesses at 510 kHz is presented in table C.3 of appendix C.3.

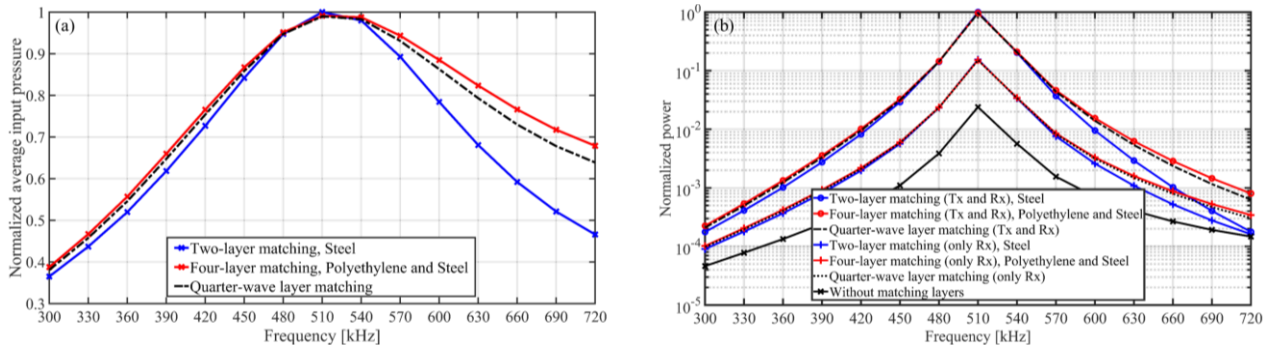

Figure 4.12. Example of the four-layer system compared with the corresponding two-layer and single quarter-wave matching system using glue C: (a) the average input pressure on the receiver excited by the matched transmitter, and (b) the subsequent electrical power output for the receiver at $d = 60$ mm excited by the acoustic source, analyzed in three scenarios, namely *without matching layers* case depicted with a cross marker, *only Rx* case depicted with plus sign markers, and *Tx and Rx* case depicted with circle markers. The thickness of the glue layers is set to 0.25 mm. The pressure values are obtained using the same experimentally measured pressure fields explained in section 4.3.3. The dashed-dot and dotted lines in (b), respectively, represent *Tx and Rx* case and *only Rx* case using glue C.

Figure 4.12a shows the average input pressure on the receiver surface considering an example of the analyzed four-layer material choices, implementing two layers of polyethylene and steel with the two layers of glue A in comparison to that of the two-layer system of using steel and glue A. Consistently, the input acoustic pressure increases for the off-resonance driving frequencies, particularly for the system excited above the fundamental resonance of the transducer, which in turn leads to a considerable power augmentation, as illustrated in figure 4.12b. However, due to the stronger attenuation effects using four layers, slightly higher input pressure and hence higher power enhancements are achieved at 510 kHz in the two-layer structure. Briefly, the foremost objective in the UPT-matching technique is the construction of wide-bandwidth transducers that can greatly transmit the acoustic energy at or near the desired resonant frequency, which is satisfactorily achieved by implementing the two-layer acoustically matching system. In conclusion, adding the number of layers, which subsequently requires more than one layer of glue, is not a practical and efficient solution since the fabrication of transducers with four or more

material layers and maintaining the required thicknesses can be extremely difficult, time-consuming and costly.

4.4 Conclusions

Contactless ultrasonic power transfer (UPT) is a new technology with broad applications, e.g., to support distributed automotive sensing in the automobile industry and wireless networks in biomedical sensors. Current UPT systems suffer from significant acoustic losses through the transmission line from a piezoelectric transmitter to an acoustic medium (e.g., water or human tissue) and then to a piezoelectric receiver. This is due to the acoustic impedance mismatch between the PZT (lead zirconate titanate) transducers and the medium, which causes a narrow transducer bandwidth and a considerable reflection of the acoustic pressure waves at the boundary layers. We investigated the implementation of acoustic impedance matching layers deposited on the front leading surface of the source and receiver transducers to enhance the acoustic power transmission into the medium and then reinforce the input as an excitation into the receiver. A transfer matrix method was used to determine the thicknesses of selected materials in the two-layer matching structure where one of the layers is the glue and the calculated thicknesses are different from the quarter of materials' wavelength. Subsequently, an electro-elastic model was employed to couple the properties of the PZT transmitter and receiver with multiple matching layers and a single classical quarter-wave layer. A design platform was developed that can simplify the construction of acoustically matched transducers, that is, the materials selection and determination of their thicknesses. Simulations were performed to evaluate the electrical power output enhancement in UPT using the two-layer system to match the transducers to water at the resonant frequency. Different material types were selected as the first layer including mainly metals and polymers. The input acoustic pressure on the receiver was determined via the angular spectrum approach using the experimentally measured transmitter output pressure distribution. The ultrasonic material losses were also accounted for in the simulations to accurately quantify the advantages of matching layers in UPT, which is specifically important in lossy acoustic media such as human tissue. The results indicate dramatic electrical power output improvements when implementing matching layers in the UPT system. We also concluded that using more than two layers in the matching structure is not advantageous because it does not lead to a more power enhancement at the resonant frequency or to the generation of noticeably wider frequency bandwidth.

Acknowledgments

This work was supported by the National Science Foundation (NSF) Grant NO. ECCS-1711139, which is gratefully acknowledged. We would like to thank Omidreza Sadeghi for helping with experiments.

Appendix C

C.1 Measured electrical impedance

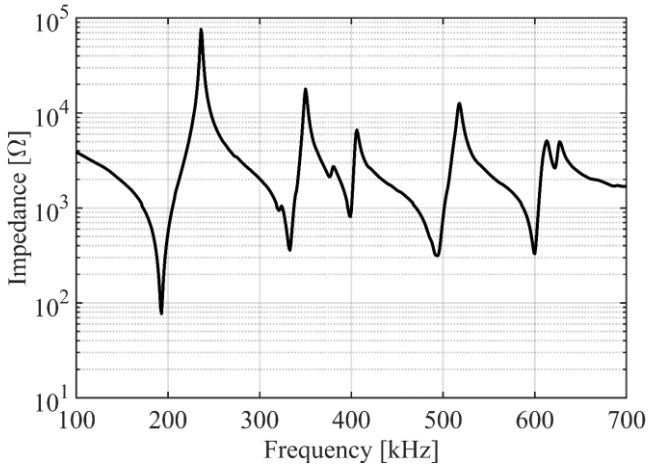

Figure C.1. Measured electrical impedance of the unloaded APC850 PZT disk in the air using the HP4192A impedance analyzer

C.2 Acoustic radiation impedance

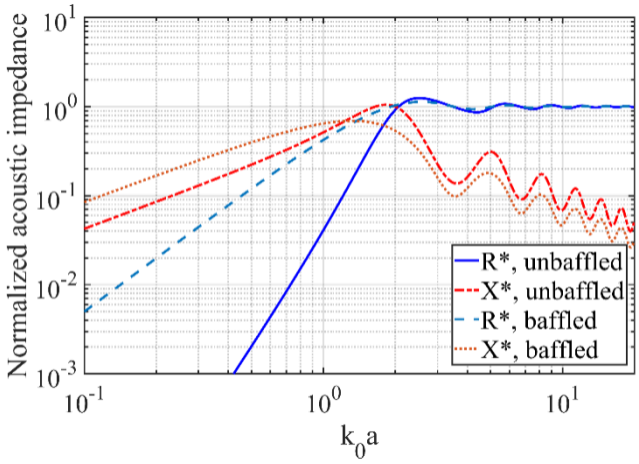

Figure C.2. Normalized acoustic radiation resistance $R^* = R_r / (\rho_0 c_0 A)$ and reactance $X^* = X_r / (\rho_0 c_0 A)$ for $1 \le ka \le 20$ of an unbaffled and a baffled piston. c_0 and k_0 are, respectively, the speed of sound and wave number in the acoustic medium (water), and ρ_0 is the density of the medium. Calculations for the unbaffled case is performed with $M = 40$ and $b = a$ (see equations (56) and (57) in [60]).

C.3 Materials used in the acoustically matching technique

Table C.1. Acoustic properties and calculated thicknesses (at 510 kHz) of the first type of materials used in the two-layer matching system. The attenuation coefficient of glue is taken as 173 Np/m [80] (measured at 4 MHz). The properties are extracted from [57], unless otherwise mentioned.

Material for ML-1	Characteristic impedance [MRayl]	Sound speed [m/s]	t_1 [mm]	t_2 (glue A) [mm]	Attenuation coefficient [Np/m]
Brick	7.4	4300	2.004	0.025	11.5 @ 100 kHz [84]
Concrete	8	3100	1.1	0.138	40.3 @ 510 kHz [85]
Marble	10.5	3800	0.858	0.25	21 @ 510 kHz[86]
Glass	11.1	4910	1.03	0.261	1.15 @ 2 MHz [79]
Porcelain	13.5	5900	0.972	0.290355	1.15 @ 2 MHz [79]
Slate	13.5	4500	0.742	0.290355	
Quartz	15.3	5750	0.82	0.303	10.8 @ 450 MHz [87]
Aluminum	17.33	6420	0.797	0.312	1.15 @ 2 MHz [79]
Indium	18.7	2560	0.293	0.316	
Silicon	19.7	8430	0.911	0.318	23 @ 286 MHz [88]
Lead Metaniobate	20.5	3300	0.342	0.32	
Bismuth	21.5	2200	0.216	0.322	
Beryllium	24.1	12890	1.125	0.32604	
Tin	24.2	3300	0.287	0.3262	

Lead	24.6	2200	0.188	0.327	
Boron carbide	26.4	11000	0.873	0.3285	
Granite	26.8	6500	0.508	0.3289	
Thorium	27.12	2400	0.185	0.329	
Titanium	27.3	6100	0.468	0.3293	1.15 @ 2 MHz [79]
Zinc	29.6	4200	0.296	0.33105	
Zirconium	30.1	4650	0.322	0.3314	
Potassium Sodium Niobate (PSN)	31	6940	0.467	0.332	
Lithium Niobate	33	7080	0.446	0.333	
PZT 5H	33	4440	0.28	0.333	
Cast Iron	33.2	4600	0.288	0.33305	
Silicon Nitride	36	11000	0.634	0.334	
Murata PZT	37.5	4720	0.261	0.3347	
Silver	38	3600	0.197	0.33486	
Brass	40.6	4700	0.24	0.3356	
Niobium	42.2	4920	0.241	0.33595	
Titanium Carbide	42.6	8270	0.402	0.33604	
Zircaloy	44.2	4720	0.221	0.33637	
Copper	44.6	5010	0.232	0.3364	
Stainless Steel	45.7	5790	0.262	0.3366	
Iron	46.4	5900	0.263	0.3368	
Inconel	47.2	5700	0.25	0.3369	

Nickel	49.5	5600	0.234	0.3372	
Uranium	63	3400	0.111	0.338527	
Molybdenum	63.1	6300	0.206	0.338534	
Gold	63.8	3240	0.105	0.33858	
Tantalum	68.06	4100	0.124	0.339	
Platinum	69.8	3260	0.096	0.3389	
Silicon Carbide	91.8	6660	0.149	0.3396	
Tungsten	101	5200	0.106	0.3398	1.15 @ 2 MHz [79]

Table C.2. Acoustic properties and calculated thicknesses (at 510 kHz) of the second type of materials used in the two-layer matching system. The attenuation coefficient of glue is taken as 173 Np/m [80] (measured at 4 MHz). The properties are extracted from [57], unless otherwise mentioned.

Material for ML-1	Characteristic impedance [MRayl]	Sound speed [m/s]	t_1 [mm]	t_2 (glue B) [mm]	Attenuation coefficient [Np/m]
Clear Polycarbonate	2.69	2270	0.994	0.706	
Parylene-C	2.7 [27]	2200 [27]	0.957	0.704	3570 @ 100 MHz [27]
Polycarbonate (Lexan)	2.75	2300	0.975	0.694	267.1 @ 5 MHz
Polysulfone (PSO)	2.78	2240	0.937	0.689	48.9 @ 2 MHz
Parylene-N	2.85 [27]	2100 [27]	0.856	0.678	1496 @ 100 MHz [27]
Nylon	2.9	2600	1.044	0.671	33.4 @ 5 MHz
Oak Wood	2.9	4000	1.606	0.671	
Teflon	2.97	1390	0.548	0.662	
Mylar	3	2540	0.994	0.659	2000 @ 50 MHz [89]
Clear Acrylic	3.26	2750	1.03	0.63	73.7 @ 5 MHz
PVC	3.27	2380	0.89	0.629	
PVDF	3.43 [58]	1930 [58]	0.709	0.613	154.3 @ 1 MHz [83]
Polyimide	3.6 [27]	2430 [27]	0.88	0.597	646.4 @ 100 MHz [27]

Bakelite	3.63	1590	0.575	0.595	
Pressed Graphite	4.1	2400	0.852	0.552	39.4 @ 1 MHz [90]
Melopas	4.93	2900	1.035	0.476	82.9 @ 2.5 MHz
Vitreous Carbon	6.26	4260	1.644	0.327	311 @ 50 MHz[b] [91]
Pyrolytic Carbon	7.31	3310	1.526	0.085	39.4 @ 1 MHz[c] [90]

Table C.3. Calculated thicknesses (at 510 kHz) of materials used in the four-layer matching system. Characteristic impedance, sound speed, and attenuation coefficient of polyethylene are, respectively, 2.33 MRayl [57], 2430 m/s [57], and 38 Np/m [58] (measured at 2 MHz).

Material for ML-3	t_1 (Clear Acrylic) [mm]	t_2 (glue A) [mm]	t_3 [mm]	t_4 (glue A) [mm]
Glass	0.28	0.2	1.031	0.2

Material for ML-3	t_1 (Polyethylene) [mm]	t_2 (glue A) [mm]	t_3 [mm]	t_4 (glue A) [mm]
Titanium	0.482	0.25	0.506	0.25
Silver	0.522	0.25	0.217	0.25
Brass	0.527	0.25	0.266	0.25
Copper	0.534	0.25	0.2586	0.25
Stainless Steel	0.535	0.25	0.292	0.25

[b] The attenuation coefficient of vitreous carbon is assumed to be the same as that of hard carbon.
[c] The attenuation coefficient of pyrolytic carbon is assumed to be the same as that of graphite.

C.4 Ultrasonic material attenuation variations with frequency

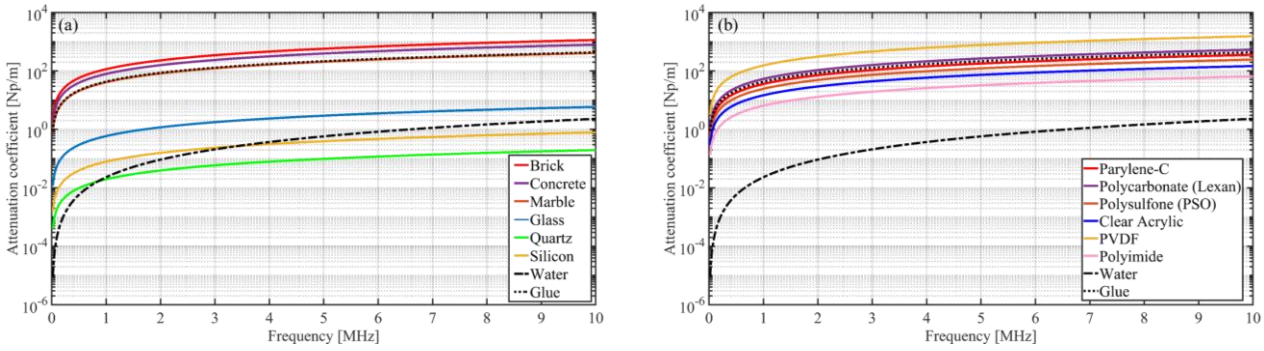

Figure C.3. Ultrasonic attenuation versus frequency for the materials analyzed in the electrical power calculations compared with that of used glue and water: (a) first material type, and (b) second material type. The variations of the attenuation with frequency for some of the analyzed materials are not presented due to the close similarity of the attenuation values with the one shown in the figure (see Appendix C.3 for other materials' attenuation coefficient value).

Bibliography

[1] Bakhtiari-Nejad, M., Hajj, M.R., and Shahab, S., *Dynamics of acoustic impedance matching layers in contactless ultrasonic power transfer systems.* Smart Materials and Structures, 2020. **29**(3): p. 035037.

[2] Shahab, S. and Erturk, A., *Contactless ultrasonic energy transfer for wireless systems: acoustic-piezoelectric structure interaction modeling and performance enhancement.* Smart Materials and Structures, 2014. **23**(12): p. 125032.

[3] Shahab, S., Gray, M., and Erturk, A., *Ultrasonic power transfer from a spherical acoustic wave source to a free-free piezoelectric receiver: Modeling and experiment.* Journal of Applied Physics, 2015. **117**(10): p. 104903.

[4] Ishiyama, T., Kanai, Y., Ohwaki, J., and Mino, M. *Impact of a wireless power transmission system using an ultrasonic air transducer for low-power mobile applications*. in *IEEE Symposium on Ultrasonics, 2003*. 2003. IEEE.

[5] Roes, M., Hendrix, M., and Duarte, J. *Contactless energy transfer through air by means of ultrasound*. in *IECON 2011-37th Annual Conference of the IEEE Industrial Electronics Society*. 2011. IEEE.

[6] Ozeri, S. and Shmilovitz, D., *Ultrasonic transcutaneous energy transfer for powering implanted devices.* Ultrasonics, 2010. **50**(6): p. 556-566.

[7] Meng, M. and Kiani, M., *Design and optimization of ultrasonic wireless power transmission links for millimeter-sized biomedical implants.* IEEE transactions on biomedical circuits and systems, 2017. **11**(1): p. 98-107.

[8] Lawry, T.J., Wilt, K.R., Ashdown, J.D., Scarton, H.A., and Saulnier, G.J., *A high-performance ultrasonic system for the simultaneous transmission of data and power*

through solid metal barriers. IEEE transactions on ultrasonics, ferroelectrics, and frequency control, 2012. **60**(1): p. 194-203.

[9] Yang, D.-X., Hu, Z., Zhao, H., Hu, H.-F., Sun, Y.-Z., and Hou, B.-J., *Through-metal-wall power delivery and data transmission for enclosed sensors: A review.* Sensors, 2015. **15**(12): p. 31581-31605.

[10] Roes, M.G., Duarte, J.L., Hendrix, M.A., and Lomonova, E.A., *Acoustic energy transfer: A review.* IEEE Transactions on Industrial Electronics, 2013. **60**(1): p. 242-248.

[11] Ozeri, S. and Shmilovitz, D., *Simultaneous backward data transmission and power harvesting in an ultrasonic transcutaneous energy transfer link employing acoustically dependent electric impedance modulation.* Ultrasonics, 2014. **54**(7): p. 1929-1937.

[12] Bhargava, A. and Shahab, S., *Coupling of nonlinear shape memory polymer cantilever dynamics with focused ultrasound field.* Smart Materials and Structures, 2019.

[13] Bakhtiari-Nejad, M., Elnahhas, A., Hajj, M.R., and Shahab, S., *Acoustic holograms in contactless ultrasonic power transfer systems: Modeling and experiment.* Journal of Applied Physics, 2018. **124**(24): p. 244901.

[14] Bakhtiari-Nejad, M., Elnahhas, A., Hajj, M.R., and Shahab, S. *Passive metamaterial-based acoustic holograms in ultrasound energy transfer systems*. in *Active and Passive Smart Structures and Integrated Systems XII*. 2018. International Society for Optics and Photonics.

[15] Meesala, V.C., Hajj, M.R., and Shahab, S., *Modeling and identification of electro-elastic nonlinearities in ultrasonic power transfer systems.* Nonlinear Dynamics, 2019: p. 1-20.

[16] Goll, J.H. and Auld, B.A., *Multilayer impedance matching schemes for broadbanding of water loaded piezoelectric transducers and high Q electric resonators.* IEEE transactions on sonics and ultrasonics, 1975. **22**(1): p. 52-53.

[17] Inoue, T., Ohta, M., and Takahashi, S., *Design of ultrasonic transducers with multiple acoustic matching layers for medical application.* IEEE transactions on ultrasonics, ferroelectrics, and frequency control, 1987. **34**(1): p. 8-16.

[18] Thiagarajan, S., Martin, R.W., Proctor, A., Jayawadena, I., and Silverstein, F., *Dual layer matching (20 MHz) piezoelectric transducers with glass and parylene.* IEEE transactions on ultrasonics, ferroelectrics, and frequency control, 1997. **44**(5): p. 1172-1174.

[19] Persson, H. and Hertz, C., *Acoustic impedance matching of medical ultrasound transducers.* Ultrasonics, 1985. **23**(2): p. 83-89.

[20] Shung, K.K. and Zippuro, M., *Ultrasonic transducers and arrays.* IEEE Engineering in Medicine and Biology Magazine, 1996. **15**(6): p. 20-30.

[21] Kossoff, G., *The effects of backing and matching on the performance of piezoelectric ceramic transducers.* IEEE Transactions on sonics and ultrasonics, 1966. **13**(1): p. 20-30.

[22] Desilets, C.S., Fraser, J.D., and Kino, G.S., *The design of efficient broad-band piezoelectric transducers.* IEEE Transactions on sonics and ultrasonics, 1978. **25**(3): p. 115-125.

[23] Souquet, J., Defranould, P., and Desbois, J., *Design of low-loss wide-band ultrasonic transducers for noninvasive medical application.* IEEE transactions on sonics and ultrasonics, 1979. **26**(2): p. 75-80.

[24] Goll, J.H., *The design of broad-band fluid-loaded ultrasonic transducers.* IEEE Transactions on Sonics and Ultrasonics, 1979. **26**(6): p. 385-393.

[25] Beerman, H.P., *Optimizing matching layers for a three-section broad-band piezoelectric PZT-5A transducer operating into water.* IEEE Transactions on Sonics and Ultrasonics, 1981. **28**(1): p. 52-53.

[26] Xu, Q., Madhavan, C., Srinivasan, T., Yoshikawa, S., and Newnham, R. *Composite transducer with multiple piezoelectric matching layers*. in *IEEE 1988 Ultrasonics Symposium Proceedings.* 1988. IEEE.

[27] Hadimioglu, B. and Khuri-Yakub, B. *Polymer films as acoustic matching layers*. in *IEEE Symposium on Ultrasonics*. 1990. IEEE.

[28] Kim, Y.-b. and Roh, Y., *New design of matching layers for high power and wide band ultrasonic transducers.* Sensors and Actuators A: Physical, 1998. **71**(1-2): p. 116-122.

[29] Rhee, S., Ritter, T., Shung, K., Wang, H., and Cao, W. *Materials for acoustic matching in ultrasound transducers*. in *2001 IEEE Ultrasonics Symposium. Proceedings. An International Symposium (Cat. No. 01CH37263)*. 2001. IEEE.

[30] Gudra, T. and Opieliński, K.J., *Influence of acoustic impedance of multilayer acoustic systems on the transfer function of ultrasonic airborne transducers.* Ultrasonics, 2002. **40**(1-8): p. 457-463.

[31] Álvarez-Arenas, T.G., *Acoustic impedance matching of piezoelectric transducers to the air.* IEEE transactions on ultrasonics, ferroelectrics, and frequency control, 2004. **51**(5): p. 624-633.

[32] Gudra, T. and Banasiak, D. *Methods for Selecting Multicomponent Layers Which Match the Acoustic Impedance of Ultrasound Transducers to Various Media*. in *2018 Joint Conference-Acoustics*. 2018. IEEE.

[33] Guo, F., Wang, Y., Huang, Z., Qiu, W., Zhang, Z., Wang, Z., Dong, J., Yang, B., and Cao, W., *Magnesium Alloy Matching Layer for PMN-PT Single Crystal Transducer Applications.* IEEE transactions on ultrasonics, ferroelectrics, and frequency control, 2018. **65**(10): p. 1865-1872.

[34] Ke, Q., Liew, W.H., Tao, H., Wu, J., and Yao, K., *KNNS-BNZH Lead-free 1-3 Piezoelectric Composite for Ultrasonic and Photoacoustic Imaging.* IEEE transactions on ultrasonics, ferroelectrics, and frequency control, 2019.

[35] Toda, M. and Thompson, M., *Novel multi-layer polymer-metal structures for use in ultrasonic transducer impedance matching and backing absorber applications.* IEEE transactions on ultrasonics, ferroelectrics, and frequency control, 2010. **57**(12): p. 2818-2827.

[36] Toda, M. and Thompson, M., *Detailed investigations of polymer/metal multilayer matching layer and backing absorber structures for wideband ultrasonic transducers.* IEEE transactions on ultrasonics, ferroelectrics, and frequency control, 2012. **59**(2): p. 231-242.

[37] Brown, J.A., Sharma, S., Leadbetter, J., Cochran, S., and Adamson, R., *Mass-spring matching layers for high-frequency ultrasound transducers: A new technique using vacuum deposition.* IEEE transactions on ultrasonics, ferroelectrics, and frequency control, 2014. **61**(11): p. 1911-1921.

[38] Gorostiaga, M., Wapler, M., and Wallrabe, U. *Novel spring-mass matching layer fabrication*. in *2015 IEEE International Ultrasonics Symposium (IUS)*. 2015. IEEE.

[39] Opieliński, K.J. and Gudra, T., *Influence of the thickness of multilayer matching systems on the transfer function of ultrasonic airborne transducer.* Ultrasonics, 2002. **40**(1-8): p. 465-469.

[40] Assaad, J., Ravez, M., and Bruneel, C., *Application of the finite-element method for modeling backed transducers.* The Journal of the Acoustical Society of America, 1996. **100**(5): p. 3098-3103.

[41] Callens, D., Bruneel, C., and Assaad, J., *Matching ultrasonic transducer using two matching layers where one of them is glue.* Ndt & E International, 2004. **37**(8): p. 591-596.

[42] Hill, R. and El-Dardiry, S.M., *A theory for optimization in the use of acoustic emission transducers.* The Journal of the Acoustical Society of America, 1980. **67**(2): p. 673-682.

[43] Lockwood, G.R. and Foster, F.S., *Modeling and optimization of high-frequency ultrasound transducers.* IEEE transactions on ultrasonics, ferroelectrics, and frequency control, 1994. **41**(2): p. 225-230.

[44] Wilcox, P., Monkhouse, R., Cawley, P., Lowe, M., and Auld, B., *Development of a computer model for an ultrasonic polymer film transducer system.* NDT & E International, 1998. **31**(1): p. 51-64.

[45] Basaeri, H., Christensen, D.B., and Roundy, S., *A review of acoustic power transfer for biomedical implants.* Smart Materials and Structures, 2016. **25**(12).

[46] Hu, Y.-C., Liao, P.-L., Shih, W.-P., Wang, X.-Y., and Chang, P.-Z. *Study on the acoustic impedance matching of human tissue for power transmitting/charging system of implanted*

biochip. in *2009 IEEE 3rd International Conference on Nano/Molecular Medicine and Engineering*. 2009. IEEE.

[47] Denisov, A. and Yeatman, E. *Ultrasonic vs. inductive power delivery for miniature biomedical implants*. in *2010 International Conference on Body Sensor Networks*. 2010. IEEE.

[48] Song, S.H., Kim, A., and Ziaie, B., *Omnidirectional ultrasonic powering for millimeter-scale implantable devices.* IEEE Transactions on Biomedical Engineering, 2015. **62**(11): p. 2717-2723.

[49] Christensen, D.B. and Roundy, S., *Non-dimensional analysis of depth, orientation, and alignment in acoustic power transfer systems.* Smart Materials and Structures, 2018. **27**(12): p. 125013.

[50] Ozeri, S., Shmilovitz, D., Singer, S., and Wang, C.-C., *Ultrasonic transcutaneous energy transfer using a continuous wave 650 kHz Gaussian shaded transmitter*. Ultrasonics, 2010. **50**(7): p. 666-674.

[51] Seo, D., Carmena, J.M., Rabaey, J.M., Alon, E., and Maharbiz, M.M., *Neural dust: An ultrasonic, low power solution for chronic brain-machine interfaces.* arXiv preprint arXiv:1307.2196, 2013.

[52] Guillermic, R.-M., Lanoy, M., Strybulevych, A., and Page, J.H., *A PDMS-based broadband acoustic impedance matched material for underwater applications.* Ultrasonics, 2019. **94**: p. 152-157.

[53] Kunkel, H., Locke, S., and Pikeroen, B., *Finite-element analysis of vibrational modes in piezoelectric ceramic disks.* IEEE Transactions on ultrasonics, ferroelectrics, and frequency control, 1990. **37**(4): p. 316-328.

[54] Guo, N., Cawley, P., and Hitchings, D., *The finite element analysis of the vibration characteristics of piezoelectric discs.* Journal of sound and vibration, 1992. **159**(1): p. 115-138.

[55] Gorostiaga, M., Wapler, M., and Wallrabe, U., *Analytic model for ultrasound energy receivers and their optimal electric loads II: Experimental validation.* Smart Materials and Structures, 2017. **26**(10): p. 105021.

[56] Kinsler, L.E., Frey, A.R., Coppens, A.B., and Sanders, J.V., *Fundamentals of acoustics.* 1999: p. 560.

[57] Selfridge, A.R., *Approximate material properties in isotropic materials.* IEEE transactions on sonics and ultrasonics, 1985. **32**(3): p. 381-394.

[58] Mark, J.E., *Physical properties of polymers handbook*. Vol. 1076. 2007: Springer.

[59] Rao, S.S., *Vibration of continuous systems*. Vol. 464. 2007: Wiley Online Library.

[60] Mellow, T. and Kärkkäinen, L., *On the sound field of an oscillating disk in a finite open and closed circular baffle.* The Journal of the Acoustical Society of America, 2005. **118**(3): p. 1311-1325.

[61] Butler, J.L. and Sherman, C.H., *Transducers and arrays for underwater sound*. 2016: Springer.

[62] Erturk, A. and Inman, D.J., *Piezoelectric energy harvesting*. 2011: John Wiley & Sons.

[63] Jacobsen, F., Moreno-Pescador, G., Fernandez-Grande, E., and Hald, J., *Near field acoustic holography with microphones on a rigid sphere (L).* The Journal of the Acoustical Society of America, 2011. **129**(6): p. 3461-3464.

[64] Sapozhnikov, O.A., Tsysar, S.A., Khokhlova, V.A., and Kreider, W., *Acoustic holography as a metrological tool for characterizing medical ultrasound sources and fields.* The Journal of the Acoustical Society of America, 2015. **138**(3): p. 1515-1532.

[65] Maynard, J.D., Williams, E.G., and Lee, Y., *Nearfield acoustic holography: I. Theory of generalized holography and the development of NAH.* The Journal of the Acoustical Society of America, 1985. **78**(4): p. 1395-1413.

[66] Veronesi, W. and Maynard, J.D., *Nearfield acoustic holography (NAH) II. Holographic reconstruction algorithms and computer implementation.* The Journal of the Acoustical Society of America, 1987. **81**(5): p. 1307-1322.

[67] Williams, E.G., *Fourier acoustics: sound radiation and nearfield acoustical holography*. 1999: Academic press.

[68] Kim, A., Zhou, J., Samaddar, S., Song, S.H., Elzey, B.D., Thompson, D.H., and Ziaie, B., *An Implantable Ultrasonically-powered Micro-Light-source (μLight) for photodynamic therapy.* Scientific reports, 2019. **9**(1): p. 1395.

[69] Whitworth, G., *Discussion of 1-D piezoelectric transducer models with loss.* IEEE transactions on ultrasonics, ferroelectrics, and frequency control, 2001. **48**(3): p. 844-846.

[70] Gorostiaga, M., Wapler, M., and Wallrabe, U., *Analytic model for ultrasound energy receivers and their optimal electric loads.* Smart Materials and Structures, 2017. **26**(8): p. 085003.

[71] https://www.americanpiezo.com/.

[72] https://www.americanpiezo.com/apc-materials/piezoelectric-properties.html.

[73] Melde, K., Mark, A.G., Qiu, T., and Fischer, P., *Holograms for acoustics.* Nature, 2016. **537**(7621): p. 518.

[74] International, A., *Handbook of materials for medical devices*. 2003: ASM international.

[75] Krimholtz, R., Leedom, D.A., and Matthaei, G.L., *New equivalent circuits for elementary piezoelectric transducers.* Electronics Letters, 1970. **6**(13): p. 398-399.

[76] Gorostiaga, M., Wapler, M., and Wallrabe, U., *Optimizing piezoelectric receivers for acoustic power transfer applications.* Smart Materials and Structures, 2018. **27**(7): p. 075024.

[77] Castillo, M., Acevedo, P., and Moreno, E., *KLM model for lossy piezoelectric transducers.* Ultrasonics, 2003. **41**(8): p. 671-679.

[78] Liu, D.-L. and Waag, R.C., *Propagation and backpropagation for ultrasonic wavefront design.* IEEE transactions on ultrasonics, ferroelectrics, and frequency control, 1997. **44**(1): p. 1-13.

[79] Krautkrämer, J. and Krautkrämer, H., *Ultrasonic testing of materials.* 1983.

[80] Wilt, K., Lawry, T., Scarton, H., and Saulnier, G., *One-dimensional pressure transfer models for acoustic–electric transmission channels.* Journal of Sound and Vibration, 2015. **352**: p. 158-173.

[81] Wells, P.N., *Ultrasonic imaging of the human body.* Reports on progress in physics, 1999. **62**(5): p. 671.

[82] Hoskins, P.R., Martin, K., and Thrush, A., *Diagnostic ultrasound: physics and equipment*. 2010: Cambridge University Press.

[83] Bloomfield, P.E., Lo, W.-J., and Lewin, P.A., *Experimental study of the acoustical properties of polymers utilized to construct PVDF ultrasonic transducers and the acousto-electric properties of PVDF and P (VDF/TrFE) films.* IEEE transactions on ultrasonics, ferroelectrics, and frequency control, 2000. **47**(6): p. 1397-1405.

[84] Kojima, T., Haya, H., Minegishi, K., and Nguyen, R.T. *Ultrasonic velocity measurement for analysis of brick structure*. in *2008 IEEE Ultrasonics Symposium*. 2008. IEEE.

[85] Philippidis, T. and Aggelis, D., *Experimental study of wave dispersion and attenuation in concrete.* Ultrasonics, 2005. **43**(7): p. 584-595.

[86] Auberger, M. and Rinehart, J.S., *Ultrasonic velocity and attenuation of longitudinal waves in rocks.* Journal of Geophysical Research, 1961. **66**(1): p. 191-199.

[87] Lamb, J. and Richter, J., *Anisotropic acoustic attenuation with new measurements for quartz at room temperatures.* Proceedings of the Royal Society of London. Series A. Mathematical and Physical Sciences, 1966. **293**(1435): p. 479-492.

[88] Lambade, S., Sahasrabudhe, G., and Rajagopalan, S., *Temperature dependence of acoustic attenuation in silicon.* Physical Review B, 1995. **51**(22): p. 15861.

[89] Rajagopal, S., Sadhoo, N., and Zeqiri, B., *Reference characterisation of sound speed and attenuation of the IEC agar-based tissue-mimicking material up to a frequency of 60 MHz.* Ultrasound in medicine & biology, 2015. **41**(1): p. 317-333.

[90] Serabian, S., *Influence of attenuation upon the frequency content of a stress wave packet in graphite.* The Journal of the Acoustical Society of America, 1967. **42**(5): p. 1052-1059.

[91] Lasjaunias, J., Saint-Paul, M., Bilušić, A., Smontara, A., Gradečak, S., Tonejc, A., Tonejc, A., and Kitamura, N., *Acoustic and thermal transport properties of hard carbon formed from C 60 fullerene.* Physical Review B, 2002. **66**(1): p. 014302.

Chapter 5

Focused ultrasound-induced stable cavitation and acoustic holograms for ultrasonic manipulation of particles

This chapter contains excerpts from an article published in *Acoustics* journal (*MDPI*) [1], and a conference paper published in *SPIE Smart Structures/Nondestructive Evaluation* proceeding [2]. In this chapter, we investigate the effects of acoustic nonlinearity on oscillations of focused ultrasound (FU)-excited microbubbles, as well as possible implementations of acoustic transmission holograms in microfluidic devices for particle manipulation.

Abstract

Many biomedical applications such as ultrasonic targeted drug delivery, gene therapy, and molecular imaging entail the problems of manipulating microbubbles by means of high-intensity focused ultrasound (HIFU) pressure field; namely stable cavitation. In the high-intensity acoustic field, bubbles demonstrate translational instability, well-known erratic dancing motion, which is caused by shape oscillations of the bubbles that are excited by their volume oscillations. The literature of bubble dynamics in the HIFU field is mainly centered on experiments, lacking a systematic study to determine the threshold for shape oscillations and translational motion. In this work, we extend the existing multiphysics mathematical modeling platform on bubble dynamics for taking account of (1) the liquid compressibility which allows us to apply high-intensity acoustic field, (2) the mutual interactions of volume pulsation, shape modes, and translational motion, as well as (3) the effects of nonlinearity, diffraction and absorption of HIFU to incorporate the acoustic nonlinearity due to wave kinematics or medium; all in one model. The effects of acoustic

nonlinearity on the radial pulsations, axisymmetric modes of shape oscillations, and translational motion of a bubble, subjected to resonance and off-resonance excitation and various acoustic pressure, are examined. The results reveal the importance of considering all the involved harmonics and wave distortion in the bubble dynamics, to accurately predict the oscillations, translational trajectories, and the threshold for inertial (unstable) cavitation. This result is of interest in understanding the bubble dynamical behaviors observed experimentally in the HIFU field. Furthermore, the use of acoustic phase holograms is investigated for microfluidic devices for possible cell and particle manipulation, which has potential applications in medical diagnostic and therapeutic ultrasound systems.

5.1 Introduction

Acoustic cavitation is categorized into two main mechanisms: stable (non-inertial) cavitation and inertial (unstable) cavitation. Stable cavitation, the focus of this research, refers to the oscillations of bubbles in size and shape about their equilibrium radius with the insonation frequency, and are accompanied by higher harmonics, in addition to the linear driving frequency component (see figure 5.1a). The inertial cavitation refers to the sudden and rapid growth of bubbles (several times their initial radius) and is accompanied by a violent collapse [3-6]. The importance of investigating stable cavitation is evident from the studies reporting that it reduces the risk of brain damage during the use of microbubbles in a focused ultrasound (FU)-induced blood-brain barrier (BBB) opening [7-9]. Furthermore, the thermal effects as well as the mechanical effects of stable cavitation, are considerably lower than that of inertial cavitation [10]. In this chapter, we consider the stable cavitation caused by the oscillations of a gas bubble under an assumption that the bubble pre-existed in the FU field and is not generated by thermal effects.

Studies have been conducted reporting the use of ultrasound in acoustic energy transfer systems [11, 12], ultrasound imaging [13, 14], and drug delivery [3, 15-17]. McDannold *et al.* [18] evaluated the feasibility of a targeted drug delivery method for brain tumors (such as glioma) treatment. The method utilizes a FU system to disrupt the BBB temporarily with the help of an intravenous microbubble agent. Acoustic waves can be focused deeply into the targeted tissue for noninvasive therapeutic applications. Microbubbles which are injected into the bloodstream and exposed to FU start to oscillate (stable cavitation) due to successive compression and rarefaction cycles of the acoustic wave causing the bubbles to shrink and grow (figure 5.1a), respectively, spreading the endothelial cells apart and thus opening the BBB (figure 5.1b). Mesiwala *et al.* [19] investigated a high-intensity focused ultrasound (HIFU)-induced BBB disruption and showed that

FU is capable of opening the BBB transiently without causing significant damages to the brain architecture.

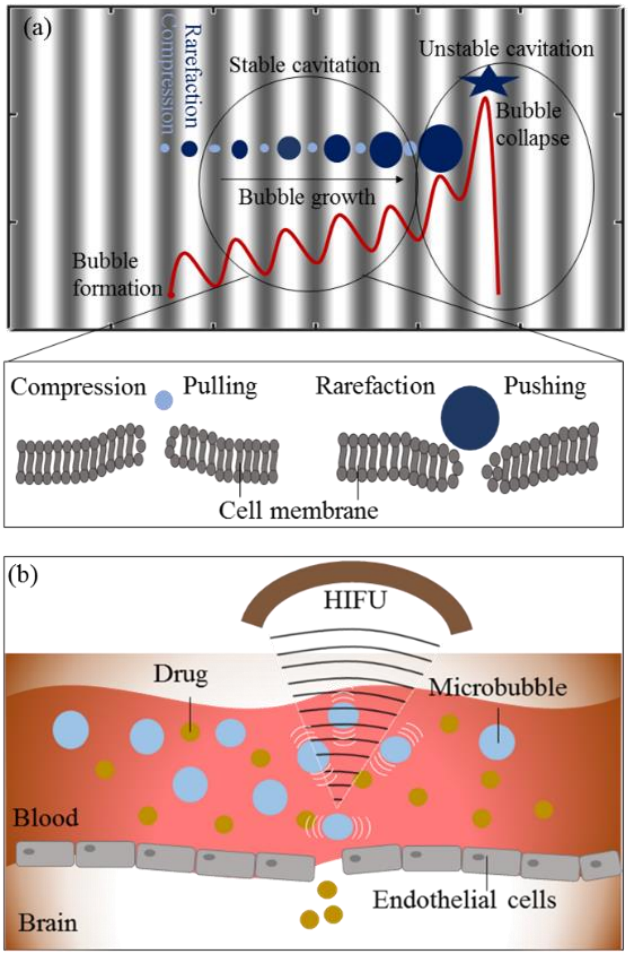

Figure 5.1. (a) Formation, growth, and collapse of an ultrasound-induced cavitated bubble in response to regions of positive pressure (compression; dark gray) and negative pressure (rarefaction; light gray) shown in the background; our study focuses only on the stable cavitation regions, and (b) FU-induced stable cavitation mechanism for opening the blood-brain barrier.

HIFU transducers can deliver therapeutic energy locally to targeted tissues and generate a lesion for selective tissue necrosis in the treatment of fibroid and tumors such as a prostate tumor, liver tumor, pancreatic tumor, and breast tumor [20]. Nonlinearities imposed by the acoustic wave propagation and cavitation can accelerate the lesioning process and therefore enhance the HIFU therapy, such as in hemostasis [21]; the distortion and migration of the lesion toward the transducer are caused by bubbles [22]. On the other hand, when the predetermined size and position of the lesion is needed, the lesion distortion can hinder the therapeutic process [23]. Boiling is a way of bubble formation (vapor bubbles) due to the elevated temperature (thermally generated bubbles),

whereas cavitation (gas bubbles) can be considered as mechanically generated bubbles [24]. Bailey *et al.* [25] examined the role of gas and/or vapor bubbles in a HIFU lesion using overpressure conditions in their experiments and found that the bubbles contribute to the lesion distortion. Kennedy [26] provided a comprehensive review detailing the use of clinical HIFU in the treatment of solid tumors with the help of bubbles in cell necrosis. Vaezy *et al.* [27] implemented a HIFU transducer to monitor the ultrasound treatment. They speculated the existence of bubbles in an observed hyperechoic region at the focal point of the transducer.

The study of gas bubble dynamics during FU insonation has been the subject of interest in many applications such as medical fields in diagnostic and therapeutic procedures [3, 23, 26]. In diagnostic applications, ultrasound-activated microbubbles are used as contrast agents in ultrasound scatter imaging methods. Acoustic image guidance benefits from microbubbles since the nonlinear response of the bubbles in a FU field produces a strong backscattered pressure. As an example, microbubbles can be injected into the bloodstream in which the healthy areas are determined by bright, colorful signals (hyperechoic region), and the blood clot (necrosed tissue) is diagnosed by negative contrast [23, 28, 29]. In the therapeutic ultrasound, acoustic cavitation is one of the main physical mechanisms to enhance the treatment of several diseases and for tumor ablation. Ultrasound microbubble-based therapeutic approaches include enhanced gene delivery and localized active drug delivery into the eye or through the skin, lipoplasty (a surgical operation that removes excessive or undesirable fat from many different sites on the human body), phacoemulsification (a modern cataract surgery), lithotripsy [30] (kidney stone removal), and brain tumor surgery [31]. Other examples include hemostasis (a process to stop bleeding), histotripsy [32, 33] (a non-thermal tissue ablation method for the treatment of malignant diseases such as liver cancer) as well as muscle and bone therapies.

The early observations of single-bubble sonoluminescence by Barber and Putterman [34] and Gaitan *et al.* [35] motivated researches to study the fundamentals of the coupled dynamics of ultrasonic cavitated gas bubbles spanning a wide range of nonlinear and multiphysics processes. A gas bubble excited by acoustic pressure moves either toward or away from the pressure antinode. When the amplitude of acoustic pressure approaches a threshold value (in the high-intensity field), the ultrasound excited bubble begins to translate erratically. This phenomenon is called dancing motion which is of great importance in many applications such as cell sorting [36-38]. A brief review of the literature of the spherical bubble dynamics in a standing wave provides examples of proof-of-concept demonstrations. After initial investigations by Gaines [39] and Kornfeld and

Suvorov [40], Eller and Crum [41] reported that the parametrically excited mode shape oscillations of a gas bubble caused by its radial pulsation in a standing sound wave leads to its translational instability [42] and hence dancing motion. To the best of authors' knowledge, Doinikov in 2002 [43], presented the comprehensive mathematical model for analyzing the translational motion of a spherical bubble in a high-intensity acoustic field. He modified the equation of radial motion to allow for the effects of acoustic medium compressibility. However, in this model [43], the interaction between the shape modes and translational motion was not investigated for a high-intensity field. In a later work in 2004, Doinikov [44] presented a mathematical model for the translational motion of a bubble undergoing shape oscillations while the effects of liquid compressibility are ignored. In addition, in none of the abovementioned works which employ high intensity ultrasound, the effects of finite-amplitude sound and nonlinear acoustics are incorporated. In HIFU, as a monochromatic finite-amplitude ultrasound wave is slanted during its propagation in time and space, higher harmonics of its fundamental frequency appear. Additional phenomena including shock formation, acoustic streaming (a large scale flow in a viscous fluid [45, 46]), and acoustic saturation (the point at which the medium can no longer absorb any more energy from the wave) may take place. The wave distortion has local and cumulative effects due to localized pressure and temperature changes, that must be considered in the bubble dynamics simulations.

In this work, we extend Doinikov's works [43, 44] to take account of (1) the liquid compressibility which allow us to apply high-intensity acoustic field, (2) the mutual interactions of volume pulsation, shape modes (up to four modes) and translation motion, and (3) the effects of nonlinearity, diffraction and absorption of HIFU to incorporate the acoustic nonlinearity due to wave kinematics or medium; all in one model. The results aim to show that the radial response and onset of erratic dancing motion of the bubble are not dependent only on the pressure amplitude but also on the harmonic components of the excitation. This feature differentiates the research in this chapter from all previous studies where nonlinearity in the excitation acoustic domain was not considered.

In all other previous modeling efforts to predict bubble dynamics [28, 47-49], the wave kinematics and simulating the nonlinear focused acoustic waves were not taken into consideration. However, developing an approach based on the equations of continuum mechanics is of utmost importance to accurately incorporate the effects of acoustic nonlinearity, diffraction, and absorption; those strongly affect the acoustic wave propagation such as waveform distortion and change of pressure amplitude. The presence of higher harmonics due to the transfer of energy from a fundamental

component to higher harmonic components and distortion of waveform characterizes a nonlinear wave [17]. The localization of the fundamental pressure field as well as the harmonics at the focal point is essential in evaluating the acoustic and thermal effects of nonlinear propagation of FU on the dynamics of stable cavitation; the amount of energy deposition is directly proportional to frequency-dependent absorption and higher harmonics associated with the FU. Thus, stronger nonlinear effects lead to the stronger and higher number of harmonics creating enhanced localized energy deposition and therefore enhanced pressure amplitude and temperature rise in the medium surrounding the bubble. In diagnostic and therapeutic ultrasound applications, the precise prediction of acoustic wave propagation and pressure amplitude is of great importance. Moreover, to reduce the risk of tissue damage, for example, if a clinical practice is intended to avoid the violent collapse of bubbles, the resultant acoustic waves from FU transducers should be precisely modeled and analyzed. In this work, the results show the importance of incorporating all the involved harmonics and wave distortion in the bubble dynamics for accurately predicting the oscillations and translational trajectories, the onset of translational instabilities, and the threshold for inertial (unstable) cavitation. The results will be of interest in understanding the bubble dynamical behaviors observed experimentally in the HIFU field.

The two common models used for simulating focused acoustic waves are Khokhlov-Zabolotskaya-Kuznetsov (KZK) and Westervelt equations [50-52]. In both models, the approach is based on the equations of continuum mechanics. In this work, the KZK equation is chosen to model the acoustic field of FU to reduce the computational cost. We adopt the hybrid time-frequency approach using operator-splitting technique [53], which accounts for the three effects of nonlinearity, diffraction, and absorption separately at every integration step (a linear analytical model for the pressure field due to focused transducers without including any nonlinear effects is also given by Bhargava *et al.* [17]). In our analysis, blood is chosen as an acoustic medium and different input parameters (such as input acoustic power and frequency) are selected to investigate the effects of nonlinearities imposed by the FU field.

Following the work done by Doinikov [44], bubble dynamics based on the Keller-Miksis model is adapted in which a second-order nonlinear mathematical model is employed to include high-intensity acoustic excitation of the bubble [54]. Temporal waveform data obtained from the KZK equation is used to fit a Fourier series expansion and given as an input into the single-bubble dynamics equations. The nonlinear coupling between the radial pulsation, shape modes (up to fourth modes of oscillations), and translational motion of the oscillating bubble are analyzed and

compared in linear and nonlinear pressure fields. In this chapter, we investigate a multiphysics model that incorporates the FU field as an input parameter into the bubble dynamics equations. The proposed model accounts for nonlinearities caused by the acoustic field as well as the bubble's oscillations. We have also studied the scattered pressure in the far-field liquid domain originating from the bubble oscillations (acoustic streaming effect) in the FU field and various ranges of frequency [2].

This chapter is organized as follows. In section 5.2, we describe a multiphysics KZK-Keller-Miksis theoretical model that interconnects the nonlinear acoustic field from a FU transducer to the dynamics of a single microbubble at the focal point. In addition, the numerical solution is presented. In section 5.3, we present the numerical results which entail the linear and nonlinear input acoustic pressure waveforms along with the corresponding bubble volume oscillations, shape modes, and translational motion for the varying frequency of excitation (section 5.3.1) and the input power to the focused transducer, which generates various input pressure at a fixed frequency (section 5.3.2). Moreover, in section 5.4, the possible use of acoustic transmission holograms for cell sorting and patterning in microfluidic channels is investigated and the conclusions are summarized in section 5.5.

5.2. Theoretical models for FU-excited microbubbles

5.2.1 Nonlinear acoustic pressure from FU transducer

The KZK equation is used to predict the nonlinear acoustic pressure field generated by a FU transducer in thermoviscous fluid domains, solved by a numerical approach. This model incorporates diffraction, absorption, and nonlinearity in the parabolic wave equation. In cylindrical coordinates, the KZK equation for an axisymmetric sound beam propagating in the axial direction (positive *z*) is given as [55-57]

$$\frac{\partial^2 p_{ex}}{\partial z \partial t'} = \frac{c}{2}\nabla_{\perp}^2 p_{ex} + \frac{\delta}{2c^3}\frac{\partial^3 p_{ex}}{\partial t'^3} + \frac{\beta}{2\rho c^3}\frac{\partial^2 {p_{ex}}^2}{\partial t'^2}, \tag{5.1}$$

where p_{ex} is external acoustic pressure, *z* is the distance in the axial direction, $t' = t - z/c$ is the retarded time, *c* is the small-signal sound speed in a fluid medium, and ρ is the ambient density of the fluid. The first term on the right-hand side of equation (5.1) represents diffraction, the second term signifies absorption with δ as the diffusivity of sound and nonlinearity is given by the third term, where $\beta = 1 + B/2A$ is the coefficient of nonlinearity and B/A is defined as the parameter

of nonlinearity. The transverse Laplacian operator is given as $\nabla_{\perp}^2 = \partial^2 / \partial r^2 + (1/r)\partial / \partial r$, where r is the transverse radial coordinate.

The focused source condition is given as $p_{ex} = p_0\, f(r, t + r^2/2cd)|_{z=0,\, r \le a}$ [58], where p_0 is the characteristic source pressure calculated as $p_0 = [2\rho c P / \pi(a^2 - b^2)]^{1/2}$, d is the focal length, a and b are the characteristic inner and outer radius of the sound source, respectively (shown in figure 5.2), and P is the input acoustic power. The function $f(r, t + r^2/2cd)$ indicates the dependence of source condition on time as a function of the radial coordinate.

A dimensionless form of the KZK equation is written as [59]

$$\frac{\partial^2 \bar{p}_{ex}}{\partial \tau\, \partial \bar{z}} = \left(\frac{1}{4G} \nabla_{\bar{r}}^2 + \bar{A} \frac{\partial^3}{\partial \tau^3} \right) \bar{p}_{ex} + \frac{N}{2} \frac{\partial^2 \bar{p}_{ex}^{\,2}}{\partial \tau^2}, \tag{5.2}$$

where $\bar{p}_{ex} = p_{ex} / p_0$ is a dimensionless pressure and $\bar{z} = z/d$ is a dimensionless form of propagation distance. The retarded time is nondimensionalized with angular source frequency ω as $\tau = \omega(t - z/c)$. Dimensionless parameter G, N, and $\bar{A}$ account for focusing gain, nonlinearity, and absorption, respectively. The parameter $G = z_0 / d$ is the linear focusing gain, where $z_0 = \omega a^2 / 2c$ is the Rayleigh distance. The term nonlinearity is $N = d / z_s$, where $z_s = \rho c^3 / \beta \omega p_0$ is the plane-wave shock formation distance. Furthermore, the parameter $\bar{A}$ is defined as $\bar{A} = \alpha d$, where $\alpha = \delta \omega^2 / 2c^3$ is the thermoviscous attenuation coefficient. The dimensionless form of transverse Laplacian operator is given as $\nabla_{\bar{r}}^2 = \partial^2 / \partial \bar{r}^2 + (1/\bar{r})\partial / \partial \bar{r}$, where $\bar{r} = r/a$. The dimensionless source condition becomes $\bar{p}_{ex} = f(\bar{r}, \tau + G\bar{r}^2)|_{\bar{z}=0}$, which is valid under the following three assumptions: $\sin^2\phi << 2$, $G << 8\pi / \sin^2\phi$, and $1 << k\,a << 16\pi / \sin^3\phi$ [59, 60], where $k = \omega / c$ is the wave number. Here ϕ is the half aperture angle (figure 5.2) and $\sin\phi = a/d$. While the first assumption is a relatively weak restriction which requires the half aperture angle to be less than 25°, the other two are analogous and restrict the maximum focusing gain for a given aperture angle. Therefore, the given assumptions limit the domain of validity of the KZK equation for a focused transducer. Since, the transducers geometries used for our study satisfy the aforementioned conditions, the KZK equation is used to predict the FU acoustic pressure field applied on the surface of the bubble.

In equation (5.2), the diffraction is included by the equation

$$\frac{\partial \overline{p}_{ex}}{\partial \overline{z}} = \frac{1}{4G} \int_{-\infty}^{\tau} \left(\nabla_{\bar{r}}^2 \overline{p}_{ex} \right) d\tau'. \tag{5.3}$$

Equation (5.3) is solved numerically using a finite-difference numerical approach to take into account the diffraction effects in the KZK equation. Absorption refers to the thermoviscous attenuation of the waves as they propagate through a medium leading to loss of energy of the wave. The KZK equation includes the absorption by the equation

$$\frac{\partial \overline{p}_{ex}}{\partial \overline{z}} = \overline{A} \frac{\partial^2 \overline{p}_{ex}}{\partial \tau^2}, \tag{5.4}$$

where $\overline{A}$ depends on the attenuation coefficient. The attenuation follows a power-law dependence on frequency given as [61, 62]

$$\alpha(\omega) = \alpha_0 \omega^{\nu}, \tag{5.5}$$

where α_0 and ν are empirical constants, with the value of ν typically given as $0 < \nu \leq 2$.

Nonlinearity results from variations of the pressure with variations of the density in a medium. The nonlinearity parameter B/A can also be expressed in terms of variations in the speed of sound. In nonlinear acoustics, as the wave propagates, waveform peaks may travel faster than troughs, thus distorting and steepening the profile of the wave.

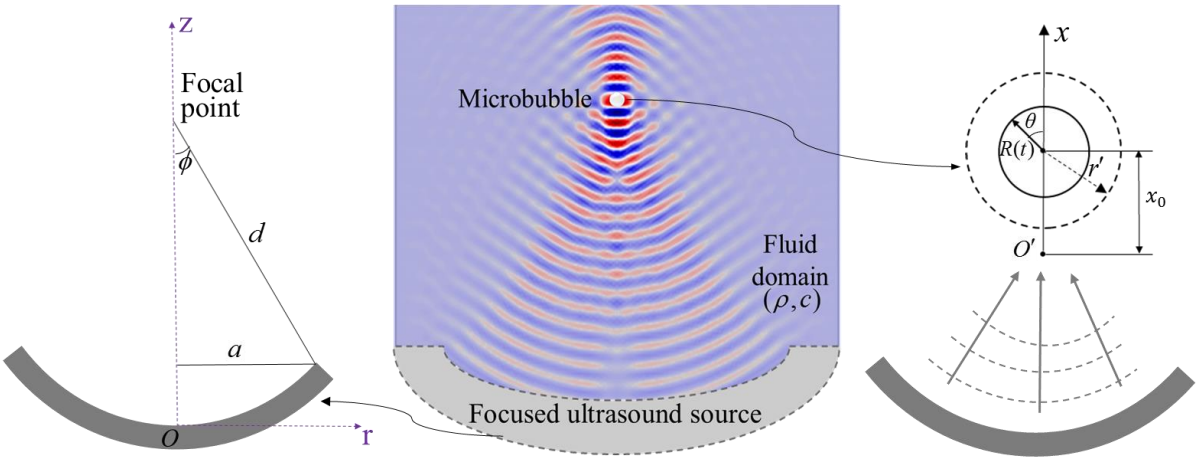

Figure 5.2. Schematic representation of acoustic waves from a focused source to a bubble at the focal point.

The equation of state $p = p_{ex}(\rho, s)$ is expressed by Taylor series expansion as follows [51]

$$p = p_0 + A\left(\frac{\rho - \rho_0}{\rho_0}\right) + \frac{B}{2}\left(\frac{\rho - \rho_0}{\rho_0}\right)^2 + ..., \tag{5.6}$$

where *p* is the pressure, *s* is the specific entropy, p_0 and ρ_0 represent the pressure and density in the unperturbed state, respectively. The values of *A* and *B*, which are the coefficients of first and second-order terms of equation (5.6), are obtained as $A = \rho_0(\partial p / \partial \rho)|_{\rho=\rho_0, s=s_0} \equiv \rho_0 c^2$ and $B = \rho_0{}^2(\partial^2 p / \partial \rho^2)|_{\rho=\rho_0, s=s_0}$, where s_0 indicates that equation (5.6) is carried out in an isentropic process. Consequently, the nonlinearity parameter B/A is written as $B/A = \rho_0 / c^2(\partial^2 p / \partial \rho^2)|_{\rho=\rho_0, s=s_0}$ and alternative expression of B/A yields $B/A = 2\rho_0 c(\partial c / \partial p)\big|_{\rho=\rho_0, s=s_0}$. In equation (5.2), the parameter N integrates β into the KZK equation. Thus, the nonlinearity term in the KZK equation, while neglecting the diffraction and absorption effects, is expressed as

$$\frac{\partial \overline{p}_{ex}}{\partial \overline{z}} = \frac{N}{2}\frac{\partial \overline{p}_{ex}{}^2}{\partial \tau}. \tag{5.7}$$

Equation (5.7) has its origin in a simpler model known as the lossless Burger's equation [63]. The KZK equation is an augmentation to the Burger's equation, in which it comprises the diffraction, absorption, and nonlinearity effects in a focused acoustic field. The numerical method applied in this work, to solve the KZK equation, is based on the split-step method [64] employed in MATLAB® (2016a, Mathworks, Natick, MA, USA). In this method, the linear parts (equations (5.3) and (5.4)) and nonlinear term (equation (5.7)) are integrated separately. At each integration, the linear parts are calculated in the frequency-domain and then the solution is converted to the time-domain using the fast Fourier transform algorithm to solve the nonlinear part of the KZK equation. After integration, the result is again transformed into the frequency-domain. This method is repeated for each of the harmonics used in the solution.

To convert the KZK equation to frequency-domain representation, a time-harmonic representation of the pressure field is expressed as [65, 66]

$$p_{ex}(r, z, t) = \frac{p_0}{2}\sum_{n=1}^{\infty}\left[u_n(\overline{r}, \overline{z})e^{in\omega t} + u_n{}^*(\overline{r}, \overline{z})e^{-in\omega t}\right], \tag{5.8}$$

where u_n is the dimensionless complex pressure corresponding to *n*th harmonic and u_n^* is the conjugate of dimensionless complex pressure. After substituting equation (5.8) into equation (5.2), the dimensionless KZK equation becomes

$$\frac{\partial u_n}{\partial \bar{z}} + \frac{i}{4nG}\nabla_{\bar{r}}^2 u_n + \Upsilon_n u_n = \frac{inN}{4}\sum_{m=1}^{\infty} u_m \left(u_{n-m} + 2u^*_{m-n}\right), \tag{5.9}$$

where Υ_n is a complex number representing both absorption and sound velocity dispersion. Equation (5.9) accounts for the frequency-domain representation of the dimensionless KZK equation. The real part of Υ_n is proportional to the absorption parameter, which follows the frequency-dependent power law (equation (5.5)). The imaginary part of Υ_n accounts for dispersion (phase velocity) effects. The dispersion effects are necessary to maintain the causality of the system and are determined using Kramers-Kronig relations as [67]

$$\frac{1}{c_0} - \frac{1}{c(\omega)} = \frac{2}{\pi}\int_{\omega_0}^{\omega} \frac{\alpha(\omega')}{\omega'^2}\, d\omega', \tag{5.10}$$

where c_0 is the sound velocity at reference frequency ω_0 and $c(\omega)$ represents the phase velocity. Equation (5.10) takes into account the local generalized ultrasonic attenuation-dispersion relations. As a result, the linear part of equation (5.9), written as $\partial u_n / \partial \bar{z} + (i/4nG)\nabla_{\bar{r}}^2 u_n + \Upsilon_n u_n = 0$ is solved in frequency-domain while the remaining nonlinear term is solved in time-domain as mentioned earlier. The boundary conditions, which satisfy parabolic approximations of a spherically converging harmonic wave having a uniform pressure distribution, are given as $\bar{p}_{ex}(\bar{r}, 0, \tau) = f(\bar{r}, \tau + G\bar{r}^2)$ and $\partial \bar{p}_{ex} / \partial \bar{r}\,|_{\bar{r}=0} = \bar{p}_{ex}(\bar{r} \to \infty, \bar{z}, \tau) = 0.$

Soneson and Myers [65] proposed criteria to determine cases for which nonlinear effects can be neglected without significant errors to improve computing efficiency in time-domain. The criteria use attenuation, nonlinearity parameter, and linear focusing gain to determine a cutoff value and decide if the linear model is sufficient for the analysis. Thus, in this work, before the model computes for nonlinearity, a threshold cutoff amplitude of the solution is determined. If the amplitude is greater than the cutoff value, then the model accounts for nonlinearity and integrates equation (5.7) using the upwind method. The number of harmonics (*n*) included in the model is given by $n = 2^k$, where *k* is an integer. To accurately model nonlinear effects, $k \geq 6$ is used. To solve in frequency-domain, second-order, diagonally-implicit Runge-Kutta (DIRK) and Crank-Nicolson (CN) method, which is based on trapezoidal rule [68] are used. The second-order DIRK

method is used in the near-field in the boundary layer while the CN method is used in the far-field region [64].

5.2.2 Single-bubble dynamics in a FU field

The surface of a spherical gas bubble, assuming axisymmetric deformations (with respect to the *x*-axis, figure 5.2) is defined as

$$S = r - R(t) - \sum_{n=2}^{\infty} a_n(t) P_n(\cos\theta) = 0 \tag{5.11}$$

where *r* and θ are the local spherical coordinates, originating at the center of the bubble, $R(t)$ is the time-dependent radius of the bubble corresponding to the fundamental mode, $a_n(t)$ is the time-dependent amplitude of shape modes, and P_n is the Legendre polynomial of order *n*. The dynamical equations describing the radial pulsation, translational motion, and shape oscillations of the bubble up to the fourth shape mode are derived and given as [44].

$$\left(1-\frac{\dot{R}}{c}\right)R\ddot{R}+\left(\frac{3}{2}-\frac{\dot{R}}{2c}\right)\dot{R}^2-\frac{1}{\rho}\left(1+\frac{\dot{R}}{c}\right)P_{sc}-\frac{R}{\rho c}\frac{dP_{sc}}{dt}=\frac{\dot{x}^2}{4}+H_0(t), \tag{5.12}$$

$$\left(R-\frac{7}{5}a_2\right)\ddot{x}+\left(3\dot{R}-\frac{12\dot{R}}{5R}a_2-\frac{9}{5}\dot{a}_2\right)\dot{x}+\frac{2}{\rho}A_1=H_1(t)-\frac{18\mu\dot{x}}{\rho R}, \tag{5.13}$$

$$R\ddot{a}_2+3\dot{R}\dot{a}_2+\left(\frac{12\sigma}{\rho R^2}-\ddot{R}\right)a_2+\frac{3}{\rho}A_2=-\frac{9}{4}\dot{x}^2+H_2(t)+I_2(t), \tag{5.14}$$

$$R\ddot{a}_3+3\dot{R}\dot{a}_3+\left(\frac{40\sigma}{\rho R^2}-2\ddot{R}\right)a_3+\frac{4}{\rho}A_3=H_3(t)+I_3(t), \tag{5.15}$$

$$R\ddot{a}_4+3\dot{R}\dot{a}_4+\left(\frac{90\sigma}{\rho R^2}-3\ddot{R}\right)a_4+\frac{5}{\rho}A_4=H_4(t)+I_4(t), \tag{5.16}$$

where P_{sc} accounts for scattered pressure in the surface of the bubble, which is expressed as

$$P_{sc}=\left(P_0+\frac{2\sigma}{R_0}\right)\left(\frac{R_0}{R}\right)^{3\gamma}-\frac{2\sigma}{R_0}-P_0-A_0-\frac{4\mu\dot{R}}{R}, \tag{5.17}$$

where the coefficient A_0 represents the external acoustic pressure and the coefficients $A_n(n=1,...,4)$ indicate the acoustic excitations of the shape modes owing to the radial pulsation of the bubble. Moreover, P_0 is the ambient (hydrostatic) pressure, σ is the surface tension of the

infinite incompressible host liquid medium, μ is the dynamic viscosity of the liquid, γ is the specific heat ratio of the gas within the bubble, and $\dot{x} = v,$ which is the translational velocity of the bubble.

It should be noted that the left-hand side of equation (5.12) originates from the well-known dynamical model of bubble oscillation called Rayleigh-Plesset equation [69], which is written as follows

$$R\ddot{R} + \frac{3}{2}\dot{R}^2 - \frac{1}{\rho}P_{sc} = \frac{\dot{x}^2}{4} + H_0(t). \tag{5.18}$$

However, it is observed that a high-intensity acoustic field leads to nonlinear oscillations of a bubble with a higher amplitude. As a result, the radial velocity of the bubble can no longer be assumed small compared to the speed of sound in the liquid. Moreover, the effects of liquid compressibility in nonlinear and high-intensity oscillations of the bubble must be taken into consideration. To account for the aforementioned effects and acoustic radiation, the left-hand side of equation (5.18) is replaced by the Keller-Miksis model [70] (equation (5.12)).

Furthermore, the functions $H_n(\mathrm{t})$ $(n = 0,1,...4)$ and $I_n(t)$ $(n = 2,3,4)$ are defined as follows

$$\begin{aligned} H_0(t) = {} & \frac{1}{30}\left(\frac{8\dot{R}^2}{R^2}a_2^2 - 6a_2\ddot{a}_2 + \frac{8\dot{R}}{R}a_2\dot{a}_2 - 7\dot{a}_2^2\right) + \frac{1}{56}\left(\frac{12\dot{R}^2}{R^2}a_3^2 - 8a_3\ddot{a}_3 + \frac{12\dot{R}}{R}a_3\dot{a}_3 - 9\dot{a}_3^2\right) \\ & + \frac{1}{90}\left(\frac{16\dot{R}^2}{R^2}a_4^2 - 10a_4\ddot{a}_4 + \frac{16\dot{R}}{R}a_4\dot{a}_4 - 11\dot{a}_4^2\right) - \frac{3\gamma\left(P_0 + \frac{2\sigma}{R_0}\right)R_0^{3\gamma}}{\rho R^{3\gamma+2}}\left(\frac{a_2^2}{5} + \frac{a_3^2}{7} + \frac{a_4^2}{9}\right), \end{aligned} \tag{5.19}$$

$$\begin{aligned} H_1(t) = {} & \frac{3}{35}\left[4\left(\frac{\ddot{R}}{R} + \frac{3\dot{R}^2}{R^2}\right)a_2a_3 + 2\ddot{a}_2a_3 - 3a_2\ddot{a}_3 + \frac{12\dot{R}}{R}\left(\dot{a}_2a_3 + a_2\dot{a}_3\right) - 3\dot{a}_2\dot{a}_3\right] \\ & + \frac{1}{21}\left[6\left(\frac{\ddot{R}}{R} + \frac{3\dot{R}^2}{R^2}\right)a_3a_4 + 3\ddot{a}_3a_4 - 4a_3\ddot{a}_4 + \frac{18\dot{R}}{R}\left(\dot{a}_3a_4 + a_3\dot{a}_4\right) - 3\dot{a}_3\dot{a}_4\right], \end{aligned} \tag{5.20}$$

$$
\begin{aligned}
H_2(t) = {} & \frac{2}{7}\left(\frac{2\dot{R}^2}{R^2}a_2^2 + \frac{2\dot{R}}{R}a_2\dot{a}_2 - \dot{a}_2^2\right) \\
& + \frac{2}{21}\left[8\left(\frac{\ddot{R}}{R} + \frac{2\dot{R}^2}{R^2}\right)a_2a_4 + 7\ddot{a}_2a_4 - 3a_2\ddot{a}_4 + \frac{20\dot{R}}{R}\left(\dot{a}_2a_4 + a_2\dot{a}_4\right) + \dot{a}_2\dot{a}_4\right] \\
& + \frac{1}{42}\left[\left(\frac{4\ddot{R}}{R} + \frac{23\dot{R}^2}{R^2}\right)a_3^2 + 2a_3\ddot{a}_3 + \frac{35\dot{R}}{R}a_3\dot{a}_3 - \frac{13}{4}\dot{a}_3^2\right] \\
& + \frac{8}{693}\left[\left(\frac{10\ddot{R}}{R} + \frac{41\dot{R}^2}{R^2}\right)a_4^2 + 5a_4\ddot{a}_4 + \frac{71\dot{R}}{R}a_4\dot{a}_4 - \dot{a}_4^2\right],
\end{aligned}
\tag{5.21}
$$

$$
\begin{aligned}
H_3(t) = {} & \frac{2}{15}\left(\frac{9\dot{R}^2}{R^2} - \frac{\ddot{R}}{R}\right)a_2a_3 + \frac{4}{15}\ddot{a}_2a_3 + \frac{2\dot{R}}{5R}\left(\dot{a}_2a_3 + a_2\dot{a}_3\right) - \frac{3}{5}\dot{a}_2\dot{a}_3 - \frac{1}{15}a_2\ddot{a}_3 \\
& + \frac{2}{11}\left(\frac{\ddot{R}}{R} + \frac{7\dot{R}^2}{R^2}\right)a_3a_4 + \frac{3}{11}\ddot{a}_3a_4 + \frac{10\dot{R}}{11R}\left(\dot{a}_3a_4 + a_3\dot{a}_4\right) - \frac{1}{11}\dot{a}_3\dot{a}_4,
\end{aligned}
\tag{5.22}
$$

$$
\begin{aligned}
H_4(t) = {} & -\frac{1}{35}\left[16\left(\frac{3\ddot{R}}{R} + \frac{2\dot{R}^2}{R^2}\right)a_2^2 + 6a_2\ddot{a}_2 + \frac{176\dot{R}}{R}a_2\dot{a}_2 + 71\dot{a}_2^2\right] \\
& + \frac{8}{77}\left[2\left(\frac{6\dot{R}^2}{R^2} - \frac{\ddot{R}}{R}\right)a_2a_4 + 5\ddot{a}_2a_4 - a_2\ddot{a}_4 + \frac{3\dot{R}}{R}\left(\dot{a}_2a_4 + a_2\dot{a}_4\right) - 6\dot{a}_2\dot{a}_4\right] \\
& + \frac{9}{616}\left[4\left(\frac{9\dot{R}^2}{R^2} - \frac{4\ddot{R}}{R}\right)a_3^2 + 8a_3\ddot{a}_3 - \frac{12\dot{R}}{R}a_3\dot{a}_3 - 27\dot{a}_3^2\right] \\
& + \frac{9}{1001}\left[\frac{8\dot{R}^2}{R^2}a_4^2 + 2a_4\ddot{a}_4 + \frac{8\dot{R}}{R}a_4\dot{a}_4 - \dot{a}_4^2\right],
\end{aligned}
\tag{5.23}
$$

$$
I_2(t) = \frac{9}{14}\left(\frac{6\dot{R}}{R}a_3\dot{x} + 4a_3\ddot{x} + 5\dot{a}_3\dot{x}\right), \tag{5.24}
$$

$$
I_3(t) = \frac{2}{9}\left(\frac{24\dot{R}}{R}a_4\dot{x} + 17a_4\ddot{x} + 21\dot{a}_4\dot{x}\right) - \frac{6}{5}\left(\frac{4\dot{R}}{R}a_2\dot{x} + a_2\ddot{x} + 5\dot{a}_2\dot{x}\right), \tag{5.25}
$$

$$
I_4(t) = -\frac{5}{14}\left(\frac{18\dot{R}}{R}a_3\dot{x} + 4a_3\ddot{x} + 21\dot{a}_3\dot{x}\right). \tag{5.26}
$$

It should be pointed out that the equations of motion are derived up to the second-order terms due to the fact that amplitudes of the surface modes are assumed to be small compared to its radius [71]. For simplicity, the time dependency of R, a_n, x, and A_n is excluded in the equations. The coefficients A_n are calculated based on equations (5.27)-(5.30) [44].

$$P_{ac}\,|_S = \sum_{n=0}^{\infty} A_n(t) P_n(\cos\theta), \tag{5.27}$$

where $P_{ac}\,|_S$ accounts for external acoustic pressure applied on the surface of the bubble. The external acoustic pressure originating from the plane sanding wave at any arbitrary point in the surrounding liquid is calculated from

$$P_{ac} = -p_{ex}\cos(kx + k.r'), \tag{5.28}$$

where

$$\cos(kx + k.r') = \frac{1}{2}\sum_{n=0}^{\infty}(2n+1) i^n j_n(kr')\left[\exp(ikx) + (-1)^n \exp(-ikx)\right] P_n(\cos\theta) \tag{5.29}$$

and P_a is the amplitude of driving acoustic pressure, ω is the angular driving frequency, and $k = 2\pi/\lambda$ is the wave number, where λ is the wavelength. The wavelength is expressed as $\lambda = c/f$, where f is the excitation frequency. Here, $x(t)$ is the distance between the center of the bubble to the nearest acoustic pressure antinode $(x = 0)$, r' defines the position vector originated at the center of the bubble and x_0 denotes the initial position of the bubble centroid (figure 5.2).

Substituting equation (5.28) into equation (5.27) at $r' = R(t)$, one obtains the coefficients $A_n(t)$ as follows

$$A_n(t) = -\frac{1}{2}(2n+1) i^n j_n(kR)\left[\exp(ikx) + (-1)^n \exp(-ikx)\right] p_{ex}, \tag{5.30}$$

where j_n is the spherical Bessel function of order *n*.

To incorporate p_{ex} from FU transducer into equations (5.28) and (5.30), temporal waveform data from the KZK equation is used to fit a Fourier series expansion. In our study, we assume that the bubble is located at the focal point. The corresponding Fourier series for p_{ex}, which is a sum of sine and cosine functions and forms a periodic signal, can be described by

$$p_{ex} = X_0 + \sum_{i=1}^{n} X_i \cos(i\omega t) + Y_i \sin(i\omega t), \tag{5.31}$$

where X_0, X_i, and Y_i are the Fourier constant coefficients. Using Curve Fitting toolbox in MATLAB®, we obtain the Fourier coefficients in equation (5.31) for the linear and nonlinear pressure fields.

5.3 Numerical results for FU-excited microbubbles

In this section, a comprehensive numerical investigation is carried out to analyze the effects of nonlinear ultrasonic pressure due to the change of frequency and input transducer power, at the focal point, on the bubble dynamics. We investigate the dependence of the bubble dynamics, including the bubble growth and its translational motion on the imposed acoustic pressure. Although there have been considerable theoretical and experimental studies concerning the radial oscillation and translational motion of a bubble in an acoustic field of high intensity [28, 43, 44, 48, 49, 72], a model that incorporates the effects of nonlinearity, diffraction and absorption of FU field has not yet been investigated. Moreover, fluid compressibility and shape modes (up to four modes) are considered in this work.

In the usage of FU-excited microbubbles, focused acoustic waves are strongly affected by the mutual influences of diffraction, absorption, and nonlinearity of the medium. Therefore, investigating these effects in the focal area and the resultant FU pressure field is clearly of importance. In nonlinear acoustics, energy is transferred from a fundamental component to higher harmonic components. Generation of higher harmonics due to the increased energy transfer results in waveform steepening and distortion. The results in this section will show that the radial response of the bubble and the translational trajectories are dependent on both the pressure amplitude as well as the harmonic components of the excitation.

Figure 5.3a shows time histories of the waveform of the relative external acoustic pressure (using the KZK equation) at a focal point in the water domain with the properties defined in table 5.1, in response to harmonic excitation at $f = 3.5$ MHz and $P = 2$ W of the transducer. Comparing the results obtained from the nonlinear KZK model with the linear case in water (when $\beta = 0$), one can see a distortion of the wave profile in the nonlinear case which results in waveform steepening and that the peak amplitude of the waveforms becomes narrower and increases drastically due to the cumulative effect of stronger harmonics. Figures 5.3b and c show the relative pressure at the focal point in water ($\beta = 3.6$) for various harmonic excitation frequencies (while the input power is fixed at $P = 2$ W) and input power levels (while the excitation frequency is fixed at

$f = 3.5$ MHz), respectively. It is seen that the increase in excitation frequency leads to the rise in the number of harmonics and the significant distortion of the waveform. This occurs due to the increased speed of sound in the medium with an increase in frequency.

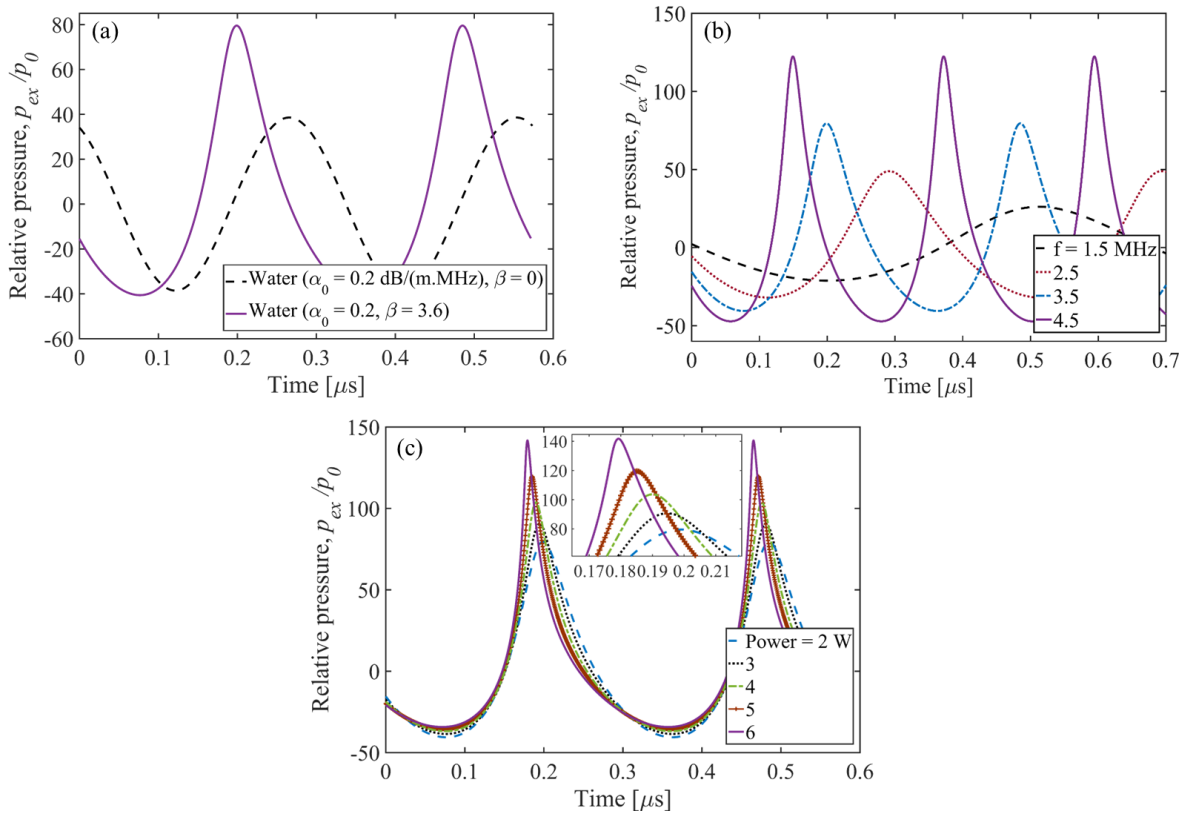

Figure 5.3. Relative pressure waveforms for (a) linear and nonlinear excitation ($f = 3.5$ MHz, $P = 2$ W), (b) for various excitation frequency ($P = 2$ W, $\beta = 3.6$), and (c) for various input power ($f = 3.5$ MHz, $\beta = 3.6$).

In figure 5.3c, as the input power is increased, the amplitudes of all the harmonics increase, which in turn adds more energy available to each harmonic and increases the amplitude of the acoustic pressure. It is inferred that with both increasing frequency and power (the inset in figure 5.3c), the peak positive pressure occurs at earlier times and that frequency plays a more significant role in inducing nonlinearity in the acoustic pressure field. The parameters of the acoustic medium (blood) used in the KZK model for single-bubble dynamics, as well as those of water, accounting for attenuation and nonlinearity effects, and the corresponding values of density and sound speed are listed in table 5.1 [73, 74]. The geometric properties of the focused transducer used in the simulations including the inner and outer radius (*a* and *b*) and focal length, *d*, are given as 25, 10, and 80 mm, respectively. The transducer is based on the case study explained by Soneson [75].

Table 5.1. Parameters of the blood and water media used in the KZK model

Parameter	Medium	
	Water	Blood
Attenuation parameter, α_0 [dB/(m.MHz)]	0.2	20
Attenuation parameter, ν	2	1.3
Coefficient of nonlinearity, β	3.6	4.1
Density, ρ [kg/m^3]	1000	1055
Sound speed, c [m/s]	1480	1570

5.3.1 Effects of excitation frequency on bubble dynamics

The numerical simulations are done assuming the bubble is excited by an external acoustic pressure at three frequencies. The excitation frequencies are selected to include fundamental resonance frequency, below and above fundamental resonance. The natural resonance frequencies of a bubble for the fundamental radial mode and axisymmetric modes of oscillations are given by [76, 77]

$$f_0 = \frac{1}{2\pi}\left(\frac{1}{R_0}\sqrt{\frac{3\gamma P_0}{\rho}+\frac{2(3\gamma-1)\sigma}{\rho R_0}}\right), \tag{5.32}$$

$$f_n = \frac{1}{2\pi}\sqrt{(n^2-1)(n+2)\frac{\sigma}{\rho R_0^{\,3}}} \quad (n=2,3,4,...), \tag{5.33}$$

where n is the number of modes. Accordingly, the value of fundamental frequency in blood domain is estimated as $f_0 = 0.5$ MHz for a gas bubble with the initial radius $R_0 = 7$ μm and the given properties, mentioned later.

To analyze the effects of change of frequency of FU excitation on single-bubble dynamics, the external acoustic pressure waveform generated by the focused transducer is obtained in the blood domain as an input parameter to the bubble dynamics. Later, based on equation (5.31), the equivalent harmonic excitation from the Fourier series expansion is derived and included in the bubble dynamics. The input acoustic pressures, considering linear and nonlinear excitations at $f = 0.3,\ 0.5$ and 3 MHz ($P = 2$ W) are illustrated in figure 5.4a. Furthermore, the corresponding frequency spectrum of nonlinear acoustic excitations, in which $\beta = 4.1$, is shown in figure 5.4b. It is observed that the nonlinearity at $f = 3$ MHz is more pronounced leading to a greater distorted

pressure waveform, which in turn gives rise to the number and strength of harmonics, predominantly in the second and third harmonics. Thus, this study is focused on involving all the harmonics in the dynamics of FU-excited microbubbles. Comparing the acoustic pressure waves in blood domain with that of obtained in water domain in [2], one can see the effects of attenuation on the pressure amplitude only at higher frequencies where the smaller value of the attenuation parameter of water, leads to higher pressure amplitude at $f = 3$ MHz; however, at $f = 0.3$ and 0.5 MHz, the amplitudes of acoustic pressure are comparable.

The coupled equations of motion, which govern radial pulsation, translational motion, and shape oscillations of a single air bubble in a free-field blood domain, are solved numerically by the program package in MATHEMATICA. The theory is given for the general case of a gas bubble in a host liquid where specific heat ratio of air in equation (5.17) and blood properties are given for the following results. The position of the bubble is set to $x_0 = 0.001\lambda$ and the surface tension and dynamic viscosity of blood are defined as $\sigma = 0.053$ N/m [78] and $\mu = 0.0035$ kg/(m.s) [79]. Also, ambient pressure is given as $P_0 = 101.3$ kPa and $\gamma = 1.4$.

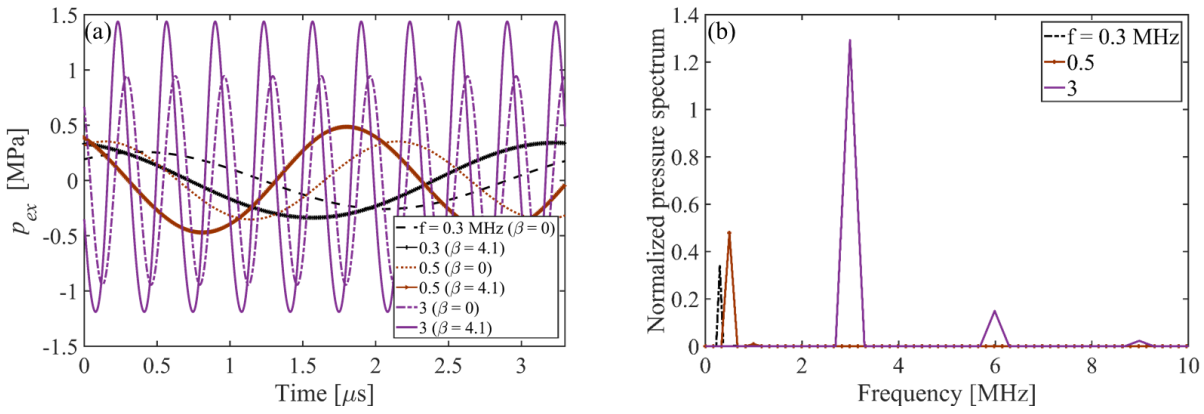

Figure 5.4. Acoustic pressure generated by the focused transducer as the input parameter to bubble dynamics at $P = 2$ W (a) for various excitation frequency; temporal waveform and (b) the corresponding Fourier spectra for $\beta = 4.1$.

The bubble dynamics under nonlinear acoustic excitation is analyzed using equations (5.12) to (5.16). The equations are nonlinearly coupled owing to functions $H_n(t)$, where $n = 0,1,2,3,4$ and $I_n(t)$, where $n = 2,3,4$. The second-order interactions of two neighboring surface modes, namely a_2 and a_3 as well as a_3 and a_4 in the term $H_1(t)$, contribute to the translational motion of the bubble (equation (5.13)). The nonlinear interactions of two neighboring surface modes are also

observed in the term $H_3(t)$, concluding that odd modes play important roles in deformations of all other modes. Similarly, the evidence of nonlinear interactions between translational motion and all other modes becomes apparent in the terms $I_n(t)$ and equations (5.12) and (5.14) due to the velocity squared term, $\dot{x}^2$. Furthermore, there are strong two-way couplings between even modes (due to the terms a_2 and a_4 in $H_2(t)$ and $H_4(t)$) which are also coupled with the radial mode as well. However, it is seen that the translational motion is mostly affected by the odd modes. Figures 5.5-5.7 show the time evolution of the amplitudes of radius and second to fourth modes of oscillations, as well as translational motion of the bubble excited by different frequencies (at resonance and off-resonance frequency) for the input power of $P = 2$ W. The corresponding linear and nonlinear acoustic pressures are given in figure 5.4a and as an example, prolonged dynamical motions of the bubble excited at $f = 3$ MHz is shown in appendix D, figure D.1. It is worthwhile to note that the bubble deformation dominates by the radial pulsation, which supports the assumption of the small amplitude of surface modes compared to the radius of the bubble.

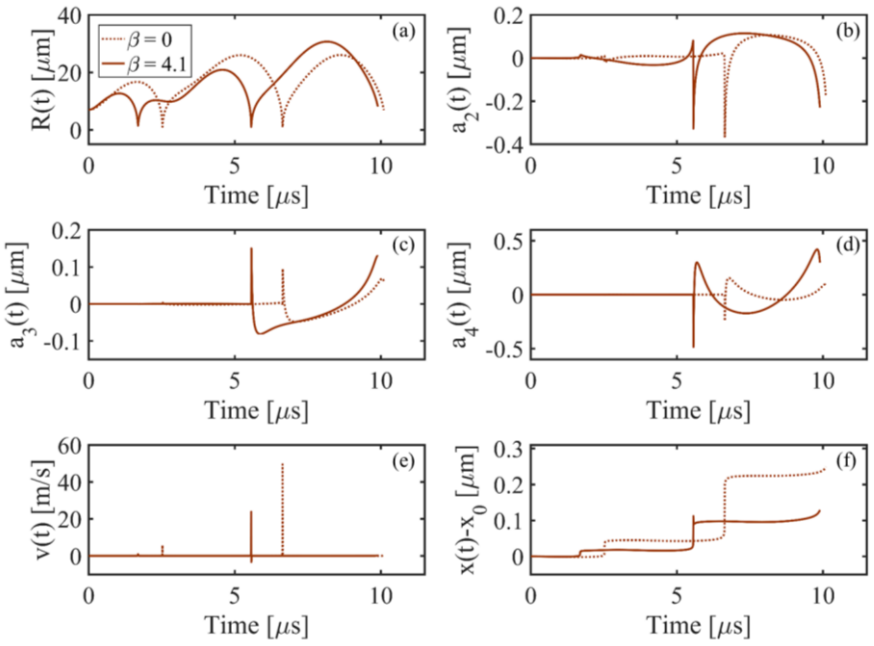

Figure 5.5. Dynamical motions of the bubble in the FU field ($R_0 = 7$ μm) and blood domain excited by the focused transducer ($f = 0.3$ MHz, $P = 2$ W): (a) radial pulsation, (b) second mode, (c) third mode, and (d) fourth mode amplitude. (e) Translational velocity and (f) translational motion ($x_0 = 5.2$ μm).

When focused ultrasound is applied, the level of bubbles' oscillations in size and shape (stable cavitation) and accurately predicting translational motion are of utmost importance in biomedical

applications such as blood-brain barrier (BBB) opening to enhance drug delivery to the brain. Hence, taking account of the nonlinearity parameter in ultrasound is important to predict bubbles' oscillatory behaviors more accurately. The results obtained by classical theory show that in a weak acoustic standing field, the bubbles congregate at pressure nodes or antinodes depending on the driving frequency [80]. However, later studies confirm that, in the acoustic field of high-intensity, bubbles show erratic dancing motion caused by shape oscillations that are excited by the bubble volume pulsations [41]. Indication of the translational instability is seen in the translational velocity and motion of the bubble (figures 5.5-5.7e and f). The swift growth of the unstable third mode, in figures 5.5-5.7c, leads to instability of the second mode in figures 5.5-5.7b due to their nonlinear interaction. Moreover, the nonlinear interaction of the third and fourth modes contributes further in erratic translational motions of the bubble.

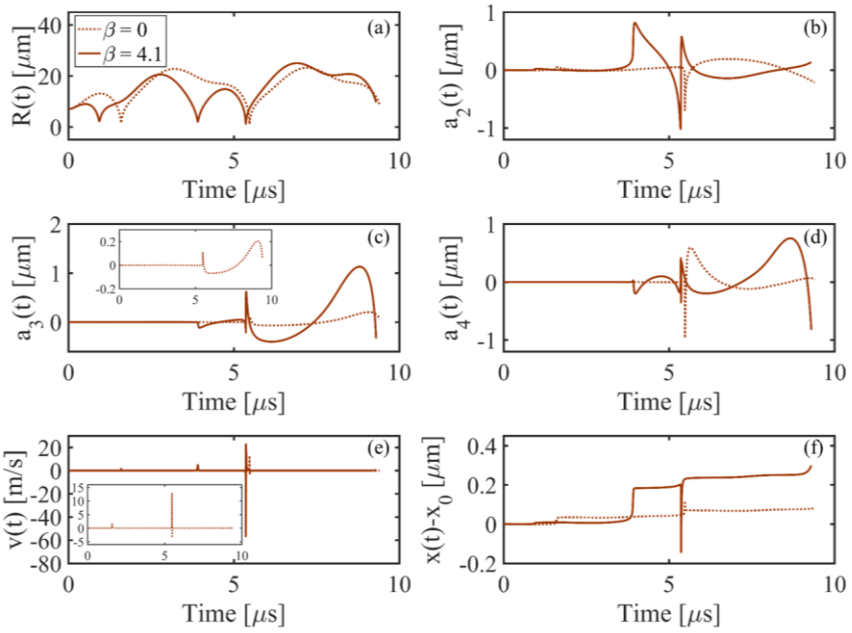

Figure 5.6. Dynamical motions of the bubble in the FU field ($R_0 = 7$ μm) and blood domain excited by the focused transducer ($f = 0.5$ MHz , $P = 2$ W): (a) radial pulsation, (b) second mode, (c) third mode, and (d) fourth mode amplitude. (e) Translational velocity and (f) translational motion $(x_0 = 3.1$ μm$)$.

The initiation of the erratic dancing motion of the bubble in the acoustic field in figures 5.5-5.7e and f is compatible with the onset of instability of other modes. Moreover, based on figures 5.5-5.7a, one can anticipate the inertial (unstable) cavitation threshold, in which the expansion ratio can be assumed around 2.3, i.e. $R_{max} / R_0 = 2.3$ [81-83] and the bubble may collapse. Accordingly, the inertial cavitation may occur at $f = 0.3$ and 0.5 MHz, after few cycles of radial pulsation of

the bubble, whereas the bubble exhibits stable cavitation at $f = 3$ MHz. In figures 5.5-5.7, it is shown that the evolutions of the third and fourth shape modes, along with the translational motion and velocity of the bubble are significantly larger or more unstable in the nonlinear excitation than that of the linear case and we observe more instability in the oscillations of the second mode. Moreover, the acoustic nonlinearity expedites the instability of the radial pulsation of the bubble in figures 5.5-5.7a. The significant effects of acoustic nonlinearity on the translational motion of the bubble are seen at the resonance frequency (see figures 5.6e and f) where the bubble abruptly turns back toward the pressure antinode and shows an erratic translational (dancing) motion. This behavior of a bubble is favorable where in-line forward and backward movement of bubbles (or particles/cells) is needed in microfluidic devices for sorting applications. Among the three ranges of frequency investigated in this study, the results show that the changes in the dynamical behavior of the bubble and the translational instability due to acoustic nonlinear effects are more significant for higher frequencies due to the stronger and higher number of harmonics creating enhanced localized energy deposition surrounding the bubble.

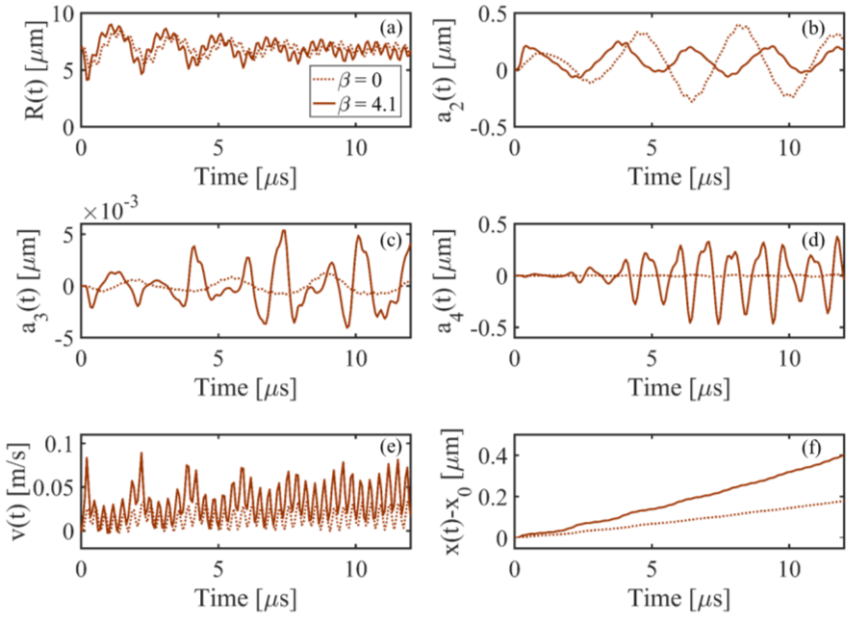

Figure 5.7. Dynamical motions of the bubble in the FU field ($R_0 = 7$ μm) and blood domain excited by the focused transducer ($f = 3$ MHz , $P = 2$ W): (a) radial pulsation, (b) second mode, (c) third mode, and (d) fourth mode amplitude. (e) Translational velocity and (f) translational motion ($x_0 = 0.52$ μm) .

Previous studies show that microbubbles exhibit nonlinear responses; however, the results in this study (figures 5.5-5.7) show that the responses of the bubble are also significantly dependent on

the excitation harmonics and hence they are different for linear and nonlinear acoustic excitations. The changes in the dynamical behavior of the bubble and the translational instability due to acoustic nonlinear effects are even more significant at higher frequencies (above resonance frequency). As shown in figure 5.8, the Fourier spectra of the radial oscillation of the bubble (based on figure D.1a) verifies the nonlinear response of the bubble for both linear and nonlinear excitations. The spectral analysis reveals that in addition to the driving frequency component (f_0) and second harmonic ($2f_0$), the bubble generates higher harmonics ($3f_0, 4f_0$....), subharmonics (less than the driving frequency component such as $0.5f_0$) and ultraharmonics (such as $1.5f_0$) [72, 84]. Although both of the excitations lead to the nonlinear response of the bubble, when the bubble is driven by the nonlinear excitation, the intensity of all the frequency components exceeds that of the linear excitation and the spectrum develops into a more complicated structure. Additionally, an approximate bandgap oscillation is found between 4 to 6 MHz frequencies for linear excitation whereas accounting for acoustic medium nonlinearity ($\beta \neq 0$) causes a broadband improvement of the oscillatory response of the bubble.

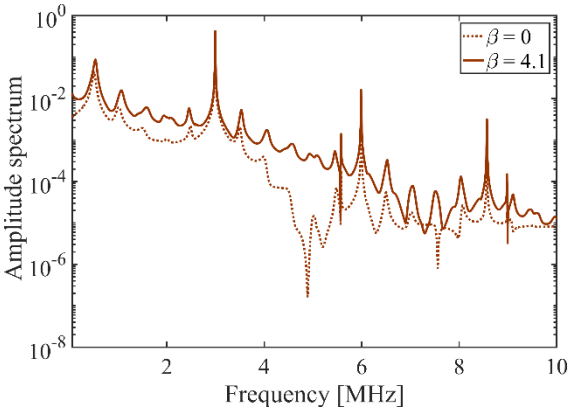

Figure 5.8. Fourier spectra of the radial oscillation of the bubble in the blood domain shown in figure D.1a. The curve is on a log scale.

5.3.2 Effects of acoustic pressure (input power to the transducer) on bubble dynamics

Figures 5.9a and b show the acoustic pressure at the focal point in time and frequency domains for various input power levels ($P = 2-8$ W), respectively. As the input power is increased at a particular frequency ($f = 3$ MHz), the amplitudes of all the harmonics increase while considering the nonlinearity parameter ($\beta = 4.1$); this leads to the wave distortion and adding more energy available to each harmonic, predominantly in the second and third harmonics (figure 5.9b). Figure

5.9c compares the pressure amplitude at the focal point for the two linear ($\beta = 0$) and nonlinear ($\beta = 4.1$) cases. In both cases, the pressure amplitude increases almost linearly by increasing the transducer input power, however at each power, the value of the pressure amplitude is greater in the nonlinear acoustic field along a steeper slope.

Figure 5.10 shows the bubble dynamics at $P = 6\,\mathrm{W}$, insonified at the focal point at the excitation frequency of $3\ \mathrm{MHz}$. Referring to figure 5.9c, the pressure amplitude for $P = 2\,\mathrm{W}$ in the nonlinear case is very close to the pressure amplitude at $P = 6\,\mathrm{W}$ in the linear field, however comparing the bubble dynamics in figures 5.7 and 5.10 show the differences in the bubble growth, shape modes and translational instability of the bubble which is evident in the velocity waveform and translational motion. This confirms that the radial growth and the onset of erratic motion of the bubble in a focused ultrasound field are reliant on both pressure amplitude and the harmonic components of the excitation.

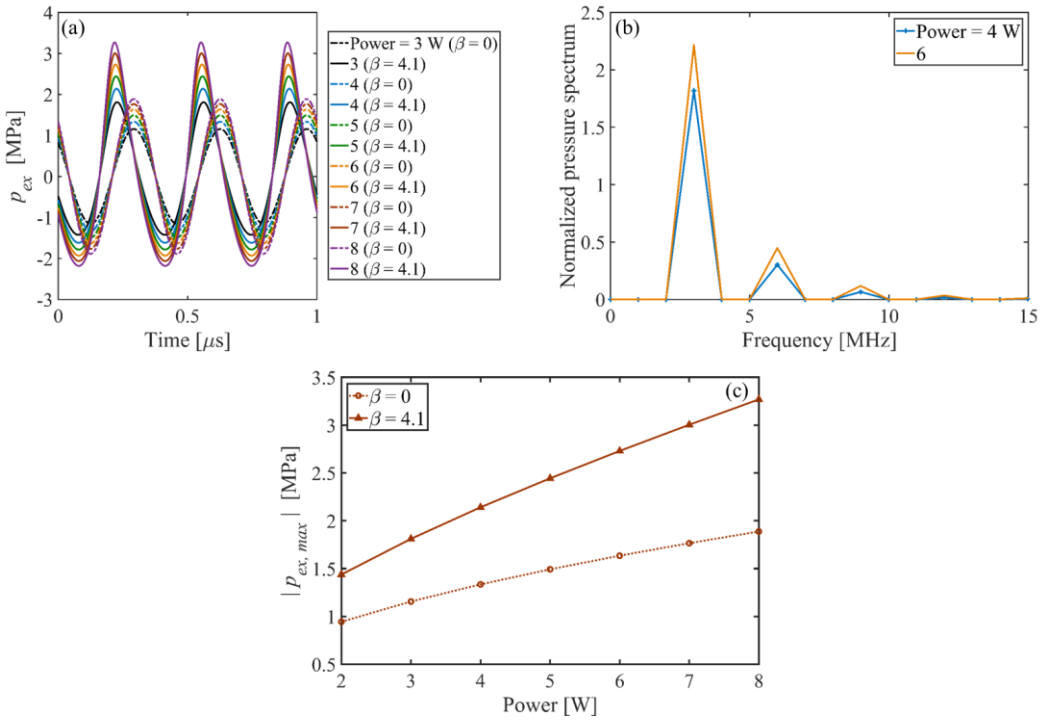

Figure 5.9. Acoustic pressure generated by the focused transducer as the input parameter to bubble dynamics at $f = 3\mathrm{MHz}$ (a) for various input power; temporal waveform and (b) the corresponding Fourier spectra for $\beta = 4.1$. (c) Pressure amplitude vs. transducer input power in linear and nonlinear cases.

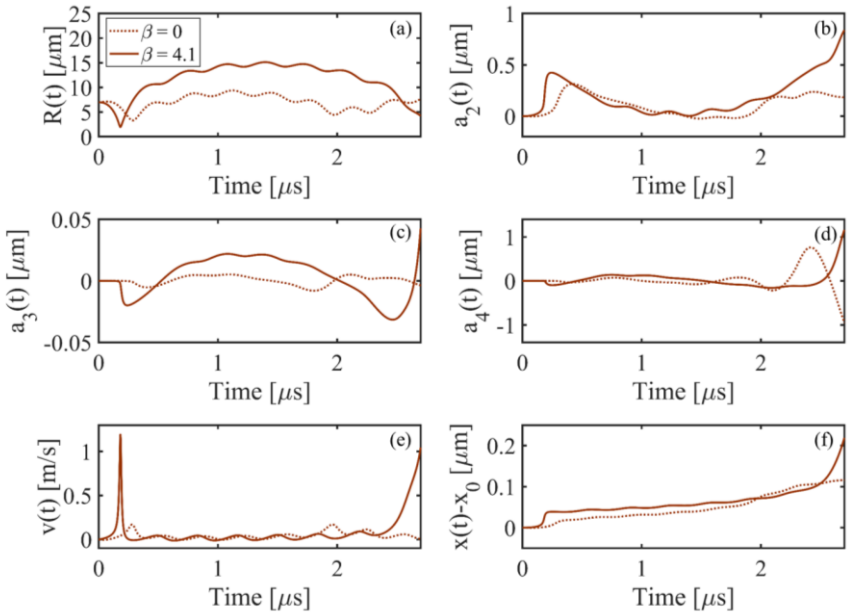

Figure 5.10. Dynamical motions of the bubble in the FU field ($R_0 = 7$ μm) and blood domain excited by the focused transducer ($f = 3$ MHz , $P = 6$ W): (a) radial pulsation, (b) second mode, (c) third mode, and (d) fourth mode amplitude. (e) Translational velocity and (f) translational motion ($x_0 = 0.52$ μm) .

The radial growth of the bubble for varying input power (leading to varying excitation acoustic field) is given in figures 5.11a and b, for linear and nonlinear acoustic excitation, respectively. In figure 5.11a, it is seen that, for all values of power, the bubble radius reaches the maximum value at the same time. However, in the nonlinear acoustic domain (figure 5.11b), as the input power increases, the radial growth of the bubble to the maximum value is delayed. Moreover, based on figure 5.11b, the bubble may collapse and show inertial (unstable) cavitation when the input power increases to 7 W and more. Hence, studying nonlinear acoustics in bubble dynamics is essential for detecting the threshold for inertial cavitation in biomedically enhanced delivery of drugs into tissue [85]. In figure 5.11c, the maximum radius of the bubble corresponds to each input power, and acoustic pressure is given. The results show that ignoring the nonlinearities of focused ultrasound can yield 56% error in the prediction of the bubble dynamics models. For low amplitude of pressure, we see a slight difference between the linear and nonlinear models, which results in a small error in the prediction of the maximum radius of the bubble. However, when the applied pressure increases considerably, the results show significant divergences; the linear model predicts stable cavitation, whereas the nonlinear model reaches the threshold for unstable cavitation.

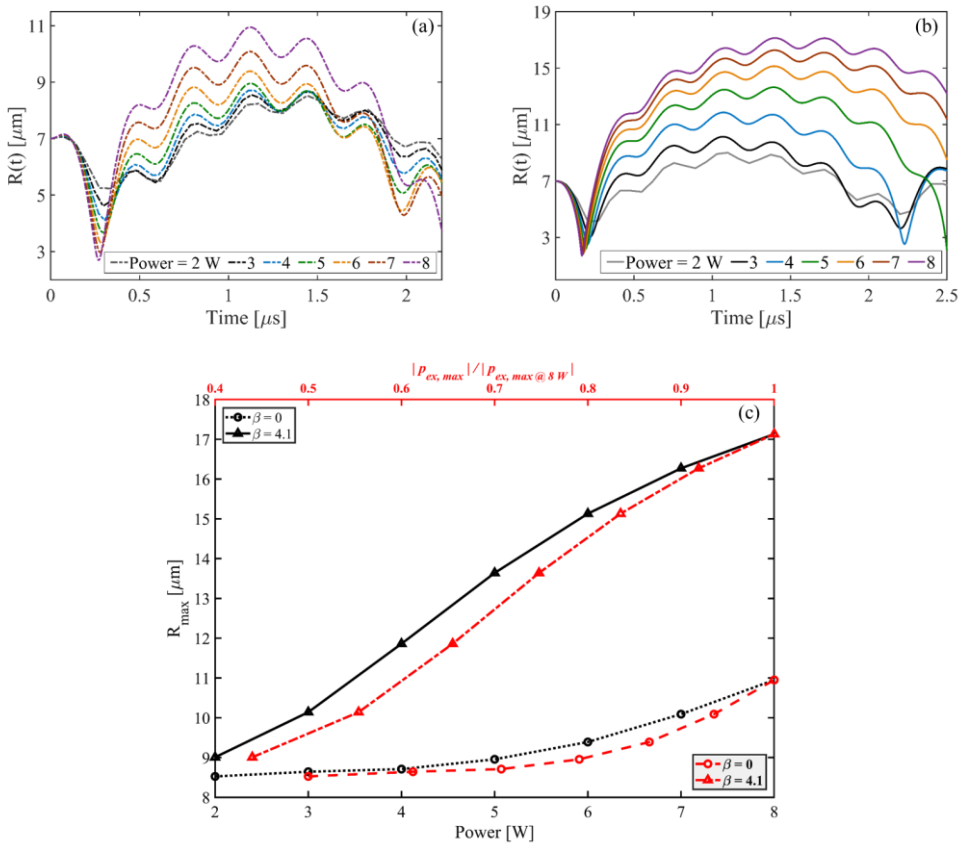

Figure 5.11. Radius versus time plot of a $7-\mu m-$radius bubble at $f=3$ MHz for various input power in (a) linear and (b) nonlinear acoustic field. (c) A comparison of the linear (dashed line) and nonlinear (solid line) model predictions for varying input power (black line) and acoustic pressure (red line).

The effects of acoustic nonlinearity on the translational instability of the spherical gas bubble for various pressure fields are investigated in figure 5.12, considering both linear and nonlinear excitations. To the best of our knowledge, most of the theoretical studies on the translational motion of a bubble in high-intensity sound wave fields are performed [43, 44] while the effects of absorption, diffraction, and nonlinear distortion in the medium are not considered. The studies show that in a high-intensity field, the translational motion of the bubble occurs in more complicated trajectories such that the instability can develop very quickly. Figure 5.12b shows the evidence of the onset of unstable movement by the steep change in the translational velocity of the bubble. Considering acoustic nonlinearity, one can see that the translational instability of the bubble accelerates and develops more intensely compared to that of linear excitation. Moreover, at higher pressure amplitudes, the shape oscillations develop strongly and reach high amplitudes, which leads to acceleration and amplification of the translational instability and dancing motion that can be seen in figures 5.12a and b.

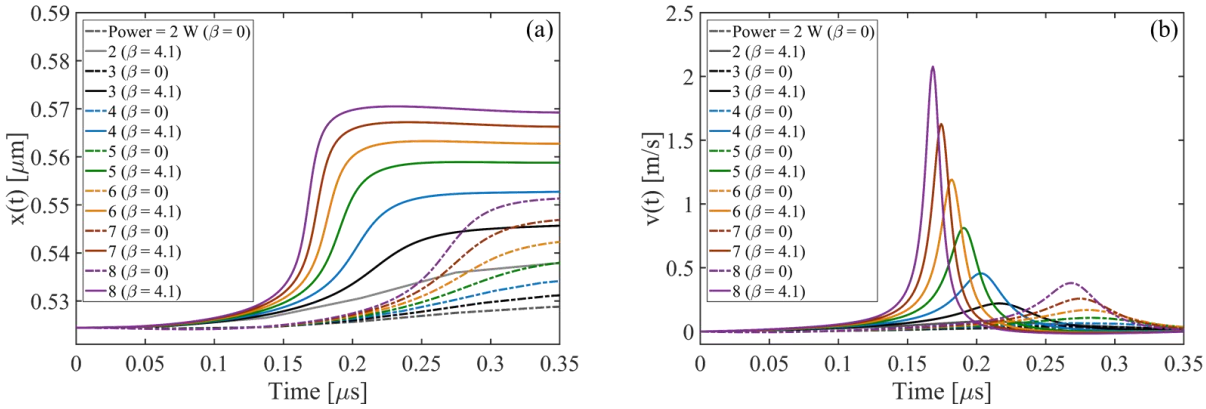

Figure 5.12. Dynamics of translation of a $7-\mu m-$radius bubble at $f=3$ MHz for various input power: (a) Translational motion and (b) translational velocity (the corresponding acoustic pressures are given in figure 5.9).

5.4 Transmission acoustic phase holograms for microfluidic devices

As mentioned before, the dancing motion of the bubble is of great importance in many applications such as particle and cell sorting [36-38] where it is believed that the cells or particles are behaving similar to bubbles. Microfluidic devices have promising potential to analyze cells for application in medicine. Researchers have developed systems that can differentiate or sort microbubbles and cells based on their size, deformability, and electrical or acoustic properties [86, 87]. Using a combination of implementing ultrasonic transducers and holographic reconstruction of different patterns using acoustic holograms, the particles or cells can be ultrasonically manipulated [88-92]. The ultimate goal of this section is to develop a new approach for microbubble-mediated ultrasound therapy and sorting particles and cells based on their acoustic properties—that is, how they are affected by sound waves and are manipulated by an acoustic transmission hologram to make arbitrarily patterning of microbubbles, particles, and cells in medical ultrasound systems.

A microfluidic planar setup in figure 5.13b is designed for the investigation of particle manipulation using acoustic transmission holograms developed in chapter 2. The microchannel is made entirely of a Polydimethylsiloxane (PDMS, Sylgard 184, Dow Corning) elastomer using standard soft lithography techniques [36, 93, 94]. Figure 5.13a displays a schematic of a setup using an acoustic hologram for a microfluidic channel. An acoustic field is applied through the bottom surface of the channel bonded on a glass slide and the surface is vibrated by a small ultrasonic transmitter disk glued at the bottom of the glass. The channel, therefore, receives the ultrasound field emitted by the surface through the elastomer, which transmits the vibration. An acoustic hologram is fixed to the transmitter and a thin layer of an ultrasound gel made of, e.g.,

glycerin [95] is used between the hologram and bottom surface of the glass slide for the bonding purpose, which also provides good acoustic coupling. Using the flow-focusing geometry, the microchannel is filled with water through two side inlet channels. If the setup involves the manipulation of microbubbles, then a nitrogen gas is also supplied through the middle inlet channel [96]. For cell or particle manipulation, we can perform the same method by filling the channel with cells or particles dispersed in a proper acoustic medium such as water or hydrogel.

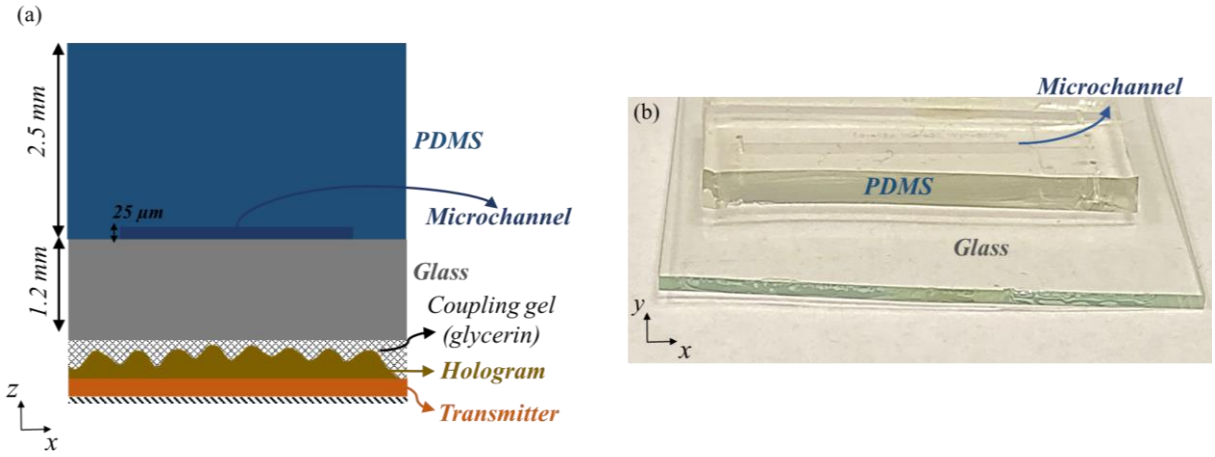

Figure 5.13. Schematic representations of (a) a microfluidic device with an acoustic hologram and (b) a close-up view of the microfluidic device including the glass slide (50 mm × 40 mm × 1.2 mm), the PDMS (44 mm × 15 mm × 2.5 mm), and the microchannel (30 mm × 2 mm × 25 µm).

The simulations are performed to design acoustic holograms that can be used for the microfluidic device shown in figure 5.13 to generate two desired patterns of a 2-mm-width VT shape and a 2-mm-diameter ring shape for possible manipulation of particles inside the microchannel. Based on currently available modern 3D printers and their build resolution limits (e.g., see specifications of a 3D printer *Objet260 Connex3, Stratasys* in [97]), and taking into account that the pattern has to be generated inside the microchannel with the width of 2 mm, we have considered six ultrasonic transducers with different element diameters and frequencies (Immersion Transducers from Olympus Corporation [98]) with properties shown in table 5.2. These transducers transmit sound waves in water with a wavelength of 100-200 µm, suitable to be used for microscale particle manipulation, in conjunction with acoustic holograms that are fabricated with a resolution of the one-half wavelength, correspond to 50-100 µm.

Table 5.2. Properties of ultrasonic transducers used for acoustic holographic microbubble, particle, and cell patterning

Transmitter	Properties			
	Part code (Olympus)	Frequency [MHz]	Diameter [mm]	Thickness [mm]
Tx1	A320S-SU	7.5	13	0.27
Tx2	A311S-SU	10	13	0.2
Tx3	A319S-SU	15	13	0.13
Tx4	A321S-SU	7.5	19	0.27
Tx5	A315S-SU	10	19	0.2
Tx6	V322-SU	10	25	0.2

5.4.1 Modified iterative angular spectrum approach (IASA) algorithm for the design of holograms in microfluidic devices

The holograms are designed via the IASA optimization algorithm as explained in chapter 2 with few modifications as follows:

1. The power transmission coefficient is calculated considering the six material layers in figure 5.13a and with the method explained in section 2.2 of chapter 2, with Z_1 and Z_6 correspond to Z_s and Z_{PDMS}, the acoustic impedance of the transmitter and PDMS. The transfer matrices (equation (2.1)) for the other four material layers are determined considering the material thicknesses and their acoustic impedances. For the microchannel component, we consider the acoustic impedance of water with 25-µm-thickness material corresponding to the thickness of the microchannel. It should be noted that the acoustic attenuation of water, glass, and the hologram and coupling gel materials are taken into account in the calculation of acoustic pressure amplitudes. The acoustic properties of the material layers can be found in table 5.3.
2. The base thickness of the coupling gel layer has to be determined for each case study in table 5.2, before performing the IASA computational simulation for the design of holograms. The thickness of the layer of the coupling gel is determined via the thickness change of the hologram pixels $\Delta t(x,y)$ (see equation (2.12)) as $\Delta t(x,y) = t_{ge}(x,y) - t_{0ge}$, where $t_{ge}(x,y)$ is the thickness of the coupling layer corresponds to the pixel of the hologram at coordinates (x,y) and t_{0ge} is the coupling gel base thickness. To find the t_{0ge},

we perform separate IASA computations for each case study with 20 iterations and sweep the coupling gel base thickness according to the dimensions of the material layers in figure 5.13a. In the last iteration of each sweep, we calculate the average power transmission coefficient and acoustic pressure in the target plane for the pixels that were imposed to have a non-zero amplitude of the desired image pattern, i.e., VT and ring shape (see figures 5.14 and 5.15). The coupling gel base thickness which gives the maximum average power transmission coefficient and high average pressure in the patterned areas is selected for each case study. Finally, the IASA optimization simulations are performed to generate the desired patterns of acoustic pressure in target planes at $z = 2.8$ mm for case studies 1 and 4 (i.e., using *Tx1* and *Tx4* transmitters), $z = 2.4$ mm for case studies 2, 5, and 6, and $z = 2$ mm for case study 3 based on the dimensions of the material layers.

Table 5.3. Parameters of the materials used in the IASA optimization algorithm for the microfluidic device

Material layers	Parameter		
	Density [kg/m^3]	Sound speed [m/s]	Acoustic coefficient [Np/m][d]
Transmitter (PZT-5A)	7800	4000	—
Hologram (VeroClear)	1185	2424	63.3 @ 2 MHz
Coupling gel (glycerine)	1050	1920	3 @ 1 MHz [99]
Glass	2260	4910	1.15 @ 2 MHz
Water	1000	1500	0.023 @ 1 MHz
PDMS (Sylgard 184) [100]	1050	1027	—

5.4.2 Computational results for acoustic holographic patterning inside the microchannel

In this section, the computational results for the design of acoustic holograms are illustrated. The simulations are performed for the six case studies defined in table 5.2 using six different

[d] The acoustic attenuation are calculated assuming a proportional increase of losses to the first power of frequency for VeroClear and glass, and to the second power of frequency for glycerin and water.

transmitters. As an illustration, figure 5.14 presents the results for the holographic reconstruction of the VT image pattern using the *Tx2* and *Tx3* transmitters, and figure 5.15 presents the computational holographic results for the ring-shaped pattern using the *Tx2* and *Tx5* transmitters. All the computational holographic images in this section are satisfactorily converged to the target patterns after 50 iterations of the IASA optimization algorithm. The aforementioned process for selecting the coupling gel base thickness can be determined from the outcomes seen in figure D.2, in appendix D. The results show how the base thickness is chosen based on the achieved maximum average power transmission coefficient, which also gives the high amplitude of average acoustic pressure. The calculated thickness profile of a hologram phase plate (figures 5.14 and 5.15c and i) alongside the corresponding thickness map of a coupling layer (figures 5.14 and 5.15d and j) is later used in the fabrication process for the implementation of holograms in the microfluidic device.

The acoustic pressure attenuation factor $\Lambda(x,y) = e^{-[\beta_h t(x,y) + \beta_{ge} t_{ge}(x,y) + \beta_{gl} t_{gl}]}$ is shown in figures 5.14 and 5.15e and k, where $t(x,y) = t_0 - \Delta t(x,y)$ is the thickness of the hologram pixel with t_0 as the hologram base thickness (that can be selected freely based on the maximum thickness change for the hologram pixels and mechanical stability of the hologram plate), $t_{ge}(x,y) = t_{0ge} + \Delta t(x,y)$, and $t_{gl} = 1.2$ mm is the thickness of the glass slide; and the computed power transmission coefficient map is also depicted in figures 5.14 and 5.15f and l. We can detect that both acoustic attenuation factor and power transmission coefficient are relatively higher in the regions that we imposed the desired patterns (i.e., x = -1 to 1 mm and y = -1 to 1 mm).

The two desired patterns of VT and ring shape are clearly realized inside the microchannel (see figures 5.14 and 5.15a, b, g, and h), which shows the functionality of acoustic transmission phase holograms for microstructures in theory, however, experiments are required to verify the outcomes of this section in practice. Figure 5.16 shows the parameter image correlations for similarity analysis between the holographic computational images, reconstructed for each case studies in table 5.2 (for VT and ring patterns), with that of the imposed target images (see equation (2.20)). The image correlation for all microscale patterning shows promising results with slightly different values and trends between VT and ring-shaped patterns. It is worth mentioning that the simple ring-shaped pattern is more applicable in practice for acoustic patterning in microfluidic channels and the results for the VT image in this section are only demonstrated to show the potential of acoustic holograms in reconstructing an arbitrary and more complex pattern for microstructures.

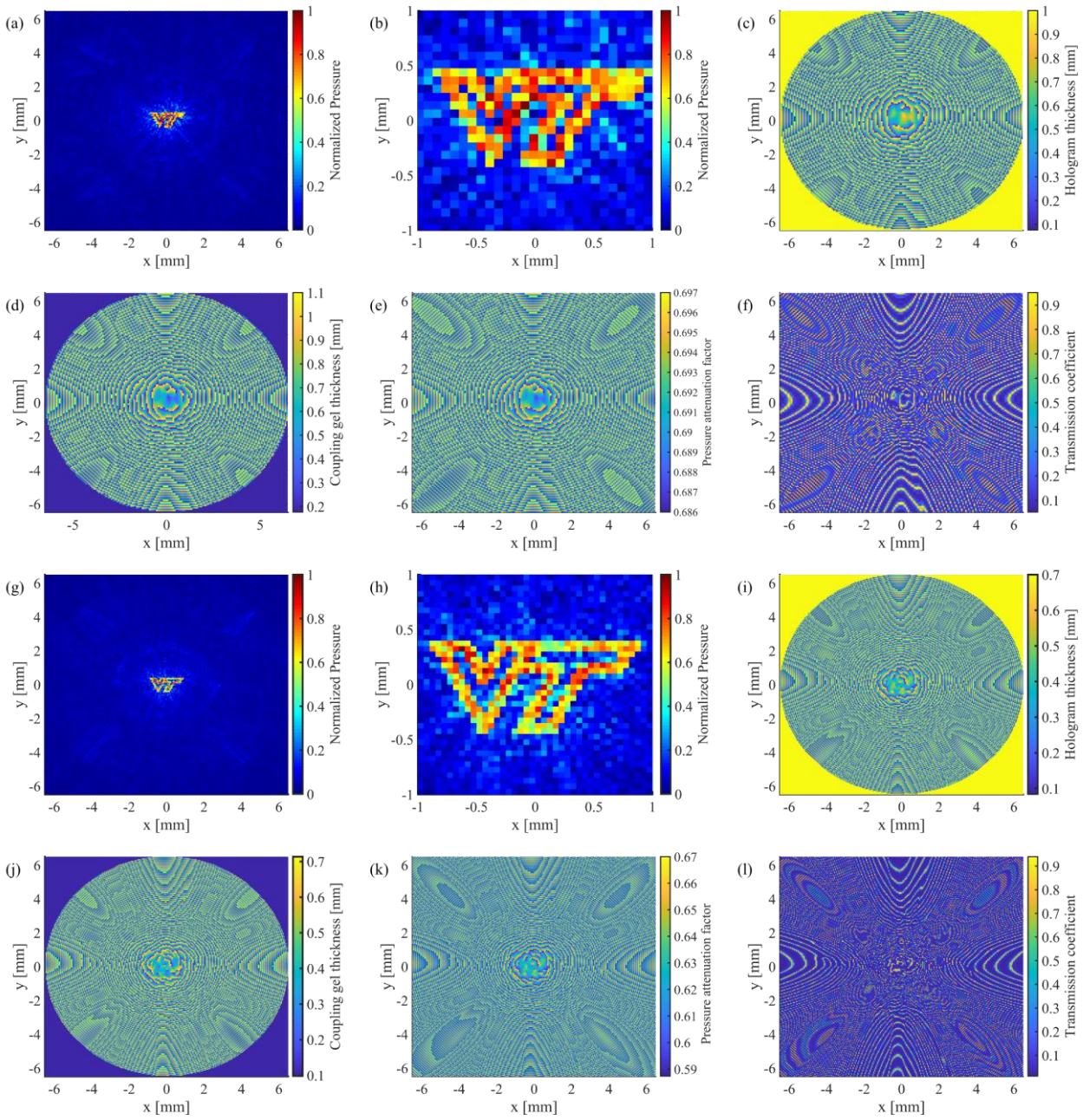

Figure 5.14. Holographic reconstruction of the VT image for the microfluidic device using *Tx2* (13-mm-diameter transmitter) operating at 10 MHz: (a) the acoustic pressure amplitude in the target plane at $z = 2.4$ mm and (b) the close-up view of the VT pattern generated in the width of the microchannel; (c) calculated hologram thickness from the hologram phase map and (d) the coupling gel thickness map $(t_{0ge} = 177\ \mu\text{m})$; (e) acoustic pressure attenuation factor, and (f) power transmission coefficient map. Holographic reconstruction of the VT image for the microfluidic device using *Tx3* (13-mm-diameter transmitter) operating at 15 MHz: (g) the acoustic pressure amplitude in the target plane at $z = 2$ mm and (h) the close-up view of the VT pattern generated in the width of the microchannel; (i) calculated hologram thickness from the hologram phase map and (j) the coupling gel thickness map $(t_{0ge} = 98\ \mu\text{m})$; (k) acoustic pressure attenuation factor, and (l) power transmission coefficient map.

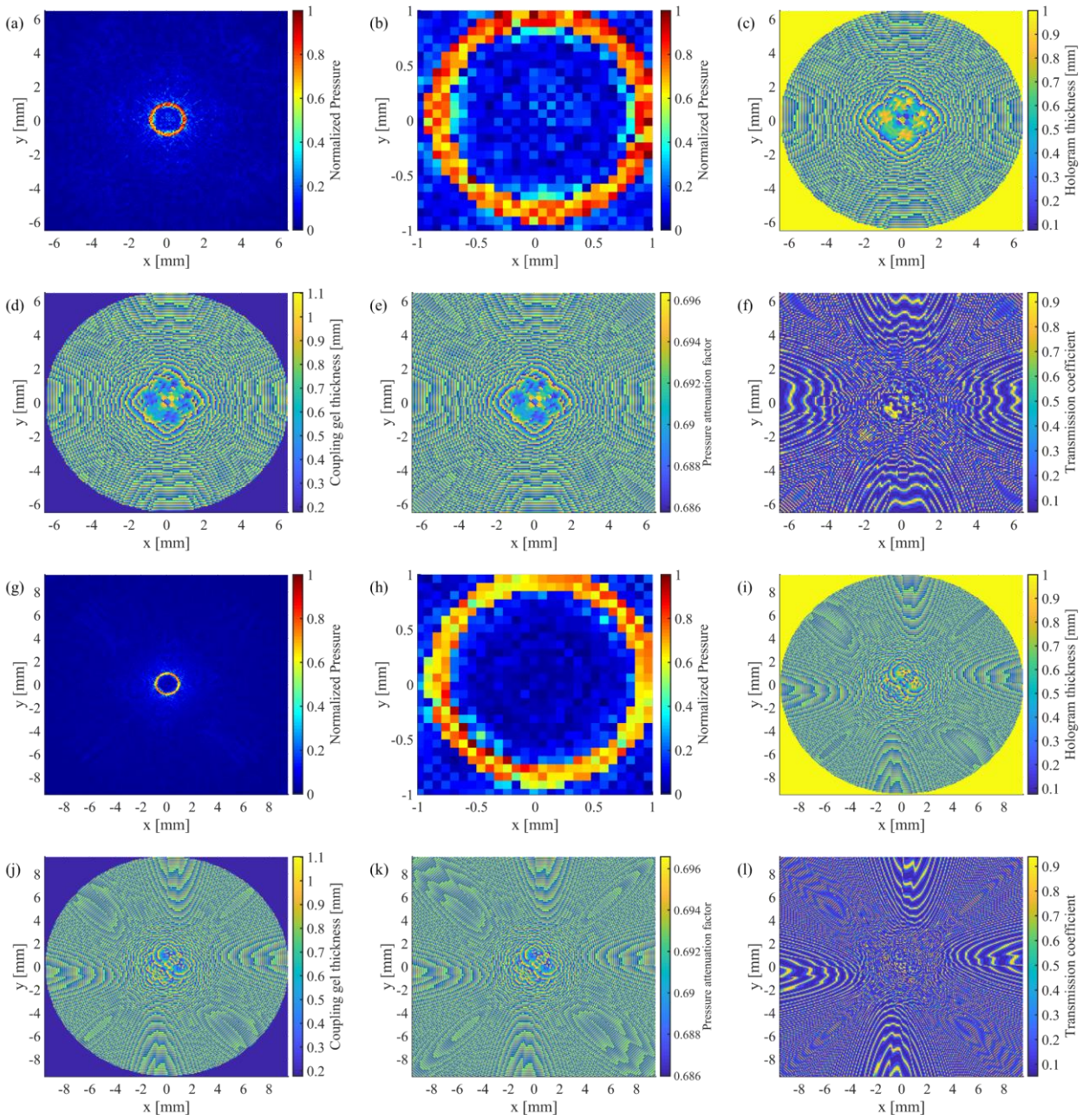

Figure 5.15. Holographic reconstruction of the ring-shaped image for the microfluidic device using *Tx2* (13-mm-diameter transmitter) operating at 10 MHz: (a) the acoustic pressure amplitude in the target plane at $z = 2.4$ mm and (b) the close-up view of the ring pattern generated in the width of the microchannel; (c) calculated hologram thickness from the hologram phase map and (d) the coupling gel thickness map $(t_{0ge} = 179\ \mu\text{m})$; (e) acoustic pressure attenuation factor, and (f) power transmission coefficient map. Holographic reconstruction of the ring-shaped image for the microfluidic device using *Tx5* (19-mm-diameter transmitter) operating at 10 MHz: (g) the acoustic pressure amplitude in the target plane at $z = 2.4$ mm and (h) the close-up view of the ring pattern generated in the width of the microchannel; (i) calculated hologram thickness from the hologram phase map and (j) the coupling gel thickness map $(t_{0ge} = 178\ \mu\text{m})$; (k) acoustic pressure attenuation factor, and (l) power transmission coefficient map.

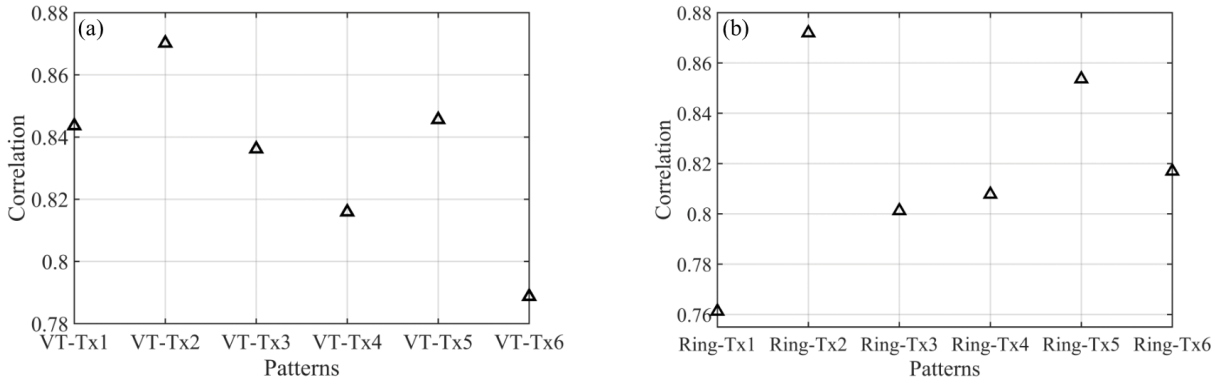

Figure 5.16. Correlation between the computational microstructured holographic images and their respective imposed target images to evaluate the holograms' quality: (a) the VT-shaped images and (b) ring-shaped images.

we expect that this cost-effective and simple holographic technique, i.e., using single acoustic transmission phase holograms alongside a simple ultrasonic transducer, arbitrary complex pressure patterns can be constructed with microscale feature sizes for a wide range of potential biomedical applications. Some of these diagnostic and therapeutic applications include microbubble-mediated drug delivery [101], trapping or separating viruses, bacteria, particles, and cells in label-free and non-invasive strategies [102-106], as well as impacts in developmental biology, tissue engineering, regenerative medicine, and mechanobiology [107-110], to name a few.

5.5 Conclusions

The studying of microbubble's oscillations in size and shape during FU insonation (ultrasound stable or non-inertial cavitation) is of immense significance in biomedical applications, such as enhancing drug delivery rate in blood-brain barrier opening. Hence, accounting of the FU-induced acoustic nonlinearity in the mathematical models of bubble dynamics is essential to accurately predict the bubble oscillations and acoustic pressure due to streaming. Following the previously established mathematical model [44], this chapter aims to investigate the effects of nonlinear propagation of FU-induced pressure fields into the dynamics of ultrasound microbubbles. A theoretical framework (based on the KZK equation) is used to predict the acoustic pressure fields due to focused transducers considering the three effects of acoustic nonlinearity, diffraction, and absorption in the medium. Then the nonlinear acoustic model is coupled with the bubble dynamics (based on the Keller-Miksis model) to predict the oscillation, shape modes and translational motion of a single air bubble excited in a FU field at a focal point. The model is used to explore the effects of medium properties (nonlinearity and absorption) and input parameters (power and frequency)

on the pressure waveform distortion and amplitude. The observations related to medium properties show that the coefficient of nonlinearity and absorption play significant roles in distorting the waveform and generating more harmonics, thus increasing the energy deposition at the focal point.

The KZK-Keller-Miksis model incorporates radial pulsations of a bubble along with its small shape oscillations and translational motion in a FU field. Nonlinear coupling between fundamental radial mode, second to fourth modes of oscillations, and translational motion of the bubble are analyzed to explain the translational instability of the bubble. It is concluded that second-order interactions of two neighboring surface modes impose instability to the system, which in turn leads to the dancing motion of the bubble. Furthermore, the analysis shows that in addition to the resonance response of the bubble, the off-resonance excitation leads to interesting results. Particularly, the acoustic pressure fluctuations and translational instability of the bubble may increase at above or below fundamental resonance excitation. The translational instability has broad applications in cell sorting which resembles the bubble dancing motion in a microfluidic device. Therefore, studying the dynamics of off-resonant bubbles is essential in acoustic bubble manipulation. Additionally, the results reveal the importance of studying nonlinear acoustics and consideration of all the involved harmonics in the dynamics of FU-excited microbubbles. A summary of the observations is as follows:

1. The results show the dynamical motions of the bubble in the FU field generated by the focused transducer at three different range of frequencies (including the resonance and off-resonance cases). Effects of the change of excitation frequency are investigated and it is shown that in all the frequency ranges, the nonlinearity expedites and amplifies the radial growth and translational motion of the bubble where the indication of the translational instability is observed by a steep rise in the translational velocity of the bubble. It is seen that the initiation of the erratic dancing motion of the bubble in the acoustic field is well-matched with the time of instability of other modes. Moreover, acoustic nonlinearity amplifies almost all the shape oscillations and the instability of the modes. Among the three ranges of frequency investigated in this study, the results show that the changes in the dynamical behavior of the bubble and the translational instability due to nonlinear effects are more significant for higher frequencies, which must be taken into account while investigating an erratic translational (dancing) motion of the bubble. However, a momentous effect of nonlinearity on the translational motion of the bubble is seen at resonance frequency where the bubble initially moves away from the pressure antinode and makes the translation jumps around the antinode. It is seen that as the excitation frequency increases, the inertial (unstable)

cavitation occurs earlier in the nonlinear acoustic field; the nonlinear excitation causes more energy deposition at higher harmonics at the focal point (where the bubble is located); therefore, the radius growth of the bubble is more pronounced at higher frequencies. Accordingly, studying nonlinear acoustics in bubble dynamics is essential for inertial cavitation prediction in biomedically enhanced delivery of drugs into a tissue.

2. As the input power is increased, the amplitudes of all the harmonics increase. Comparing the bubble dynamics for two equal pressure amplitude in linear and nonlinear cases, show significant differences in the shape modes and translational instability of the bubble. This confirms that the radial growth and onset of the erratic motion of the bubble in a focused ultrasound field are reliant on both pressure amplitude and the harmonic components of the excitation. It is seen that when the applied pressure increases, the results of the linear model gives up to 56% error for predicting the threshold for unstable cavitation (maximum radius of the bubble). In nonlinear acoustics, when the input power increases, the bubble may collapse and shows unstable cavitation as well as the amplified and accelerated translational instability.

This chapter explains a practical case of using a focused transducer for manipulating a microbubble. The model allows the readers to precisely predict the bubble dynamics considering the nonlinear effects due to a focused sound beam which are strongly affected by the mutual influences of diffraction, absorption, and nonlinearity of the medium. The effects of acoustic nonlinearity on bubble dynamics have not been yet investigated and can be an immediate need for the biomedical engineering community. Moreover, we investigated the use of cost-effective 3D-printed acoustic phase holograms for microfluidic devices, which provides new insights into microbubble, particle, and cell patterning and manipulation using the simple acoustic holography technology with promising potentials in diagnostic and therapeutic medical applications.

Appendix D

D.1 Prolonged dynamical motions of the bubble above the resonance frequency

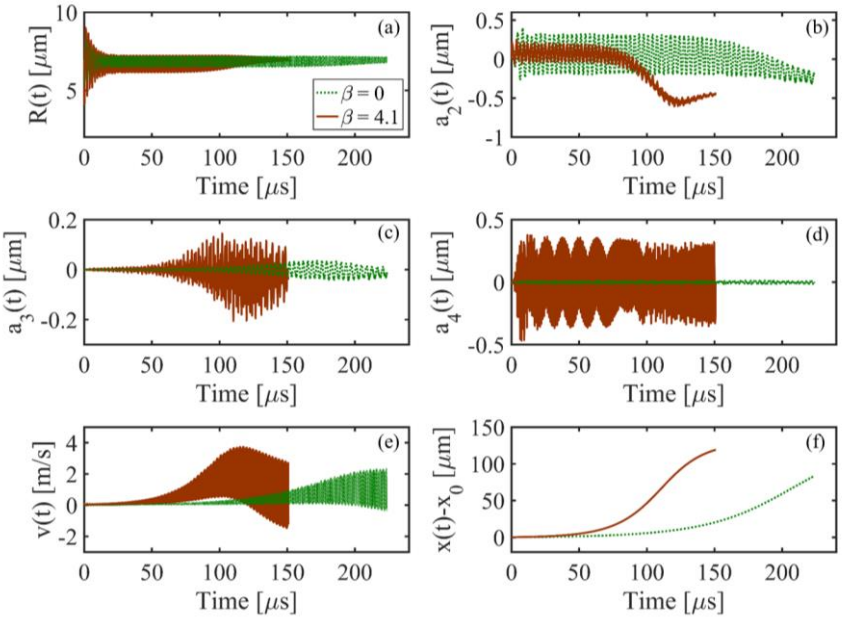

Figure D.1. Prolonged dynamical motions of the bubble in the FU field ($R_0 = 7$ μm) and blood domain excited by the focused transducer ($f = 3$ MHz, $P = 2$ W): (a) radial pulsation, (b) second mode, (c) third mode, and (d) fourth mode amplitude. (e) Translational velocity and (f) translational motion ($x_0 = 0.52$ μm).

D.2 Coupling gel base thickness determination for the microfluidic device

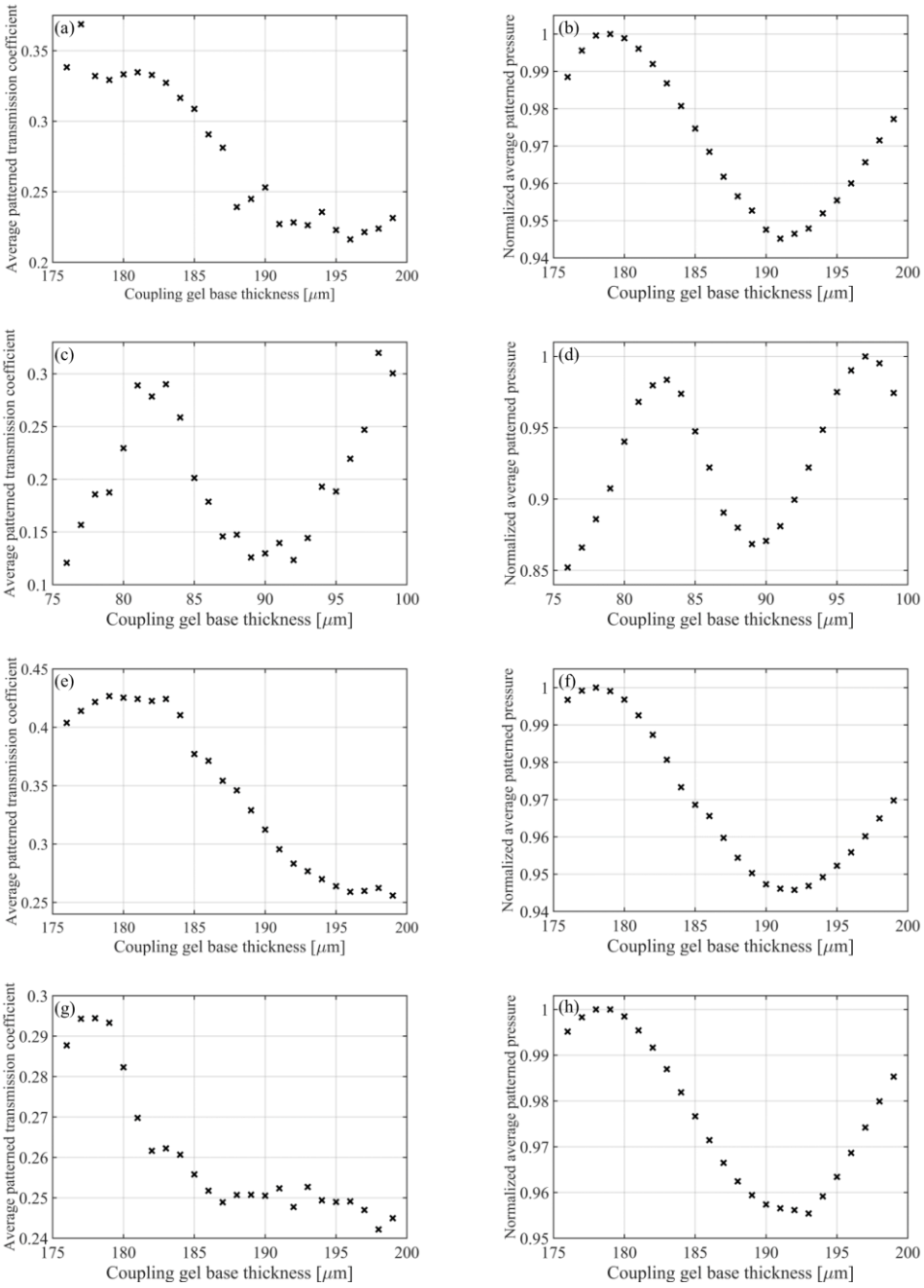

Figure D.2. Average power transmission coefficient in the patterned region varying coupling gel base thickness: holographic reconstruction of VT image (a) using *Tx2* transmitter in which t_{0ge} is selected as 177 µm, and (c) using *Tx3* transmitter in which t_{0ge} is selected as 98 µm; (b) and (d) the corresponding amplitude of average acoustic pressure in the patterned region. Average power transmission coefficient in the patterned region varying coupling gel base thickness: holographic reconstruction of ring-shaped image (e) using *Tx2* transmitter in which t_{0ge} is selected as 179 µm, and (g) using *Tx5* transmitter in which t_{0ge} is selected as 178 µm; (f) and (h) the corresponding amplitude of average acoustic pressure in the patterned region. The coupling gel base thickness in each case study is chosen after 20 iterations of the IASA.

Bibliography

[1] Bakhtiari-Nejad, M. and Shahab, S. *Effects of Nonlinear Propagation of Focused Ultrasound on the Stable Cavitation of a Single Bubble*. in *Acoustics*. 2018. Multidisciplinary Digital Publishing Institute.

[2] Bakhtiari-Nejad, M. and Shahab, S. *Investigation of bubble dynamics in nonlinear acoustic field*. in *Active and Passive Smart Structures and Integrated Systems XII*. 2018. International Society for Optics and Photonics.

[3] Mitragotri, S., *Healing sound: the use of ultrasound in drug delivery and other therapeutic applications.* Nature reviews. Drug discovery, 2005. **4**(3): p. 255.

[4] Bazan-Peregrino, M., Rifai, B., Carlisle, R.C., Choi, J., Arvanitis, C.D., Seymour, L.W., and Coussios, C.C., *Cavitation-enhanced delivery of a replicating oncolytic adenovirus to tumors using focused ultrasound.* Journal of controlled release, 2013. **169**(1): p. 40-47.

[5] Bader, K.B. and Holland, C.K., *Gauging the likelihood of stable cavitation from ultrasound contrast agents.* Physics in medicine and biology, 2012. **58**(1): p. 127.

[6] Thomas, C.R., Farny, C.H., Coussios, C.C., Roy, R.A., and Holt, R.G., *Dynamics and control of cavitation during high-intensity focused ultrasound application.* Acoustics Research Letters Online, 2005. **6**(3): p. 182-187.

[7] Fan, C.-H., Ting, C.-Y., Chang, Y.-C., Wei, K.-C., Liu, H.-L., and Yeh, C.-K., *Drug-loaded bubbles with matched focused ultrasound excitation for concurrent blood–brain barrier opening and brain-tumor drug delivery.* Acta biomaterialia, 2015. **15**: p. 89-101.

[8] Fan, C.-H., Liu, H.-L., Ting, C.-Y., Lee, Y.-H., Huang, C.-Y., Ma, Y.-J., Wei, K.-C., Yen, T.-C., and Yeh, C.-K., *Submicron-bubble-enhanced focused ultrasound for blood–brain barrier disruption and improved CNS drug delivery.* PloS one, 2014. **9**(5): p. e96327.

[9] Wang, S., Samiotaki, G., Olumolade, O., Feshitan, J.A., and Konofagou, E.E., *Microbubble type and distribution dependence of focused ultrasound-induced blood–brain barrier opening.* Ultrasound in medicine & biology, 2014. **40**(1): p. 130-137.

[10] Kim, Y.-s., Rhim, H., Choi, M.J., Lim, H.K., and Choi, D., *High-intensity focused ultrasound therapy: an overview for radiologists.* Korean journal of radiology, 2008. **9**(4): p. 291-302.

[11] Shahab, S. and Erturk, A., *Contactless ultrasonic energy transfer for wireless systems: acoustic-piezoelectric structure interaction modeling and performance enhancement.* Smart Materials and Structures, 2014. **23**(12): p. 125032.

[12] Shahab, S., Gray, M., and Erturk, A., *Ultrasonic power transfer from a spherical acoustic wave source to a free-free piezoelectric receiver: Modeling and experiment.* Journal of Applied Physics, 2015. **117**(10): p. 104903.

[13] Klibanov, A.L., *Microbubble contrast agents: targeted ultrasound imaging and ultrasound-assisted drug-delivery applications.* Investigative radiology, 2006. **41**(3): p. 354-362.

[14] Schutt, E.G., Klein, D.H., Mattrey, R.M., and Riess, J.G., *Injectable microbubbles as contrast agents for diagnostic ultrasound imaging: the key role of perfluorochemicals.* Angewandte Chemie International Edition, 2003. **42**(28): p. 3218-3235.

[15] Johnson, M.E., Mitragotri, S., Patel, A., Blankschtein, D., and Langer, R., *Synergistic effects of chemical enhancers and therapeutic ultrasound on transdermal drug delivery.* Journal of pharmaceutical sciences, 1996. **85**(7): p. 670-679.

[16] Mitragotri, S., Farrell, J., Tang, H., Terahara, T., Kost, J., and Langer, R., *Determination of threshold energy dose for ultrasound-induced transdermal drug transport.* Journal of controlled release, 2000. **63**(1): p. 41-52.

[17] Bhargava, A., Peng, K., Stieg, J., Mirzaeifar, R., and Shahab, S., *Focused ultrasound actuation of shape memory polymers; acoustic-thermoelastic modeling and testing.* RSC Advances, 2017. **7**(72): p. 45452-45469.

[18] McDannold, N., Arvanitis, C.D., Vykhodtseva, N., and Livingstone, M.S., *Temporary disruption of the blood–brain barrier by use of ultrasound and microbubbles: safety and efficacy evaluation in rhesus macaques.* Cancer research, 2012. **72**(14): p. 3652-3663.

[19] Mesiwala, A.H., Farrell, L., Wenzel, H.J., Silbergeld, D.L., Crum, L.A., Winn, H.R., and Mourad, P.D., *High-intensity focused ultrasound selectively disrupts the blood-brain barrier in vivo.* Ultrasound in medicine & biology, 2002. **28**(3): p. 389-400.

[20] He, M., Zhong, Z., Li, X., Gong, X., Wang, Z., and Li, F., *Effects of different hydrostatic pressure on lesions in ex vivo bovine livers induced by high intensity focused ultrasound.* Ultrasonics sonochemistry, 2017. **36**: p. 36-41.

[21] Vaezy, S., Martin, R., Kaczkowski, P., Keilman, G., Goldman, B., Yaziji, H., Carter, S., Caps, M., and Crum, L., *Use of high-intensity focused ultrasound to control bleeding.* Journal of vascular surgery, 1999. **29**(3): p. 533-542.

[22] Khokhlova, V.A., Bailey, M.R., Reed, J.A., Cunitz, B.W., Kaczkowski, P.J., and Crum, L.A., *Effects of nonlinear propagation, cavitation, and boiling in lesion formation by high intensity focused ultrasound in a gel phantom.* The Journal of the Acoustical Society of America, 2006. **119**(3): p. 1834-1848.

[23] Bailey, M., Khokhlova, V., Sapozhnikov, O., Kargl, S., and Crum, L., *Physical mechanisms of the therapeutic effect of ultrasound (a review).* Acoustical Physics, 2003. **49**(4): p. 369-388.

[24] Khokhlova, T.D., Canney, M.S., Lee, D., Marro, K.I., Crum, L.A., Khokhlova, V.A., and Bailey, M.R., *Magnetic resonance imaging of boiling induced by high intensity focused ultrasound.* The Journal of the Acoustical Society of America, 2009. **125**(4): p. 2420-2431.

[25] Bailey, M.R., Couret, L.N., Sapozhnikov, O.A., Khokhlova, V.A., Ter Haar, G., Vaezy, S., Shi, X., Martin, R., and Crum, L.A., *Use of overpressure to assess the role of bubbles in focused ultrasound lesion shape in vitro.* Ultrasound in medicine & biology, 2001. **27**(5): p. 695-708.

[26] Kennedy, J.E., *High-intensity focused ultrasound in the treatment of solid tumours.* Nature reviews. Cancer, 2005. **5**(4): p. 321.

[27] Vaezy, S., Shi, X., Martin, R.W., Chi, E., Nelson, P.I., Bailey, M.R., and Crum, L.A., *Real-time visualization of high-intensity focused ultrasound treatment using ultrasound imaging.* Ultrasound in medicine & biology, 2001. **27**(1): p. 33-42.

[28] Zheng, H., Dayton, P.A., Caskey, C., Zhao, S., Qin, S., and Ferrara, K.W., *Ultrasound-driven microbubble oscillation and translation within small phantom vessels.* Ultrasound in medicine & biology, 2007. **33**(12): p. 1978-1987.

[29] Sassaroli, E. and Hynynen, K., *Cavitation threshold of microbubbles in gel tunnels by focused ultrasound.* Ultrasound in medicine & biology, 2007. **33**(10): p. 1651-1660.

[30] Yoshizawa, S., Ikeda, T., Ito, A., Ota, R., Takagi, S., and Matsumoto, Y., *High intensity focused ultrasound lithotripsy with cavitating microbubbles.* Medical & biological engineering & computing, 2009. **47**(8): p. 851-860.

[31] Fong, S.W., Klaseboer, E., Turangan, C.K., Khoo, B.C., and Hung, K.C., *Numerical analysis of a gas bubble near bio-materials in an ultrasound field.* Ultrasound in medicine & biology, 2006. **32**(6): p. 925-942.

[32] Vlaisavljevich, E., Owens, G., Lundt, J., Teofilovic, D., Ives, K., Duryea, A., Bertolina, J., Welling, T.H., and Xu, Z., *Non-Invasive Liver Ablation Using Histotripsy: Preclinical Safety Study in an In Vivo Porcine Model.* Ultrasound in Medicine & Biology, 2017. **43**(6): p. 1237-1251.

[33] Vlaisavljevich, E., Greve, J., Cheng, X., Ives, K., Shi, J., Jin, L., Arvidson, A., Hall, T., Welling, T.H., and Owens, G., *Non-invasive ultrasound liver ablation using histotripsy: Chronic study in an in vivo rodent model.* Ultrasound in medicine & biology, 2016. **42**(8): p. 1890-1902.

[34] Barber, B.P. and Putterman, S.J., *Observation of synchronous picosecond sonoluminescence.* Nature, 1991. **352**(6333): p. 318-320.

[35] Gaitan, D.F., Crum, L.A., Church, C.C., and Roy, R.A., *Sonoluminescence and bubble dynamics for a single, stable, cavitation bubble.* The Journal of the Acoustical Society of America, 1992. **91**(6): p. 3166-3183.

[36] Rabaud, D., Thibault, P., Mathieu, M., and Marmottant, P., *Acoustically bound microfluidic bubble crystals.* Physical review letters, 2011. **106**(13): p. 134501.

[37] Shields IV, C.W., Reyes, C.D., and López, G.P., *Microfluidic cell sorting: a review of the advances in the separation of cells from debulking to rare cell isolation.* Lab on a Chip, 2015. **15**(5): p. 1230-1249.

[38] Augustsson, P., Karlsen, J.T., Su, H.-W., Bruus, H., and Voldman, J., *Iso-acoustic focusing of cells for size-insensitive acousto-mechanical phenotyping.* Nature communications, 2016. **7**.

[39] Gaines, N., *A magnetostriction oscillator producing intense audible sound and some effects obtained.* Physics, 1932. **3**(5): p. 209-229.

[40] Kornfeld, M. and Suvorov, L., *On the destructive action of cavitation.* Journal of Applied Physics, 1944. **15**(6): p. 495-506.

[41] Eller, A.I. and Crum, L.A., *Instability of the motion of a pulsating bubble in a sound field.* The Journal of the Acoustical Society of America, 1970. **47**(3B): p. 762-767.

[42] Mettin, R. and Doinikov, A.A., *Translational instability of a spherical bubble in a standing ultrasound wave.* Applied Acoustics, 2009. **70**(10): p. 1330-1339.

[43] Doinikov, A.A., *Translational motion of a spherical bubble in an acoustic standing wave of high intensity.* Physics of Fluids, 2002. **14**(4): p. 1420-1425.

[44] Doinikov, A.A., *Translational motion of a bubble undergoing shape oscillations.* Journal of Fluid Mechanics, 2004. **501**: p. 1-24.

[45] Eckart, C., *Vortices and streams caused by sound waves.* Physical review, 1948. **73**(1): p. 68.

[46] Hallez, L., Touyeras, F., Hihn, J.-Y., and Bailly, Y., *Characterization of HIFU transducers designed for sonochemistry application: Acoustic streaming.* Ultrasonics sonochemistry, 2016. **29**: p. 420-427.

[47] Kreider, W., Crum, L.A., Bailey, M.R., and Sapozhnikov, O.A., *A reduced-order, single-bubble cavitation model with applications to therapeutic ultrasound.* The Journal of the Acoustical Society of America, 2011. **130**(5): p. 3511-3530.

[48] Yang, X., Roy, R.A., and Holt, R.G., *Bubble dynamics and size distributions during focused ultrasound insonation.* The Journal of the Acoustical Society of America, 2004. **116**(6): p. 3423-3431.

[49] Chen, H., Li, X., and Wan, M., *Spatial–temporal dynamics of cavitation bubble clouds in 1.2 MHz focused ultrasound field.* Ultrasonics sonochemistry, 2006. **13**(6): p. 480-486.

[50] Rozanova-Pierrat, A., *Mathematical analysis of Khokhlov-Zabolotskaya-Kuznetsov (KZK) equation.* 2006.

[51] Hamilton, M.F. and Blackstock, D.T., *Nonlinear acoustics*. Vol. 1. 1998: Academic press San Diego.

[52] Jing, Y., Shen, D., and Clement, G.T., *Verification of the Westervelt equation for focused transducers.* IEEE transactions on ultrasonics, ferroelectrics, and frequency control, 2011. **58**(5).

[53] Tavakkoli, J., Cathignol, D., Souchon, R., and Sapozhnikov, O.A., *Modeling of pulsed finite-amplitude focused sound beams in time domain.* The Journal of the Acoustical Society of America, 1998. **104**(4): p. 2061-2072.

[54] Bakhtiari-Nejad, M., Elnahhas, A., Jung, S., and Shahab, S. *Ultrasound acoustic energy for microbubble manipulation*. in *Active and Passive Smart Structures and Integrated Systems 2017*. 2017. International Society for Optics and Photonics.

[55] Zabolotskaya, E., *Quasiplane waves in the nonlinear acoustics of confined beams.* Sov. Phys. Acoust., 1969. **15**: p. 35-40.

[56] Kuznetsov, V., *Equation of nonlinear acoustics.* Sov. Phys. Acoust., 1971. **16**(4): p. 467-470.

[57] Bakhvalov, N., Zhileĭkin, I.A.k.M., and Zabolotskai͡a, E.a.A., *Nonlinear theory of sound beams*. 1987, New York, NY, USA: Amer Inst of Physics.

[58] Lee, Y.S. and Hamilton, M.F., *Time-domain modeling of pulsed finite-amplitude sound beams.* The Journal of the Acoustical Society of America, 1995. **97**(2): p. 906-917.

[59] Hart, T.S. and Hamilton, M.F., *Nonlinear effects in focused sound beams.* The Journal of the Acoustical Society of America, 1988. **84**(4): p. 1488-1496.

[60] Lucas, B.G. and Muir, T.G., *The field of a focusing source.* The Journal of the Acoustical Society of America, 1982. **72**(4): p. 1289-1296.

[61] Waters, K.R., Hughes, M.S., Mobley, J., Brandenburger, G.H., and Miller, J.G., *On the applicability of Kramers–Krönig relations for ultrasonic attenuation obeying a frequency power law.* The Journal of the Acoustical Society of America, 2000. **108**(2): p. 556-563.

[62] Jiménez, N., Camarena, F., Redondo, J., Sánchez-Morcillo, V., Hou, Y., and Konofagou, E.E., *Time-domain simulation of ultrasound propagation in a tissue-like medium based on the resolution of the nonlinear acoustic constitutive relations.* Acta Acustica united with Acustica, 2016. **102**(5): p. 876-892.

[63] Lee, Y.-S., *Numerical solution of the KZK equation for pulsed finite amplitude sound beams in thermoviscous fluids.* 1993.

[64] Soneson, J.E. *A User-Friendly Software Package for HIFU Simulation*. in *AIP Conference Proceedings*. 2009. AIP.

[65] Soneson, J.E. and Myers, M.R., *Thresholds for nonlinear effects in high-intensity focused ultrasound propagation and tissue heating.* IEEE transactions on ultrasonics, ferroelectrics, and frequency control, 2010. **57**(11).

[66] Soneson, J.E. and Myers, M.R., *Gaussian representation of high-intensity focused ultrasound beams.* The Journal of the Acoustical Society of America, 2007. **122**(5): p. 2526-2531.

[67] O'Donnell, M., Jaynes, E., and Miller, J., *Kramers–Kronig relationship between ultrasonic attenuation and phase velocity.* The Journal of the Acoustical Society of America, 1981. **69**(3): p. 696-701.

[68] Ascher, U.M. and Petzold, L.R., *Computer methods for ordinary differential equations and differential-algebraic equations*. Vol. 61. 1998, Philadelphia, PA, USA: Siam.

[69] Plesset, M., *The dynamics of cavitation bubbles.* Journal of applied mechanics, 1949. **16**: p. 277-282.

[70] Keller, J.B. and Miksis, M., *Bubble oscillations of large amplitude.* The Journal of the Acoustical Society of America, 1980. **68**(2): p. 628-633.

[71] Hay, T.A., Ilinskii, Y.A., Zabolotskaya, E.A., and Hamilton, M.F., *Model for the dynamics of a spherical bubble undergoing small shape oscillations between parallel soft elastic layers.* The Journal of the Acoustical Society of America, 2013. **134**(2): p. 1454-1462.

[72] Doinikov, A.A. and Bouakaz, A., *Theoretical model for coupled radial and translational motion of two bubbles at arbitrary separation distances.* Physical Review E, 2015. **92**(4): p. 043001.

[73] Azhari, H., *Appendix A: typical acoustic properties of tissues.* Basics of Biomedical Ultrasound for Engineers, 2010: p. 313-314.

[74] Wells, P.N., *Ultrasonic imaging of the human body.* Reports on progress in physics, 1999. **62**(5): p. 671.

[75] Soneson, J., *HIFU simulator v1. 2 user's manual*. 2011, FDA.

[76] Longuet-Higgins, M.S., *Monopole emission of sound by asymmetric bubble oscillations. Part 1. Normal modes.* Journal of Fluid Mechanics, 1989. **201**: p. 525-541.

[77] Mei, C.C. and Zhou, X., *Parametric resonance of a spherical bubble.* Journal of Fluid Mechanics, 1991. **229**: p. 29-50.

[78] Rosina, J., Kvasnak, E., Suta, D., Kolarova, H., Malek, J., and Krajci, L., *Temperature dependence of blood surface tension.* Physiological research, 2007. **56**: p. S93.

[79] Elert, G., *Viscosity-The Physics Hypertextbook.*‖. The Physics Hypertextbook,[Online]. Available: http://physics.info/viscosity/.

[80] Eller, A., *Force on a bubble in a standing acoustic wave.* The Journal of the Acoustical Society of America, 1968. **43**(1): p. 170-171.

[81] Apfel, R., *Acoustic cavitation prediction.* The Journal of the Acoustical Society of America, 1981. **69**(6): p. 1624-1633.

[82] Apfel, R.E. and Holland, C.K., *Gauging the likelihood of cavitation from short-pulse, low-duty cycle diagnostic ultrasound.* Ultrasound in medicine & biology, 1991. **17**(2): p. 179-185.

[83] Holland, C.K. and Apfel, R.E., *An improved theory for the prediction of microcavitation thresholds.* IEEE transactions on ultrasonics, ferroelectrics, and frequency control, 1989. **36**(2): p. 204-208.

[84] Basude, R. and Wheatley, M.A., *Generation of ultraharmonics in surfactant based ultrasound contrast agents: use and advantages.* Ultrasonics, 2001. **39**(6): p. 437-444.

[85] Schoellhammer, C.M., Schroeder, A., Maa, R., Lauwers, G.Y., Swiston, A., Zervas, M., Barman, R., DiCiccio, A.M., Brugge, W.R., and Anderson, D.G., *Ultrasound-mediated gastrointestinal drug delivery.* Science translational medicine, 2015. **7**(310): p. 310ra168-310ra168.

[86] Segers, T. and Versluis, M., *Acoustic bubble sorting for ultrasound contrast agent enrichment.* Lab on a Chip, 2014. **14**(10): p. 1705-1714.

[87] Ding, X., Peng, Z., Lin, S.-C.S., Geri, M., Li, S., Li, P., Chen, Y., Dao, M., Suresh, S., and Huang, T.J., *Cell separation using tilted-angle standing surface acoustic waves.* Proceedings of the National Academy of Sciences, 2014. **111**(36): p. 12992-12997.

[88] Melde, K., Mark, A.G., Qiu, T., and Fischer, P., *Holograms for acoustics.* Nature, 2016. **537**(7621): p. 518.

[89] Melde, K., Choi, E., Wu, Z., Palagi, S., Qiu, T., and Fischer, P., *Acoustic fabrication via the assembly and fusion of particles.* Advanced Materials, 2018. **30**(3): p. 1704507.

[90] Ma, Z., Holle, A.W., Melde, K., Qiu, T., Poeppel, K., Kadiri, V.M., and Fischer, P., *Acoustic Holographic Cell Patterning in a Biocompatible Hydrogel.* Advanced Materials, 2020. **32**(4): p. 1904181.

[91] Cox, L., Melde, K., Croxford, A., Fischer, P., and Drinkwater, B.W., *Acoustic Hologram Enhanced Phased Arrays for Ultrasonic Particle Manipulation.* Physical Review Applied, 2019. **12**(6): p. 064055.

[92] Gu, Y., Chen, C., Rufo, J., Shen, C., Wang, Z., Huang, P.-H., Fu, H., Zhang, P., Cummer, S.A., and Tian, Z., *Acoustofluidic Holography for Micro-to Nanoscale Particle Manipulation.* ACS Nano, 2020.

[93] Duffy, D.C., McDonald, J.C., Schueller, O.J., and Whitesides, G.M., *Rapid prototyping of microfluidic systems in poly (dimethylsiloxane).* Analytical chemistry, 1998. **70**(23): p. 4974-4984.

[94] Mekki-Berrada, F., Thibault, P., and Marmottant, P., *Acoustic pulsation of a microbubble confined between elastic walls.* Physics of Fluids, 2016. **28**(3): p. 032004.

[95] Melde, K., Fischer, P., and Weber, P.-k., *Apparatus and method for creating a holographic ultrasound field in an object*. 2018, Google Patents.

[96] Garstecki, P., Gitlin, I., DiLuzio, W., Whitesides, G.M., Kumacheva, E., and Stone, H.A., *Formation of monodisperse bubbles in a microfluidic flow-focusing device.* Applied Physics Letters, 2004. **85**(13): p. 2649-2651.

[97] https://www.stratasys.com/3d-printers/objet260-connex3.

[98] https://www.olympus-ims.com/en/store/immersion-transducers/.

[99] Kinsler, L.E., Frey, A.R., Coppens, A.B., and Sanders, J.V., *Fundamentals of acoustics.* 1999: p. 560.

[100] Selfridge, A.R., *Approximate material properties in isotropic materials.* IEEE transactions on sonics and ultrasonics, 1985. **32**(3): p. 381-394.

[101] Baac, H.W., Ok, J.G., Maxwell, A., Lee, K.-T., Chen, Y.-C., Hart, A.J., Xu, Z., Yoon, E., and Guo, L.J., *Carbon-nanotube optoacoustic lens for focused ultrasound generation and high-precision targeted therapy.* Scientific reports, 2012. **2**: p. 989.

[102] Collins, D.J., Morahan, B., Garcia-Bustos, J., Doerig, C., Plebanski, M., and Neild, A., *Two-dimensional single-cell patterning with one cell per well driven by surface acoustic waves.* Nature communications, 2015. **6**(1): p. 1-11.

[103] Guo, F., Mao, Z., Chen, Y., Xie, Z., Lata, J.P., Li, P., Ren, L., Liu, J., Yang, J., and Dao, M., *Three-dimensional manipulation of single cells using surface acoustic waves.* Proceedings of the National Academy of Sciences, 2016. **113**(6): p. 1522-1527.

[104] Reboud, J., Bourquin, Y., Wilson, R., Pall, G.S., Jiwaji, M., Pitt, A.R., Graham, A., Waters, A.P., and Cooper, J.M., *Shaping acoustic fields as a toolset for microfluidic manipulations in diagnostic technologies.* Proceedings of the National Academy of Sciences, 2012. **109**(38): p. 15162-15167.

[105] Wu, M., Ouyang, Y., Wang, Z., Zhang, R., Huang, P.-H., Chen, C., Li, H., Li, P., Quinn, D., and Dao, M., *Isolation of exosomes from whole blood by integrating acoustics and microfluidics.* Proceedings of the National Academy of Sciences, 2017. **114**(40): p. 10584-10589.

[106] Devendran, C., Gralinski, I., and Neild, A., *Separation of particles using acoustic streaming and radiation forces in an open microfluidic channel.* Microfluidics and nanofluidics, 2014. **17**(5): p. 879-890.

[107] Marga, F., Neagu, A., Kosztin, I., and Forgacs, G., *Developmental biology and tissue engineering.* Birth Defects Research Part C: Embryo Today: Reviews, 2007. **81**(4): p. 320-328.

[108] Guven, S., Chen, P., Inci, F., Tasoglu, S., Erkmen, B., and Demirci, U., *Multiscale assembly for tissue engineering and regenerative medicine.* Trends in biotechnology, 2015. **33**(5): p. 269-279.

[109] Mao, A.S. and Mooney, D.J., *Regenerative medicine: current therapies and future directions.* Proceedings of the National Academy of Sciences, 2015. **112**(47): p. 14452-14459.

[110] Holle, A.W., Young, J.L., Van Vliet, K.J., Kamm, R.D., Discher, D., Janmey, P., Spatz, J.P., and Saif, T., *Cell–extracellular matrix mechanobiology: forceful tools and emerging needs for basic and translational research.* Nano letters, 2018. **18**(1): p. 1-8.

Chapter 6

Conclusions and future research directions

6.1 General conclusions

This dissertation aimed to develop a range of new techniques to enhance the contactless ultrasonic transfer of power from an acoustic source or a transmitter, typically a piezo transducer disk, to receivers/sensors in an acoustic medium of interest such as water or human tissue. Particularly, we developed a technique to implement acoustic holograms in ultrasonic power transfer (UPT) systems. Using acoustic holograms alongside simple and single element transducers to arbitrarily shape complex ultrasound fields is a new approach introduced recently by Melde *et al*. [1]. This technique offers promising advantages, compared to the conventional phased array transducers, including the increased degree of freedom and phase fidelity, simplification of design and fabrication, and the ability to scale well to smaller or larger aperture size or information content and higher frequencies. We combined this simple and cost-effective approach with the ultrasonic acoustic energy transfer (UAET) systems using the diffraction-limited acoustic transmission phase holograms to selectively focus and pattern the contactless ultrasonic transfer of power to the spatially-distributed sensors [2].

The first technique, i.e., the hologram implementation in UPT, was investigated mainly in chapters 2 and 3. In chapter 2, different single and multi-focal phase holograms were designed using an optimization algorithm, iterative angular spectrum approach (IASA), in which, in each forward iteration, a binary target amplitude images were imposed on the amplitude of the acoustic fields in a particular target plane, a specific distance from the hologram plane, and the complex phase remained as a free variable. After multiple numerical forward and backward wave propagations, i.e., few tens of iterations, the acoustic fields in the target plane were converged to the desired

image patterns. The final phase maps in the hologram plane were then simply rendered into the thickness profile of low-cost 3D-printed transmission phase plates for physical implementations of holograms in UPT systems. Experimentally, it was demonstrated that using multi-focal holograms in conjunction with UAET allows for enhanced and selective transfer of energy to receivers located at predetermined focal points. In chapter 3, the IASA optimization algorithm was modified for the design of multi-functional holograms, i.e., holograms that can reconstruct multiple holographic images at different target planes and by switching the driving frequency, called, respectively, multi-image-plane and multi-frequency patterning holograms [3]. Numerically and experimentally, multiple desired acoustic patterns were reconstructed, sensitive to different target planes and frequencies. These holograms enabled the full generation of 3D volumetric fields and dynamic real-time reconfiguration of the transducer and the holographic results verified the fact that applicable multi-functional holograms can be implemented in UPT systems. 3D-printed acoustic phase holograms are also valuable to a wide range of diagnostic and therapeutic ultrasound applications, including, but not limited to, selectively and noninvasively powering medical implants, blood-brain barrier opening or neuromodulation [4], and improving ultrasound medical imaging systems [5].

The second technique, investigated in chapter 4, was the use of two-layer matching layers in UPT systems to reduce the losses associated with the reflection of sound waves due to acoustic impedance mismatch between the acoustic medium and transducer materials, including the transmitter and receiver. In the two-layer matching structure, one of the layers was selected as the used glue to bond the other layer to the front side of the transducers [6]. The input acoustic pressure on the receiver was determined via the angular spectrum approach (ASA) using the experimentally measured transmitter output pressure distribution. It was shown that using matching layers improves the ultrasonic power transmission into the medium and then to the receiver, which significantly increases the voltage delivered to an electrical load and enhances the electrical power output [7]. Considering a wide range of materials including metals, ceramics, and polymers, we developed a design platform in which the acoustically matched transducers can be simply constructed. The construction includes the determination of required material layers' thicknesses to acoustically match transducers to an acoustic medium of interest at a particular frequency. We also showed that using more than two matching layers is not only difficult, time-consuming, and costly, but also does not lead to more enhancement of ultrasonic transfer of power.

In chapter 5, an analytical model was developed for the nonlinear dynamics of microbubbles [8] (stable cavitation) exposed to a high-intensity focused ultrasound (HIFU) field, which includes the effects of acoustic nonlinearity, diffraction, and absorption of the medium [9]. This was motivated by several biomedical ultrasound applications that entail the problems of manipulation of microbubbles in the HIFU field. The examples include diagnostic applications such as ultrasound-activated microbubbles used as contrast agents in ultrasound scatter imaging methods and therapeutic applications such as enhanced gene delivery and localized active drug delivery. Finally, the technique of acoustic holography using cost-effective 3D-printed acoustic phase holograms for microfluidic devices were investigated for patterning, sorting, and manipulation of microbubbles, particles, and cells, which expected to have the enhanced impact in medical ultrasound systems.

6.2 Future research directions

Several potential future research directions can develop from this dissertation, including, but not limited to, the following areas:

- Simultaneous modulation of both phase and amplitude of complex acoustic fields by using two hologram plates [10] in UPT systems. This new technique leads to more uniformity of the target pressure amplitude and higher phase fidelity compared to that of using a single phase hologram.
- Using an acoustic hologram in conjunction with a curved transducer (instead of a flat transducer) [4] in UPT systems to further enhance the electrical power output, or in ultrasound medical systems, e.g., generating selective heating using a HIFU transducer alongside a hologram for thermal ablation or lesioning in brain therapy.
- Using an acoustic hologram in conjunction with a phased 2D array transducer with a small number of elements [11] constructing full 3D assembly in UPT systems to benefit from both the patterning of the acoustic holography and the adaptivity of the dynamical reconfigurable real-time system. Alternatively, to circumvent the static nature of a single hologram in UPT systems, one can implement multiple holograms stacked together to reconfigure the resulting field in real-time by changing the position of the holograms [12].
- Implementing the designed multi-image-plane and multi-frequency holograms for UPT systems in practice, by placing a sufficient number of receiver elements in a 2D array at particular target planes. The enhanced electrical power output from targeted receivers

sensitive to the distances from the hologram plane and to the driving frequencies can be verified.

- Modification of the designed acoustic holograms allowing for the correction of medium-induced wavefront aberrations that occur due to the distortion of sound waves passing through media with different sound speeds such as tissue aberrations [4, 13-15].
- Construction of ultrasonic transducers using the developed two-layer matching configuration in UPT systems, implementing some of the materials listed in chapter 4, to practically verify the significant enhancement of electrical power output using acoustic impedance matching layers.
- Implementing the designed holograms for microfluidic channels in practice and verification of their functionality to manipulate, pattern, and sort cells and particles [1, 16-18], as well as ultrasound-activated microbubbles for enhanced drug delivery [19].

Bibliography

[1] Melde, K., Mark, A.G., Qiu, T., and Fischer, P., *Holograms for acoustics.* Nature, 2016. **537**(7621): p. 518.

[2] Bakhtiari-Nejad, M., Elnahhas, A., Hajj, M.R., and Shahab, S., *Acoustic holograms in contactless ultrasonic power transfer systems: Modeling and experiment.* Journal of Applied Physics, 2018. **124**(24): p. 244901.

[3] Brown, M.D., Cox, B.T., and Treeby, B.E., *Design of multi-frequency acoustic kinoforms.* Applied Physics Letters, 2017. **111**(24): p. 244101.

[4] Maimbourg, G., Houdouin, A., Deffieux, T., Tanter, M., and Aubry, J.-F., *3D-printed adaptive acoustic lens as a disruptive technology for transcranial ultrasound therapy using single-element transducers.* Physics in Medicine & Biology, 2018. **63**(2): p. 025026.

[5] Kruizinga, P., van der Meulen, P., Fedjajevs, A., Mastik, F., Springeling, G., de Jong, N., Bosch, J.G., and Leus, G., *Compressive 3D ultrasound imaging using a single sensor*. Science advances, 2017. **3**(12): p. e1701423.

[6] Callens, D., Bruneel, C., and Assaad, J., *Matching ultrasonic transducer using two matching layers where one of them is glue.* Ndt & E International, 2004. **37**(8): p. 591-596.

[7] Bakhtiari-Nejad, M., Hajj, M.R., and Shahab, S., *Dynamics of acoustic impedance matching layers in contactless ultrasonic power transfer systems.* Smart Materials and Structures, 2020. **29**(3): p. 035037.

[8] Doinikov, A.A., *Translational motion of a bubble undergoing shape oscillations.* Journal of Fluid Mechanics, 2004. **501**: p. 1-24.

[9] Bakhtiari-Nejad, M. and Shahab, S. *Effects of Nonlinear Propagation of Focused Ultrasound on the Stable Cavitation of a Single Bubble*. in *Acoustics*. 2018. Multidisciplinary Digital Publishing Institute.

[10] Brown, M.D., *Phase and amplitude modulation with acoustic holograms.* Applied Physics Letters, 2019. **115**(5): p. 053701.

[11] Cox, L., Melde, K., Croxford, A., Fischer, P., and Drinkwater, B.W., *Acoustic Hologram Enhanced Phased Arrays for Ultrasonic Particle Manipulation.* Physical Review Applied, 2019. **12**(6): p. 064055.

[12] Brown, M.D., Cox, B.T., and Treeby, B.E., *Stackable acoustic holograms.* Applied Physics Letters, 2020. **116**(26): p. 261901.

[13] Hertzberg, Y. and Navon, G., *Bypassing absorbing objects in focused ultrasound using computer generated holographic technique.* Medical physics, 2011. **38**(12): p. 6407-6415.

[14] Ferri, M., Bravo, J.M., Redondo, J., and Sánchez-Pérez, J.V., *Enhanced numerical method for the design of 3-d-printed holographic acoustic lenses for aberration correction of single-element transcranial focused ultrasound.* Ultrasound in medicine & biology, 2019. **45**(3): p. 867-884.

[15] Jiménez-Gambín, S., Jiménez, N., Benlloch, J.M., and Camarena, F., *Holograms to focus arbitrary ultrasonic fields through the skull.* Physical Review Applied, 2019. **12**(1): p. 014016.

[16] Ma, Z., Holle, A.W., Melde, K., Qiu, T., Poeppel, K., Kadiri, V.M., and Fischer, P., *Acoustic Holographic Cell Patterning in a Biocompatible Hydrogel.* Advanced Materials, 2020. **32**(4): p. 1904181.

[17] Gu, Y., Chen, C., Rufo, J., Shen, C., Wang, Z., Huang, P.-H., Fu, H., Zhang, P., Cummer, S.A., and Tian, Z., *Acoustofluidic Holography for Micro-to Nanoscale Particle Manipulation.* ACS Nano, 2020.

[18] Melde, K., Choi, E., Wu, Z., Palagi, S., Qiu, T., and Fischer, P., *Acoustic fabrication via the assembly and fusion of particles.* Advanced Materials, 2018. **30**(3): p. 1704507.

[19] Baac, H.W., Ok, J.G., Maxwell, A., Lee, K.-T., Chen, Y.-C., Hart, A.J., Xu, Z., Yoon, E., and Guo, L.J., *Carbon-nanotube optoacoustic lens for focused ultrasound generation and high-precision targeted therapy.* Scientific reports, 2012. **2**: p. 989.